國立臺灣大學生物資源暨農學院生物機電工程學系

碩士論文

Department of Biomechatronics Engineering

College of Bioresources and Agriculture

National Taiwan University

Master Thesis

基於實驗、理論和有限元素法增加雷射誘導前向轉移於金屬積層製造之附著力與電特性

Enhancing adhesion and electrical properties for laser-induced forward transfer based additive manufacturing of metals

Ankit Das

指導教授：丁健芳 博士

Advisor: Chien-Fang Ding, Ph.D.

中華民國 112 年 7 月

July 2023

doi:10.6342/NTU202301493

國立臺灣大學碩士學位論文
口試委員會審定書

基於實驗、理論和有限元素法增加雷射誘導前向轉移於金屬積層製造之附著力與電特性

Enhancing adhesion and electrical properties for laser-induced forward transfer based additive manufacturing of metals

本論文係 Ankit Das 君（R09631048）在國立臺灣大學生物機電工程學系、所完成之碩士學位論文，於民國 112 年 07 月 07 日承下列考試委員審查通過及口試及格，特此證明

口試委員：丁健芳 （簽名）

（指導教授）

黃振康 教授 黃振康

李貫銘 教授 李貫銘

系主任、所長 （簽名）

doi:10.6342/NTU202301493

Acknowledgement

I feel honored to express my deepest and most sincere gratitude to my Master's advisor Professor Chien-Fang Ding, for his valuable guidance, suggestions and encouragement throughout the progress of this research work. I am grateful to him for providing me with the freedom in my research work. Apart from his professional support as an advisor in my research, Prof. Ding has been kind and understanding, who have supported me emotionally and morally during my difficult times and guided me in the right path.

I would take this opportunity to express my sense of gratitude to the defense committee members for saving time from their busy schedule to attend my oral thesis defense and generously providing their invaluable remarks on my research to help me improve my work. I would also I like to thank other faculty members for their kind help and encouragement, and to all the non-teaching staff of the department, without whose help, I would not have completed this study.

I would like to acknowledge the support of my lab members, Mr. Pang-Pin Liu, Mr. Dian-Hong Wu, Mr. Hong-Lin Huang and Mr. Ping-Jian Huang for always being helpful in my research work and other issues. I would like to thank all lab member for being helpful and making my Master's study easy. I am extremely grateful to be a part of this laboratory with the wonderful advisor and lab mates.

I would also like to express my thankfulness to my dear friends Tzu-Chun Lin, Kalpana Shankhwar, Sandeep Paral, Nilanjana Pal, Chia-Hsiu Kuo, Samarpan Deb Majumder, Sumit Das, Arindam Samanta, Pavitra Srivastava, Arvind Singh Rathode, and Ashish Gaurav for their good company, care and emotional support during my stay at National Taiwan University.

Last but not the least, I wish to express my gratitude to my father Mr. Alok Kumar Das, my mother Mrs. Tanusree Das and my brother Mr. Arnab Das for their love, patience and constant support during my period of stay in Taiwan. I deeply thank my family for their belief in me, for encouraging me to achieve my goals and for celebrating the small steps of my research success during all the years of my Master's study. I wish everyone great health, joy and happiness.

doi:10.6342/NTU202301493

摘要

近年來，雷射誘導前向轉移 (Laser-induced forward transfer, LIFT) 已成為一種廣泛使用的製造技術。這種先進的一步式、非接觸式、省時且經濟高效的方法已在各種電子、生物和化學應用的各種感測器的製造中得到普及。基於 LIFT 的製程技術具有高分辨率和靈活性等優點，因此，使用 LIFT 在積層製造上之各種應用中有著巨大的潛力。LIFT 幾乎有能力轉移任何材料，可利用這種技術可以製作出各種具有複雜細節的結構。本論文聚焦在使用 LIFT 對金屬進行積層製造以展示未來的應用，因此，利用 LIFT 來轉移銅 (Cu)、銀 (Ag) 和鉑 (Pt)等金屬。

先期實驗顯示，沉積金屬材料和接收基板之間有低的附著力；沉積結構中的不連續性降低了導電率，再者，Ag 和 Pt 薄膜的脆性和不同材料特性的差異使得通過 LIFT 進行的積層製造極具挑戰性。因此，在本論文中作出了許多實驗來提高轉移質量。例如，使用雷射表面紋理化 (Laser surface texturing, LST) 和光聚合固化技術將表面粗糙度引入接收基板。此外，探討了在低壓和大氣環境中進行 LIFT 實驗。最後，LIFT 轉移過程是根據實驗和相關表徵來進行優化，包括 SEM、EDS、XRD 和電阻測試，以了解沉積材料作為軟性感測元件電極的可行性。此外，本論文也使用有限元素法 (Finite element method, FEM)來分析 LIFT 轉移過程，以有效地將實驗參數優化。最後，使用已建立的理論和 FEM 結果進行了能量研究，以實現影響 LIFT 過程的主要物理現象。

關鍵詞：雷射誘導前向轉移（LIFT）；雷射表面紋理化(LST)；積層製造（AM）；能量分析；有限元素法 (FEM)

doi:10.6342/NTU202301493

Abstract

Laser-induced forward transfer (LIFT) has been a widely used manufacturing technique in recent times. The novel one-step and contactless method have gained popularity in the manufacturing of a wide range of sensors for various electronic, biological, and chemical applications. Nevertheless, LIFT based printing has advantages such as high resolution and flexibility. Additive manufacturing has shown significant potential in various applications. LIFT has the ability to manufacture almost any materials; therefore, utilizing such a process in additive manufacturing enables printing of a wide range of materials with intricate details. This research concerns about the additive manufacturing of metals via LIFT to demonstrate future applications. Therefore, this research utilizes LIFT for printing copper (Cu), silver (Ag) and platinum (Pt).

However, experimental evidence has shown weak adhesion between the deposited material and receiver substrate. Moreover, the discontinuities in the deposit structure reduces the conductivity. In addition, the brittle nature and difference in distinct material properties of Ag and Pt thin films make additive manufacturing via LIFT extremely challenging. Therefore, numerous efforts are made in this work to enhance the printing quality. For instance, surface roughness is introduced to the receiver substrate using laser surface texturing (LST) and vat photopolymerization. Furthermore, conducting LIFT in low pressure and ambient environments are investigated. Simultaneously, the effects of the aforementioned efforts shall be investigated on soft and hard polymers with variable thickness based on their shore hardness. Finally, the LIFT process shall be optimized based on the aforementioned experiments and relevant characterizations. Scotch tape tests are carried out for determining the adhesion strength. Further characterizations include SEM, EDS, XRD and conductivity tests for understanding the feasibility of the deposited materials as flexible sensor electrodes. In addition, finite element methods (FEM) has been utilized for the LIFT process for effective implementation in process optimization. Finally, energy studies have been made using pre-established theory and FEM results for realizing the major physical phenomena affecting the LIFT process. Considering the potential benefits of the LIFT process, successful fabrication of sensor electrodes may be carried out in future.

Keywords: Laser-induced forward transfer (LIFT); Laser surface texturing (LST); Additive manufacturing (AM); Energy analysis; Finite element methods (FEM)

doi:10.6342/NTU202301493

Table of Contents

doi:10.6342/NTU202301493

doi:10.6342/NTU202301493

List of Figures

doi:10.6342/NTU202301493

doi:10.6342/NTU202301493

doi:10.6342/NTU202301493

doi:10.6342/NTU202301493

doi:10.6342/NTU202301493

doi:10.6342/NTU202301493

List of Tables

doi:10.6342/NTU202301493

doi:10.6342/NTU202301493

doi:10.6342/NTU202301493

Chapter 1 Introduction

One of the major medical care burdens and challenges of the present is diabetes. As per WHO, it is expected that there will be a population rise of 37% between 2000 and 2030, and the number of people will escalate by 114% (Wild et al., 2004). In 2019, according to WHO reports, 422 million adults have acquired diabetes, resulting in 3.7 million deaths due to diabetes and high blood glucose and approximately 1.5 million deaths caused solely by diabetes (Wild et al., 2004). It is known that diabetes originally from European populations has been reproduced in Asia. Asia is one of the major diabetes hubs. According to the rising population and urbanization rates, the two leading countries in terms of diabetic population will be India and China with 79.4 million and 42.3 million respectively by 2030 (Wild et al., 2004, Sicree et al., 2006). Other Asian countries which follow are Indonesia, Pakistan, Bangladesh and Philippines. Statistics predict the world's population to be around 7.9 billion by 2025. Among which India, China and Pakistan contributes to one of the highest populations at 21%, 12% and 5%, respectively. Strong genetic component is seen in Type II diabetes and first degree relative is observed in Asian patients (Viswanathan et al., 1996, Ng et al., 2001).

Diabetes has become one of the top ten cause of death in the world. Taiwan itself has over 2 million patients and numbers are still rising at 25,000 patients annually. Asymptomatic diabetes is found in young age children (3-5 years) and out of those, one-fourth of the children become diabetes patients. The rising cases of diabetes all over the world has struck major concerns over the countries. In order to treat diabetes, successful monitoring of blood glucose levels is necessary. Significant research is being made to fight against diabetes. One way to contribute to this is to fabricate cost effective, simple, quick and accurate sensors for monitoring blood glucose levels constantly. Traditional blood glucose monitoring techniques have a number of limitations. These techniques (traditional) are intrusive, discontinuous and do not have the ability to monitor blood sugar levels in real time. Furthermore, drawing blood can often lead to complications and discomfort to patients.

doi:10.6342/NTU202301493

Human sweat has a small amount of glucose content which directly represents the blood glucose levels. Numerous studies in the past suggested accurate estimation of blood glucose levels can be made from sweat glucose concentrations. Moyer et al. (Moyer et al., 2012) studied the glucose in sweat obtained from forearm using chromatography methods. Suitable comparisons were made with blood glucose meter results and it was found that significant relations exist between sweat and blood glucose levels. The only limitation was the contamination of the sweat from skin surface, if eliminated, sweat can be a suitable indicator of blood glucose levels. Recently, Sempionatto et al. (Sempionatto et al., 2021) developed a novel method to accurately determine the blood glucose levels by an electrochemical touch-based fingertip sweat sensor. Such sensor is a major breakthrough towards diabetes management by enabling patients to self-monitor glucose levels without any discomfort or complications.

The commonly used methods to fabricate glucose sensors are inject printing and screen printing (Klonoff, 1997, Kong et al., 2014). However, the mentioned processes are time consuming, complicated and multistep processes. Therefore, need for an alternative simple and quick method to fabricate sensors has become important. Laser-writing has the potential to simply manufacture sensors in a one-step time and cost-effective process. Past research shows that laser-based manufacturing led to successful fabrication of sensors such as memristors, humidity and tactile sensors (Zhou et al., 2019, Liu et al., 2020a, Li et al., 2020). Furthermore, laser-writing provides additional advantages like contactless and maskless process, adaptable to wide range of substrates (i.e. glass, silicon polyamide etc.) and controllable laser parameters; thereby, it increases the field of application (Back and Kang, 2018, Soltani et al., 2015, Peng et al., 2019). Recently, Zhou et al. (Zhou et al., 2021) developed a low-cost glucose sensor based on Cu_2O/Cu structure by laser-writing. Cu promoted the conductivity and the porous structure increased glucose sensing reaction sites. Excellent performance was observed (detection potential: 0.3V, linear range: 0–2.5 mM, LOD: 0.34 μM, response time: 3 s). Therefore, it is evident that laser-writing can pave way for manufacturing of wearable (flexible) biosensors and with the rising demand which opens new direction in wearable electronics.

doi:10.6342/NTU202301493

Another possible and efficient way to fabricate sensors, which is the focus of the proposed research is laser-induced forward transfer (LIFT). LIFT was first introduced by Bohandy et al. (Bohandy et al., 1986) in 1986. The LIFT process was motivated from the research of Levene et al. (Levene et al., 1970) where, Nd:YAG laser was used to transfer black ink on to a substrate. The first application of LIFT was a deposition of Copper (Cu) metal on fused silica and silicon. Following the invention of LIFT, Adrian et al. (Adrian et al., 1987) from Bohandy's group studied the metal deposition mechanism for the first time in 1987. Numerous researches were made to establish and study various process parameters for better understanding of the LIFT process (Sano et al., 2002). With the improvement in the process, LIFT has been successfully been incorporated for sensor fabrication (Papazoglou and Zergioti, 2017). Details on the process are discussed in the subsequent sections. Therefore, considering the above limitations, the proposed research serves as the founding steps to utilize LIFT to additively manufacture metals which can be potentially be utilized as sensor electrodes in the near future. Therefore, achieving the objective to fabricate sensors with continuous glucose measurement would be a novel and unique application for the health care domain, enabling this research to have great future potential.

According to the Institute for Scientific Information (ISI) web of science statistics, a rapid rise in the number of publications and citations. Fig. 1.1 shows the statistics with the keyword "Laser induced forward transfer" is observed over the years. In addition to publications, number of patents also provide an insight on the innovation aspect of LIFT with a firm legal protection of the technology. Public patent databases from European Patent Office (EPO) and the United States Patent and Trademark Office (USPTO) show a continuous rise in the number of patents and patent publications (with keywords "laser induced forward transfer") (Florian and Serra, 2023). Florian and Serra (Florian and Serra, 2023) outlined three major areas which will see commercialization in the upcoming future in laser printing, namely (i) additive manufacturing, (ii) paper printing and (iii) medicine, with a total gross value of 75.3M, 48.5M and 1500M USD, respectively, in 2022. Therefore, the revenues provide opportunity for LIFT in the foreseeable future.

Albeit research on LIFT has been vastly made; however, almost none have reported the critical issues associated to LIFT. Identifying the challenges and limitations of the process is

doi:10.6342/NTU202301493

essential for its successful utilization. Therefore, this study focuses on the critical issues related to the LIFT process and provides valuable insights on how to mitigate them. First, a background on the LIFT process is introduced and is classified on a broad basis. Subsequently, important process parameters which affect the quality of the transfer process are introduced. Secondly, detailed discussions on phenomena like shockwave generation, weak bonding between transfer material, weak deposit-receiver substrate adhesion, and nonuniform deposition, which greatly influences the transfer process are reported. Furthermore, important process highlights and their notable limitations are summarized. Simultaneously, encouraging discussions are made to provide effective solutions to the mentioned limitations of the LIFT process. Subsequent to the discussions, experimentations have been made to mitigate the mentioned limitations; therefore, this study has successfully deposited additive layers of Cu, Ag and Pt for future sensor electrode applications. The deposits are characterized using various mechanical and materials characterizations for validation of the proposed mitigation methods. Finally, an energy analysis model is proposed and validated using finite element methods (FEM) and theoretical (analytical) approximations, enabling a greater insight on the transfer mechanisms involved in LIFT.

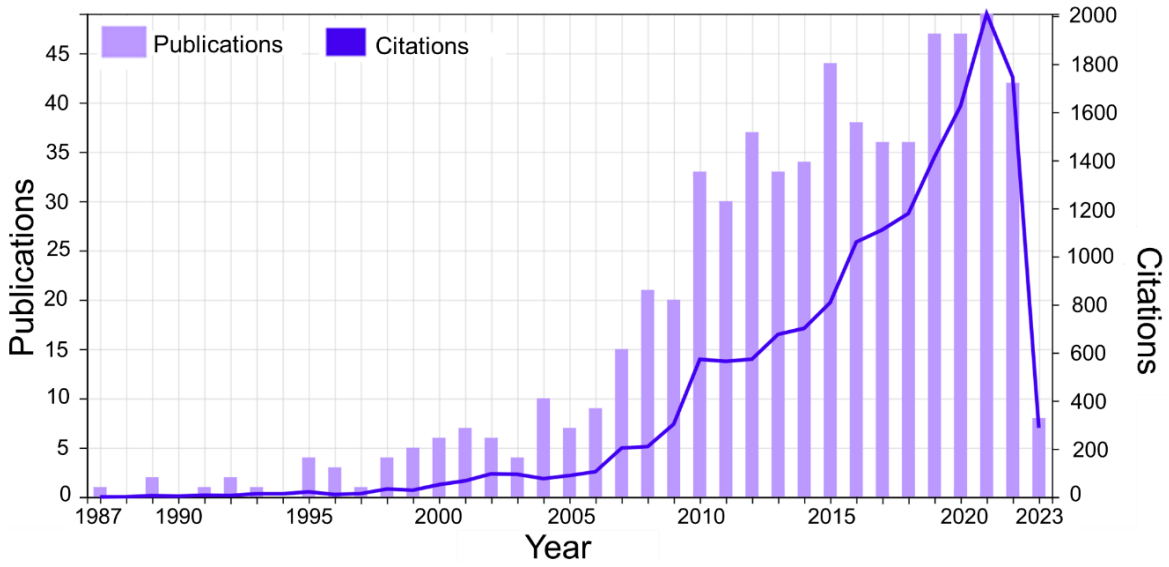

Fig. 1.1: Web of science statistics for publications and citations made for LIFT over the years as of 25/02/2023.

doi:10.6342/NTU202301493

Chapter 2 Theoretical background

Additive manufacturing is one of the rapidly developing manufacturing processes that is being incorporated in our daily lives. Additive manufacturing have a variety of synonyms in technological aspects, such as 3D printing, rapid prototyping, layered manufacturing, etc. (Bose et al., 2019). Additive manufacturing has broken the chains of limitations for traditional manufacturing. Thereby, it makes manufacturing easier, cost effective, accurate and rapid. Some of the widely used AM processes are stereolithography (SLA), selective laser melting (SLM), selective laser sintering (SLS), 3D printing, coating technologies, etc. In light of the advantages offered by additive manufacturing, one such process is laser-induced forward transfer (LIFT) which has wide application in sensor industry.

LIFT is a high-resolution printing/transfer process used for depositing smidgen of materials on a substrate. Either solid or liquid phase media can be used in this process. In short, the desired material is transferred from a donor material to a substrate material with the help of pulsed laser irradiation. Various researches have utilized LIFT for material specific application like DNA (Serra et al., 2004), polymers (Thomas et al., 2007), nanotubes (Palla-Papavlu et al., 2010a), biomaterials (Zergioti et al., 2005, Doraiswamy et al., 2006), metals (Berg et al., 2015, Grant-Jacob et al., 2013), particles (Florian et al., 2015, Kim et al., 2009, Rapp et al., 2009b), and inks (Palla-Papavlu et al., 2010b, Kononenko et al., 2009). Nearly all materials can be deposited using the LIFT process, thereby providing evidence for sensitive material printing in a one-step solvent free method. Other applications of LIFT are utilized as an alternative manufacturing process for fabrication of transistors (Rapp et al., 2009b, Makrygianni et al., 2013, Rapp et al., 2012), MEMS (Birnbaum et al., 2010, Wang et al., 2010), organic LEDs (Fardel et al., 2007, Shaw-Stewart et al., 2013, Kattamis et al., 2011), sensors (Tsuboi et al., 2007, Palla-Papavlu et al., 2014, Di Pietrantonio et al., 2012, Boutopoulos et al., 2011), etc.

Human senses receive and process information from the surrounding environment; however, human senses have limitations (Powner and Yalcinkaya, 1995). Therefore, the need of practical sensors, which overcome the limitations posed by nature (Powner and Yalcinkaya, 1995). For example, a device with an output signal in the form of a digital number or some

doi:10.6342/NTU202301493

other light intensity, fabricated using a current generator, voltage amplifier, and signal converter (analog to digital), is also termed as a sensor (D'Amico and Di Natale, 2001). LIFT has been widely utilized for sensor fabrication and have gained popularity recently. Advantages of the LIFT process outperforms the disadvantage of debris generation. Some of the advantages offered by the LIFT process is the ability to deposit sensitive materials, thereby providing the potential to improve the sensor selectivity (Di Pietrantonio et al., 2012). Subsequently, the fact that LIFT can utilize a wide variety of materials, thereby enabling fabrication of high sensitive sensors, and making the process versatile for a wide range of applications (Mattle et al., 2013a).

In addition to the aforementioned works, numerous modelling works have been incorporated for LIFT processes. One of the early works by Prof. Arnold's group at Princeton University set the beginning of the LIFT modelling process (Pohanka and Skládal, 2008). They used a pressure induced transfer for thin liquid films with two phase level set method for efficient modelling of the LIFT process. Followed by this, a number of researches works introduced and discussed methods to model the LIFT process. Morales et al. (Morales et al., 2017) modeled the blister-actuated LIFT process using a laminar two-phase flow with a moving wall level set interface. Labella et al. (Moreno Labella, 2021, Moreno-Labella et al., 2020) modeled LIFT and BA-LIFT processes using two phase flow phase field FEM model. Therefore, with successful modeling of the LIFT process, several parametric optimizations can be made, saving time and expenses.

2.1. Laser induced forward transfer (LIFT)

2.1.1. History and process description

Laser induced forward transfer was first introduced by Bohandy et al. (Bohandy et al., 1986) in 1986. The LIFT process was motivated from the research of Levene et al. (Levene et al., 1970) where Nd:YAG laser was used to transfer black ink on to a substrate. The first application of LIFT was to deposit Copper (Cu) metal on fused silica and silicon. Following the invention of LIFT, Adrian et al. (Adrian et al., 1987) from Bohandy's group studied the metal deposition mechanism for the first time in 1987. In the early days after the introduction of the LIFT process, droplets and condensed vapor was proposed to be the mechanism for

doi:10.6342/NTU202301493

the transfer and deposition of the film material onto the receiver substrate (Ehrlich et al., 1988). A model based on partial evaporation of the film material was introduced. According to this model, a gas-molten particle mixture was responsible for the material transfer from the donor support to the receiver (target) substrate (Ehrlich et al., 1988).

The direct-write technique is analogous to digital printing, which is a combination of processes used to deposit functional materials on to a substrate in digitally defined locations (Serra and Piqué, 2019). The printing press invention, which requires the use of masks and molds allowing mass production methods, lacks the customization possibilities and adaptability in any changes of production change. In comparison to mass production-based methods, the direct-write technique offers customization for every product. Similar to direct-write technique, laser-induces forward transfer (LIFT) is a type of digital printing technique which transfers materials from the donor film onto the receiver substrates (Palla-Papavlu et al., 2014, Serra et al., 2010). A pulsed laser beam is employed to project material from the donor film on to the receiving substrate, where the material is deposited as a voxel. Graphical illustration of the LIFT process is shown in Fig. 2.1 (Feinaeugle et al., 2017). The LIFT can operate on both solid and liquid donor films, which makes it versatile for various applications such as droplet printing, graphics production, printing of functional materials, bioprinting and printed electronics with wide range of ink viscosities and loading particles (Feinaeugle et al., 2017). LIFT can be simply described in three main steps (Zergioti et al., 2005). In the first step, the film material is ablated from the donor (initial) base support. Subsequently, transfer of the ablated material takes place, i.e. from the donor to the receiver (target) substrate. The ejection velocity of ablated solid materials/pixels/voxels are in the range of 200 m/s to 1200 m/s (approx. more than three times the speed of sound in air) (Delaporte and Alloncle, 2016). Finally, in the third step, the flyer (as voxel) material is deposited.

doi:10.6342/NTU202301493

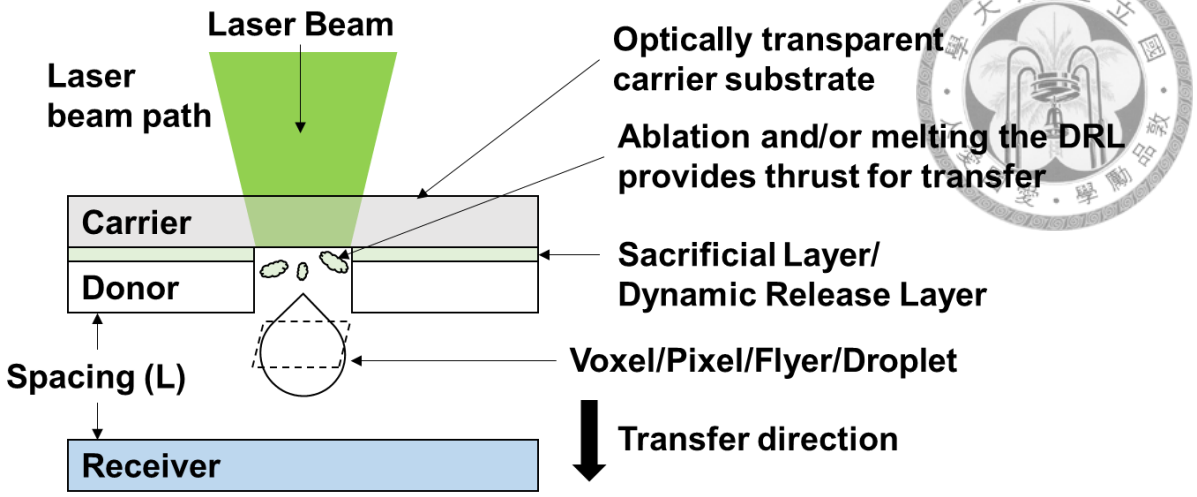

Fig. 2.1: Graphical illustration of the LIFT process (Feinaeugle et al., 2017).

LIFT can be broadly classified in a number of ways. Fig. 2.2 shows classification of LIFT on the basis of interaction. Simultaneously, LIFT can be classified on the basis of the phase of its working materials (Delaporte and Alloncle, 2016). For instance, LIFT of (i) solids, (ii) liquids (Wu et al., 2001), (iii) paste (Piqué et al., 1999) and (iv) solid in liquid. It evident to note that the phase involved in the LIFT process largely depends on the process and material parameters, and sometimes difficult to distinguish. A few other LIFT processes excluding the ones shown in Fig. 2.2 are: **LIMJ**: Laser-induced Microjet Transference; **TIN-LIFT**: Thermal-induced Nozzle LIFT; **LITV**: Laser-induced Thermal Voxels; **LIIFT**: Laser-Interference-induced Forward Transfer; **LIIBT**: Laser-interference-induced Backward Transfer; **LTD**: Laser Transfer Doping; **LIBT**: Laser-induced Backward Transfer; **HILIRT**: High Intensity Laser-induced Reverse Transfer; **LIST**: Laser-induced Side Transfer.

doi:10.6342/NTU202301493

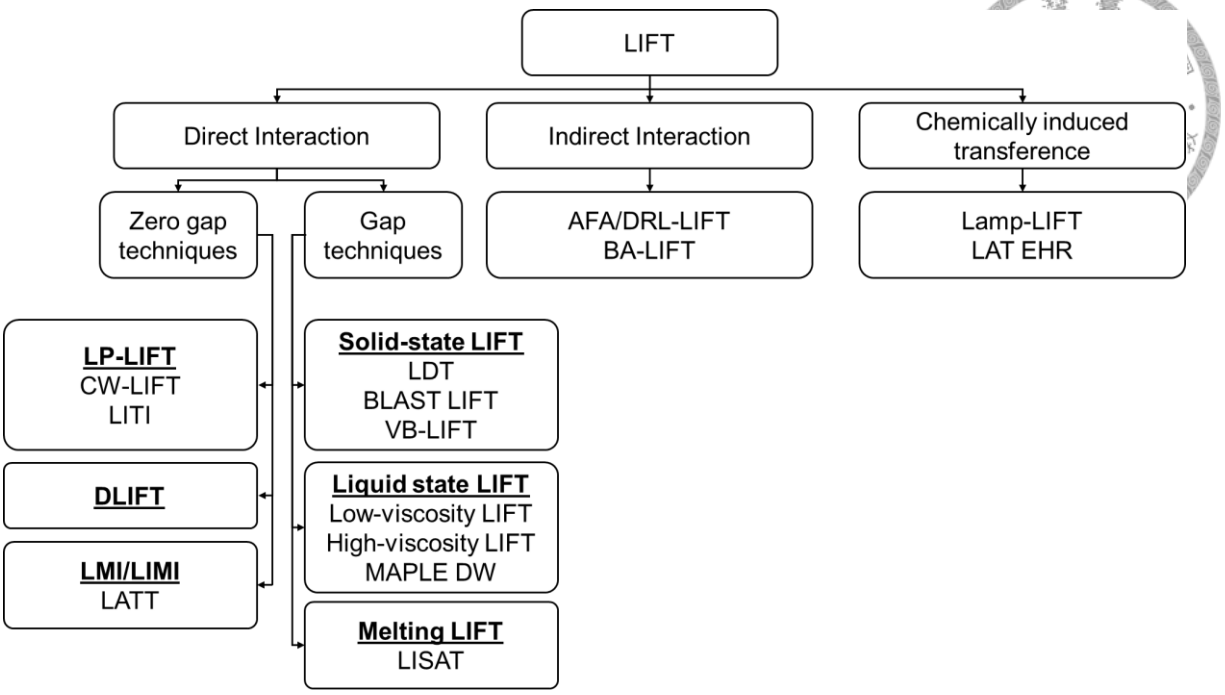

Fig. 2.2: Classification of LIFT. **LP-LIFT**: Long Pulsed LIFT; **CW-LIFT**: Continuous Wave LIFT; **LITI**: Laser-induced Thermal Imaging; **DLIFT**: Laser-induced Forward Transfer Doping; ; **LMI**: Laser Molecular Implantation/**LIMI**: Laser-induced Molecular Implantation; LATT: Laser-Assisted Tissue Transfer; **SS-LIFT**: Solid-state LIFT; **LDT**: Laser Decal Transfer; **BLAST LIFT**: Ballistic Laser-Assisted Solid Transfer; **VB-LIFT**: Voxel based LIFT; **LS-LIFT**: Liquid-state LIFT; **MAPLE DW**: Matrix Assisted Pulsed Laser Evaporation Direct Write; **LISAT**: Laser-induced Self Alloying Transfer; **DRL-LIFT**: Dynamic Release Layer LIFT/**AFA-LIFT**: Absorbing Film Assisted LIFT; **BA-LIFT**: Blister Actuated LIFT/**BB-LIFT**: Blister Based LIFT; **LAT HER**: Laser-Assisted Transfer by Explosive Hydrogen Release; **Lamp-LIFT**: Lamp-induced Forward Transfer

2.1.2. Process parameters

Quality of LIFT printed materials are dependent on various process parameters. Major process parameters can affect the LIFT process to a great extent. These parameters are fluence (J/cm^2), film-acceptor substrate distance (μm), scan rate (mm/s) and focus position of the laser beam. However, before diving further into the details of the LIFT process parameters, a few important fundamental relations must be understood. Therefore,

doi:10.6342/NTU202301493

knowledge on the fluence, peak power and intensity in a laser process is a must. The following equations (Eqs. (2.1), (2.2) and (2.3)) are widely used:

$$Fluence\ (J/cm^2) = \frac{Laser\ pulse\ Energy\ (J)}{Effective\ focal\ spot\ area\ (cm^2)} \quad (2.1)$$

$$Peak\ Power\ (W) = \frac{Laser\ pulse\ energy\ (J)}{Pulse\ duration\ (s)} \quad (2.2)$$

$$Intensity\ (W/cm^2) = \frac{Laser\ peak\ power\ (W)}{Effective\ focal\ spot\ area\ (cm^2)} \quad (2.3)$$

2.1.2.1. Fluence

Fluence is defined as the energy of the laser pulse over the effective focal spot area or simply energy per unit area. Appropriate fluences are important for ablation of material from donor support. Past research shows that ablation can take place not only through evaporation (for bulk materials) but also in solid phase (for thin films) when exposed to certain laser fluence (Ehrlich et al., 1988, Jadin et al., 1990). At low fluences (in an order of mJ/cm^2), ablation starts, and above this, film material takes off completely from the donor support without any collateral damage to the substrates. If the fluence is maintained at certain magnitudes, then the ablation of the material takes place without any melting (in solid phase). In addition to limitations of the solid phase, between the deposited voxels by LIFT have poor adhesion properties. At higher fluences, melting of the film material takes place, leading to liquid phase transfer. However, this leads to messy ablation and incomplete removal due to resolidification of material droplet on the donor support. Upon further increase in fluence magnitudes, evaporation of the film material takes place, and the materials are deposited on the receiver (target) substrate through condensation leading higher material removal and transfer efficiency. A single pulse with high fluences (above 1 J/cm^2) evaporates the entire layer of the material, resulting in complete ablation. However, several disadvantages are encountered at such extreme fluences like enlargement of the ablated area, debris, and thermal damage (Kántor et al., 1992, Cullen et al., 1990, Willis and Grosu, 2005). Therefore, although adherence between the deposited voxels is low in solid phase (low fluence), there is propitious possibility of continuous and high-quality LIFT deposited patterns.

Sano et al. (Sano et al., 2002) extensively described the problems regarding improper fluence.

doi:10.6342/NTU202301493

Optimum fluence leads to high size accuracy and good adherence with substrate with desired film thickness. Bad appearance due to incomplete material removal, and spreading of deposited structure due to big shocks were observed from lower and higher fluence magnitudes respectively. Furthermore, fluence also has significant effects on the flyer velocity (Delaporte and Alloncle, 2016).

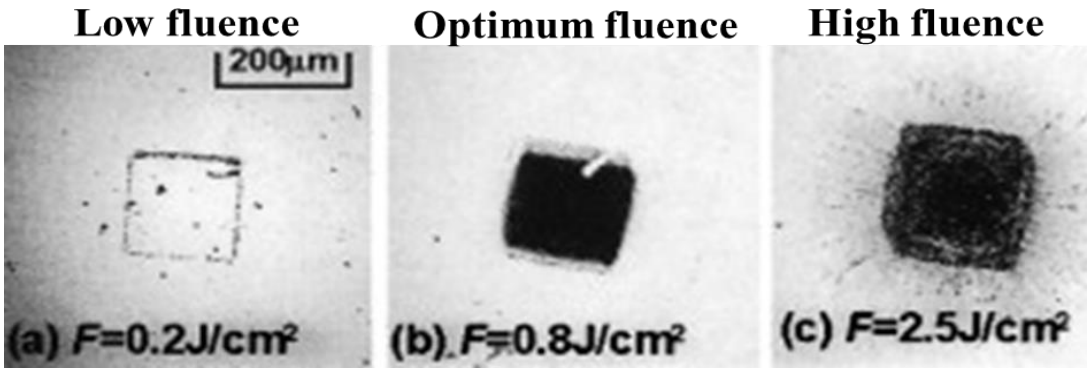

Fig. 2.3: LIFT deposition characteristics at different Fluence magnitudes (Sano et al., 2002). (a) Low fluence, (b) Optimized fluence, (c) High fluence.

2.1.2.2. Film-acceptor substrate distance

The film acceptor substrate distance *(L)* is one of the important parameters that affects the LIFT process. The ablated material velocity during transfer decreases with the increase in L (Toth et al., 1994). Additionally, *L* affects the cooling (radiation and convection) of flyer material. This, can in turn affect the deposition adhesion. Therefore, the distance *L* plays an important role in controlling the transfer yield and transfer efficiency (Kantor et al., 1995). One of the earliest investigations made by Kántor et al. (Kántor et al., 1992) attempted to study the effects of film to substrate distance on LIFT in 1992. They provided evidence showing highest transfer efficiency for low film substrate distance at fluence generating boiling point temperatures.

Sano et al. (Sano et al., 2002) described how deposition spread depends on the film–receiver distance (*L*). Fig. 2.4(a) shows the deposited pixel (from Ni thin film, thickness: 180 nm, fluence: 1.5 J/cm^2, *L*: 20 μm). Material spread is denoted by a length *d*, which is a function of *L* (shown in Fig. 2.4(b)). Results show linear relationship between *d* and *L* for a few

doi:10.6342/NTU202301493

hundred μm, this due to the absence of external force on the transfer material. However, for $L \leq 100$ μm, d starts to increase in a non-linear fashion, which is due to the influence of external force derived from the flowing gas in the region. At optimum fluence, short L leads to high size accuracy of the deposited structure.

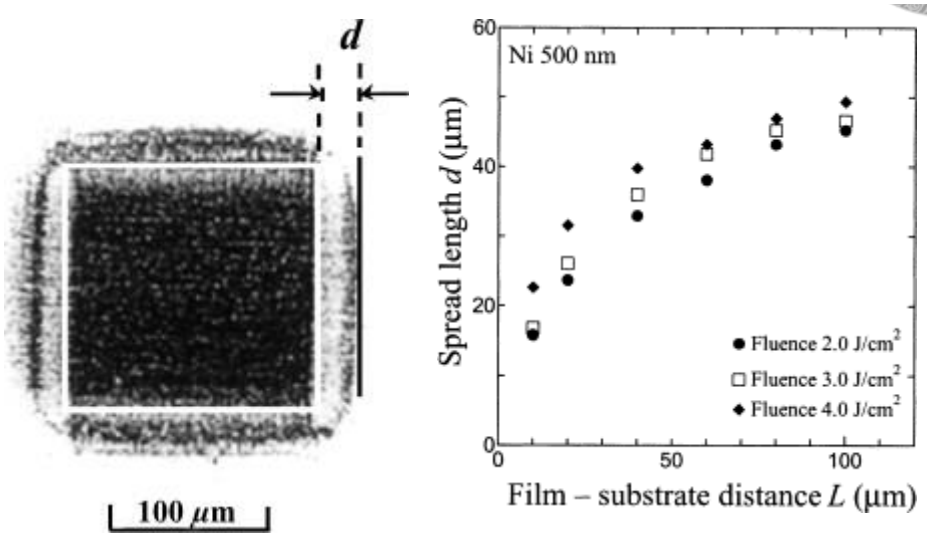

(a) (b)

Fig. 2.4: (a) Deposited structure. Relationship between *d* and *L* (Sano et al., 2002).

Dinca et al. (Dinca et al., 2008) studied phosphate buffered saline (PBS) and glycerol solution transfer using a 10 nm thick Au sacrificial layer, and concluded no significant variation in deposits occurred (distance varied from 20 μm to 1 mm). Subsequently, Palla-Papavlu et al. (Palla-Papavlu et al., 2011, Kántor et al., 1994) studied the effects of target substrate distance using triazene polymers (TP) over Au or Ti layers as sacrificial layers. TP shows no debris formation (rare for other materials (Rapp et al., 2009a)), and the size-shape of the transferred patterns was not affected by the changes in target-substrate distance (from 50 μm to 2 mm). Additionally, the droplet size was affected with variation in the target-substrate distance (for 150 and 350 nm thick TP films).

2.1.2.3. Material selection

Materials selection is a characteristic of the application. However, one must know which materials require low-fluence and high fluence values for proper ablation, transfer and adhesion. Some clean ablated materials at low-fluences are V (Chakraborty et al., 2007), Sn

doi:10.6342/NTU202301493

(Kántor et al., 1992), Ti (Mogyorósi et al., 1989, Kántor et al., 1992), Cu (Bohandy et al., 1986, Zergioti et al., 1998b, Zergioti et al., 1998a), W (Tóth et al., 1993) and Ge (Mogyorósi et al., 1989) (substrates: glass or quartz). Past evidence shows that for achieving a clear ablation, onset of the film melting marks the upper limit of the fluence domain (Zergioti et al., 2005). Subsequently, for optimizing the lower limit, the thermomechanical properties of the metal film and its support along with their interface are considered. Additionally, a material (metal) with high melting point can offer a wider clean ablation domain. For example, Tungsten has a wide clean ablation domain due to its high melting point (100 nm film: solid phase ablation with fluence of 40 to 200 mJ/cm^2) (Rapp et al., 2011). Furthermore, strong adhesion is expected between the deposit material and the target (receiver) substrate when flyer materials are transferred at high temperature (due to transport of higher energy).

2.1.2.4. Pulse characteristics

A lot of efforts have been made in the past to study the effects of pulse characteristics on LIFT (Kántor et al., 1994, Kántor and Szörényi, 1995, Kantor et al., 1995). According to Sano et al. (Sano et al., 2002) and Kantor et al. (Kántor et al., 1994, Kántor and Szörényi, 1995, Kantor et al., 1995), they studied long pulsed (100-1000 μs) and short pulsed (nanosecond) lasers, and compared them in detail for the LIFT process. They concluded that for short pulsed lasers showed complete ablation but limited adherence with the acceptor/target substrate. However, when using long pulsed lasers, enhanced adherence was achieved for tungsten micrometer sized deposits, due to solid phase transfer. Further investigations like time resolved transmittance, temperature calculations and reflectance measurements revealed that ablation is not dependent on pulse width and pulse shape, and starts at a price temperature for long pulsed laser.

LIFT process initially employed nanosecond lasers; however, several advancements and changes like femtosecond lasers result in positive effects such as, reduced heating effects and precise material processing (Zergioti et al., 1998b, Banks et al., 2008). Klini et al. (Klini et al., 2008) studied the effects of temporally shaped femtosecond laser pulses on LIFT. It was reported that temporal shape and the time scale of the excitation pulse affects the size and morphology of the deposits (Klini et al., 2008). Past literature suggests spatial characteristics

doi:10.6342/NTU202301493

of the transferred films can be controlled through the variation in pulse shapes by accessing the time scales of the aforementioned fundamental processes. Subsequently, these femtosecond laser pulses can be effectively used for size and morphology control of micron-sized metallic structures.

Recently, numerous research has been made to transfer nanoscale features using picosecond and femtosecond lasers (Zergioti et al., 1998a, Ghindilis et al., 1998). Wills et al. (Willis and Grosu, 2005) deposited microdroplets using nanosecond pulses. Nanosecond pulses are limited by the focal spot size of laser (Zergioti et al., 1998a, Papakonstantinou et al., 1999). Subsequently, fluence and laser pulses have little interrelations. For nanosecond pulses, transferred material area is greater or equal to the laser spot size. The flyer velocity is not significantly affected by the pulse duration (when changed between ps and μs). However, it is interesting to note that when the order of the pulse duration is reduced to femtosecond, the flyer velocity is reduced (to about 34 m/s) with negligible shock wave generation (material: PZT; pulse duration: 100 fs) (Feinaeugle et al., 2012). Furthermore, controlling the pulse duration has additional advantages: the possibility of heat affected zone (HAZ) and thermal menace can be minimized by using ultrashort pulses. However, the ultrashort pulses may induce high stresses. Short pulse duration in the femtosecond order also restricts formation of uniform top hat energy beam profile which is an essential requirement for most printing applications. Therefore, in such cases where uniform beam profile is a necessity, ns and ps beams are used.

In LIFT, when transfer takes place by liquid droplets, it shows a little different characteristic with pulse duration. Short laser pulse generates liquid jets and cavitation bubbles, however, since as cavitation is a thermally driven mechanism, short pulses does not affect the LIFT process. On the contrary, when ultrashort pulses are used, printing of tiny droplets are favored by limiting thermal diffusion (Delaporte and Alloncle, 2016). After discussion on the short and ultrashort laser pulses, longer pulse durations are discussed subsequently. For μm-sized thin tungsten patterns with long (100-1000 μs) laser pulses a number of facts (Kántor et al., 1992): (i) regardless of the LIFT pulse shape and duration, the onset of characteristic processes is a well-defined constant temperature, (ii) on-site annealing of deposited patterns

doi:10.6342/NTU202301493

takes place by proper shaping the second part of the processing pulse, thereby achieving good adherence with the target substrate. Additionally, with longer pulses, conventional description of LIFT is not applicable (like distinct differences between material removal, transfer and deposition). Past research suggests that using long pulse durations resulted in high debris formation when transferring liquid metal drops from solid metal film (Pohl et al., 2015a, Pohl et al., 2015b). However, this limitation was addressed by Zenou et al. (Zenou et al., 2015c, Zenou et al., 2015b) where they adjusted the parameters (400 ps pulse; ~100 nm; fluence) to melt through the total film thickness. Additionally, the double pulse approach has also been seen to be effective for countering such problems. In summary, it can be inferred that μm-sized patterns cannot be significantly optimized by altering (few tens of) ns. Additionally, optimizing the pulse energy and duration can lead to successful deposition with required properties.

2.1.2.5. Laser spot size

Laser spot size can be altered to control the feature size (Yan et al., 2012). For lasers with similar fluences, incident energy and deposit thickness is lower for the smaller spot size. However, the deposit thickness is not significantly affected (reduced) at higher fluences with reduction in spot sizes. Printing quality is predominantly affected by the spreading effect, which again is not significantly affected for higher viscosity droplets. Therefore, printing quality can be improved by variation in spot sizes. However, this may hamper the productivity due to additional layering. Albeit efficient transfer of materials takes place at higher fluences (since energy per pulse = laser fluence × spot size), cell damage is more likely to occur (Lin et al., 2009, Lin et al., 2010). Large spot sizes are sometimes essential as well, particularly for thick structures, as small spot sizes might lead to buckling and collapse of the structure. Furthermore, for printing biomaterials like oligonucleotide, spot size along with laser fluence affects the coverage (%) of receiver substrate (membrane) (Zergioti et al., 2005). Increase in the spot size increases the coverage percentage.

2.2. LIFT challenges

Considering the advantages of the LIFT process, efforts have been made to employ the process in more applications over the years. However, due to certain process limitations,

doi:10.6342/NTU202301493

application of LIFT on industrial and mass scale is still negligible. Therefore, one must know the limiting factors of the process to be able to take plausible measures to avoid them. The following subsections highlight some of the important challenges to the LIFT process and provides ideas on possible mitigation methods.

2.2.1. Shockwave generation

In LIFT, voxel/pixel transfer can be assisted via a number of mechanisms. However, in simple terms, mechanical forces led by the absorption of laser beam energy is responsible for the transfer. During the process, there is a rapid spike in temperature and pressure inside a small volume which disintegrates (in case of a presence of the sacrificial layer) and pushes the pixel material toward the receiver. Simultaneously, a shockwave develops in front of the transferring pixel. One of the major drawbacks of LIFT is its shockwave formation. When the shockwave reaches the receiver, it reflects back and stops and disintegrates the pixel. Additionally, mechanical force generation makes printing of thin film, brittle materials and materials having thick layers (> μm) extremely challenging (Delaporte and Alloncle, 2016). Consequently, achieving a successful LIFT is only possible with a few μm gap between the substrates and a narrow fluence window. Therefore, shockwaves in LIFT has been widely discussed producing significant research (Mahmood and Popescu, 2021, Delaporte and Alloncle, 2016). Nagel and Lippert (Nagel and Lippert, 2012) studied shockwaves extensively. This section reports details on shockwave formation associated with different pulses (ns-fs) and materials.

Before, diving further into the shockwave generation particularly in LIFT, a little introduction into shockwaves due to variation in pulse width may be helpful. Zeng et al. (Zeng et al., 2005) investigated the dynamics of shockwaves due to laser ablation of ns and fs pulses. Their study inferred different shock wave characteristics for ultraviolet ns and fs pulses. Simultaneously, UV fs pulses showed greater ablation efficiency with fast reduction of electron number density and temperature. Furthermore, the fs-induced shockwaves expanded in 1D, compared to the ns pulses induced 3D shockwaves.

doi:10.6342/NTU202301493

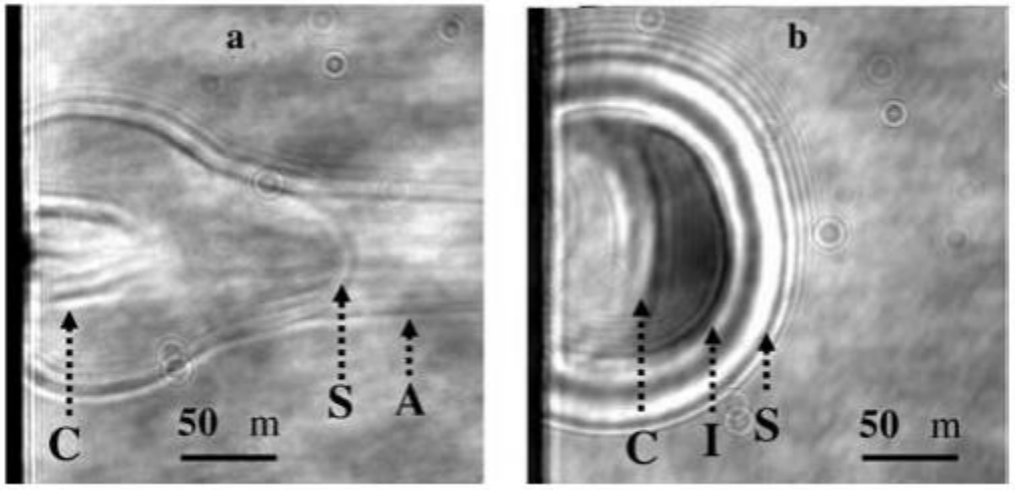

Fig. 2.5: Image of (a) femtosecond and (b) nanosecond plasmas after 10 ns delay post laser shot. S: shock front, I: ionization front, C: contact front, A: air break down (Zeng et al., 2005)

Fardel et al. (Fardel et al., 2009a) reported shockwave formation during ablation and LIFT of a polymer (triazene). In addition, they reported the effects of fluence and film thickness on shockwave characteristics (see Fig. 2.6). Feinaeugle et al. (Feinaeugle et al., 2012) studied shockwaves in the LIFT of ceramics, namely Bismuth selenide (Bi_2Se_3) and Lead zirconate titanate (PZT) using 100 fs laser pulse. They demonstrated the possibility to eliminate shockwaves by achieving limited pixel velocity of 34 m/s. The laser irradiation heats, fractures and ejects the donor towards the receiver. Accordingly, ideal conditions for LIFT can be explained in 3 ways: (i) limited thermal diffusion in donor substrate for mitigating impairment and molten droplet generation; (ii) majority of laser energy utilized for substrate fracture and steady short interval pixel velocity ensuring flat flyer transfer to receiver; (iii) fs pulsed laser can be efficient for certain materials to achieve the aforementioned conditions related to energy distribution. Therefore, mitigating factors like high velocity and shockwave presence were eliminated using fs-LIFT when compared to that of ps or ns LIFT, enabling efficient transfer of thick donor films without DRL.

doi:10.6342/NTU202301493

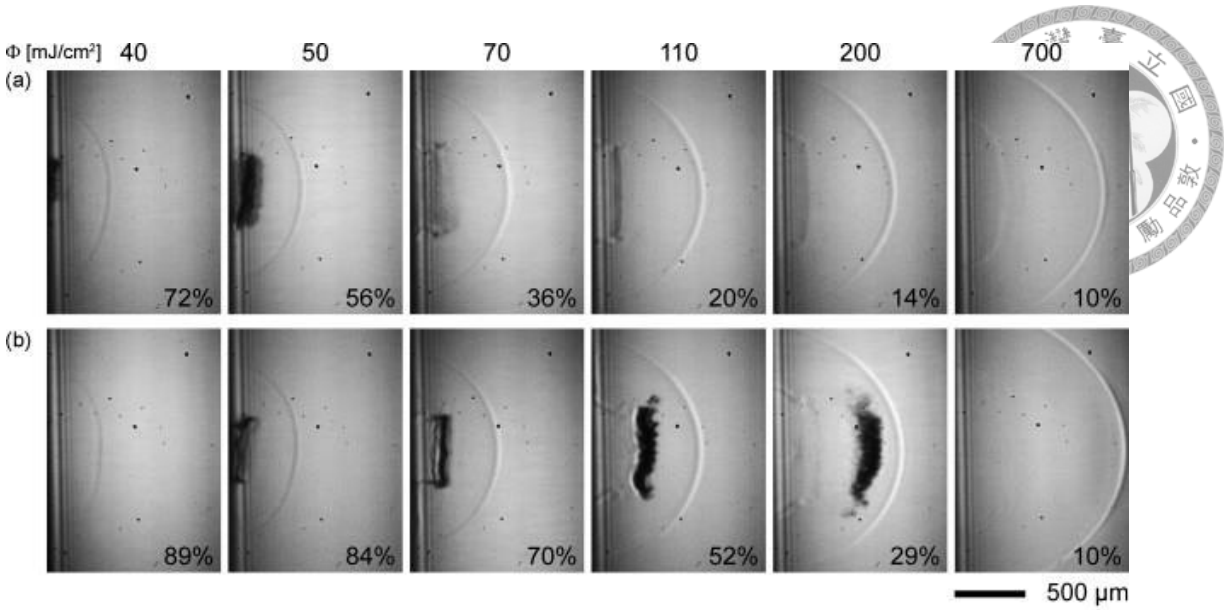

Fig. 2.6: Captured images (1.2 ms post laser irradiation) of the flyer for different donor (triazene polymer films) material thickness and at increasing fluences (a) 190 nm, and (b) 460 nm at increasing fluence (from left to right). % values denote the undecomposed ratio (Fardel et al., 2009a).

In addition to above discussions, several numerical calculations have been made over the years to study shockwaves in the LIFT process. Fardel et al. (Fardel et al., 2009b) estimated the shockwave energy and subsequently discussed its effects on the LIFT process (Fardel et al., 2010, Fardel et al., 2007).

Fig. 2.7 shows the shockwave position measured through images captured following the beginning of the ablation pulse. Deceleration is observed due to initial energy distribution to an increasing air volume over time. Thicker flyers are observed for fluences slightly above the transfer threshold, whereas for higher fluences, thinner flyers are observed. Additionally, different shockwaves appeared for different flyer thickness i.e. shockwaves tend to overlap for thinner flyers.

doi:10.6342/NTU202301493

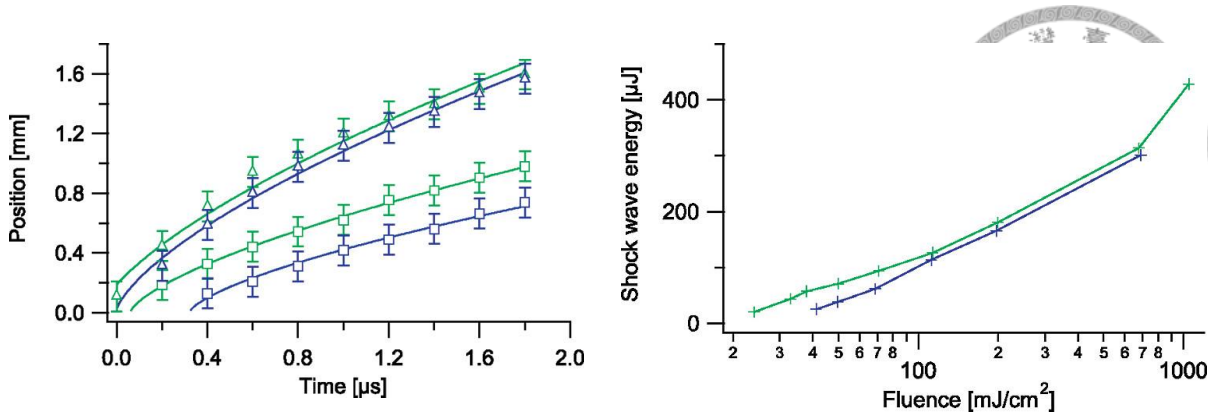

(a) (b)

Fig. 2.7: Shock wave front position (perpendicular to the sample) measured over time, (b) Shock wave energy vs. fluence. (green and blue: front and back side ablation respectively) (fluences: (Δ) 700 and (□) 50 mJ/cm^2). For detailed calculations refer to reference (Fardel et al., 2009b).

Table 2.1: Summary of studies utilizing LIFT to discuss shockwaves through the years.

Investigators	**Materials investigated**	**Notable highlights/inferences**	**Notable limitations**
Papazoglou et al. (Papazoglou et al., 2002)	Indium oxide (InO_x)	• Sub-ps (~0.5 ps) LIFT investigated through time-resolved shadowgraphy. • Ejected material fraction by sub-ps LIFT is highly directional (~angular divergence of 3°). • Small divergence of ejected material is due to the very low material thickness, when compared to the area of irradiation, the shockwave is practically a plane wave. • Plausible reason for generation of small pieces may be due to the instabilities and nonuniformities of the laser beam. Additionally, fragmentation may be due to vaporization and/or due to high stress wave amplitude.	• Although shockwaves minimized, but still significant shockwaves exist in the transfer process. • InO_x transfer as small particles instead of an intact plate.
Hopp et al. (Hopp et al., 2005)	Biological: Trichoderma longibrachiatum conidia	• A KrF excimer laser (λ: 248 nm, FWHM: 30 ns) utilized for AFA-LIFT. • A nitrogen laser pumped Coumarine 153 dye laser beam (λ: 453 nm, FWHM: 1 ns) used for material illumination and imaging purposes. • Survival of conidia was observed post AFA-LIFT was carried out, suggesting suitability for biological applications. • AFA-LIFT divided into four parts: (i) localized excitation caused UV photon absorption by the silver layer, (ii) fast shock wave generated from metal evaporation, causing gentle collisions between the evaporated silver with the conidia, accelerating the material onto the receiver substrate, (iii) Conidia transferred at supersonic velocity following the shock wave front, (iv) Culture medium	• Results were said to be a little inconsistent. • Trichoderma conidia showed damage due to transfer, but it did not produce significant issues due to its reproduction abilities, meaning transfer needs to be more efficient. • Argument on conidia survival is controversial since real life experiments did not include the extremely short duration (from 0 to ~100 ns) of acceleration.

doi:10.6342/NTU202301493

		(glass) provides nutrient and minimizes impact shock. Impact energy (K.E.): 10−8 J (considered to be very low). • Conidia are considered to be very resistant, generating avenues for space research.	
Zeng et al. (Zeng et al., 2005)	Silicon	• The shock front and the ionization front are separated by a thin layer of shocked and ionized air. • Very high laser irradiation (112 TW/cm^2) led to laser induced air breakdown for fs case, when compared to the ns laser (3.7 GW/cm^2). • ns laser generates shock wave which expands spherically. • Initially (< 1 ns), expansion of fs-plasma is primarily perpendicular to the receive substrate. Subsequently, over time expansion is observed in both (lateral and perpendicular) directions, with perpendicular being the faster one. • ns laser shows equal plasma expansion in both directions. • At 5 ns, perpendicular expansion velocities for fs and ns plasmas were 13.6×105 cm/s and 7.9×105 cm/s respectively. ($K.E_{fs\text{-}plasma} > K.E_{ns\text{-}plasma}$ at the early times) • Theoretical formulations show higher shocked air (behind shock front) pressure and temperature fs plasma. However, experimental results (by spectroscopy) show higher temperature for ns-plasma. • The controversy between theoretical and experimental results arise due to different plasma expansion dimensionality. • fs plasma (1D expansion) show less ion and atom collisions than ns plasma (3D expansion) due to local thermal equilibrium (LTE) for the later. • LTE not established initially for fs plasma due to the low excitation temperature and high kinetic energy.	• Higher fluences lead to strong shockwave formations, unsuitable for intact flyer transfer for LIFT associated applications
Kattamis et al. (Kattamis et al., 2007)	glycerol: cell media [Dulbecco's modification of eagle's medium (DMEM) + 35% embryonic stem (ES) certified fetal bovine serum (FBS)]	• LIFT for delicate organic and inorganic materials deposition using thin absorbing films is difficult due to contamination and induction of stresses. • Sensitive materials printed by utilizing polymer absorbing layer (thicker than laser absorption length), which dissipate thermal and mechanical shock energy through mechanical deformation. • Laser energy associated multiple transfer mechanisms demonstrated for viable and contamination-free living mammalian embryonic stem cell transfer for tissue engineering and disease treatment applications.	• Only at higher fluences, damaged cells are observed, reducing overall efficiency of the process considering the field of application (biological), due to the explosive transfer kinetics and corresponding cell rupture.
Menezes et al. (Menezes et al., 2008)	Aluminum (Al) and tungsten (W) microparticles	• Shockwaves utilized for particle delivery (deliver vaccine coated dry microparticles) into soft human-body targets. • Upon laser irradiation, ionized Al vapor shockwave launched through Al (waves return as expansion waves from the air-foil interface due to acoustic impedance mismatch between Al and air) ejected particles forward at high velocity like microbullets.	• No notable limitations associated with shockwaves since the researchers utilized it positively in this research.

doi:10.6342/NTU202301493

		• Although classical shockwave theory suggests total reflection of incident shockwave (during acoustic impedance mismatch), transmitted shockwave was observed. • Transmitted shockwave increases pressure of air, thereby increasing particle drag. • Shock speed (shock speed determined by considering the shock ahead of the particle cloud) initially unsteady, reaches steady state subsequently. • According to the classical theory, air density increases by 3.7 times (velocity: 965 m/s, pressure: 1 atm, density: 1.2 kg/m^3, temperature: 20ºC) due to the shock speed, increasing drag on the particles.	
Kaur et al. (Kaur et al., 2009)	Ceramics: gadolinium gallium oxide and ytterbium doped yttrium aluminium oxide	• LIFT of Gd–Ga–O and Yb:YAG using a triazene TP-DRL carried out with time-resolved ns-shadowgraphy. • Increase in fluence show increased propagation distance and velocity of shockwave and flyer. • The travelled flyer distance decreases with increasing donor film thickness. 50nm TP shows better transfer characteristics with less shockwave intensity compared to 350 nm TP. • Finally, an optimal TP layer thickness is determined along with donor material, donor thickness, and fluence for efficient transfer.	• Weak shockwave observed for the best reported low TP thickness experiments. • Long distance transfer with intact flyer needs attention. • Experiments conducted for two TP thicknesses, hence more studies may be made for better optimizations.
Fardel et al. (Fardel et al., 2009a, Fardel et al., 2009b, Fardel et al., 2010)	Polymer: Trianzene	• Flyer is consistently flat (w.r.t the ablated area) initially, and subsequently loses its accuracy and initial profile. • Single laser pulse insufficient for complete trianzene ablation. • Flyer consists of undecomposed polymer generated by thrust pressure associated with ablation and breakdown. • Increased fluence leads to greater penetration, thicker material decomposition and pressure (gases to eject the flyer) and decreases remaining film thickness. • Increased fluence leads to greater instabilities in the flyer due to higher energies. • Flyer shape and properties are dependent on film thickness and fluence. • Higher undecomposed layer thickness suggests partial ejection and lower percentages suggest complete flyer decomposition. Therefore, optimal flyer is restricted to a narrow window.	• Inappropriate fluence lead to complete decomposition of the flyer. • Significant shockwave generation at increased fluences
Stewart et al. (Stewart et al., 2010a)	Aluminum	• ns and ps LIFT with a UV-absorbing triazene polymer (TP) utilized as DRL for front and back Al ablation. • ps (355 nm) ablation shows faster flyers and greater shockwaves than the ns laser systems (Nd:YAG and excimer). • Both ns system shows similar flyer and shockwave velocities (within experimental error). • Flyer quality degrades with shortening of pulse length. • ps has lower ablation rate, yet generates greater velocity for ns pulses, due to greater pressure buildup for smaller volume.	• Shockwaves are minimized using nanosecond pulses from more homogenous excimer laser system, yet significant shockwave generation reported.

doi:10.6342/NTU202301493

		• Nd:YAG lasers (gaussian) show lower beam homogeneities than its excimer (flat top) counterparts, leading to low flyer quality (fragmented) for the former.	
Stewart et al. (Stewart et al., 2010b)	Aluminum	• Triazene-based LIFT of Al for OLEDs functioning. • Possibility of transfer with minimal donor-receiver gap investigated. • Reduced air pressure removed air drag, strong shockwave formation and high flyer speed.	• Functional OLED pixels could not be transferred as made in other research (Fardel et al., 2007).
Palla-Papavlu et al. (Palla-Papavlu et al., 2010a)	Polystyrene (PS) microbead	• LIFT of PS-microbead (8 μm in diameter) pixels (200 × 200 μm^2) using 30 ns UV (308 nm) XeCl laser • Fluence variation: 80 mJ cm^{-2} to 3.5 J cm^{-2}. • One polystyrene microbead pixel printed using one pulse and arranged in a matrix of points. • Successful 'flyer' (PS-μ bead pixel) transfer seen for low gaps ~30 μm. • At higher gaps (~100 μm) PS-μ beads pixels do not reach the receiver substrate due to the shockwave reflection.	• Shockwaves observed for the LIFT experiments. • The ns-shadowgraphs shows zero possibility of obtaining homogeneous PS-μ bead pixels with a donor receiver gap.
Kaur et al. (Kaur et al., 2011)	zinc oxide	• Fs-LIFT with pre-machined (using focused ion beam (FIB), depth~0.8 μm) donor films utilized for thick (1 μm) ZnO films. • Debris-free micro-pellets with extreme smooth edges and surface uniformity observed for pre-machined donors. • Non-pre-machined ZnO donor films using DRL compared to pre-machined donor, indicating superiority of the pre-machining technique. • Weak shockwaves expected through the use of low fluence requirement due to the pre-machined technique.	• Requires additional machining since, 12 μm ZnO pellets are transferred from a non-machined 1 μm thick donor show shattering, non-uniform, irregular shaped and splashy deposits with rough edges.
Feinaeugle et al. (Feinaeugle et al., 2012)	Ceramics: Bi_2Se_3, PZT, Terfinol-D	• fs laser irradiation utilized for the LIFT process. • Shockwaves not observed for film thickness between 0.5-1.8 μm. • Initially, shockwaves were argued to be generated only in the presence of decomposing polymer layer, however, evidence show shockwave formation without the mentioned explosive layer (Menezes et al., 2008). • Additionally, an argument is made that weaker shock waves are transmitted into the area beyond the donor surface, when compared to the reflected one, generated due to a strong acoustic impedance mismatch from the auxiliary foil/air interface. • At low flyer speed, with decomposing DRL and high acoustic impedance at the flyer(donor)/air interface led to no shockwave generation. • High velocity and shock wave generation must be mitigated for successful transfer. • Intact flyers with low velocity observed for fs LIFT compared to that of its ns or ps counterparts. • fs-LIFT of thick donor films in absence of DRL suitable for solid and intact transfer under atmospheric conditions.	• Almost no shockwave generation due to low transfer speeds of the flyer.
Stewart et al. (Shaw-Stewart et al., 2011)	silver/organic film (Alq_3 or PFO)	• LIFT of bilayer Alq_3 or PFO using triazene DRL at reduced air pressure with PEDOT:PSS coated receiver (poly[3,4-ethylenedioxythiophene] blended with poly[styrenesulfonate]) .	• Post optimizations, SEM images show evidence of ripples, irregular tearing at

doi:10.6342/NTU202301493

		• Fluence up to ~200 mJ/cm^2 and donor-receiver substrates gap from 2–3 μm to 40 μm. • Alq_3, shows almost no transfer at atmospheric pressures whereas PFO shows little success (*doughnut* transfer). • Ag/PFO bilayers transferred best at reduced pressures (100mbar), but shows minimal transfer with the addition of a PFO layer onto the receiver substrate at atmospheric conditions at low gaps < 20 μm.	flyer edges, and folding at lower fluences. • Presence of non-decomposed TP film on the back of flyer, at low fluences. • Silver transfer is slightly more defective than Al.
(Mattle et al., 2012)	Aluminum	• LIFT of Al using triazene sacrificial polymer layer studied using time resolved imaging (side and front-on). • At high fluences (~800 mJ/cm^2), flyer shows stablility up to 400 ns, and decomposes completely afterwards by shockwave (after 1 μs) interaction. • At low fluences (200 mJ/cm^2) shape integrity maintained up to 1 μs. However, triazene polymer decomposes generating back pressures which bends the flyer towards the flight direction.	• Weak shockwaves appear for transfers at lower fluences. • Flyer edges show material detachments at early stages of the ablation process (<200 ns), causing material loss in the printed pixel.
Hopp et al. (Hopp et al., 2012)	Living cells: human neuroblastoma, chronic myeloid leukemia, and osteogenic sarcoma cell lines, and primary astroglial rat cells	• KrF laser used for fs-LIFT (500-fs) with absorbing film for transfer of living cells. • Absorbing materials: (50 nm) gelatine, Matrigel each 50 μm thick, and polyhydroxybutyrate, 2 μm). • Spot diameter: 250-μm, fluence: 225 mJ/cm^2, donor-receiver distance: 0.6 mm, Receiver plate: glass slide (pure/biomaterials covered). • Biomaterial absorbing layers ineffective for cell transfer, due to low-absorptivity. • Amelioration of cell impact takes place through wet gelatine and Matrigel layers. • neuroblastoma and astroglial cells show a best short-term and long-term survival rate between 65% and 70% respectively.	• Transferred osteosarcoma cells show low long-term survivability, whereas the myeloid leukemia cells couldn't survive at the experimental conditions. • Strong photomechanical effects (intensive shock waves and extreme acceleration and deceleration) during AFA-LIFT damaged large numbers of living cells.
Mattle et al. (Mattle et al., 2013b)	SnO_2 precursor films: $SnCl_2(acac)_2$ and SnO_2 nanoparticles	• LIFT of $SnCl_2(acac)_2$ and SnO_2 nanoparticles, with and without triazene DRL investigated and compared to Al transfer with triazene DRL using time resolved imaging (investigation time: 0-2 μs post ablation onset). • Triazene DRL did not affect shockwave and flyer speed characteristics. • Flyer velocity of 200 m/s with a weak shockwave observed under transfer conditions.	• Shockwaves were not eliminated by the use of DRL layer
Rapp et al. (Rapp et al., 2014a)	Semiconductor and conductor polythiophene-based derivatives: *poly (3,3‴ didodecylquaterthiophene)* (PQT-12), *poly(3,4-ethylenedioxythiophene)/po*	• Low pressure environment setup initially utilized to eliminate shockwave generation. • Subsequently, background pressure of 90 mbar to reduce shockwave energy and transfer quality of the pixels. • LIFT of thin layers of semiconducting PQT-12 and laser printing of PEDOT:PSS (transistor conductor) carried out. • Background pressure reduction and increasing film thickness carried out for optimization purposes. • Polymeric thin-film transistor devices fabricated having mobilities up to 0.02 cm^2 V^{-1} s^{-1} using LIFT.	• The functional polymeric thin film transistor (TFT) illustrated low dimensional accuracy and control.

doi:10.6342/NTU202301493

	ly(*styrenesulfonate*)(PEDOT:PSS)		
Rapp et al. (Rapp et al., 2015, Rapp et al., 2014b)	hybrid organic polymer: parylene-C and silver thin films	• Multilayer donor transfer carried out using smart beam shaping (SBS) setup. • Fluence at the center (F_{center}) is half the transfer threshold fluence (150 mJ/cm^2). • Fluence at the edges ($F_{contour}$) is increased until desired deposition is obtained (200 mJ/cm^2). Greater $F_{contour}$ values (~250 mJ/cm^2) destroys and fragments the contour. • Lower fluence to the pixel guards the multilayer from laser irradiation damage, and reduces shock wave intensity. • Homogeneous, sharp edges with no spattering/debris and fair adhesion to substrate observed with the optimized beam profile. • SBS utilizes the common LIFT mechanism, i.e. pressure increment at the substrate–multilayer interface leads to pixel detachment. However, variation in fluence (higher at the edges) results in slower ejection speed at the center, resulting in weaker impact forces and shockwave intensity on the receiver substrate.	• Pixel obtained with F_{center} only is defective (i.e. it is not square nor flat on the silver pad/bottom electrode) with holes, meaning partial material transfer. • Gap observed between the pixel contour and its main central part. Therefore, additional laser pulse required to eliminate the contour cut (using only the contour mask), without any square pixel damage. • Light debris contamination observed and contour formation limits close proximity series printing of micro-capacitors.
Jalaal et al. (Jalaal et al., 2019)	Anynomous ink	• Destructive mechanisms for LIFT identified to be originated by cavitation- (i) multiple optical breakdowns (due to inadequate optical system corrections), and (ii) rarefaction waves (originating from impurities). • Irreproducibility in LIFT experiments identified via fluid dynamics studies (experimental and numerical). • Repeatability can be improved by liquid ink purification and degassing. Cavitation cloud size directly related to impurities and dissolved gas. Furthermore, purification reduces multiple breakdown possibilities. • Optical breakdowns may be mitigated by using beam expander before the beam enters the focusing objective lens. Additionally, modification of the size and number of plasmas with a digital hologram. • BA-LIFT system/absorption layers can minimize shock propagations by maximum energy absorption, causing weak preheating reducing cavitation cloud formation. • Finally, ink rheology modifications (if not constrained by the area of application) may control bubble dynamics, and bursting. For instance, small bubble migration can be limited by increasing effective viscosity and the yield stress in elasto-viscoplastic materials.	• Achievement of a complete degassed and purified ink is difficult due to the free surface gas diffusion, spontaneously increasing cavitation possibilities. • Shockwave formation is avoidable, but can be limited by using BA-LIFT or metal absorption layer, leaving only small secondary bubbles.

Based on the aforementioned discussions, insights on shockwave formation and its plausible causes have been identified. Considering the above, efforts have made to minimize and eliminate shockwave formations due to their negative impact on the LIFT process. Briefly, shockwaves can be minimized/ eliminated in the following ways: (i) low pressure

doi:10.6342/NTU202301493

environments (LPE) or vacuum; (ii) utilizing fs laser pulses; (iii) laser beam shaping; (iv) introducing receiver surface modifications (proposed in this study).

From the above discussions and illustrations, it is evident that if experiments are conducted in near LPE conditions, the shockwave energy reduces (since, E_{gas}~0). According to the investigations by Rapp et al. (Rapp et al., 2014a), presence of air during LIFT in ambient conditions comprises of a background pressure generates a shockwave. This shockwave is responsible for pixel cracks and folds. Therefore, eliminating air (introducing near LPE condition, i.e. low pressures) can result in shockwave elimination. On the contrary, near LPE conditions will lead to no cushioning effect with limited heat transfer possibilities during the pixel impact (kinetic energy (K. E.) transformed into heat generation which leads to structural and morphological degradation). Additionally, LPE conditions will lead to high velocity of the transferring flyer, which when impacts with the receiver surface will disintegrate. Therefore, an optimization must be made by compromising the LPE conditions by introducing low working pressures of about 10 mbar to 100 mbar (Shaw-Stewart et al., 2011, Delaporte and Alloncle, 2016).

In addition, past research provides evidence that use of fs laser irradiation can limit shockwave formations due to DRL absence and high acoustic impedance at the interface (film/air) (Feinaeugle et al., 2012). However, experiments with fs pulses must be made carefully at low laser energy densities since past research have also reported presence of shockwaves due to fs laser pulses at high energy densities (Zeng et al., 2005).

Furthermore, it has been noted that to print transparent materials by using DRL is used, (commonly UV-sensitive aryltriazene polymer (TP)), due to its ability to decompose into volatile fragments at very low laser fluences. Limiting direct laser irradiation interactions, causes in photothermal and photochemical degradation of sensitive materials. In such cases, utilizing ultrashort pulses limit the heat-affected zone and thermal degradation in donor material. However, sometimes ultrashort pulses generate high stress concentrations and it is difficult to attain top hat beam profiles over a few μm. During such exceptions, ps and ns pulses may be required.

doi:10.6342/NTU202301493

LIFT for brittle materials or thick layers (> a few micrometers) is challenging due to the involved mechanical forces. Suitable alterations in the laser beam and shaping can overcome this issue. Rapp et al. (Rapp et al., 2014b, Rapp et al., 2015) modified the laser beam profile regulating the energy with focused beam edge for successful LIFT of polymer films (>1 mm thickness) with promising resolution. The variation in laser fluence in the center (low) and the edges (high) enables utilization of low fluences for pixel transfer. Simultaneously, helping in reduction of shockwave intensity. Furthermore, previously Kaur et al. (Kaur et al., 2011) utilized similar approach with less beam energy for transfer by patterning a 1 µm thick zinc oxide (ZnO) film down to 0.8 µm by employing a focused ion beam. Therefore, allowing smooth and undamaged transfer ZnO pixels.

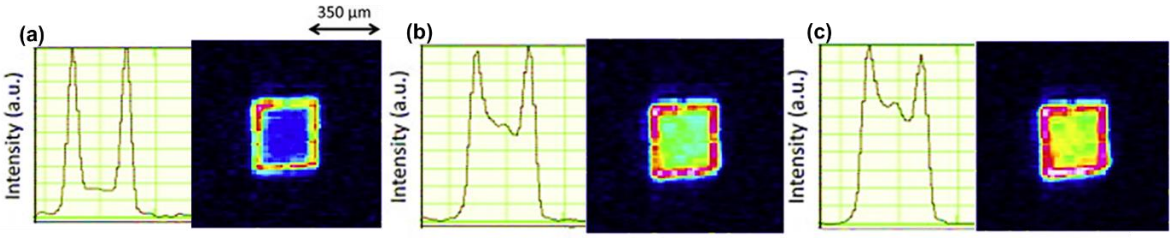

Fig. 2.8. Smart beam shaping (SBS) profiles (imaged using beam profiling camera). (a) using mask 2 (contour) at high intensity ratio, (b,c) using masks (mask 1: square pixel + mask 2: contour) at medium intensity ratio, and low intensity ratio respectively (Rapp et al., 2014b).

Finally, a method of utilizing changes in the receiver substrate surface is proposed to reduce the effects of shockwave reflection. Considering the simple mechanism of shockwave generation and its reflection from the receiver substrate for transfer material disintegration, if the shockwaves are vanquished at the receiver substrate, it will leave no scope for reflection, keeping the flyer intact. Fujisawa et al. (Fujisawa et al., 2019) studied the impact of shockwaves on modified surfaces (see Fig. 2.9). It is evident from Fig. 2.9 that introduction of surface modifications leads to disintegration of shockwaves and reduces the surface pressure variation. Albeit presence of shockwaves, expansion waves remain through continuous reflection on the free surface and propagate through the groove trough, a gradual

doi:10.6342/NTU202301493

decrease in the pressure magnitude is observed with increase in the elapsed time (Fujisawa et al., 2018).

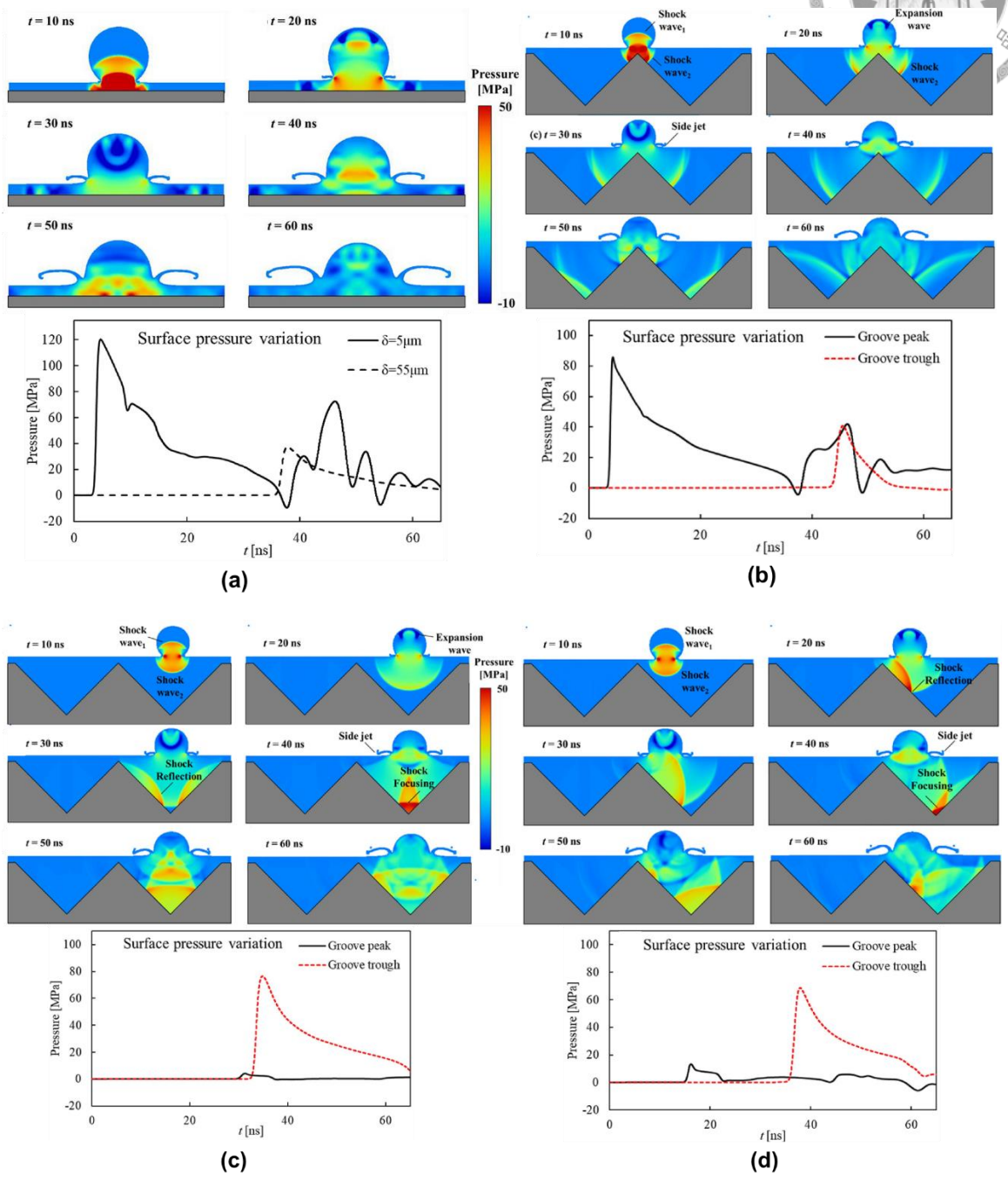

Fig. 2.9: Pressure contours and surface pressures over time (t = 10–60 ns) on (a) smooth wall (δ = 5 μm), (b) groove peak impact, (c) groove trough impact, (d) groove middle impact (Fujisawa et al., 2019)

doi:10.6342/NTU202301493

2.2.2. Bond strength between deposits

Past research shows evidence of LIFT's capability to produce free standing and 3D structures. However, in order to produce free standing and 3D structures through LIFT, bonding strength between the subsequent depositions must be sufficient to avoid material buckling or failure. Therefore, this section discusses relevant research works made to provide insights on additively manufactured structures using LIFT.

Breckenfeld et al. (Breckenfeld et al., 2016) provided a detailed guide on how to successfully use LIFT to transfer silver nanopaste for printing various line, bridging (cantilever), high aspect ratio and complex structures. Additionally, they demonstrated crossover interconnects in multiple steps (first: vertical posts, second: free-standing top metal interconnect connecting the posts) (Wang et al., 2010) as shown in Fig. 2.10. Kim et al. (Kim et al., 2013) first demonstrated the use of LIFT to deposit multilevel 3D interconnects alongside two orthogonal planes on the same substrate (3D microstructures that fold along an edge) without defects. They adjusted the laser energy to the threshold, enabling transfer and folding of the voxel around the substrate edge as shown in Fig. 2.11. Such interconnects are limited for lithography. Kuznetsov et al. (Kuznetsov et al., 2010) showed that Au pillar structures by fs laser (on Au film <200 nm) are limited to low aspect ratio. Subsequently, Visser et al. (Visser et al., 2015) shows that higher aspect ratio pillar structures can be fabricated by utilizing transfer threshold fluence, which minimized oxidation, enhanced adhesion and produced flattened disk depositions. Similarly, a number of research works demonstrate use of different materials such as Cu, Au, Ag and Al to develop 3D structures (Zenou et al., 2015a, Zenou et al., 2015d).

doi:10.6342/NTU202301493

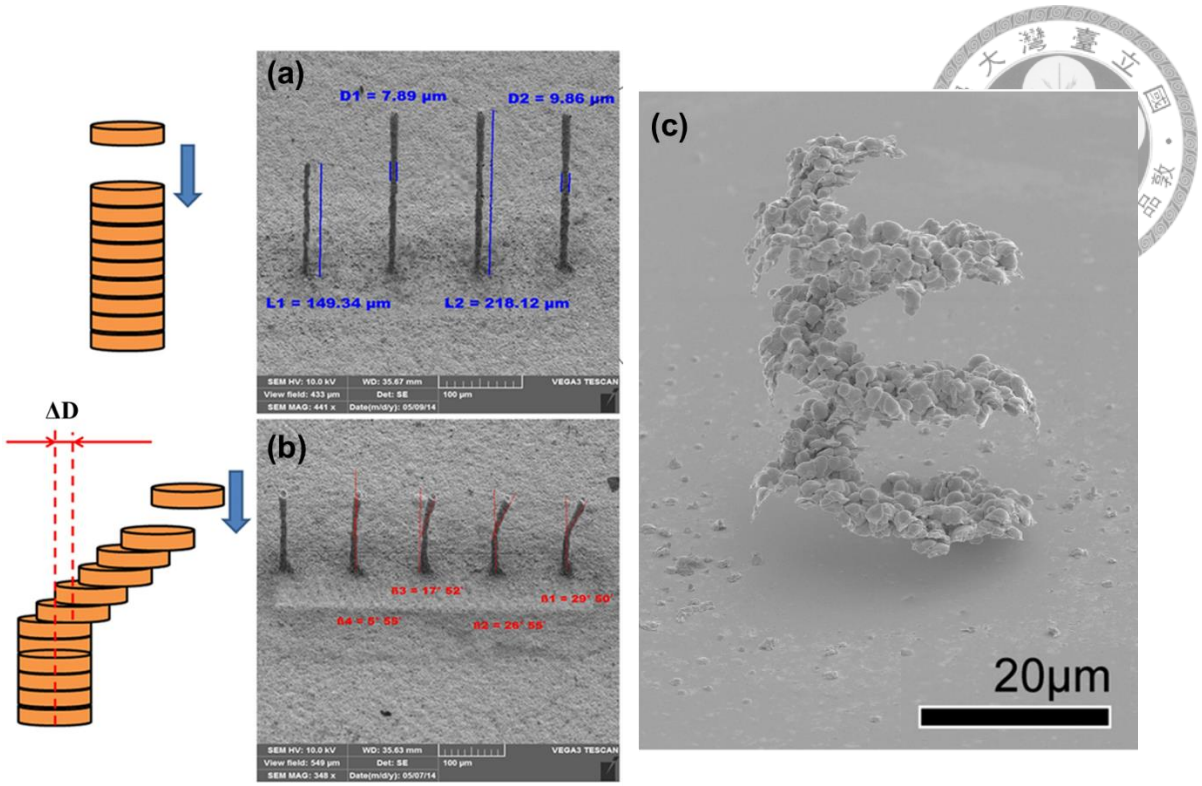

Fig. 2.10: SEM images of free-standing structures. (a) Cu pillars fabricated using 400 droplets. fluence used (left to right): 0.8, 0.84, 0.88, and 0.92 J/cm^2. (b) two-segment bent pillars, each fabricated using 100 droplets (ΔD = 0, 0.1, 0.2, 0.3, 0.4 µm (left to right)). (c) Au helix structure obtained post etching of Cu having a total height of 48 µm (view angle: 60°). Refs. (Zenou et al., 2015d, Feinaeugle et al., 2018)

Considering the aforementioned application of LIFT to fabricate 3D structure, a number of challenges must be considered: (i) control of spatial placement of individual voxels; (ii) adhesion between voxels; (iii) adhesion to receiver substrate must be sufficient to withstand various mechanical and thermal strains experienced during processing and use. In addition, in order to achieve successful 3D structure, parameters such as donor-receiver substrate distance must be controlled closely to achieve good voxel placement accuracy (Breckenfeld et al., 2015). High fluences lead to material spraying which will cause inaccuracies in the 3D structure. Shockwaves must be minimized (mentioned in previous section) as it may damage/disintegrate the previously deposited material layer for 3D structures. Moreover, adhesion between voxels decrease for presence of particles (> 0.1 µm) in solids or pastes.

doi:10.6342/NTU202301493

Therefore, to mitigate this, nanosuspensions or high post processing sintering temperatures must be utilized. Additionally, ps and fs lasers mitigate the mentioned problem in metals as melting and solidification occurs due to the jet formation, binding the previously transferred droplets. Finally, although a number of plausible precautions and suggestions are made, strong mechanical adhesion between voxels still remains a challenge.

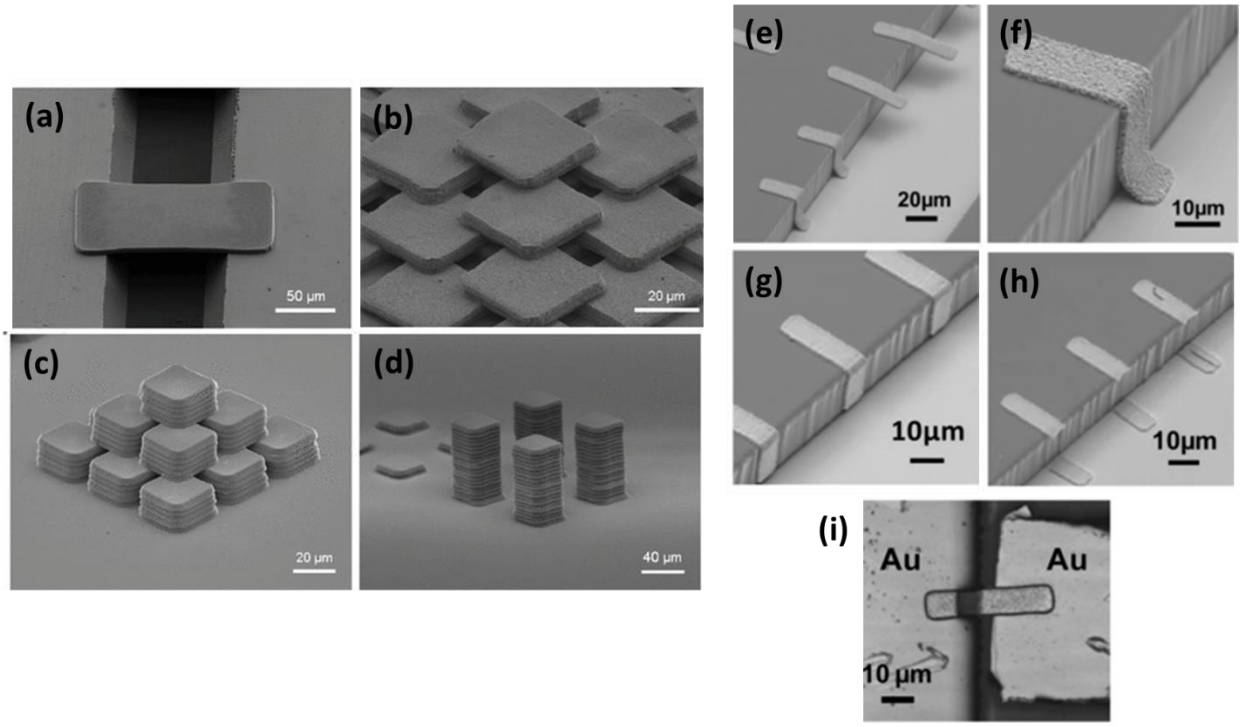

Fig. 2.11: SEM images of various Ag based stacked 3D structures and interconnects. (a) A rectangular voxel interconnect over a 100 µm wide Si channel, (b) Multilayer scaffold structure, (c) high aspect ratio micro pyramid, (d) High aspect ratio micro pillars, (e) voxels transferred (low and intermediate laser fluences). (f) post oven cured voxel transferred on to the top, side and bottom surfaces of a 20 µm high receiver substrate, (g) intermediate (27–29 mJ/cm^2), and (h) high fluence (32–34 mJ/cm^2) voxel transfer, (i) Confocal microscope image of the interconnecting voxel (height difference: 20 µm thick SU-8 (Shipley) layer). Note: structures cured at (a-d) 70ºC, 1h and (e-i) 180 ºC, 1h post transfer (Wang et al., 2010, Kim et al., 2013).

doi:10.6342/NTU202301493

Table 2.2: Summary of studies utilizing LIFT to discuss weak bonding strength between the deposits through the years.

Investigators	Materials investigated	Notable highlights/inferences	Notable limitations
(Kuznetsov et al., 2010)	Gold	• fs-LIFT (λ: 800 nm, pulse energy: 3 mJ, 30 fs) of Au films (10-60 nm) • melting results in a jet-like structure with a droplet on its top, where height and shape depends on fluence. • 3D structures with metal particles can be utilized. • Second droplet splashes on the first if the receiver substrate has significantly lower heat conductivity (slower cooling and solidification of droplets). • Metal coating (high conductivity) on receiver substrate enables fast cooling and solidification of droplets mitigating before splashing. • Particles show spheroid shape with aspect ratio ~1.17, due to the impact of liquid droplets onto the receiver surface and their fast cooling and solidification. • If solidification is faster than surface tension, perfect spherical shape can be preserved.	• Splashing of droplets for low thermal conductivity receiver substrates, limiting the transfer on high heat conductivity receiver materials or coatings only.
(Wang et al., 2010)	Silver Nanopastes	• A frequency-tripled Nd:YVO_4 laser (λ = 355 nm, 30 ns FWHM) used. • fabrication of 3D freestanding Ag interconnects with various widths (8–75 μm), loop heights (1–10 μm) and bond lengths (8–100 μm) printed on glass, silicon and polyimide substrates. • Ultrafine (<10 μm) pitch bonds and interconnects for LEDs embedded in flexible polyimide substrates generated. • Superior than wire bonding technologies for precisely printing and assembling building blocks of varying shapes and sizes may lead to the implementation of electronic and MEMS devices for a wide range of applications with reduced cost and complexity. • Enhanced mechanical stability of the interconnects upon 0.5 h of ultrasonic cleaning, checked as a function of ultrasonic treatment time with resistance. • Good interconnect bonding and reliability under high-frequency mechanical vibration. • Ability to connect dissimilar materials over uneven surfaces (height mismatch ~15 μm). Post curing (150 °C, 1 h) shows LEDs operational over repeated bending of substrate for 500 cycles with 12 mm radius.	• Fair demonstration of mechanical stability and bond strength between interconnects presented using nanopastes. However, LIFT process which cannot incorporate curing might lead to poor mechanical properties of the deposited structures.
(Kim et al., 2013)	Silver nanopaste	• Nd:YVO_4 pulsed UV laser system (355 nm, 30 ns FWHM) utilized for LIFT. • Laser fluence controlled to print freestanding tabs, side contacts on vertical walls without using sacrificial layers, chemical etching or electroplating. • Low fluence (22–24 mJ/cm^2) utilized to obtain freestanding structures extended over edges. Pixel velocity < 1 m/s produces gentle landing.	• Reproducibility of experiments require high control over laser fluence, leading to requirement of lasers with pulse-to-pulse energy variation of less than 5 %.

doi:10.6342/NTU202301493

		• Higher fluence (27–29 mJ/cm^2) utilized for conformal printing. Above 32 mJ/cm^2, fracture observed (Ag donor thickness 1.5 μm). • Good electrical properties of the transferred printed interconnects for utilization in 3D microelectronics. • Generation of the aforementioned patterns cannot be generated using lithography or other non-contact direct-write techniques such as inkjet.	
(Zenou et al., 2015c)	Aluminum	• A frequency-doubled, passively *Q*-switched, sub-ns (400 ps) pulse Nd:YAG laser (λ: 532 nm). • Highly stable molten Al (donor: 500nm) micro-droplet jet having low divergence (<2 mrad), larger gap distances (300 μm) under ambient atmospheric conditions • Lower droplet volume shows reduced positional accuracy compared to the larger ones due to the morphological deformations during transfer through air. • Smaller droplets however show low surface roughness ~0.8 μm, whereas larger droplets have twice the value. • Larger volume droplets have higher structure buildup rate, and is done using thicker donor. • Surface roughness increases with the Al donor layer thickness.	• Cross-sectional profilometry using 3D microscope shows irregularities in the surface, meaning negligible bonding between the deposits. • Instant droplet solidification (within ns) and negligible heat load for re-melting lower solid layer results in low surface layer deposit bonding and higher roughness level.
(Zenou et al., 2015a)	Copper and copper alloys	• A passively Q-switched 400 ps laser (λ: 532 nm and pulse energy: 30 μJ) • The right matching between pulse duration and donor layer thickness (sub-μm) guarantees a stable, single droplet jetting regime crucial for quality printing of 3D structures. • Copper transferred with high resolution, oxidation free under ambient environment. • Incorporating heat-sensitive substrates eliminates post printing treatment requirements such as thermal sintering. • LIFT of Au, Ag and Al gold follow the aforementioned guidelines. • Laser induced self-alloying transfer (LISAT) introduced using multilayer donor structure (alloy formed by material mixing during jetting process). Copper with low silver concentration used to generate free standing, 3D, micrometer scale, and metal structures.	• The printed 3D objects show fair morphological compactness, > 95%. • Surface roughness of ≈2 μm and could be reduced to < 0.5 μm. • The aforementioned qualities such as compactness and surface roughness can be improved by optimizing parameters and introduced post thermal treatment.

doi:10.6342/NTU202301493

(Zenou et al., 2015d)	Copper and gold	• sub-ns (400 ps) pulse Nd:YAG laser (λ: 532 nm) utilized for LIFT. • At optimal conditions a solid nozzle known as thermally induced nozzle (TIN) (quasi-nozzle in the metal layer) is formed, providing stability and directionality to the femto-liter droplets which are printed from a large gap in excess of 400 μm. • TIN regime at sub-ns laser pulses with metal donor <1 μm is in line with the theoretical prediction. • Wetting related complications are mitigated through the ultra-fast solidification rates, allowing high-resolution, ultra-high aspect ratio and locally tuned printed material density. • Individual droplet lands and conforms to the shape of the metal substrate in molten state before complete solidification. • Rapid droplet solidification, when extremely fast leads to incomplete wetting, creating nanometric voids in the structure. • Each droplet shows its unique grain structure and grain boundary due to lack of remelting. • Wide range of materials, such as metals and dielectrics are compatible to TIN-LIFT, due to the jetting characteristics and ease of donor preparation. • Micron scale copper pillars with high aspect ratio (A/R > 20) can be fabricated in upright and arbitrarily bent structures.	• Random nanometric voids observed (< 4% of the print volume) through image processing at the junction between the electroplated and LIFT copper track. • Formation of copper oxide leads to generation of air gap between the two structures, preventing adhesion. • At certain locations lack of remelting led to absence of grain continuity • Au tracks have significantly higher porous structure than the copper base slab, since optimal parameters were not determined for Au, instead the same process parameters were used.
(Breckenfeld et al., 2015)	Silver nanopaste	• A frequency-tripled Nd:YVO_4 pulsed laser (λ: 355 nm, 65 ns FWHM, f: 30 kHz). • 50 μm × 50 μm voxels (thicknesses: 0.8-8.7 μm) transferred under variety of laser fluences, determining a thickness-fluence regime. • All voxels were transferred at the threshold laser fluence. • Two thicknesses for each set of voxel dimensions, where "thicker" voxels were found to have more rounded edges and "thinner" voxels were found to have sharper, squared edges. • 1 mm and 3 mm long voxels chain (single layer and double layer) fabricated with simple end-to-end chains (single layer) and brick-wall-like stacks (double layer). • Microwave properties of several devices on different dielectric substrates show relatively low losses up to 10 GHz.	• Porosities observed for both (i) 2.5 μm × 2.5 μm voxel (thickness: 400 nm), (ii) 5 μm × 5 μm voxel (thickness: 300 nm), with the later having the significant porosity. • Discontinuity in voxel chains observed post curing (250 ºC, ambient conditions), representing low bonding between transferred voxels.
(Feinaeugle et al., 2018)	Gold and copper	• 6.7 ps laser (λ: 515 nm, f: 400 kHz, fluence: 100–500 mJ cm^{-2}, beam radius: 3.7 μm and Gaussian spatial profile: $M^2 < 1.3$) utilized for LIFT. • LIFT and chemical etching utilized simultaneously to fabricate complex, free-standing, 3-dimensional gold structures. • Post Au and Cu transfer, ferric chloride used to completely etch out Cu (mechanical support)	• Highlighted challenges to produce small features are: (i) deposition precision, and (ii) low mechanical stability of the structures.

doi:10.6342/NTU202301493

		• Feature sizes of <10 µm achieved having surface roughness of 0.3 to 0.7 µm. • Negligible interfacial mixing of Cu and Au proves the viability of the work.	• Resolution of the deposited Au hampered by deposition accuracy and splashing. • Smaller and structurally weak structures collapsed due to residual stresses from solidification and cooling. • Distorted structure due to forces from rinsing and evaporation of the liquids during etching. • Significant Au porosity observed.
(Charipar et al., 2018)	Silver nanopaste	• A frequency-tripled Nd:YVO_4 pulsed laser (λ: 355 nm, 30 ns FWHM, f: 30 kHz) was used to perform LIFT experiments. • Interconnects fabricated via LIFT on RF switches post curing show similar capabilities wire-bonded device. • Laser printed interconnects are compatible with high frequency devices, allowing for a wide range of device compatibility. • LIFT utilized for high-aspect ratio micro-pillars and free-standing structures to be employed as interconnects. • Printed micro-pillars: diameter ~ 30 µm, height ~ 115 µm, aspect ratio ~ 4-1.	• Curing in air at 220°C required for obtaining desired electrical properties (resistivity of ~ 1.9 x 10-7 Ωm).
(Levy et al., 2021)	Copper	• A passive Q-switch pulsed laser (λ: 532 nm; f: 75 kHz), • Combination of stereolithography (SLA) and LIFT for structural material buildup, and conductive/resistive elements respectively. • Structural material: dry photoresists film exposed and laminated, forming a stack. • Interconnection made between structural material stacks using penetration of high aspect ratio pillars. • Height, size and distance between pillars optimized for successful film penetration during lamination. • Subsequently, conductive lines printed on top of the film layer for continuous conductivity across stack layers (penetration yield of > 95%).	• Rigorous testing to mechanical stress must be tested as failure of an interconnecting pillar between stacks may lead to shorting of the device. • At present, the processes require three different setups and facilities, therefore, integration into a single system is essential. • Finally, present scenarios show high material acquisition cost (epoxy based dry films and roll to roll copper donor).

doi:10.6342/NTU202301493

2.2.3. Deposit-receiver substrate adhesion and morphological uniformity

Despite the numerous advantages of LIFT, it cannot meet real life applications due to low efficiency and a small transfer gap. Challenges associated with poor adhesion due to lack of metallurgical bonding between the deposit material and the receiver substrate limit the applicability of LIFT. For sensor applications where conductivity is essential, and poor adhesion causes insufficient redox reactions. Liu et al. (Liu et al., 2023) proposed a concept of surface modification for enhanced adhesion. They adhered aluminum nitride (AlN) ceramic to copper using laser-induced metallization by introducing groove interface structure at the interface. The micro-groove structures produced a mechanical interlocking effect, improving shear strength and heat transfer performance. Levy et al. (Levy et al., 2021) discussed the effect of surface roughness on LIFT deposits. They observed good adhesion strengths between LIFT deposited material and receiver substrate for similar roughness and droplet diameters/geometries (see Fig. 2.12). Simultaneously, Germain et al. (Germain et al., 2007) and Zenou et al. (Zenou et al., 2015a) demonstrated the use of modified receiver substrate surfaces for enhanced adhesion. They incorporated surface patterns and roughening techniques for the same. Furthermore, Huang et al. (Huang et al., 2023) introduced a new type of LIFT known as the arc beam LIFT (AB-LIFT), which demonstrated superior quality deposits in terms of adhesion and bonding. The deposits withstood ultrasonication in water, tape test and sand paper polishing. Finally, a number of past researches related to deposition-receiver adhesion have been summarized in Table 2.3.

doi:10.6342/NTU202301493

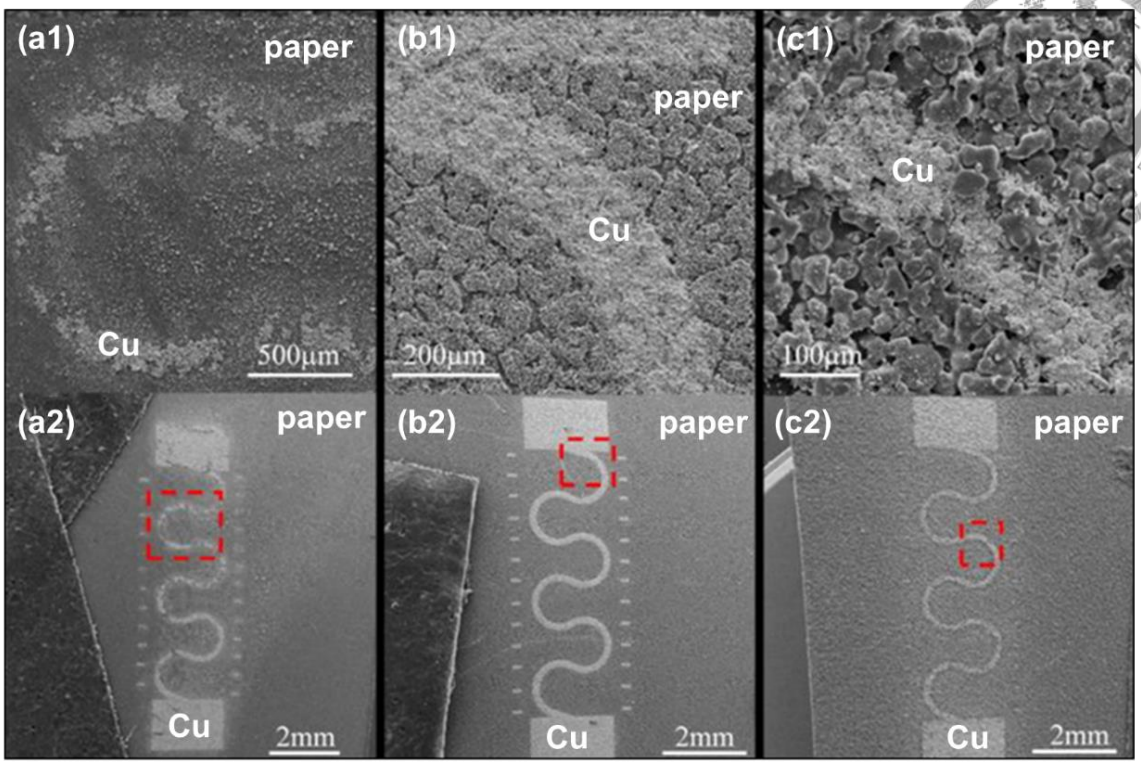

Fig. 2.12: SEM micrographs of LIFT printed copper droplets on different roughness lapping paper (a1,a2) 1 µm, (b1,b2) 9 µm and (c1,c2) 30 µm. Overall print coverage of copper: (a1,a2) 44.8%, (b1,b2) 91.3%, and (c1,c2) 99.8%. (Levy et al., 2021)

doi:10.6342/NTU202301493

Table 2.3: Summary of studies utilizing LIFT to discuss weak adhesion strength between deposit and receiver substrate through the years.

Investigators	Materials investigated	Notable highlights/inferences	Notable limitations
(Germain et al., 2007)	Gold	• Ti:Sapphire 110 fs laser (λ: 800 nm, f: 1 kHz, pulse energy: ~500 μJ). • Conductive lines and pads printed using LIFT under ambient conditions, utilized for repair of heaters for microfluidic applications and print electrodes for control of electro-osmotic flow in microfluidic devices. • Printed electrodes (widths: 10-50 μm) measured for their resistance having 1-4 mΩ. m and electrical curing improved conductivity • Gaseous-like LIFT transfer chosen to minimize mechanical movement effects and produce good adhesion. • The lines were reasonably well adhering. Mechanical shaking and tapping the substrate had no effect on line structure or conductivity. • Au has better adhesion to Pt or Cr compared to glass.	• Porosities observed with no conductivity in the printed structures, without post treatment. • Resistivities of deposited structure shows ten times higher resistance than bulk Au after post treatment (electrical heating ~100 mW/mm). • Ultrasonic cleaning and scotch tape test led to loss in material and conductivity.
Kaur et al. (Kaur et al., 2014)	Indium	• A Time bandwidth Duetto laser (355 nm, 12 ps, Fluence: 270 mJ/cm^2) utilized for LIFT of In micro-bumps fabrication for the flip-chip (FC) bonding of single vertical-cavity surface-emitting laser chips. • Mechanical ruggedness tests show complete separation from the contact pads (average force applied: 34.3 gf, or 4.3 gf per bond site). Centerline fracture is seen indicating good adhesion of the bumps to the contact/bond pads both on the substrate and on the chips. • The optical, electrical, and mechanical reliability of the bonded devices illustrate LIFTs applicability in interconnect technology, such as single chip bumping, high-density flip-chip interconnections (high accuracy, and fine pitch).	• Scotch tape test was passed and tests show good strength.
(Zenou et al., 2015d)	Copper and gold	• 6.7 ps laser (λ: 515 nm, f: 400 kHz, fluence: 100–500 mJ cm^{-2}, beam radius: 3.7 μm and Gaussian spatial profile: M^2 < 1.3) utilized for LIFT. • Adhesion of the printed copper droplet to metal oxides is typically poor, hence pre-treatment for oxide removal (for Al or Cu, with their native oxides). • Noble metals show negligible adhesion problems. • Plastic, ceramic or epoxy materials show bouncing of jetted droplet due to contact point heating and resulting pressure. Pre-treatment such as surface patterning through laser ablation or mechanical roughening can enhance adhesion.	• Issues associated to adhesion and their countermeasures have been addressed in detail.
(Levy et al., 2021)	Copper	• A passive Q-switch pulsed laser (λ: 532 nm; f: 75 kHz),	• The proposed solutions are not so favorable due to requirement of a

doi:10.6342/NTU202301493

		• Combination of stereolithography (SLA) and LIFT for structural material buildup, and conductive/resistive elements respectively. • Adhesion problems in LIFT of epoxy based dry films arise due to droplet bounce off, which can be minimized through substrate surface roughening. • The aforementioned concept was tested using a variety of lapping paper grades (diverse roughness levels). • Best quality printing observed for lapping paper of 9 µm particle size *Sq* = 9.35 roughness with a 99.8% coverage and 5.3 Ω. • LIFT copper droplet size is nearly similar to lapping paper grade i.e. ~5-10 µm in diameter. • Other techniques such as embossing, lamination of corrugated dies and drop casting utilized for surface roughening, produced line widths ~50 µm accurately.	planned hybrid single tool for enhanced printing throughput. • Resolution could be hampered due to particles scattering due to dry film exposure post roughening.
Huang et al. (Huang et al., 2023)	Copper	• MAC series microchip 1.8 ns laser (λ: 532 nm, f: 1 kHz utilized for the LIFT based process. • Gaussian beam LIFT (GB-LIFT) modified into an Arc beam LIFT (AB-LIFT) by altering the gaussian beam using a liquid crystal on silicon spatial light modulator (LCOS-SLM). • Flight distance of AB-LIFT (~120 µm) is twice of GB-LIFT at the optimized process parameters (1.94 µJ, scanning velocity: 3 mm/s). • AB-LIFT shows stable transfer, large receiving gaps, high bonding strength and low resistance (7.46 µΩ·cm). • AB-LIFT method utilized for microcircuit defect repair is verified. • An arc-shaped cavitation bubble is generated by the arc beam, which produces a driving force toward the central axis for stable transfer with large receiving gaps in the AB-LIFT process. • Constant porosity (~40%) observed on the microcircuit's surface for ns LIFT due to the combined effect of the thermal action and surface tension of the droplets.	• Optimized process parameters lead to resistances which is about 4 times that of Cu bulk (1.76 µΩ·cm). • Cu circuit resistant to damage post adhesion test (ultrasonication and tape test). Additionally, circuits withstood physical polishing by 3000 grit sandpaper.
Bonciu et al. (Bonciu et al., 2023)	PEDOT:PSS: GO composites	• 15 ns ArF laser (λ: 193 nm, f: 1 Hz). • LIFT of PEDOT:PSS: GO composites (25:75 %wt and 50:50 %wt) onto flexible screen-printed electrodes (fluence: 450–750 mJ/cm^2). • DRL affects the electrochemical response of the fabricated sensor, showing higher oxidation peak current to reduction peak current ratio (~2×) for the sensor with a 50:50 %et PEDOT:PSS: GO pixel.	• Validation of presence of DRL improves the interfacial adhesion of the pixel to the SPE electrode needs further investigation.

In addition to deposit and receiver adhesion discussion, one of the parameters closely related to the deposition quality is the uniformity in the deposit morphology. Defects such as voids and cracks. cause discontinuities in the printed structure, which often is a drawback for

doi:10.6342/NTU202301493

continuity applications where continuous conductivity is required. Fig. 2.13 illustrates LIFT deposited continuous structures having defects and porosities. It was observed that porosities and defects were generated for continuous deposits irrespective of single material transfer (Huang et al., 2023) or interdigitated structures (Paula et al., 2023). Albeit certain LIFT depositions show smooth transfer morphology, but it must be noted that these are single voxels, not continuous areal/volume depositions. Processes like VB-LIFT or single voxel-based LIFT process can ensure precise dimensional accuracy by proper parameter optimizations. Therefore, for continuous areal depositions have smooth and uniform morphologies/surface, post treatments like laser heating, low temperature annealing and sintering should be utilized. Finally, for the sake of brevity, separate section with summary is not presented for this issue as discussion can be made with all researches mentioned above.

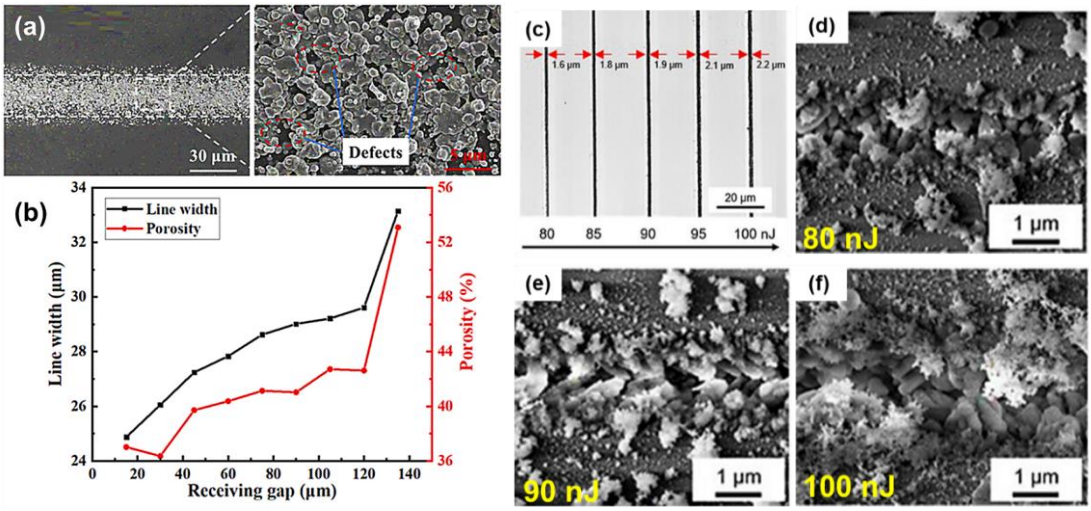

Fig. 2.13: Porosity and defects analysis for LIFT deposits (a) Morphology of Cu deposits on glass substrate, (b) Relationship between receiving gap and microcircuit line width and porosity, (c) continuous fs-LIFT GO/Silica deposits with increasing pulse energy, (d-f) SEM images of the deposits shown in (c). Refs. (Huang et al., 2023, Paula et al., 2023).

2.3. Future application: LIFT for Biosensor manufacturing

Electrochemical biosensors dominate over others due to their low cost, militarization capabilities, automotive and easy-to-use properties (Arduini et al., 2016). A number of manufacturing processes have been used to fabricate electrochemical biosensors. Of which

doi:10.6342/NTU202301493

printing technologies have been the most popular techniques. These include screen printing, inkjet printing, and roll-to-roll printing (gravure printing, roll-to-roll nanoimprinting and flexographic printing) (Maddipatla et al., 2020).

In 1980s, MediSense team adapted screen printing, and at present, it is utilized in most disposable glucose sensors (Turner, 2013), due to its reproducibility, reliability, low-cost and mass production capabilities (Arduini et al., 2016). Other properties of the screen-printed electrodes for biosensors include ability to develop ductile devices, which can be made of different materials (enzymes, antibodies, DNA, etc.) in various shapes. Screen printing has paved the way for numerous applications such as enzyme-based biosensors (nanomaterial, wearable and paper-based microfluidic devices) (Arduini et al., 2016), DNA biosensors (Yamanaka et al., 2016), biosensors for monitoring metal pollutants (Honeychurch, 2012), detection of biomarkers (cardiac, cancer, inflammatory) (Honeychurch, 2012), etc.

Inkjet printing is the widely used and most promising method for mass production due to its wide material range, mask-less and noncontact mode of operation. Inkjet printing consists of two main parts: (i) ink chamber, and (ii) channel connecting the ink chamber to the nozzles (Hussain et al., 2022). Since the first concept in 1878 (Strutt and Rayleigh, 1878), thermal and piezoelectric printers have been the most popular types of inkjet printing. However, both these have their respective limitations. Thermal printing introduces limitations such as high-temperature generation (Parashkov et al., 2005), thermal stability, thermal degradation of organic/biological materials (Setti et al., 2005), and can be overcome by piezoelectric printing. However, piezoelectric methods offer complicated mechanisms, less environment-friendly ink solvents and higher ink viscosities when compared to the thermal methods (Setti et al., 2005, de Gans and Schubert, 2003). Additional limitations of inkjet printing lie in its resolution at nanoscales (limited to microscales). In such cases of nanoscale level resolution requirements, scanning probe lithographic techniques are beneficial but again they are limited to the industry-level application due to its time-consuming nature. One process which saves time is microcontact printing, but it is limited due to the mask requirement. Lithography techniques are slow and therefore not preferred for mass production especially, e-beam lithography (even slower than photolithography). Albeit, MAPLE permits printing of multilayers; however, it is only suitable for low volume, prototyping and mask production or

doi:10.6342/NTU202301493

repair (Gonzalez-Macia et al., 2010). Summarizing, lithographic techniques mentioned above are not employed for mass production of biosensors, but only act as preliminary steps to manufacturing. The plasma polymerization method offers advantages like improved enzyme immobilization (by substrate functionalization), limitations like high cost of operation (due to its vacuum requirements) limits in its industrial use. Only if this technique is used in complementary to other processes for improvements in enzymatic adhesion, it might be plausible.

Gravure printing utilizes a rotating printing cylinder is used to engrave patterns. Conducting polymers (Zhu et al., 2008, Tuomikoski et al., 2006) and ITO nanoparticle dispersions (Santa-Nokki et al., 2006) are some materials that have been used. This process has not been popular due to high-pressure requirements and the resulting low resolution of the printed patterns hampering the development of high-precision devices. Furthermore, this kind of process has long and utilizes the cost of cylinders, which otherwise is expensive for short runs. Flexographic printing: the printing roll is coated through a flexography rubber having raised portions coated with a uniform film of ink. Although this printing technique is a little better than gravure printing in terms of pressure and resolution, it is only used for short and medium runs another flexographic technique which enables patterning of submicron features is roll-to-roll nanoimprinting (with speeds up to 20 m/min). This process transfers the pattern to the substrate using pressure, usually at high temperatures. Other techniques include microcontact printing, soft lithographic method (microfluidic network, (μFN), laminar flow, and metal transfer (MT) printing) (Parashkov et al., 2005, Kane et al., 1999), probe-based techniques (Dip-pen nanolithography (Tang and Shi, 2008, Lim and Mirkin, 2002), nanografting, local oxidation nanolithograhy), lithographic techniques (photolithography, electron bean and laser-assisted (Matrix-assisted pulsed laser evaporation (MAPLE)) deposition), plasma-based patterning (plasma polymerization) (Kampfrath and Hintsche, 1989, Yoshimura et al., 1991, Yoshimura and Hozumi, 1996), vapour deposition and subsequent laser ablation.

There are a number of limitations that are encountered in the aforementioned biosensor fabrication techniques and discussed subsequently. Inkjet and lithographic techniques enable direct (Roda et al., 2000, Ringeisen et al., 2001) and indirect (Britland et al., 1992, Hasenbank

doi:10.6342/NTU202301493

et al., 2008) deposition of enzymes. Simultaneously, the extreme conditions required in plasma polymerization do not support direct deposition (Muguruma et al., 2005). Furthermore, direct deposition of enzymes/proteins is possible for dip-pen nanolithography and local oxidation, whereas indirect deposition is supported by nanografting and microcontact printing.

In conclusion, from the aforementioned limitations, it is evident, that existing techniques cannot provide a short time, high precision and nanometer scale patterns at the same time. Therefore, in the past, manufacturing processes were decided according to the application, i.e. what is more important to the final device resolution, time effectiveness or precision. Upon deciding the process specific to the final device, optimizations are made, to achieve the best results. Therefore, the need for a single-step process addressing the aforementioned shortcomings is inevitable. This leads us to a process named laser induced forward transfer (LIFT), with enormous potential in the development of biosensors, due to its fast, precise, high resolution capabilities. LIFT offers unique advantages over ink jet methods, due to its wide range of printable viscosities and no important composition and material rheology restrictions in LIFT (Serra et al., 2010). Furthermore, LIFT is a non-contact process that prevents contamination. Lastly, the nozzle-free LIFT technique eliminates problems like clogging and drying which hampers the performance of printing heads for inkjet printing. The process parameters, advantages and limitations of LIFT have been emphasized in the sections above. Subsequently, an effort is made to provide evidence that LIFT can be employed to successfully develop/fabricate/manufacture biosensors. Since this research tends to form the founding steps for fabricating additively manufactured electrodes for electrochemical glucose biosensors in the future, a brief summary of past research works has been made.

doi:10.6342/NTU202301493

Table 2.4: Summary of studies on manufacturing biosensors using LIFT through the years.

Investigators	Biosensor type	Important highlights and prominent results/inferences	Notable limitations
Serra et al. (Serra et al., 2004)	Functional DNA microarray biosensor	• Buffer solution spotted at different laser pulse energies. • Uniform spots of ~40 μm (diameter) deposited. • Full functionality of the microarray was demonstrated (proving the potential of LIFT for DNA microarray production). • Resulted hybridization is specific in nature (allowing multiple different genes discrimination).	• Spot diameter not been optimized. Smaller droplets can be deposited by tuning laser focus, liquid film thickness etc.
Zergioti et al. (Zergioti et al., 2005)	DNA/Protein micro array biosensor	• The high directionality (ultrafast laser) results in high spatial resolution (down to 10 mm) and quality. • Ultrafast laser pulses prevent melting and vaporization, and deposits with minimum spread, narrow angular divergence and high spatial resolution. • Superior printing quality achieved at ultrafast pulses <1ps due to minimum thermal effects and negligible damage to the deposited material. • Adverse thermal effects prevented, thereby not damaging labile biomaterials (for < ns pulse width regime). • Simple method to deposit biomaterials on substrates (without requiring any transfer matrix material). • Efficient patterning of DNA and protein micro-arrays in a one step process, with repetitive and reproducible properties. • Facilitates in-vitro studies (protein function at genome-wide levels).	• Negligible notable limitations associated to LIFT.
Serra et al. (Serra et al., 2006)	DNA microarray biosensor	• Material transfers through ejection of liquid from the film to the receptor substrate as a microdroplet. • Micrometric patterns of biomolecules produced. • Liquid solvent is the transport vector of biomolecules. • Negligible biomolecule decomposition and bioactivity loss (transferred material remains in the liquid state). • Micron-sized droplets with high spatial resolution. • DNA microarray (biosensor), has the ability to sense specific DNA strands and discriminate between two different human genes. • Microarray signal proves DNA concentration of the transferred material equal to the liquid film (no biomolecule damage).	• Results show some loss in the shape accuracy of the larger deposited structures.
Fernández-Pradas et al. (Fernández-Pradas et al., 2007)	Functional miniaturized biosensors	• Lasers are adequate tools for high spatial resolution • LIFT transfers biological solutions onto solid substrates (μm biomolecule patterns. • LIFT is more viable for miniaturized biosensors fabrication, providing higher degrees of integration, prevents contamination and clogging issues. • Droplet deposition with diameters < 10 μm. • LIFT is an effective method for protein microarrays deposition, preserving biomolecule bioactivity.	• Comparative studies show similar fluorescence intensity and unspecific hybridization levels for both LIFT and pin micro-spotting.

doi:10.6342/NTU202301493

Duocastella et al. (Duocastella et al., 2010)	DNA/Protein miniaturized biosensor	• High degrees of reproducibility and resolution can be achieved. • Microarray preparation (proteins and DNA) shows potential of LIFT for miniaturized biosensors manufacturing. • User-friendly, uniform, reproducible, well-defined microdroplets deposition. • Selective protein and DNA detection, suitable for miniaturized biosensors preparation. • Contamination risks are minimized through LIFT.	• Deep laser focusing is a limitation which results in no material deposition.
Palla-Papavlu et al. (Palla-Papavlu et al., 2011)	Liposome micropatterning based biosensor	• Liposomes employed in micro and nano-sized biosensors. • LIFT enables μm sized well defined patterns with no splashing (at 193 nm irradiation; sacrificial layer: TP). • Sacrificial layer thickness > 150 nm (for clean, debris-free patterns) • Liposome integrity and chemical composition maintained (40 to 60 mJ/cm^2) • Target-substrate distance does not affect micropattern morphology. • Economical and time-effective technique for liposome array production. • LIFT shows potential application in in-vitro and in-vivo studies.	• Au or Ti donor layers produce debris. • Results show incomplete TP (sacrificial layer) removal for fluence range with regular patterns. • The shape and size (transferred patterns) dependence for TP DRL layer with laser fluence not established.
Boutopoulos et al. (Boutopoulos et al., 2011)	Amperometric biosensor	• Photosynthetic material deposited on low cost nonfunctionalized SPEs. • High kinetic energy (transferred material) results in direct immobilization of the thylakoids on the electrodes. • Efficient electrochemical contact (proteins-electrode: stable photosynthetic biomolecule and efficient transport of electrons. • Complete wetting of the rough electrode surface. • High photocurrent signals (335 nA), high signal to noise ratio, reduced response time (5 min), no diffusion limitations, and higher life time (48 h).	• Response time of 5 minutes can be improved, considering the current advancements of the process.
Touloupakis et al. (Touloupakis et al., 2012)	Electrochemical biosensors	• Efficient electron transfer from photosynthetic biomaterial immobilized on SPE through LIFT. • Enhanced efficiency of energy production of a photosynthetic system. • Efficient and sensitive detection of herbicides (~nM conc.). • Biological molecules, supramolecules, and living cells combined with artificial supports show enhanced performance. • LIFT enhances energy conversion in electrochemical sensors. • High-spatial-resolution (liquid biomaterials: ~μm). • Efficient electrochemical contact (between proteins and electrode). • No damage of materials and functions during interfacing (with solid substrates). Extreme solid junctions created (with electrodes).	• Half-life of 24h. • Storage requirements for immobilized electrodes (−20°C: maintained properties for 3 months) • Expensive SPE material (gold, carbon paste, and carbon-nanotubes).

doi:10.6342/NTU202301493

		• High stable response signal (335 ± 13 nA) and excellent signal-to-noise ratio for low photosynthetic mass of 28 ± 4 ng). • Au SPEs show the best performance.	
Tsekenis et al. (Tsekenis et al., 2012)	Micro-membrane array capacitive DNA biosensor	• Au and 3-glycidoxypropyl-tri-methoxy silane (GOPTS) used to immobilize thiol-modified oligonucleotides on low temperature oxide (LTO) silicon (Si) surfaces • Probe and target concentrations along with thickness and roughness of functional layer affect sensitivity of sensor by increasing the surface stress developed upon probe immobilization and target hybridization. • GOPTS suited as a functionalization layer (enhanced hybridization efficiencies and relative stability over time, and ability to regenerate post analyte recognition). • LIFT uniformly deposited probe oligonucleotides at μm scale on GOPTS-functionalized surfaces.	• GOPTS functionalized surfaces are not highly stable at room temperatures, therefore, limiting its use storage in normal conditions.
Di Pietrantonio et al. (Di Pietrantonio et al., 2013a)	Surface acoustic wave biosensor	• LIFT employed for wtpOBPs transfer onto SAW resonators for odor detection applications. • Excellent surface coverage (overlap of ~50% for droplets) (20% glycerol solution; laser fluence: 650 mJ/cm^2). • Lowe detecting agent consumption. • Good repeatability and linear response curves obtained. • Sensitivity of 20.7 Hz/ppm and of 13.8 Hz/ppm for octenol and carvone respectively. • Detection limit of 0.48 ppm and 0.72 ppm for octenol and carvone respectively.	• Low individual printed droplet resolution. • Sensitivities are not exceptionally advantageous when compared to other methods (Di Pietrantonio et al., 2013b).
Chatzipetrou et al. (Chatzipetrou et al., 2013)	Label-free capacitive biosensor	• Biosensor for the detection of the DNA hybridization process. • Deposition of thiol-modified oligonucleotides onto (LTO)/Si membranes. • Interaction forces deflects ultrathin LTO membranes, resulting in a capacitance shift (hybridization of target oligonucleotides with their immobilized complementary strands). • Printing parameters affected oligonucleotides conditions, maximum deflection of the membranes leading to variation in capacitance. • Biomaterials deposition without bioactivity loss. • Percentage coverage of the sensor's membranes. • Printing multiple biomaterials without mixing. • LIFT ensured high resolution deposition of oligonucleotides, enabling multi-analyte detection. • The fabricated biosensors can be reused.	• Percentage coverage of the membrane was limited to a maximum of ~80% (usually between 60-80%).
Touloupakis et al. (Touloupakis et al., 2014)	Amperometric biosensor	• Improved sensitivity and detection limit (LOD). • Direct immobilization of laccase enzyme (no toxic reagents interfering/attenuating the signal. • Stable and highly sensitive biosensor. • Laccase (active) successfully immobilized on graphite SPE. • Biologic materials directly immobilized onto rough supports (without any functionalization).	• Reproducibility may be improved. • Compromised response stability to catechol (at 4 °C) after 35 days (90% of the initial response).

doi:10.6342/NTU202301493

		• Fair reproducibility (RSD: 11.7%) and detection limit (150 nM).	
Palla-Papavlu, et al. (Palla-Papavlu et al., 2014)	Surface acoustic wave (SAW) odor biosensor	• Successful development of surface acoustic wave (SAW) biosensors for odor detection in the food industry. • SAW biosensors coated with wild-type bovine odorant binding protein (wtbOBP) solutions containing 20% and 50% glycerol. • High resolution, individual droplet printing of 50% glycerol solution. • High uniformity (over active surface) and coffee ring effect suppression, despite low resolutions for 20% glycerol printed droplets. • Surface density of LIFT deposit 4 times higher than pipette deposit. • Fair sensitivity, (5 Hz/ppm) and detection limit (low ppm range) was obtained, with low detecting agent consumption.	• Resolution has to be compromised to achieve high uniformity and coverage over active area. • No significant improvement in sensitivity and detection limit for LIFT printed sensors.
Tsekenis et al. (Tsekenis et al., 2015)	Capacitive micro-mechanical sensor	• DNAzyme strand immobilized on the sensor surface and hybridized with the substrate strand through laser printing. • Change in surface stress leads to capacitance change. • 10 M of Pb^{2+} detected selectively. • LIFT enabled achievement of high spatial resolution in biological material spotting and different DNAzymes printing for multiple heavy metal water pollutants detection simultaneously. • The fabricated sensor can be modified into a microfluidic device which can lead to portable miniaturized sensor for onsite detection of Pb^{2+} or other heavy metals.	• Negligible notable limitations associated to LIFT.
Skotadis et al. (Skotadis et al., 2016)	Nanoparticle based electrochemical biosensor	• Fast, easy, highly specific and label free optimized biosensor for in situ detection of DNA hybridization. • Response range covers four orders of magnitude, LOD of 1 nM and ability to detect a single base pair mismatch between probe and complementary DNA. • LIFT utilized to deposit ssDNA probes. • Increased structural, electrical response at nanoparticle surface coverage of 46% • Inter-nanoparticle distance adjusted through deposition time. • Extremely flexible biosensor has multipurpose scenarios such as environmental monitoring, specific disease detection and integrated with other sensing devices.	• Negligible notable limitations associated to LIFT.

doi:10.6342/NTU202301493

Khairullina, (Khairullina et al., 2021)	Electrochemical biosensor	• Electrodes suitable for non-enzymatic detection of biologically essential analytes e.g. glucose. • High-rate metallization of various dielectrics. • Promising results for Cu-Au electrode structures manufactured on glass-ceramics. • Sensitivity of 3060 μA mM^{-1} cm^{-2} glucose sensing. • Linear range of glucose detection (0.3 and 1000 μM). • High selectivity and long-term stability of electrodes. • Quick and efficient manufacturing of Cu electrodes on various dielectric substrates. • Cu and Cu–Au electrodes on glass ceramics (i.e. Cu surface with Au nanoparticles) significantly increases the sensitivity (3060 *vs.* 911 μA mM^{-1} cm^{-2}), enhances the detection limit and increases the linear range of detection of the electrode towards dopamine sensing. • Additionally, Cu and Cu-Au sensors have good selectivity and excellent stability.	• Use of Au may be expensive when the biosensor is considered for mass production. • The long run stability for non-enzymatic glucose sensing is limited to 15 days (~93-96 % of the initial electrocatalytic activity was retained).

2.4. Finite element methods for LIFT

Over the years, the mechanisms involved in the ejection process have been studied. However, evidences show a number of phenomena involved in the LIFT process, from solid state physics to fluid dynamics to accurately model and understand the ejection process (Pohl, 2015). Computational tools have the ability to provide the insights into a process, therefore attempts are made to study the LIFT process.

Seifert et al. (Seifert et al., 1996b, Seifert et al., 1996a, Seifert and Betz, 1998) utilized Navier-Stokes equations to model gold droplet formation and ejection. The models showed thermal and hydrodynamic behavior under pulsed laser irradiation. Finally, it was inferred that gold droplets were influenced by equilibrium of surface tension and inertial forces. Willis et al. (Willis and Grosu, 2007) put forward that the ejected volumetric fluid motion sufficiently induced deformations which could be retained post solidification, i.e. impingement of a solidified droplet below the transfer threshold at certain laser fluence levels. They utilized volume of fluid (VOF) method with a 2-D axis-symmetric numerical model incorporating heat transfer, phase change, and fluid flow in the donor. Other modelling research made by Ivanov et al. (Ivanov et al., 2008) demonstrated the initial stages of LIFT transfer process, where they utilized a number of concepts such as Classical molecular dynamics (MD), lattice superheating, and fast phase transformations. Banks et al. (Banks et

doi:10.6342/NTU202301493

al., 2009) analyzed variations in threshold fluence levels and deposit morphology due to changes in intensity distribution. The model considered pulsed (fs) laser and distance between the donor and acceptor substrates.

A number of investigations have been made on BA-LIFT. Initially, Brown et al. (Brown et al., 2012) utilized a finite volume (FVM) and the volume-of-fluid (VOF) method to analyze the mechanisms involved in the transfer process (includes expansion of the laser induced bubble, fluid dynamics of ejected droplet). Subsequently, Arnold group at Princeton University utilized Level set method to model the BA-LIFT and LIFT process (Kattamis et al., 2011). However, recently, a number of research works by Labella et al. (Moreno-Labella et al., 2020, Moreno Labella, 2021, Moreno-Labella et al., 2021, Moreno-Labella et al., 2019) investigated and modelled the BA-LIFT and LIFT process using a 2-D axis-symmetry laminar flow phase field model. Labella et al. (Moreno Labella, 2021) argued that the laminar flow phase field model had the enhanced capability to closely simulate minute phenomena in the BA-LIFT and the LIFT process. For example, the secondary effects (observed by Brasz (Brasz, 2015)) in case of BA-LIFT were simulated accurately using the phase field method (Moreno Labella, 2021).

Summarizing the aforementioned literature, three main methods are adopted to model the fluid interface in the LIFT process namely, volume of fluid, level set and phase field. Out of the three, level set and phase field methods are quite similar, taking diffusion laws into consideration. Phase field can be considered superior of the two, considering its ability to incorporate tree phases while being computationally cheap. Therefore, considering the aforementioned progress made in the past in simulating various LIFT processes, an attempt has been made to utilize the 2D axisymmetric laminar flow phase field equation to simulate the LIFT process.

Navier-Stokes equations closely govern the fluid dynamics under the laminar flow regime. Laminar flow is a type of flow which has no turbulences and can be closely distinguished using the Reynold's number (Re).

Simultaneously, the phase field method enables the tracking of a two phase (fluid/air) interface using two variables namely, the Phase field variable (φ) (continuous with sharp changes at the air-fluid boundary, i.e. from -1 to 1 respectively) and a phase field help

doi:10.6342/NTU202301493

variable (ψ). Each contribute to a transport equation, solved for accurate interface tracking. The zero value isoline is utilized to define the interface at its middle value. Since surface tension effects can be highly significant in the LIFT process, therefore, the phase field method is advantageous to study the variation in the number of phase boundaries. Since a 2D axis-symmetric model is utilized, isosurface and isoline are simply interchangeable. The tracking of the phase boundaries is from an auxiliary function, which is the phase field function. The phase field function is thus determined by minimizing the mixing energy (surface energy + bulk energy). Simultaneously, the free energy of the system is minimized for determining the position and the surface tension contribute to the Navier-Stokes equation as the body force (Chemical potential × gradient of φ).

Cahn-Hilliard equation related to Chemical potential (G) governs the phase field variable (φ)

$$\frac{\partial \varphi}{\partial t} + u.\nabla\varphi = \nabla.\gamma\nabla\mathrm{G} \tag{2.4}$$

$$G = \lambda\left[-\nabla^2\varphi + \frac{\varphi(\varphi^2-1)}{\varepsilon^2}\right] \tag{2.5}$$

Where, G: Chemical potential (SI: Pa), λ: mixing energy density (SI: N), ε: capillary width related to the interface thickness (SI: m), γ: mobility (SI: m^3.s/kg). Furthermore, since the Cahn-Hilliard equation has a fourth order derivative, Eq. (2.4) can be represented into Eqs. (2.6, 2.7) in COMSOL utilizing the Phase field help variable (ψ).

$$\frac{\partial \varphi}{\partial t} + u.\nabla\varphi = \nabla.\frac{\gamma\lambda}{\varepsilon^2}\nabla\psi \tag{2.6}$$

$$\psi = -\nabla.\varepsilon^2\nabla\varphi + \varphi(\varphi^2 - 1) \tag{2.7}$$

Eq. (2.6) can be further simplified into Eq. (2.8) considering that the divergence of the velocity field is zero.

$$\frac{\partial \varphi}{\partial t} + \nabla.u\varphi = \nabla.\frac{\gamma\lambda}{\varepsilon^2}\nabla\psi \tag{2.8}$$

One of the important parameters that influences the time scale in the Cahn-Hilliard equation is the mobility parameter. Higher values can lead to over damping of the convective terms, whereas low values lead to constant interfacial thickness. Cahn-Hilliard equation ensures

doi:10.6342/NTU202301493

decrease in the system energy; therefore, researchers argue that the phase field method produces physically accurate results when compared to the level-set method.

In addition, G can be expressed using ψ as shown in Eq. (2.9). Furthermore, initializing phase near the interface results in smoothening of φ, as shown in Eq. (2.10),

$$G = \lambda \frac{\psi}{\varepsilon^2} \tag{2.9}$$

$$\varphi_0 = \frac{1}{1+e^{\pm W/\varepsilon}} = \pm \tanh\left(\frac{W}{\varepsilon\sqrt{2}}\right) \tag{2.10}$$

Another important aspect is the free energy which is dependent on φ and is shown in Eq. (2.11). Furthermore, the phase-field parameter is shown in Eq. (2.12),

$$F\ \varphi, \nabla\varphi, \mathrm{T}) = \int \left(\frac{1}{2}\varepsilon^2 |\nabla\varphi|^2 + f\varphi, \mathrm{T})\right)\mathrm{dV}\Big) = \int f_{tot} dV \tag{2.11}$$

$$\frac{\partial\varphi}{\partial t} + u.\nabla)\varphi = \nabla.\gamma\nabla\left(\frac{\partial f_{tot}}{\partial\varphi} - \nabla.\frac{\partial f_{tot}}{\partial\nabla\varphi}\right) \tag{2.12}$$

Where, f_{tot}: total free energy (SI: J/m^3), u: advective velocity field. The right side of Eq. (2.12) determines the total free energy minimization incorporating a relaxation time controlled using the mobility parameter γ. Furthermore, since the free energy density is the sum of the elastic energy and mixing energy, determining them is important as given by the Ginzburg-Landan form (Eq. (2.13)). The mixing energy density (λ) and capillary width parameter (ε) can be used to define the surface tension parameter as seen in Eq. (2.14). Moreover, φ can be used to define the volume fractions of the two fluids as given in Eq. (2.15). Finally, any additional energy sources can be added to the system by modifying Eq. (2.7) in Eq. (2.16)

$$f_{mix}\ \varphi, \nabla\varphi) = \frac{1}{2}\lambda|\nabla\varphi|^2 + \frac{\lambda}{4\varepsilon^2}(\varphi^2 - 1)^2 \tag{2.13}$$

$$\sigma = \frac{2\sqrt{2}}{3}\frac{\lambda}{\varepsilon} \tag{2.14}$$

$$V_{f1} = \frac{1+\varphi)}{2};\ V_{f2} = \frac{1-\varphi)}{2} \tag{2.15}$$

$$\psi = -\nabla.\varepsilon^2\nabla\varphi + (\varphi^2 - 1)\varphi + \left(\frac{\varepsilon^2}{\lambda}\right)\frac{\partial f}{\partial\varphi} \tag{2.16}$$

A number of other boundary conditions and terms have been defined to successfully carry out the COMSOL simulations. These are gravity (F_g) (Eq. (2.14)), surface tension (F_{st}) (Eq. (2.18)), external forces contributing to the free energy (F_{ext}) (Eq. (2.19)), wetted wall

doi:10.6342/NTU202301493

assumptions (Eq. (2.20)), inlet and outlet boundary conditions (Eq. (2.21)), and the material properties.

$$F_g = \rho g = \begin{pmatrix} 0 \\ 0 \\ -g_z \end{pmatrix} \tag{2.17}$$

$$F_{st} = \left(G - \frac{\partial f}{\partial \varphi}\right) \nabla \varphi \tag{2.18}$$

$$F_{ext} = \left(\frac{\partial y}{\partial x}\right) \nabla \varphi \tag{2.19}$$

where g_z: gravity constant, and F_{ext} is utilized phase field method as in Eq. (2.16) above. The wetted wall consideration is extremely important as it determines how the fluid interacts with the donor and receiver substrates. Furthermore, the wetted wall model restricts mass flow across the boundary and creates a contact angle (θ_ω).

$$n.\varepsilon^2 \nabla \varphi = \varepsilon^2 \cos \theta_\omega) |\nabla \varphi| \tag{2.20}$$

$$n \frac{\gamma \lambda}{\varepsilon^2} \nabla \psi = 0 \tag{2.21}$$

where n: perpendicular vector to the interface.

The inlet and outlet boundary conditions must be defined using a stress condition since pointwise pressure constraint would fail due to over-constraining, and is given as:

$$F_n = -p + 2\mu \frac{\partial u_n}{\partial n} \tag{2.22}$$

where u_n: Normal velocity component; F_n: reference pressure value at the boundary. Although the aforementioned stress condition can be defined using a pressure magnitude and velocity component, problems such as null pressure values may result at low Re. Therefore, an alternate solution to this is to utilize the tangential velocity (u_t) instead of normal velocity (u_n) as shown in Eq. (2.23)

$$\mu \frac{\partial u_t}{\partial n} = 0 \tag{2.23}$$

doi:10.6342/NTU202301493

Chapter 3 Research methods

The proposed research related to improvement of the LIFT process has been segmented into a number of parts, exploring critical aspects of the LIFT process. The research is divided into 4 broad categories: (i) conventional LIFT process, (ii) modified LIFT process, (iii) Finite element methods and (iv) energy analysis/studies. A number of experiments are made to study the conventional LIFT process. Subsequently, LIFT modifications have been made to enhance the LIFT process. Additionally, since the LIFT process has two critical phenomena taking place, i.e. the laser heating and the transfer of the material, these phenomena are analyzed using FEM. Finally, the past literature theories, analytical approximations and FEM results are utilized to conduct the energy analysis studies. An overview of the research work is shown in Fig. 3.1.

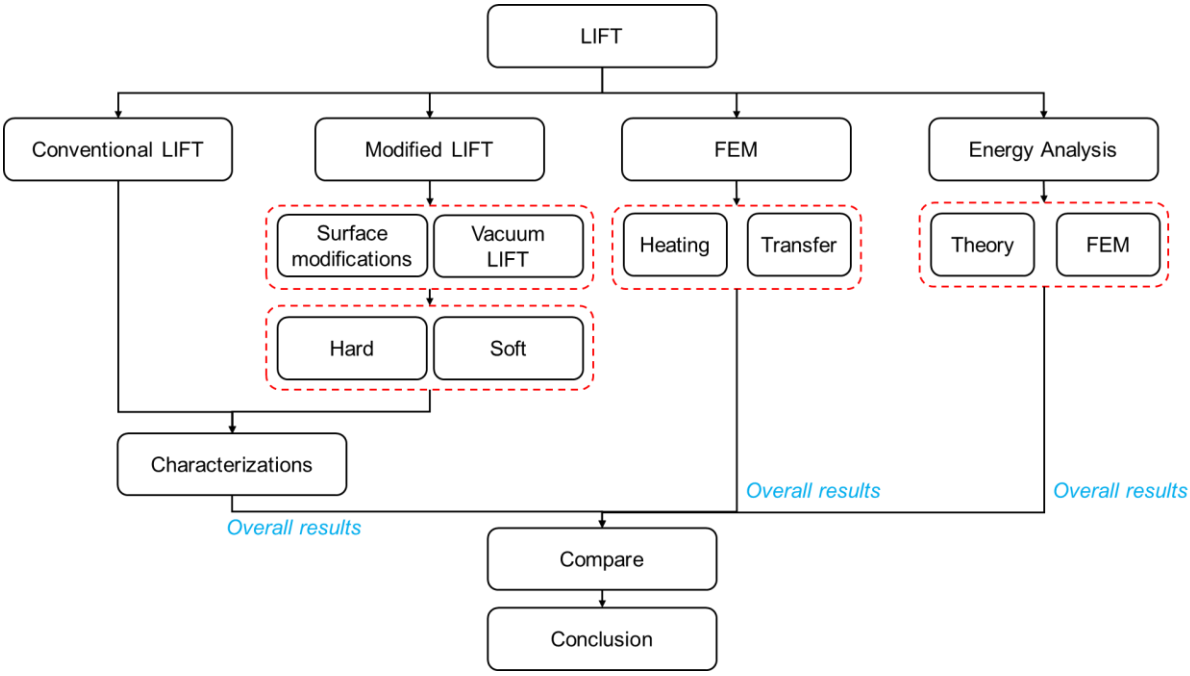

Fig. 3.1: Block diagram of the methodology. (LIFT: Laser induced forward transfer).

Before diving into the experiments, a number of setup optimizations must be made, which includes finding the accurate focus position of the beam for determining the beam diameter (d_{beam}). For this purpose, laser scans are made on paper at variable focal lengths as shown in

doi:10.6342/NTU202301493

Fig. 3.2. Therefore, from Fig. 3.2, the beam diameter is approximated to be 52 ± 2 μm (Laser parameters: Power 1 W, Speed 100 mm/s, Frequency 30 kHz).

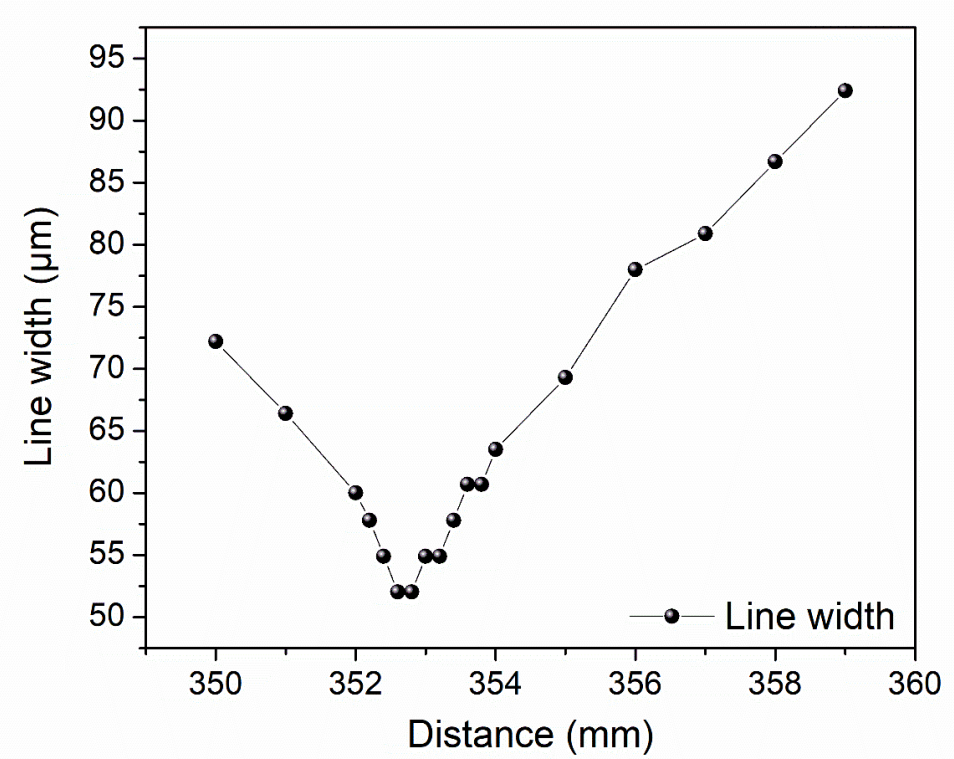

Fig. 3.2: Determining focus of the Laser beam. Laser parameters: Power 1 W, Speed 100 mm/s, Frequency 30 kHz.

Subsequently, setups must be made for conventional LIFT experiments which are capable of controlling the donor-receiver gap length accurately for LIFT experimentations. The experimentations require two types of setups, one for experiments in ambient air and the other for low pressure (LPE) experiments. For LIFT in ambient conditions, a four-stage controller (Stepping Motor Drive, SHOT-204MS, SIGMA KOKI Co. Ltd., Japan) with a z-axis stage with minimum increment value of 10 μm (Model SGSP60-10ZF, SIGMA KOKI Co. Ltd., Japan) is utilized as shown in Fig. 3.3(a). In to set and calibrate the 0 μm distance a calibration fixture is used as shown in Fig. 3.3(b).

doi:10.6342/NTU202301493

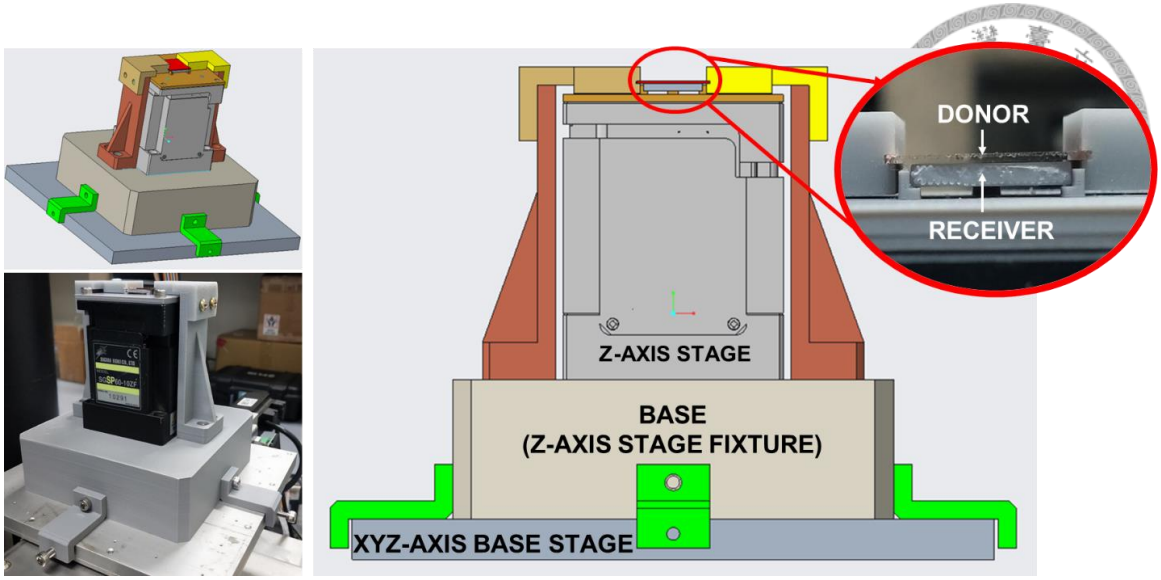

(a)

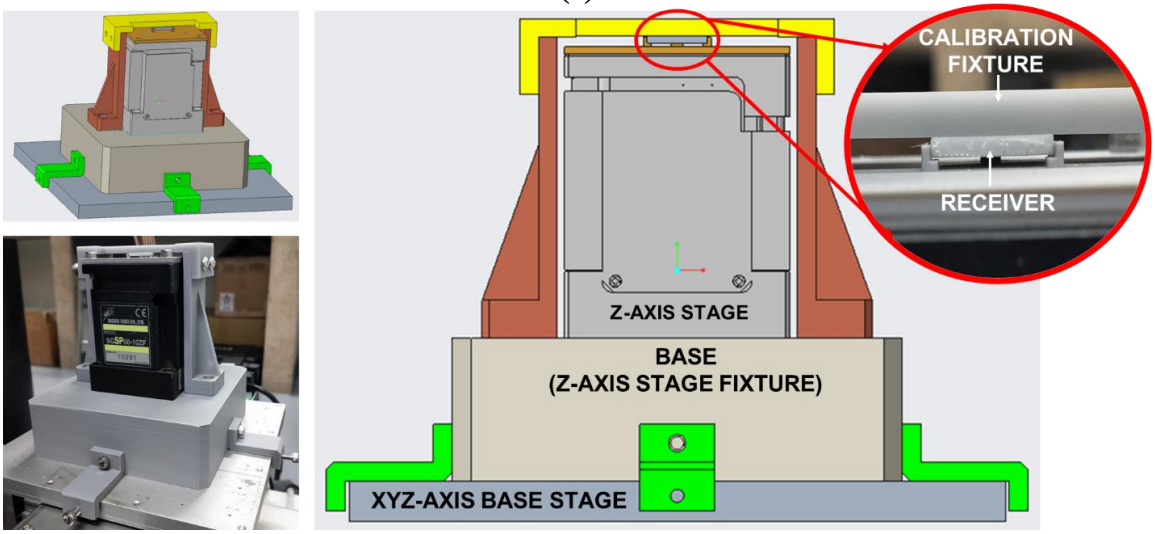

(b)

Fig. 3.3: Setups utilized to control the donor-receiver length (L) for conventional LIFT experimentations in ambient air.

In addition to the ambient experimentations, LIFT is performed under LPE environments. The setup, as shown in Fig. 3.4, is complicated to be enclosed in a controlled environment. Therefore, a special set of fixtures are made which can be simply placed inside the controlled environment as shown in Fig. 3.4. In this setup, the donor-receiver distance (L) is fixed, and five fixtures with 5 different donor-receiver distance (L) are manufactured independently using vat polymerization 3D printing.

doi:10.6342/NTU202301493

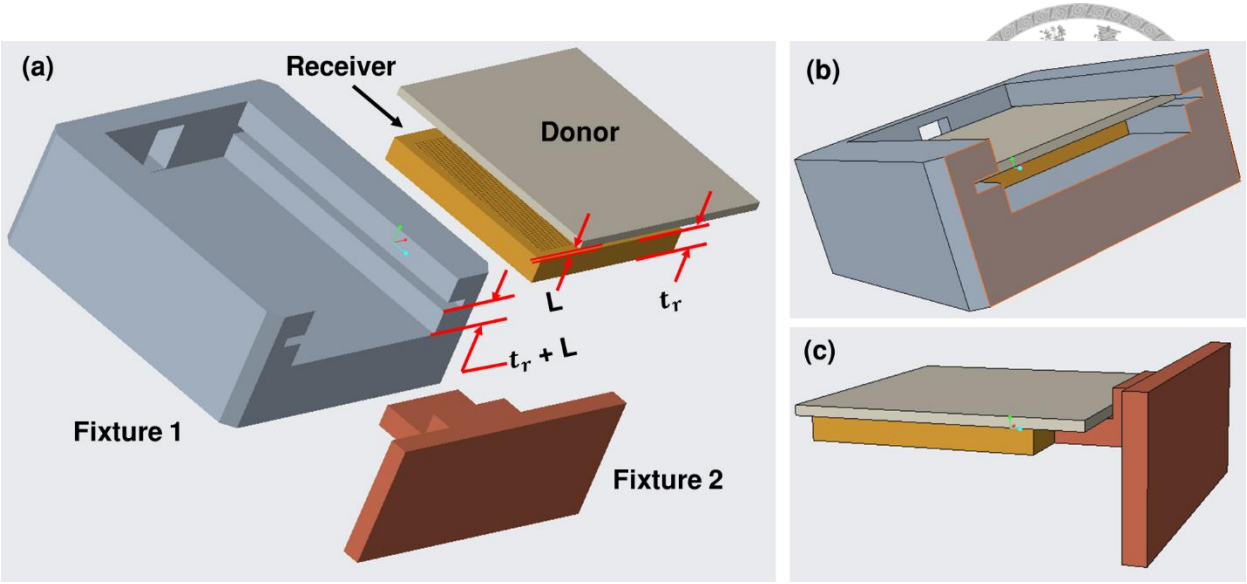

Fig. 3.4: Self-designed fixture to hold the donor and receiver substrates and accurately control the donor to receiver distance (*L*) for the LPE LIFT experiments. (a) Disassembled parts of the LIFT setup, (b) illustration showing the donor and receiver substrates positioned into fixture 1 with *L*= 0, 100, 200, 300, 400 µm (Fixture 2: hidden), (c) illustration of fixture 2 supporting the donor and receiver substrates in position (Fixture 1: hidden).

Preliminary investigation for successful planing of the experiments were carried out using the aforementioned setups (shown in Fig. 3.3 and 3.4). Post preliminary experimentations, the donor-reciever distance (*L*) was fixed to 400 µm to obtain significant differences in observations between the control and modified LIFT experimental results. Therefoe, all the experiments and results shown in this research correspond to LIFT with *L*= 400 µm. The complete setup for the LIFT process can be divided into two parts: (i) the laser path made on the optical table and (ii) the LIFT setup (see Fig. 3.5). The laser path starts with the laser coming out the laser source and entering the scanner through a set of mirrors (designated as M1, M2, M3 and M4), iris (designated as I1, I2, I3 and I4) and a beam expander (Jenoptik beam expander AD 0078 2x-10x, Jena, Germany). The laser after being expanded, enters the scanner with a f-θ theta lens (F-Theta-Roner, f = 250 mm, Rodenstock, Munich, Germany). Subsequently, the laser reaches the LIFT setup. The donor is placed at the focus of the f-θ

doi:10.6342/NTU202301493

lens to utilize the minimum spot diameter. The donor-reciever distance (L) is adjusted using a 400 μm thick tape provided by 3M (Minnesota, U.S.A). The donor thickness (t) and the donor-receiver distance (L) is varied according to experimental requirements. In addition, experiments conducted under low pressure environment (LPE) conditions (~60 cmHg).

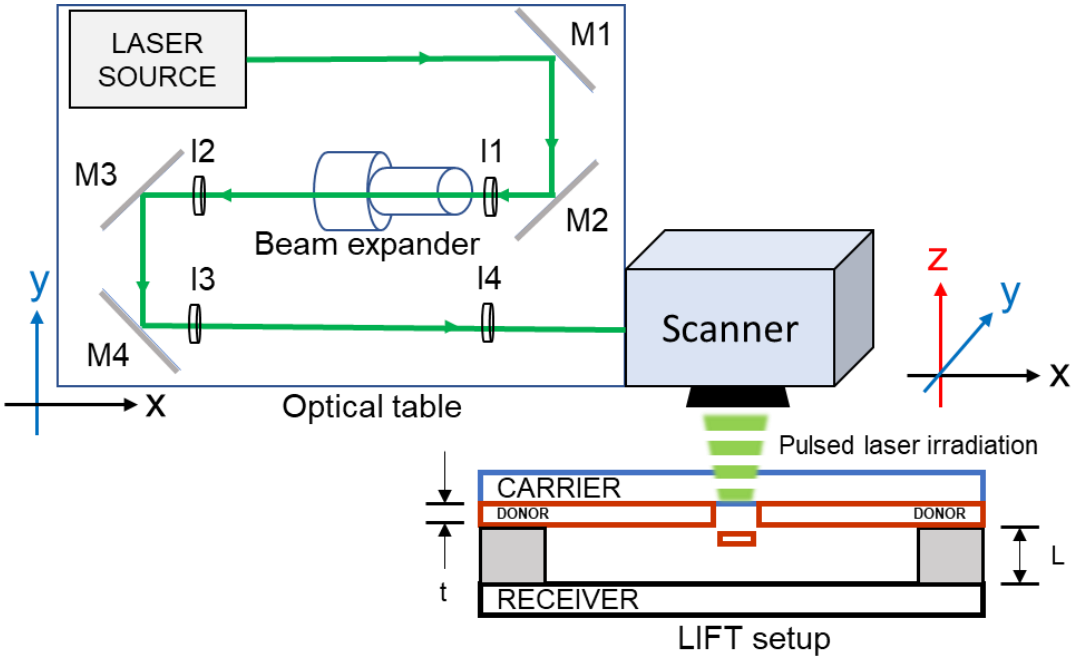

Fig. 3.5: Graphical illustration of the laser path and LIFT setup. The optical table corresponds to the x-y axis. The scanner and the LIFT ssetup corresponds to the x-y-z axis.

3.1. Materials

The research is targeted to be utilized for fabricating electrodes for biosensors for healthy sweat glucose monitoring in the future. Therefore, the proposed research requires precise and careful material selection for fabricating the following: (i) working electrode, (ii) reference electrode, (iii) auxiliary electrode/counter electrode, (iv) current collector/conductor, and (v) substrate. Working electrode material to be used is CuO, motivated by the work of Zhou et al. (Zhou et al., 2019) and Sedaghat et al. (Sedaghat et al., 2021), where Cu_2O/Cu is used as working electrodes. Reference and counter/auxiliary electrodes to be used are Ag and Pt respectively, which are widely used in literature (Gamella et al., 2014, Jia et al., 2013). Furthermore, for the conductor (current collector), copper (Cu) is used. The substrate

doi:10.6342/NTU202301493

materials which can be used is polyester (PET), which has excellent physical properties like tensile strength, thermal stability, and electrical insulation properties (HIFI Polyester Film Company, (Limited)). Therefore, the mentioned materials are efficiently utilized to additively manufacture material depositions via LIFT. The donor materials are prepared in the form of thin films through sputtering (procured commercially from Ruilong Co. Ltd. (銳隆光電) Taiwan). The donor specifications for Cu, Ag and Pt are as follows: (i) Cu: 1000 nm prepared on a glass substrate of 20 mm × 20 mm × 0.7 mm, (ii) Ag: 500 nm on glass substrate of 20 mm × 20 mm × 0.7 mm, and (iii) Pt: 500 nm prepared on sapphire substrate of 20 mm × 20 mm × 0.65 mm.

3.2. Donor ablation and conventional LIFT

The main objective of this section is to optimize the LIFT process by adjusting suitable process parameters. At first, laser irradiation at various process control parameters: fluence, donor-receiver substrate distance, scan rate and frequency are carried out to observe significant results. First, the parameters such as donor-receiver substrate distance (L), scan rate and frequency are fixed. Consequently, the frequency is fixed at 50 kHz for LIFT experiments. Interestingly, the overlapping of the laser spots will be optimized by changing the scan rate (mm/s): higher scan rate will create negligible overlapping and slow scan rates can result in significant overlapping. Likewise, the scan rate is fixed at 1300 mm/s for LIFT experimentations. Subsequently, the laser power is varied to determine the optimal laser power for efficient ablation and transfer in LIFT. The reason for the optimal power determination is due to the variation in the thermophysical values of the donor materials (Cu, Ag and Pt).

3.3. LIFT modifications

A number of methods have been utilized to modify the LIFT process for desired properties such as improved adhesion between Cu and receiver substrate. The modifications are explained in the subsequent sections in detail.

3.3.1. Change in receiver hardness

According to the company Smooth-On, polymers have been categorized from extra soft to extra hard as shown in Fig. 3.6. Therefore, in order to understand the effect hardness on

doi:10.6342/NTU202301493

transfer efficiency i.e. sample having high adhesion strength, LIFT on soft and hard receiver films are investigated. Since surface modifications on the receiver substrate will be made by laser surface texturing (LST) and vat photopolymerization (VPP), the material properties have outlined in detail, with the VPP parameters for substrate printing (see Table 3.1). The details on the surface modifications have been made subsequently. The Vat photo polymerization parameters are material specific. Therefore, Table 3.1 show the material properties and process parameters for the soft and hard materials respectively.

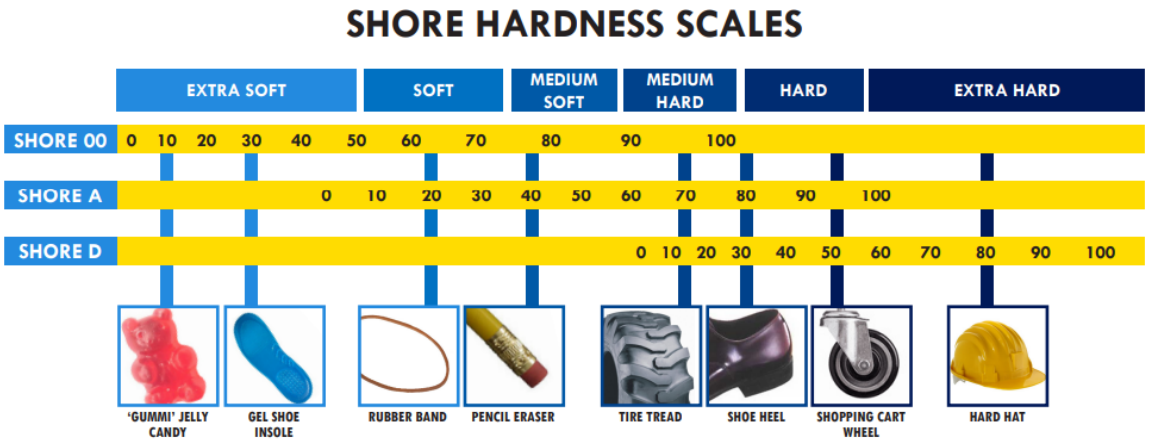

Fig. 3.6: Hardness classification according to Smooth-On Company (Smooth-on).

doi:10.6342/NTU202301493

Table 3.1: Material properties and process parameters for VPP of hard and soft material.

	Hard	Soft
Material Properties		
Viscosity (cP)	67	80
Density (g/cm^3)	1.10	1.1-1.2
Surface Hardness	76 (Shore D)	8 (Shore A)
Tensile Stress at Break (MPa)	10	1.1
Tensile modulus (MPa)	116	--
Elongation at Break (%)	3	709
Notched Izod Impact (J/m)	1.44	--
HDT at 0.45MPa (ºC)	46	--
Vat photo polymerization parameters		
Layer Height (mm)	0.05	0.05
Bottom Layer count	6	4
Exposure Time (s)	3	7
Bottom exposure time (s)	32	35
Bottom lift distance (mm)	5	6
Lifting distance (mm)	5	6
Bottom lift speed (mm/min)	30	30
Lifting speed (mm/min)	30	30
Bottom retract speed (mm/min)	120	120
Retract speed (mm/min)	120	120

3.3.2. Surface modifications

A number of methods can be utilized to modify the surface of the receiver substrate. One of the most effective way is through laser surface texturing (LST) as it can be accurately controlled. However, there are some challenges, such as determining the correct laser parameters when working with thin films. In addition, designing accurate texturing with a resolution of < 100 μm using the available green and CO_2 laser is difficult and tedious due to the variation in laser absorptivity of materials with laser wavelengths. Additionally, higher laser powers of the CO_2 laser degrade the polymer. Therefore, in addition to the LST made on PET, vat photo polymerization is utilized, which has a print resolution of 38 μm. Moreover, using vat photo polymerization helps in avoiding complications related to laser process parameters such as laser power, scanning speed and in accurately determining the focal point.

doi:10.6342/NTU202301493

Surface texturing using vat polymerization is applied on receiver substrate in the form of squared meshing as shown in Fig. 3.7. A number of parameters have been assigned to the texturing pattern, such as inter slot distance, slot width and the slot depth (see Fig. 3.7). The mentioned parameters are then varied arbitrarily between an upper and lower limit value to check for relevant relations or trends, if any (see Table 3.3). Creo 5.0 (a Computer aided design (CAD) software) is used to design the texture on the surface of polymer film.

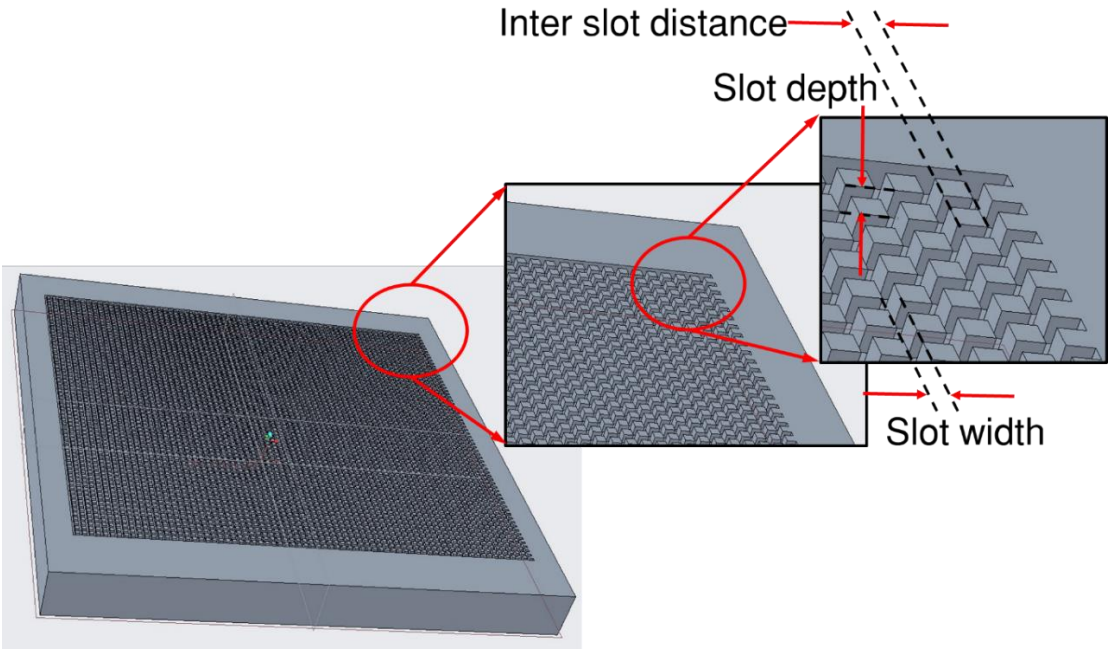

Fig. 3.7: Illustration of surface texturing CAD model used for Vat photopolymerization.

Table 3.2: Upper and lower limits of the surface texturing pattern made using Vat photopolymerization.

Parameter	Lower limit	Upper limit
Inter slot distance (μm)	50	150
Slot width (μm)	50	150
Slot depth (μm)	50	150

In addition to the aforementioned Vat photo polymerization process, nanosecond pulsed green laser have been used to scribe the receiver substrate. Laser surface texturing have been

doi:10.6342/NTU202301493

made on three types of substrates: (i) PET, (ii) vat photo polymerized substrates (hard), (iii) vat photo polymerized substrates (soft). In order to successfully ablate polymer material optimal power, scanning pitch and beam diameter must be determined. Therefore, the optimal power is determined using hit and trial method, and kept constant for a particular substrate type mentioned above, while the scanning pitch (see Fig. 3.8) is varied. Other parameters like scanning speed, frequency and pulse width are kept constant.

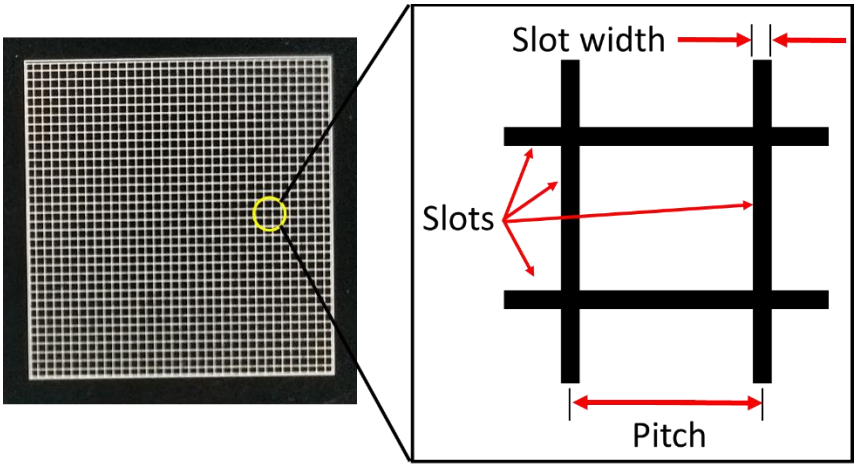

Fig. 3.8: Illustration of laser surface texturing pattern.

Table 3.3: Experimental design for laser surface texturing (LST) on various receiver substrates with variable pitch and orientations.

Experiment No.	**Pitch (mm)**	**Orientation**

doi:10.6342/NTU202301493

1a	0.02	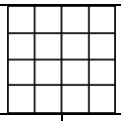
1b	0.02	 (horizontal)  (vertical)
1c	0.02	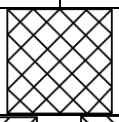
1d	0.02	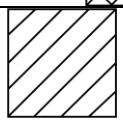 or 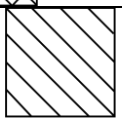
2a	0.04	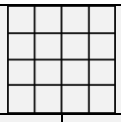
2b	0.04	 (horizontal) 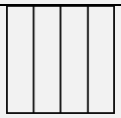 (vertical)
2c	0.04	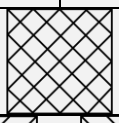
2d	0.04	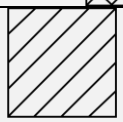 or 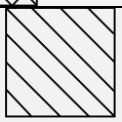
3a	0.1	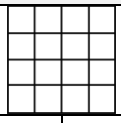
3b	0.1	 (horizontal) 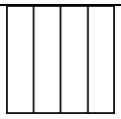 (vertical)
3c	0.1	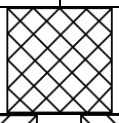
3d	0.1	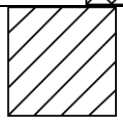 or 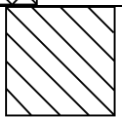
4a	0.5	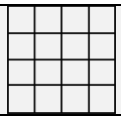

doi:10.6342/NTU202301493

4b	0.5	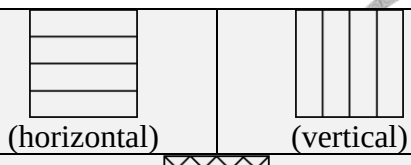 (horizontal) (vertical)
4c	0.5	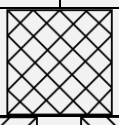
4d	0.5	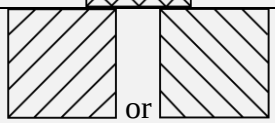 or

3.3.3. Shockwave and low-pressure environment LIFT

One of the major drawbacks of LIFT is its shockwave formation. Therefore, investigations are made to estimate the shockwave energy theoretically and through FEM. One of the earliest analytical formulations put forward for the estimation of shockwaves was given by Sir Geoffrey Taylor (Taylor, 1950) in 1941, which served as the founding steps for blast wave description, also known to be the Taylor-Sedov approximation. Considering the Taylor-Sedov approximation, Freiwald and Axford (Freiwald and Axford, 1975) published a method to approximate the shockwaves energy that is relevant for the LIFT process using a spherical blast theory which included source mass in 1974. According to the proposed theory, the energy of the shockwave was the sum of source debris energy (E_d) and the shock heated ambient gas energy (E_g). These energies were approximated through the following equations (using the blast theory including source mass) (Freiwald and Axford, 1975):

$$E_s = E_d + E_g \tag{3.1}$$

$$E_g = \frac{4}{3}\pi R^3 \rho_g \left(\frac{1}{2}v_g^2 + e_g\right) \tag{3.2}$$

$$E_d = \frac{4}{3}\pi R^3 \bar{\rho}_d \left(\frac{1}{2}v_d^2 + e_d\right) \tag{3.3}$$

According to the assumptions, $v_g = v_d$, as the pressure and flow speed are conserved across the surface. E_g is the integral of the driven gas obtained from the T-S approximate theory. Subsequently, ρ, v and e refer to the density, velocity and the specific internal energy for gas and debris with subscripts "g" and "d", respectively. In addition, for this research, the average debris density $\bar{\rho}_d$ is assumed to be equal to the density of the material at the estimated

doi:10.6342/NTU202301493

theoretical maximum temperature. Therefore, the aforementioned analytical approximations are utilized for the theoretical estimation of the LIFT process energy analysis in the subsequent sections.

Subsequent to the analytical solutions proposed above, FEM results are utilized to estimate the shockwaves in LIFT. Recently, shockwaves in LIFT has been widely discussed producing significant research (Mahmood and Popescu, 2021, Delaporte and Alloncle, 2016). Fardel et al. (Fardel et al., 2009b) estimated the shockwave energy and subsequently discussed its effects on the LIFT process (Fardel et al., 2010, Fardel et al., 2007). A simple description of the energy balance and estimation is given by Fardel et al. (Fardel et al., 2009b):

$$E_{laser} + E_{decomposition} = E_{shockwave} + E_{pixel} + E_{loss} \tag{3.4}$$

where E_{laser} is the laser energy given as area × laser fluence × transmittance, $E_{decomposition}$ is the decomposition energy introduced by the decomposition enthalpy ($\Delta_{dec}H$) given as $\Delta_{dec}H.m$. Subsequently, $E_{shockwave}$, E_{pixel} and E_{loss} are given as:

$$E_{shockwave} = E_{debris} + E_{gas} = \left[\frac{Ad}{8}\left(\frac{2}{\gamma+1}\right)^2 \rho_f\right] v^2 + \left[\frac{\rho_g}{\gamma+1}\left(\frac{1}{\gamma-1}+\frac{4}{\gamma+1}\right)\right] v^2 x \tag{3.5}$$

$$E_{pixel} = \frac{1}{2}\rho_f A h {v_{pixel}}^2 \tag{3.6}$$

where, A: ablated area, d: depth of ablation, ρ_f: density of the pixel/flyer, ρ_g: density of surrounding environment, γ: adiabatic ratio, v: pixel/flyer velocity, x: position (function of time f(t)).

$$x = \frac{\left(\frac{2}{3}C_5 E_{SW}^{\frac{1}{2}}(t-t_0)+C_4^{\frac{3}{4}}\right)^{\frac{2}{3}} - C_4}{C_5} \tag{3.7}$$

$$C_4 = \frac{Ad}{8}\left(\frac{2}{\gamma+1}\right)^2 \rho_f \tag{3.8}$$

$$C_5 = \frac{\rho_g A}{\gamma+1}\left(\frac{1}{\gamma-1}+\frac{4}{\gamma+1}\right) \tag{3.9}$$

where t_0 is the time delay and t are the time at which the shockwave properties are analyzed (Fardel et al., 2009b). Finally, it must be noted that the foundation of the mentioned process

doi:10.6342/NTU202301493

by Fardel et al. (Fardel et al., 2009b) has its foundations from the analytical approximations made in the past research works (Mattle et al., 2013b, Freiwald and Axford, 1975).

From the above discussion, it is evident that if experiments are conducted in near LPE conditions, the shockwave energy reduces (since, E_{gas}~0). According to the investigations by Rapp et al. (Rapp et al., 2014a), presence of air during LIFT in ambient conditions comprises of a background pressure generates a shockwave. This shockwave is responsible for pixel cracks and folds. Therefore, eliminating air (introducing near LPE condition, i.e. low pressures) can result in shockwave elimination. On the contrary, near LPE conditions will lead to no cushioning effect with limited heat transfer possibilities during the pixel impact (K. E. transformed into heat generation which leads to structural and morphological degradation). However, the cushioning effect can be introduced by reducing the hardness or thickness of the receiver substrate as proposed in this research. Furthermore, introduction of surface modifications will enable flyer trapping, therefore, lowering the spreading of material due to the impact.

3.4. Characterizations

A number of characterizations have been made to validate the success of the LIFT depositions. The characterizations can be divided into three major classifications: (i) electrical, (ii) materials, and (iii) mechanical. Resistance measurements have been carried out for the deposited structure to determine its feasibility to fabricate electrodes for sensors. Subsequently, materials characterizations such as FESEM, EDS, XRD, laser confocal microscopy have been carried out to validate the presence of the deposited materials. Additionally, other discussions have been made related to the materials characterizations in the subsequent sections. Finally, mechanical characterization in terms of adhesion tape test is carried out. Overview of the cauterizations are shown in Fig. 3.9.

doi:10.6342/NTU202301493

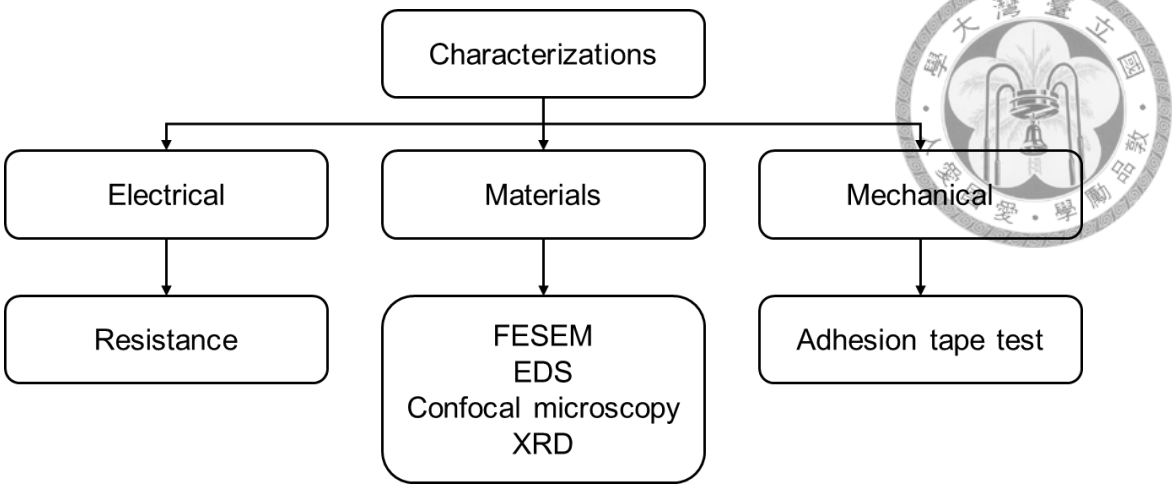

Fig. 3.9: Characterizations made on the LIFT deposited structures.

3.4.1. Electrical

Resistance tests were made on the LIFT deposited Cu material to characterize the LIFT-printed products not only in terms of mechanical strength but for its potential applicability as electrodes. Resistance measurements for thin film applications usually includes determination of the sheet resistance using a four-point probe technique. However, since we intend to deposit additive layers and possible micropillar structure fabrications, an easier approach is made. Finally, to account for the experimental errors and deviations in measurement, each experiment has been conducted thrice and represented as the average with ± error. Fig. 3.10 illustrates the resistance measurement setup.

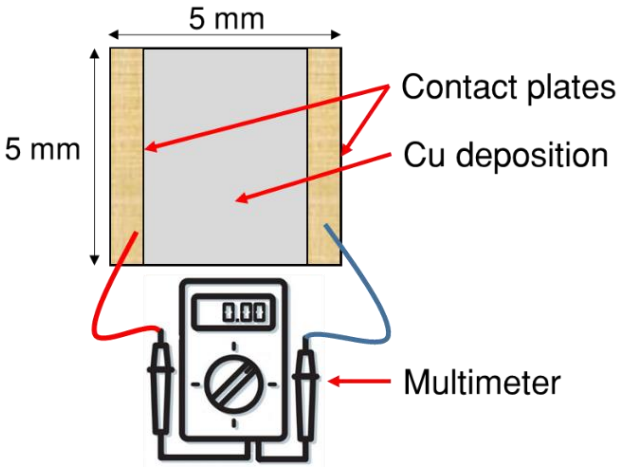

Fig. 3.10: Apparatus for resistance measurement in LIFT deposited samples.

doi:10.6342/NTU202301493

3.4.2. Materials characterizations

In this research, one of the key material characterizations is the study of microstructure and deposition morphology. Past research gives clear evidence that porosity of the working electrode enhances the number of reaction sites thereby assisting and improving the glucose sensing capabilities (Zhou et al., 2021). Therefore, the fabricated laser induced deposited film in this research needs to undergo extensive microstructure and morphology analysis using field emission scanning electron microscope (FESEM) or any other relevant apparatus. FESEM (NOVA NANO SEM 450, FEI (currently supported by Thermo Fisher), U.S.A) imaging is carried out on Cu, Cu-Ag and Cu-Pt to check the morphologies of the depositions. In addition, images of the LIFT deposited Cu cross-section is captured for LST and conventional samples using a laser confocal microscope (KEYENCE VK-9710, Osaka, Japan). Simultaneous to the SEM images, EDS (Oxford, INCA x-act, EDS for SEM, U.K) is carried out on the Cu, Cu-Ag and Cu-Pt surfaces to check for additive layer depositions (i.e. the Ag and Pt layer on Cu). Moreover, the areal elemental scatter plot can provide the efficiency of the additive layer (Ag/Pt) covering the initial material layer (Cu). Furthermore, EDS line plot over the additive layer cross-section can validate the presence of the additive layer. X-ray diffraction (XRD) analysis for LIFT deposited structures can give insights to a number of discussions such as (i) changes in crystal structures (Li and Ching-Yue, 2009), (ii) formation of metastable phases (Gorodesky et al., 2022), and (iii) presence of any oxidation states. Subsequently, Crystal structure of the deposited film can be beneficial in understanding the porosity mechanism (Zhou et al., 2021). Therefore, XRD analysis can be made to identify the chemical composition, crystal structure and physical properties of deposited materials.

3.4.3. Mechanical

At first adhesion tape tests were carried out on the samples to determine which type of sample shows the best adhesion strength. In order to conduct the adhesion tests, standardized methods were used such as the ASTM D3359 tape test (D-17, 2017, ASTM, 2009).

An area of 8×8 mm^2 was chosen to conduct the test on the LIFT deposited material. It is important to note that the surface is blemish/imperfection free and the environmental conditions (temperature and humidity) are not at their extremes. Two small cuts are made

doi:10.6342/NTU202301493

inside the 8×8 mm^2 area such that they intersect as shown in Fig. 3.11. Subsequently, a tape with an additional length of about 30 mm was cut out. The tape was placed on the center of the cuts made and the pulling direction was along the smaller angles. It is necessary to ensure that the tape is smoothened which can be identified through the uniform color distribution under the transparent tape. The tape is rested on the coating for about 90 s and then it is removed rapidly at an angle of 180° without jerk. Finally, the cut area is inspected. Qualitative analysis was made as per ASTM D3359 which had the following scales:

5A: No peeling or removal,

4A: Trace peeling or removal along incisions or at their intersection,

3A: Jagged removal along incisions up to 1.6 mm (1⁄16 in.) on either side,

2A: Jagged removal along most of incisions up to 3.2 mm (1⁄8 in.) on either side,

1A: Removal from most of the area of the X under the tape, and

0A: Removal beyond the area of the X.

Since the coating area is very small, the above standardized test which gave qualitative results, is difficult to analyze, therefore the weight of the tape was measured before and after the test. In this way, a quantitative measurement could be made on the quality of the adhesion. Higher difference between the measured weights indicates poor adhesion. However, the quantitative measurement is out of scope of this work and shall be incorporated in the study in near future.

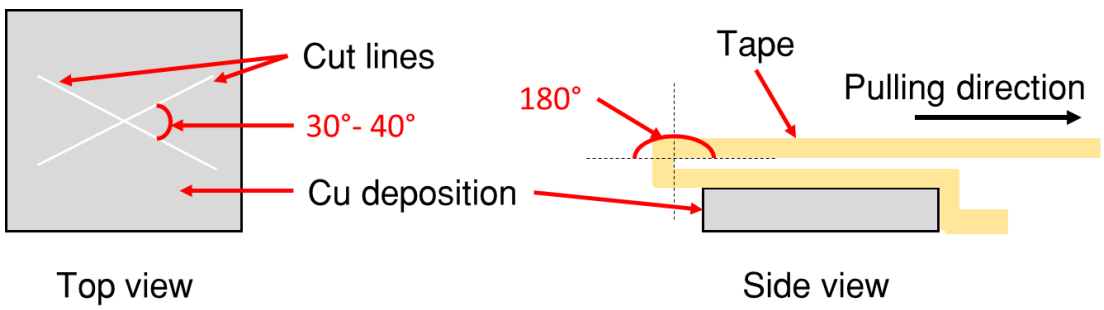

Fig. 3.11: Illustration of the ASTM D3359 tape test.

3.5. FEM setup

Finite element modeling (FEM) has been extensively utilized for simulating different stages of the LIFT process. Additionally, simulating the process will enable researchers to visualize

doi:10.6342/NTU202301493

the mechanisms and intricate details of various LIFT processes for intended applications. To understand, analyze and optimize the LIFT process, modeling is conducted in two steps: (i) pulsed laser heating and thermal analysis of the transfer material, and (ii) transfer process. In addition, post transfer phenomena (e.g. solidification and deposit characteristics) can be simulated as future work and currently out of scope of this thesis.

The laser heating modelling is motivated from the work of Vora et al. (Vora et al., 2013). A simple 2D model is utilized as satisfies the objective of determining the maximum temperature attained during laser heating. Therefore, considering past methods, pulsed laser heating of copper (Cu) thin films are performed in COMSOL 4.4. Important thermophysical, material and geometrical properties are defined under global definitions. Subsequently, the laser pulse is defined using a rectangle and piecewise function, accounting for the active number of pulses and their time delay. Additionally, a variable function is used to define the average energy density (E_d) (Eq. (3.10)), Gaussian space (G) (Eq. (3.11)) and laser heat source (P_g) (Eq. (3.13)). Finally, Eq. (3.12) is defined as the extreme end where the travelling heat source is terminated. Finally, governing equations and the boundary conditions incorporated for the heating simulations are given by Eq. (3.13) (average laser power density with a gaussian distribution), Eq. (3.14) (governing equation for whole geometry), Eq. (3.15) (heat flux natural convection and radiation cooling), Eq. (3.16) (analytic function), and Eq. (3.17) and (3.18) (natural convection cooling and radiation). The boundary conditions are applied on the respective boundaries as shown in Fig. 3.12(a).

$$E_d = \frac{E_p}{P_w \times \frac{\pi}{4} \times D^2} \tag{3.10}$$

$$G = e^{-\left(\frac{(x-x_r)^2}{2\varphi^2}\right)} \tag{3.11}$$

$$x_r = x_0 + Vt \tag{3.12}$$

$$P_g = AE_dGP_w = A\frac{E_p}{\frac{\pi}{4} \times D^2} e^{-\left(\frac{(x-x_r)^2}{2\varphi^2}\right)} \tag{3.13}$$

$$\rho C_p \left[\frac{\partial T}{\partial t}\right] = k\left[\left(\frac{\partial^2 T}{\partial x^2}\right) + \left(\frac{\partial^2 T}{\partial y^2}\right)\right] \tag{3.14}$$

doi:10.6342/NTU202301493

$$-k\frac{\partial T}{\partial y} = \beta P_g - h[T - T_a] - \varepsilon\sigma[T^4 - T_a^4] \quad (3.15)$$

$$\beta = rect1\left(mod\left(t, \frac{1}{t}\right)\right) \quad (3.16)$$

$$-k\frac{\partial T}{\partial y} = h[T - T_a] - \varepsilon\sigma[T^4 - T_a^4] \quad (3.17)$$

$$-k\frac{\partial T}{\partial x} = h[T - T_a] - \varepsilon\sigma[T^4 - T_a^4] \quad (3.18)$$

where E_p: pulse energy, P_w: pulse width; D: laser beam diameter; φ: standard deviation; A: Absorptivity (function of wavelength and temperature (Hess et al., 2011)); x_0: location of the center of the laser beam, V: scanning speed, t: time taken to travel the scanned distance, h: convective heat transfer coefficient, k: conductive heat transfer coefficient, T: temperature, T_a: ambient temperature. Finally, after the above functions are defined, a domain probe is introduced to capture the temperature data of domain 1. In this work, a thin film of length 200 μm and thickness 2.5 μm is chosen. A domain of length 60 μm and thickness of 2 μm is defined in the center of the film from the top surface (see Fig. 3.12(a)). Since this domain attracts most phenomena, fine meshing is employed (Fig. 3.12(b)) and temperature is recorded for this domain.

New material was defined in COMSOL for introducing temperature dependent properties of Copper. Density, thermal conductivity and specific heat were defined using piecewise function for various temperature range as given by Demin et al. (Demin et al., 2020). Convective heat transfer coefficient was utilized as determined by Yener et al. (YENER et al., 2019). Additional properties like dynamic viscosity (Assael et al., 2010) and surface tension (Udin, 1949, Matsumoto et al., 2005) were defined using the piecewise function. Simultaneously, the modulus of elasticity (Toolbox) and coefficient of thermal expansion (James et al., 2001) were utilized using the interpolation function. Relevant functions (for determining temperature dependent material properties) are provided in Table 3.5. Subsequently, the physics namely, heat transfer in solids was chosen. Suitable edges were defined for laser input, convective cooling and surface to ambient radiation as shown in Fig. 3.12(a). An unstructured mesh is generated with triangular elements having maximum an

doi:10.6342/NTU202301493

element size of 0.1 μm and minimum element size of 0.05 μm. Finally, a time dependent study was employed with intermediate steps taken by solver, as defined by the user.

Table 3.5: Past literature-based temperature dependent relations determining thermophysical properties of Cu.

Thermophysical property	**Temperature dependent data/functions**
Density (ρ)	• $8.81 + \left((-4.25 * 10^{-4}) * (T - 300)\right)(-6.12 * 10^{-8}) * ((\mathrm{T} - 300)^2) + \left(-2.77 * 10^{-11} * ((\mathrm{T} - 300)^3)\right)$; for 293 < T < T_m • $7.89 + \left((-7.96 * 10^{-4}) * (T - 300)\right) + (8.69 * 10^{-8}) * ((T - 300)^2) + \left(-2.383 * 10^{-11} * ((T - 300)^3)\right)$; for T_m < T < 5620 K
Thermal conductivity (k)	• $11.627 + \left((-4.2781 * 10^{-2}) * (T - 300)\right) + \left((9.2403 * 10^{-5}) * (T - 300)^2\right) + ((-9.6577 * 10^{-8}) * (T - 300)^3) + \left((3.686 * 10^{-11}) * (T - 300)^4\right)$; for 300 K < T < T_m • $1.29 + \left((-5.01 * 10^{-4}) * (T - 300)\right) + ((1.31 * 10^{-7}) * (T - 300)^2) + \left((-1.2 * 10^{-11}) * (T - 300)^3\right)$; for T_m < T < 5700 K
Dynamic viscosity (μ)	• 0.1; for 293 < T < T_m • $2.71828\text{^}(log(1) + (2.3025 * (-0.4220 + 1393.4/T)))$; for T_m < T < 1970 K
Surface Tension (γ)	• $2170 - (0.53 * T)$; for 293 < T < T_m • $1257 - 0.20 * (T - 1356)$; for T_m < T < 1998 K
Heat capacity (C_p)	• $24.27 + ((1.23 * 10^{-2}) * (T - 300)) + ((-2.05 * 10^{-5}) * (T - 300)^2) + ((1.53 * 10^{-8}) * (T - 300)^3) + ((-2.88 * 10^{-12}) * (T - 300)^4)$; for 293 < T < T_m • $31.0018 + ((3.28 * 10^{-3}) * (T - 300)) + ((-2.91 * 10^{-6}) * (T - 300)^2) + ((7.06 * 10^{-10}) * (T - 300)^3) + ((-4.68 * 10^{-15}) * (T - 300)^4)$; for T_m < T < 5800 K

doi:10.6342/NTU202301493

Coefficient of thermal expansion (α)	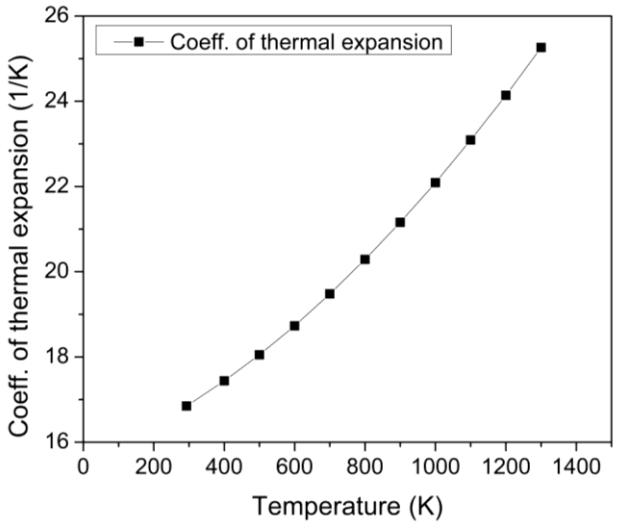
Modulus of Elasticity	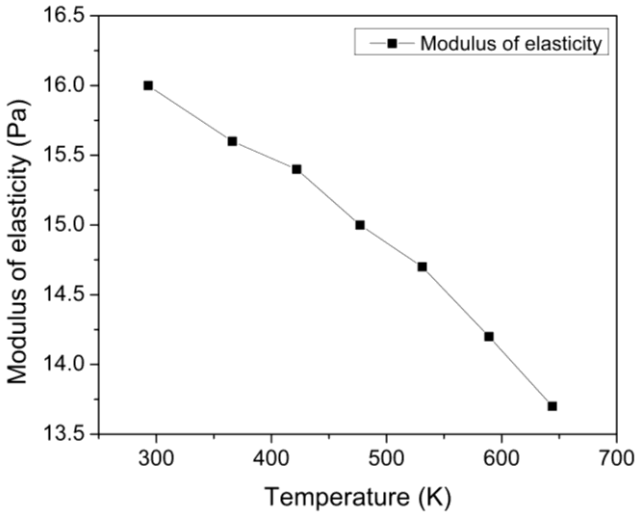

doi:10.6342/NTU202301493

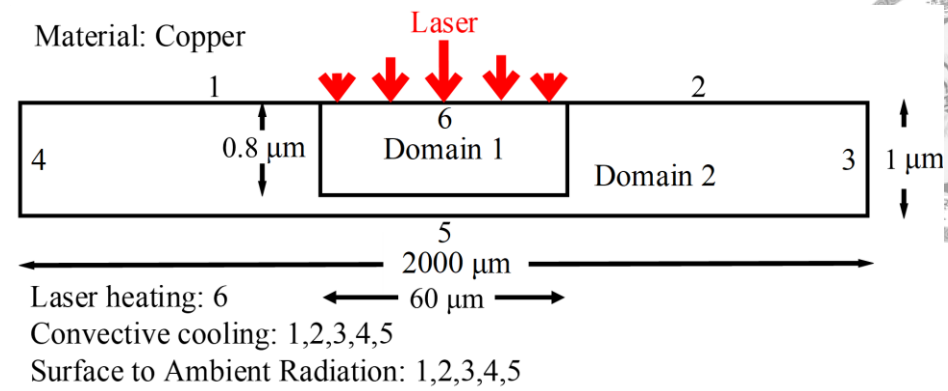

(a)

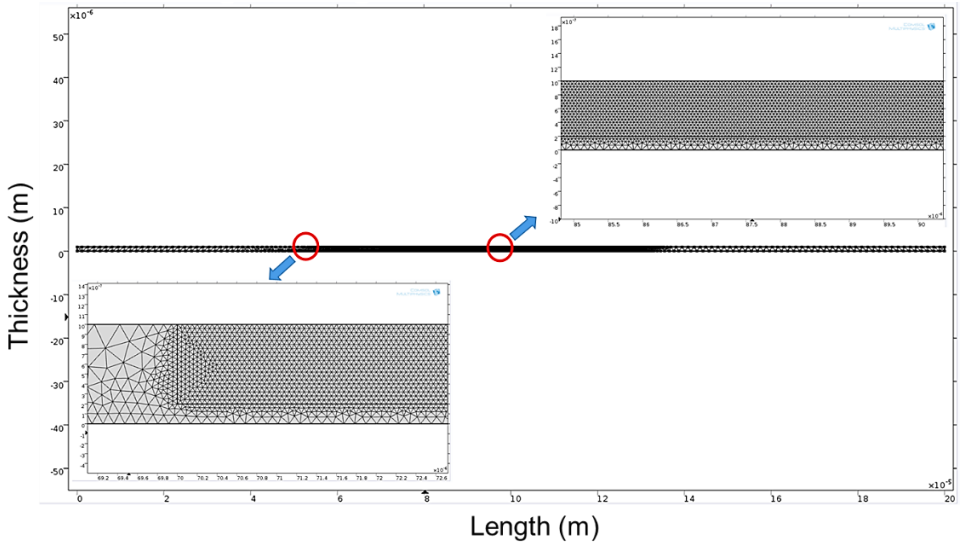

(b)

Fig. 3.12: Geometrical illustration of the two-dimensional model (for thin film heating model).

After successful modeling of heat transfer and thermal characteristics in the transfer material at the donor substrate, the transfer process is simulated. The LIFT transfer process is modeled using a laminar two phase, phase field method in COMSOL 4.4. A set of assumptions are made for successful modeling of the material transfer. First, from the initial (heating) simulations it is evident that the Cu thin film is nearly isothermal during laser heating. Therefore, for the transfer modelling, liquid copper is defined as fluid 1, and air as fluid 2. Secondly, instead of laser heating, a pressure force is applied on top of the film. This pressure is responsible for pushing the donor material out of the donor film, which in the real scenario is initiated by the laser heating. Additionally, this pressure is responsible for the material flow

doi:10.6342/NTU202301493

downwards (since gravity effects are neglected). During the model setup, first, the geometry is drawn and defined as shown in Fig. 3.13(a). Subsequently, two materials (fluids: copper and air) were imported from the inbuilt materials library. Subsequently, a laminar two-phase flow, phase field (tpf) model is used in COMSOL 4.4. The wall, initial surface, inlet and outlets are chosen as shown in Fig. 3.13(a). Initial values are added for two fluids and fine mesh with free triangular domains are defined as shown in Fig. 3.13(b). The transfer simulations are based on the research work of Juan Jose Moreno Labella (Moreno Labella, 2021). Finally, the last part of the LIFT modeling targets to determine the deposit characteristics on the acceptor substrate (flexible PET substrate). However, at present, the third modelling part of LIFT process is beyond the scope of the thesis work, but shall be carried out in the near future.

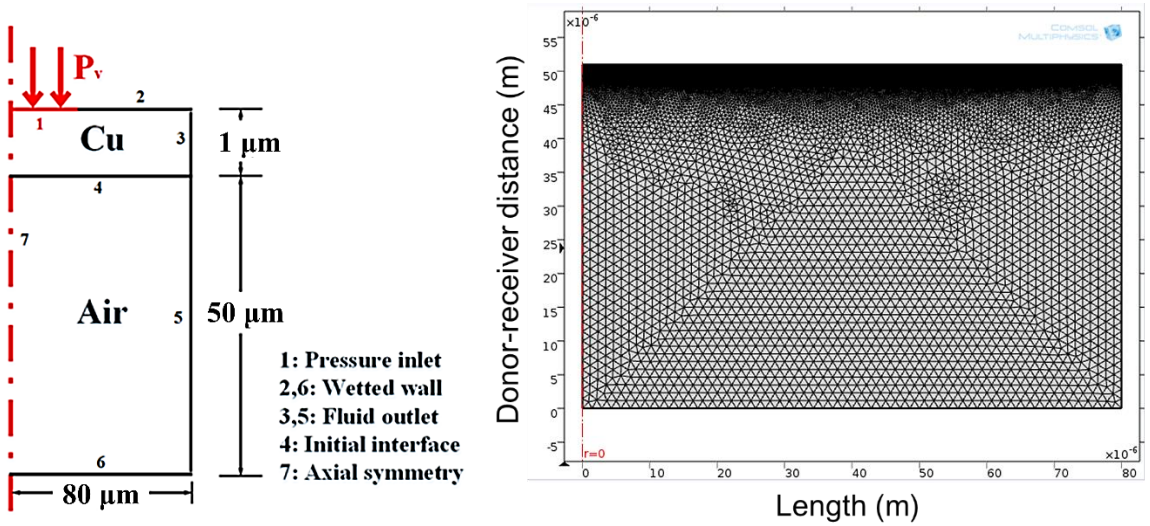

(a) (b)

Fig. 3.13: Schematic diagram of the setup for transfer modeling in COMSOL. (a) Geometrical illustration, (b) meshing illustration of the given geometry.

3.6. Theoretical studies

Based on past literature evidence, a number of theoretical formulations such as energy analysis and velocity estimations. have been carried out. According to Luo et al. (Luo et al., 2022), ejection behavior of voxels change with change in laser fluence. It is assumed that the absorbed laser pulsed energy is converted into three other energies, namely internal energy (E_{in}), kinetic energy (E_k) and interfacial binding energy (E_{ib}). The aforementioned

doi:10.6342/NTU202301493

assumptions are based on a voxel-based LIFT process which is quite similar to a LIFT process except the fact that the transferred voxels are already separated before the transfer. Additionally, viscous dissipation and thermal losses were neglected.

$$E_a = E_{in} + E_k + E_{ib} \tag{3.19}$$

$$E_a = A_v F \tag{3.20}$$

$$E_{in} = \rho h A_v [C_l (T - T_0) + H_m] \tag{3.21}$$

$$E_k = 0.5 \rho h A_v V^2 \tag{3.22}$$

$$E_{ib} = A_v W \tag{3.23}$$

where F: fluence, ρ: density, A_v: voxel area, C_l: specific heat capacity, H_m: melting enthalpy of copper, T_0 & T: initial and final voxel temperature post laser irradiation respectively, V: velocity of the microdroplet, $W = 2$ J/m^2: specific interfacial binding energy between Cu and glass (Ohring, 2002). Subsequently thermal properties of pure Cu were elucidated from reference (Assael et al., 2010). T_0 was set to 25°C (room temperature).

The only parameters which were unknown were the voxel velocity (V) and the temperature (T). The mentioned parameters were derived from COMSOL simulations, since experimental validations are expensive and time consuming. Moreover, the COMSOL simulations were compared with past literature evidence to account for relevant validations. Furthermore, if only one (V or T) is derived successfully, the other could be derived from the equations Eqs. (3.19) - (3.23). Due to simulation conditions, temperature of the free flying voxel is difficult to simulate. Therefore, the voxel velocity is determined and the temperature is calculated accordingly (using Eqs. (3.19) - (3.23)).

Another aspect of validating the aforementioned analysis is through experiments, however, it is beyond the scope of the thesis. However, limited experimental validations have been done by researchers in the past for determine the micro-droplet temperature due its small size, and further investigations can be made for relevant validation. Considering the past literature evidence, and extensive literature survey, a detailed energy balance equation is proposed, which considers a number of other phenomena to produce a more accurate model which can

doi:10.6342/NTU202301493

predict the LIFT mechanism and provide greater insights to the LIFT process. The proposed energy balance equation is as follows:

$$E_a = E_{in} + E_k + E_{ib} + E_f + E_{SW} + E_{loss} \quad (3.24)$$

where *E* stands for the respective energies as described through their subscripts. Past research evidence shows that laser materials processing (a type of thermal processing) induces localized heat and induces thermal stress during material removal (Schaaf, 2010). Therefore, fracture energy (energy required for crack propagation) is an essential consideration for energy analysis in the proposed model. E_f is the fracture energy or the plastic dissipation energy for 1 μm Cu film derived from the research work of Volinsky et al. (Volinsky et al., 1998). It must be noted that, since this research is not VB-LIFT, therefore the dimensions of the voxel/pixel is derived from the ablated region of the donor film. The beam diameter (*D*), beam area (*A*), ablated diameter (*d*) and ablated area (*a*) are approximated from relevant experimental observations, and given in the subsequent results section below. E_{SW} accounts for the shockwave energy (E_{sw}), which is a function of E_g (gas energy) and E_d (debris energy), as described in the section 3.3.3 above. Furthermore, E_{loss} is expected to represent heat losses through conduction, convection and radiation.

doi:10.6342/NTU202301493

Chapter 4 Results and discussion

4.1. Laser heating and ablation results

LIFT of Cu using different film thickness (1000 nm, 500 nm, 50 nm) in order to determine an approximate threshold energy has been made. However, for the sake of brevity, only observations for Cu donor of thickness 500 nm is illustrated and tabulated (see Table 4.1 and Fig. 4.1). In order to check the ablation of the Cu material, and understand its related mechanisms or underlying phenomena, the donor films were qualitatively and quantitively analyzed as shown in Table 4.1 and Figs. 4.1, 4.2, 4.3 and 4.5. Linewidth is defined as the thickness of the laser affected region or simply, the maximum diameter of the ablation spot. Simultaneously, the aforementioned investigation is made for platinum (Pt) and silver (Ag) with film thickness of 500 nm. The mentioned linewidths are derived from the diameter of the ablations observed on the donor. The mention ablation diameter (*d*) is used to approximate the voxel/pixel dimensions for theoretical studies in the subsequent sections below

Table 4.1: Laser scans of single line is made for variable laser power at constant frequency (30 kHz), scan rate (1300 mm/s), pitch (0.02 mm), and pulse width (15 ns).

Power (W)	**Linewidth (μm)**		
	Cu	**Pt**	**Ag**
	500 nm		
0.2	10.0172	--	--
0.4	14.3103	8.6160	5.7241
0.6	17.1724	9.3292	7.9031
0.8	18.6034	9.5997	8.5862
1.0	19.3189	10.2446	14.3103
1.2	20.7500	10.7327	20.7623
1.4	21.4655	12.8793	22.1925
1.6	22.1810	13.5948	23.6229
1.8	23.6120	14.3282	26.4838
2.0	25.0431	16.4724	29.3362

doi:10.6342/NTU202301493

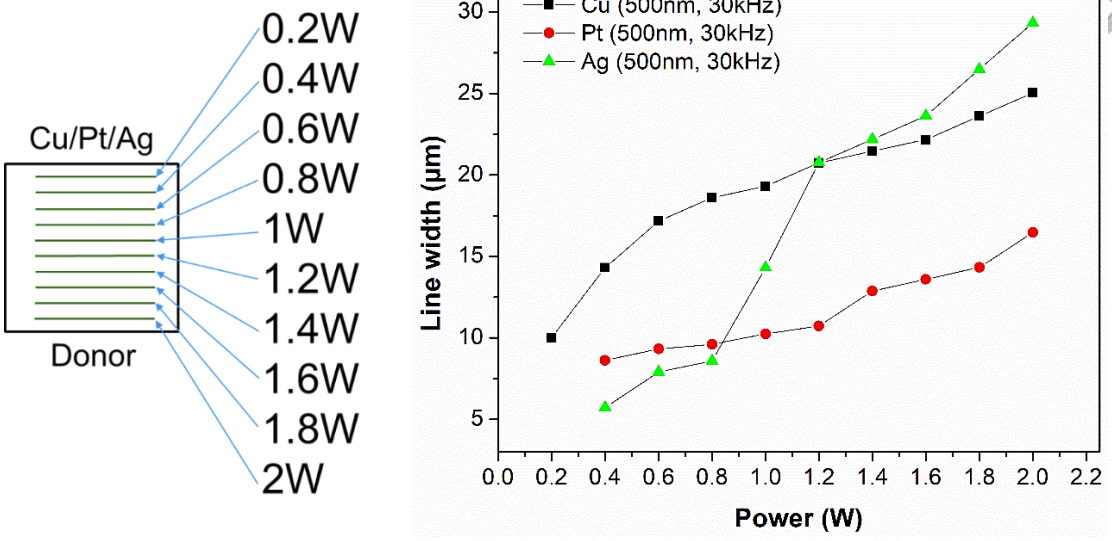

(a) (b)

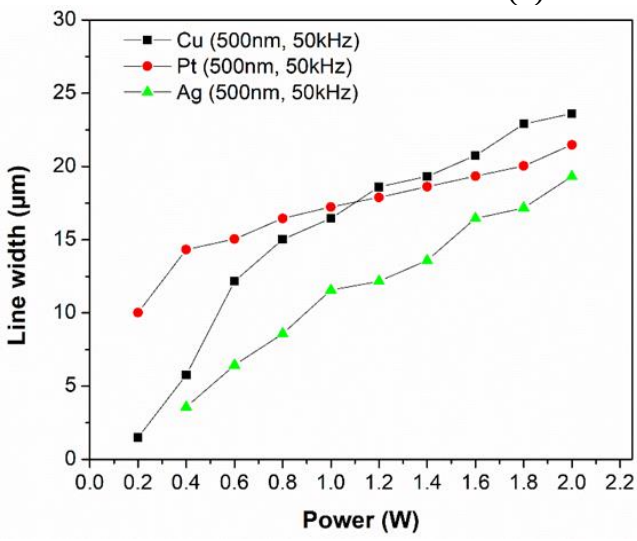

(c)

Fig. 4.1: Ablation line width (on donor) vs Laser power for Cu, Pt and Ag thin films (500 nm); (a) illustration of experimental design, (b) working frequency: 30 kHz, and (c) 50 kHz.

doi:10.6342/NTU202301493

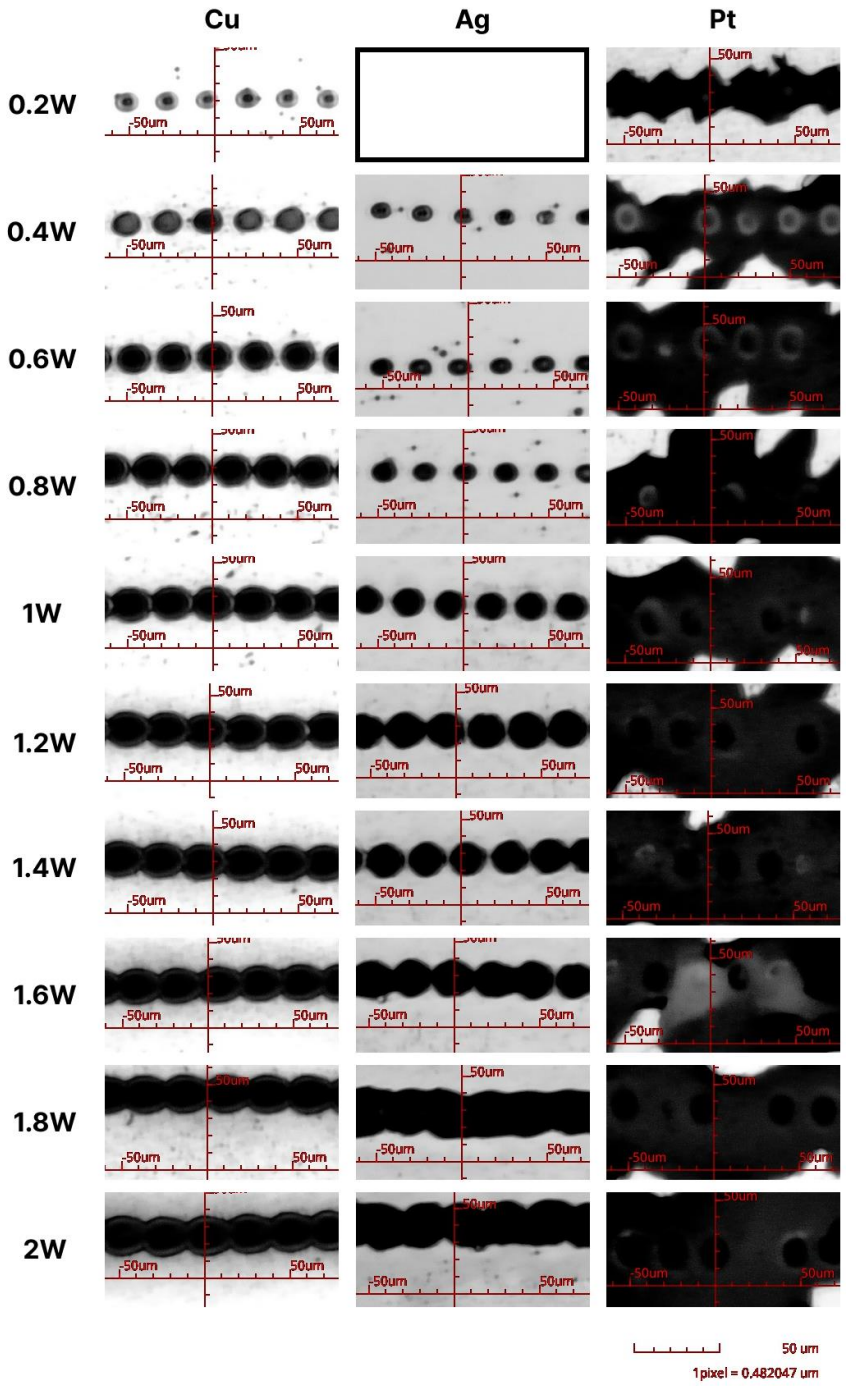

Fig. 4.2: Microscopic illustrations of 500 nm Cu, Ag and Pt donor post laser irradiation at increasing average laser power and constant frequency of 30 kHz. Blank box denotes no ablation.

doi:10.6342/NTU202301493

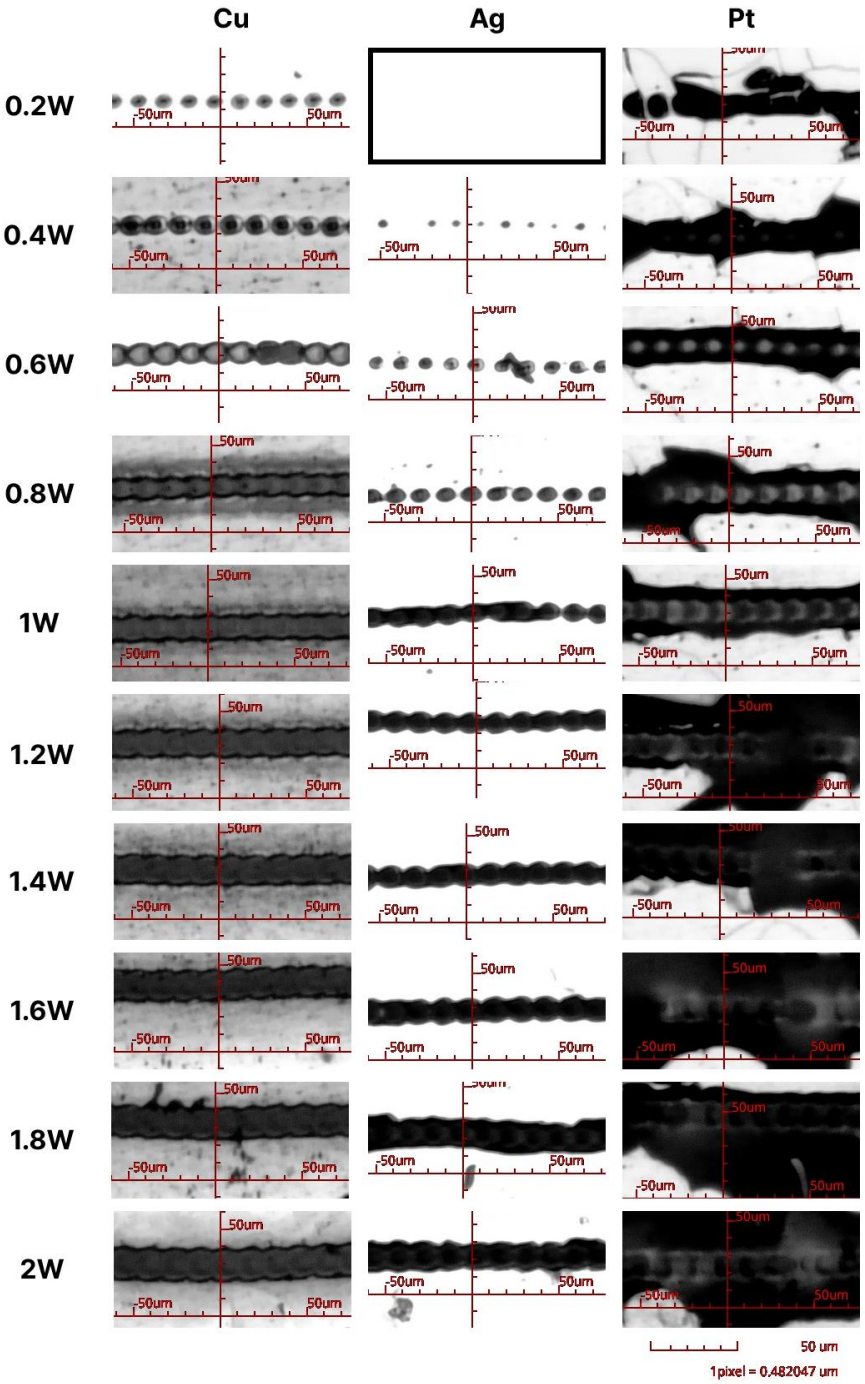

Fig. 4.3: Microscopic illustrations of 500 nm Cu, Ag and Pt donor post laser irradiation at increasing average laser power and constant frequency of 50 kHz. Blank box denotes no ablation.

doi:10.6342/NTU202301493

Fig 4.1 shows interesting observations. A generic trend of increase in line width is observed with increase in laser power, which is expected. Since input energy increases with increasing power, the heat affected area increases, thereby, increasing the linewidth. Considering the melting points of Cu (~1357.8 K), Ag (~1234.8 K) and Pt (~2041 K), Ag should have the highest linewidth among all for the corresponding power due to its low melting point. However, Ag has very low absorptivity, followed by Pt and subsequently, Cu having the highest among the three (Bennett and Ashley, 1965, Mafuné et al., 2003, Biondi, 1956).

In order to deepen studies on the pulse energy and its effects on the material ablation, the frequency of the laser irradiation is changed from 30 kHz (Fig. 4.1(b)) to 50 kHz (Fig. 4.1(c)). Lower line widths are observed with 50 kHz laser irradiation, this is because the pulse energy decreases as the frequency increases for a defined average laser power. For example, a pulse energy of 66.66 µJ and 40 µJ is observed for 30 kHz and 50 kHz respectively when irradiated with an average laser power of 2 W at a scan rate of 1300 mm/s. The aforementioned observations assisted in determining suitable LIFT parameters for optimized ablation and transfer. However, complications arise during LIFT of Pt. Pt thin films show a network of microcracks throughout the surface (see Fig. 4.4). This is a common observation for Pt thin films, when manufactured via sputtering, due to the formation of grain boundary ridges. Therefore, flaking of Pt takes place during laser heating and ablation trials, resulting in Pt flakes flying everywhere. In addition to the above discussions and observations, it is important to understand that the ablation in the LIFT process can be highly material specific. Figs. 4.2 and 4.3 shows the ablation characteristics of Cu, Ag, and Pt under different laser irradiation frequency (i.e. 30 kHz and 50 kHz).

doi:10.6342/NTU202301493

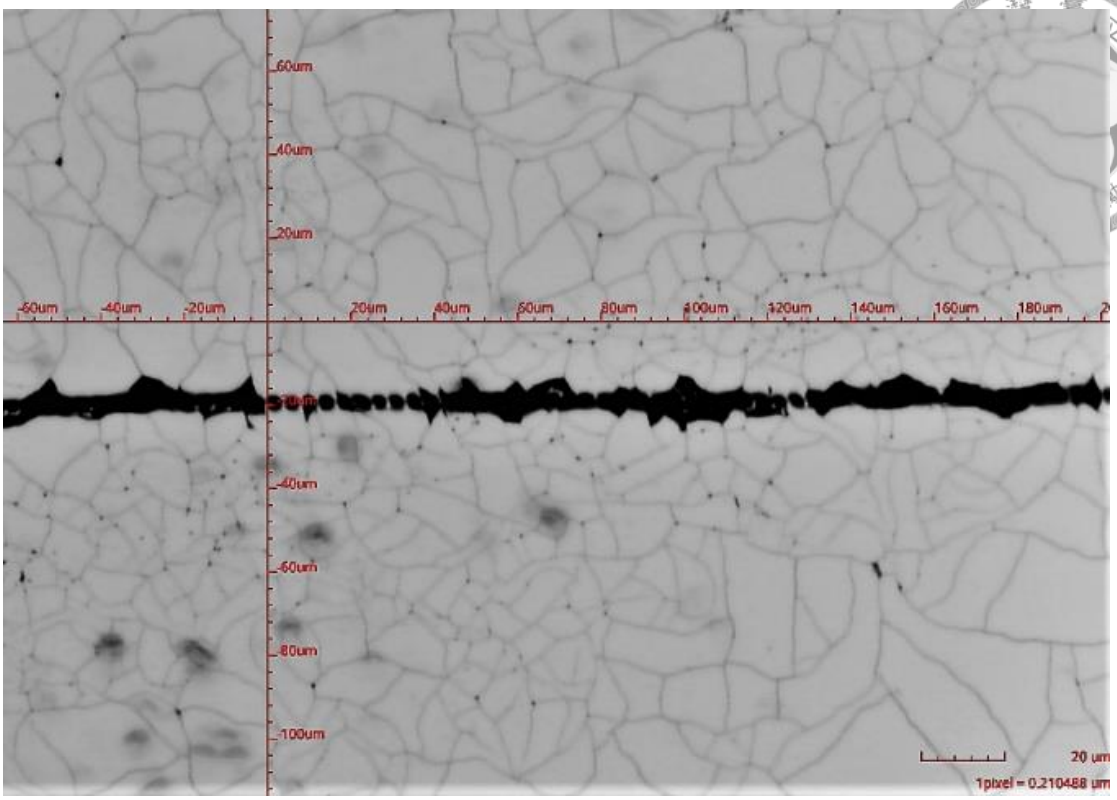

Fig. 4.4: Microscope image of Pt donor substrate.

doi:10.6342/NTU202301493

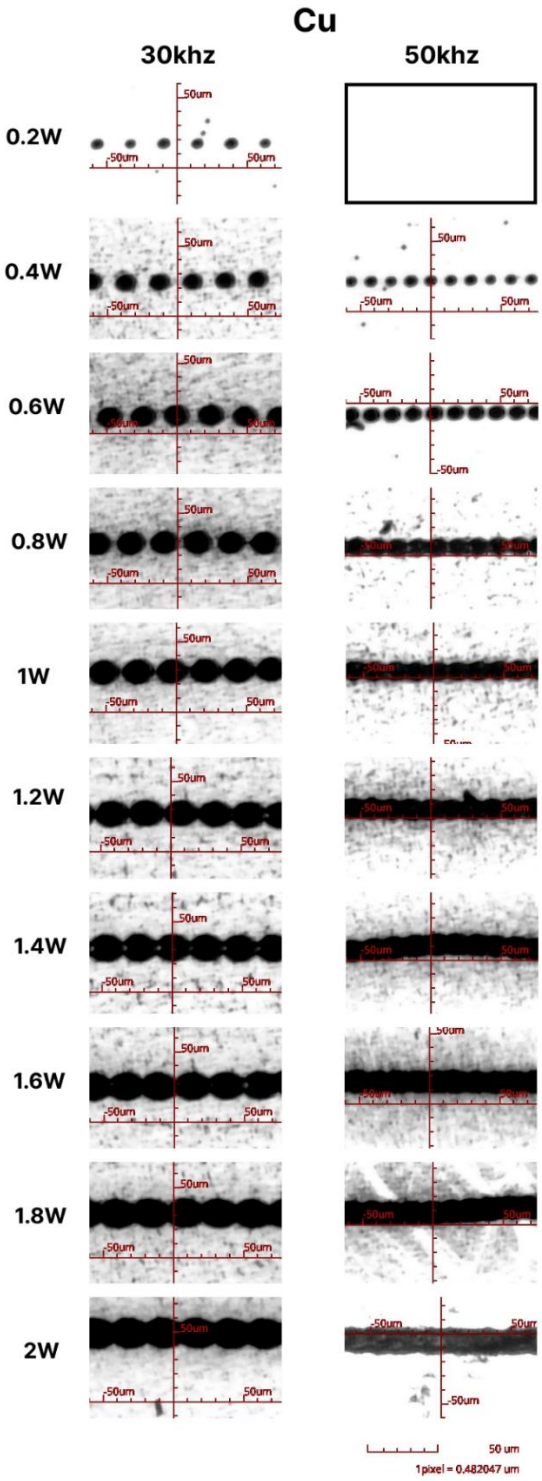

Fig. 4.5: Microscopic illustrations of 1 μm Cu donor post laser irradiation at increasing average laser power. Blank box denotes no ablation.

doi:10.6342/NTU202301493

4.2. Laser surface texturing and Vat photopolymerization

Laser surface texturing of PET and Vat photopolymerized VPP substrates have been illustrated in sections above. Optimal LST parameters must be determined to achieve desired textures without leading to polymer degradation. For PET receiver substrates, the parameters are as follows: power = 1.62 W, frequency = 30 kHz, pulse width = 15 ns, speed = 100 mm/s. Fig. 4.6 show the textures obtained for various pitch lengths and orientations. Textures with pitch 0.02 mm and 0.04 mm (Fig. 4.6(1a),(1c),(2a),(2c)) show little degradation of the polymer. This is due to the enhanced heat accumulation in the polymer. Therefore, parameters cannot be fixed for large variation in pitch lengths. However, since subsequent results with LIFT depositions show enhanced properties for pitch lengths 0.1 mm and 0.5 mm, the pitch lengths of 0.02 mm and 0.04 mm are discarded.

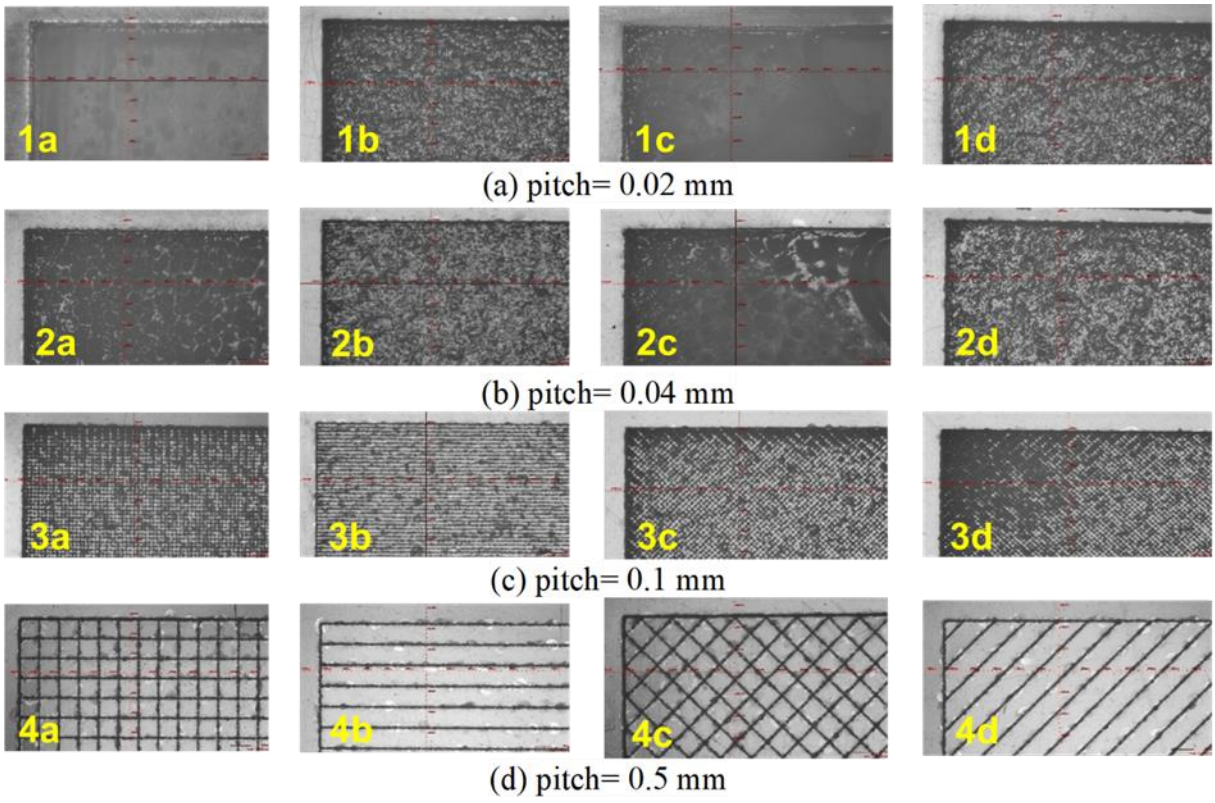

Fig. 4.6: Laser surface texturing (LST) parameters on PET using nanosecond pulsed green laser.

doi:10.6342/NTU202301493

Subsequently, Vat polymerized (hard) substrates are utilized for LST. The optimized LST parameters are: power = 4.5 W, frequency = 30 kHz, pulse width = 15 ns, speed = 250 mm/s. However, similar to the observation in PET substrates, VPP samples also show degradation for lower pitch values (0.02 mm and 0.04 mm) as shown in Fig. 4.7. Additionally, superior properties in LIFT deposits for 0.1 mm and 0.5 mm led to the elimination of analysis for pitch lengths 0.02 mm and 0.04 mm. Finally, LST parameters optimized for VPP (soft) substrates is determined: power = 6.5 W, frequency = 50 kHz, pulse width = 15 ns, speed = 30 mm/s. However, since the vat polymerized soft polymer samples show very poor LIFT structures and characteristics, therefore, they have not been illustrated.

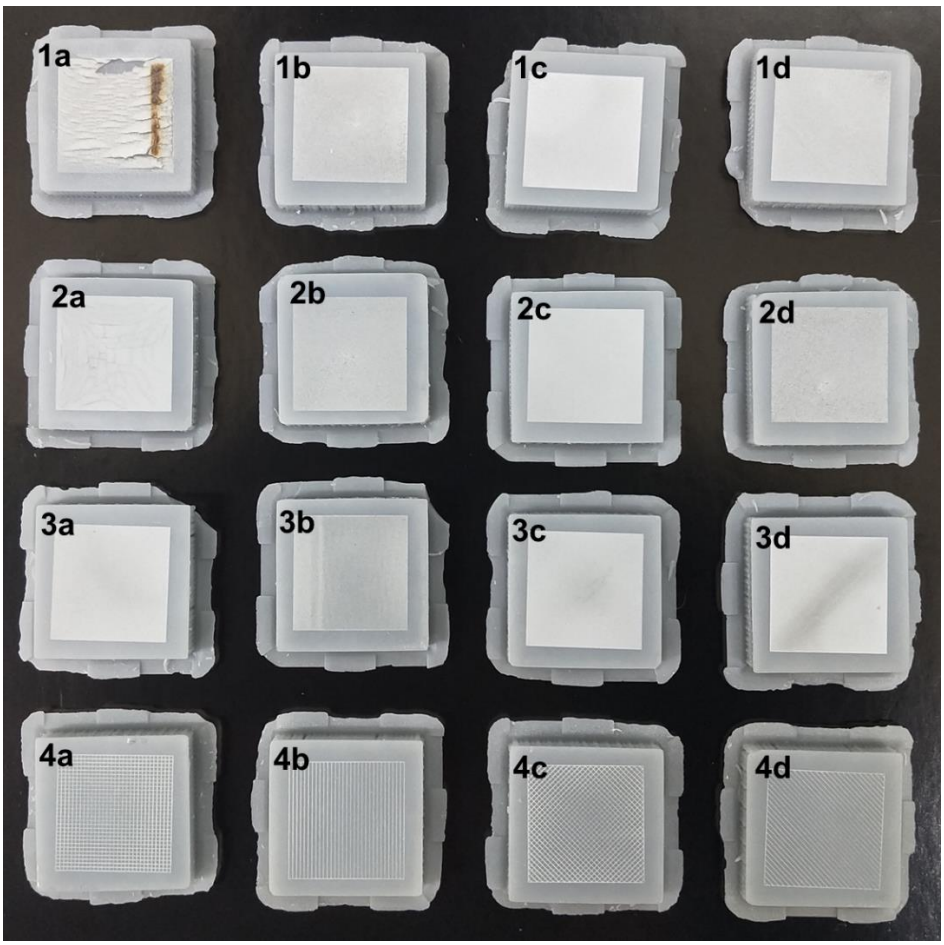

Fig. 4.7: Laser surface texturing (LST) parameters on VPP receiver substrates (hard) using nanosecond pulsed green laser.

doi:10.6342/NTU202301493

4.3. LIFT results

A number of trials have been made to determine the optimal LIFT parameters for different transfer materials i.e., Cu, Pt and Ag. In addition to the variation in materials, optimizing LIFT for optimal conductivity and adhesion a number of experiments have been made.

4.3.1. LIFT of Cu

In reference to the discussions made on shockwave generation and its adverse effects on the LIFT process, efforts have been made to mitigate them. Therefore, LIFT experiments are carried out in LPE and ambient environments, for comparable analysis of transfer efficiency. Vacuum or LPEs remove presence of shockwaves or reduce the shockwave intensity. This mitigates the flyer disintegration due to flyer shockwave interaction. Subsequent to deposition, LIFT in air shows higher resistance values compared to its LPE counterparts. In other words, compact and intact deposition of donor material in transfer under LPE conditions lead to lower resistance values of the LIFT Cu deposits. Table 4.2 illustrate that LPE environments enable high accuracy deposits with low resistance to the ambient (air) environment experiments. Additionally, some discussions were made on the possibility that introducing surface roughness can help in suppressing the shockwave intensity after reflection from the receiver substrate. Table 4.2 shows that the control experiment (without any surface modifications) in air show the highest resistance compared to most of the other surface modified LIFT experiments in ambient (air) environment. A number of different surface textures are investigated on PET (receiver substrates), and it is evident from the results that the combined effects of LPE and surface texturing can lead to better electrical properties in the printed deposits.

doi:10.6342/NTU202301493

Table 4.2: LIFT experiments (with 1 μm donor) for optimization of electrical properties with laser surface texturing (LST) on PET receiver substrates (thickness= 0.125 mm)

Sample Description	Resistance (Ω)	
	LPE	Air
Control	0.940 ± 0.010	21.550 ± 5.250
3a	1.000 ± 0.100	2.000 ± 0.200
3b-horizontal	0.850 ± 0.050	30.400 ± 19.700
3b-vertical	1.005 ± 0.025	10.500 ± 0.100
3c	0.970 ± 0.010	15.300 ± 3.000
3d	0.860 ± 0.020	4.215 ± 0.555
4a	0.960 ± 0.030	5.500 ± 2.500
4b-horizontal	1.000 ± 0.001	2.350 ± 0.030
4b-vertical	0.845 ± 0.025	46.500 ± 1.100
4c	0.895 ± 0.095	2.100 ± 0.100
4d	0.910 ± 0.040	--

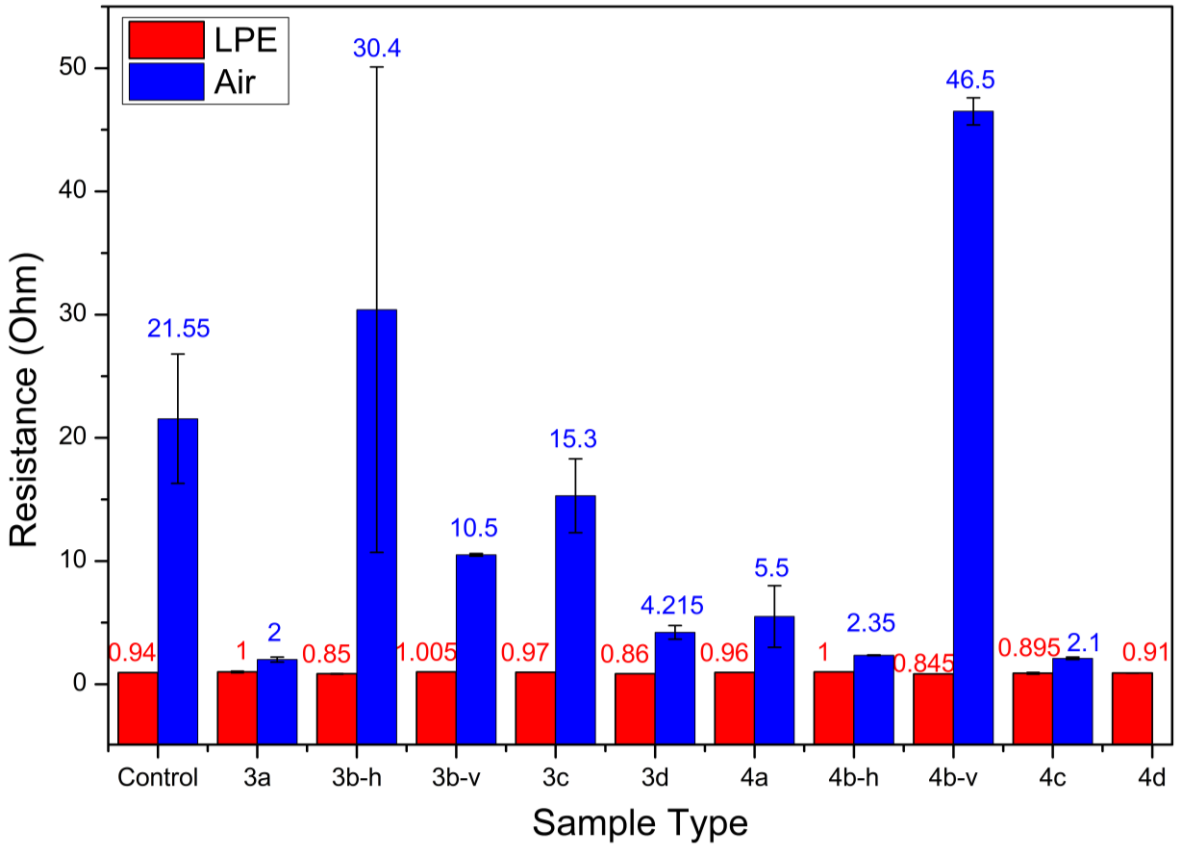

Fig. 4.8: Resistance for LIFT experiments (with 1 μm Cu donor) with laser surface texturing (LST) on PET receiver substrates (thickness= 0.125 mm)

doi:10.6342/NTU202301493

In order to compare the effects of receiver substrate hardness on the electrical properties, LIFT in LPE and ambient environments are carried out for hard and soft substrates (prepared using vat photopolymerization). Results for LPE environments show better or comparable electrical conductivity, compared to its ambient counterparts (see Table 4.3). However, it must be noted that the LIFT experiments conducted in air show variable electrical properties. It is guessed that the mentioned variability in resistance is contributed by the combined effects of (i) type of surface texture, and (ii) increased hardness at laser created slots. The increased hardness may possibly be due to over-curing of the polymer when introduced to green laser, as green laser is close near UV region (curing wavelength of the VPP process), or due to melting solidification of the polymer. However, the proposed explanation is investigated in detail subsequently.

Table 4.3: LIFT experiments (with 1 μm donor) for optimization of electrical properties with laser surface texturing (LST) on hard VPP manufactured receiver substrates (thickness= 2 mm).

Sample Description	**Resistance (Ω)**	
	LPE	**Air**
Control	2.20 ± 0.02	46.15 ± 4.05
3a	2.80 ± 0.10	--
3b-horizontal	2.15 ± 0.05	--
3b-vertical	2.70 ± 0.10	--
3c	7.50 ± 1.00	--
3d	8.75 ± 1.25	--
4a	2.88 ± 0.01	196.50 ± 5.00
4b-horizontal	1.55 ± 0.05	52.10 ± 13.00
4b-vertical	1.65 ± 0.05	27.20 ± 0.90
4c	3.60 ± 0.10	--
4d	1.80 ± 0.10	67.65 ± 18.55

doi:10.6342/NTU202301493

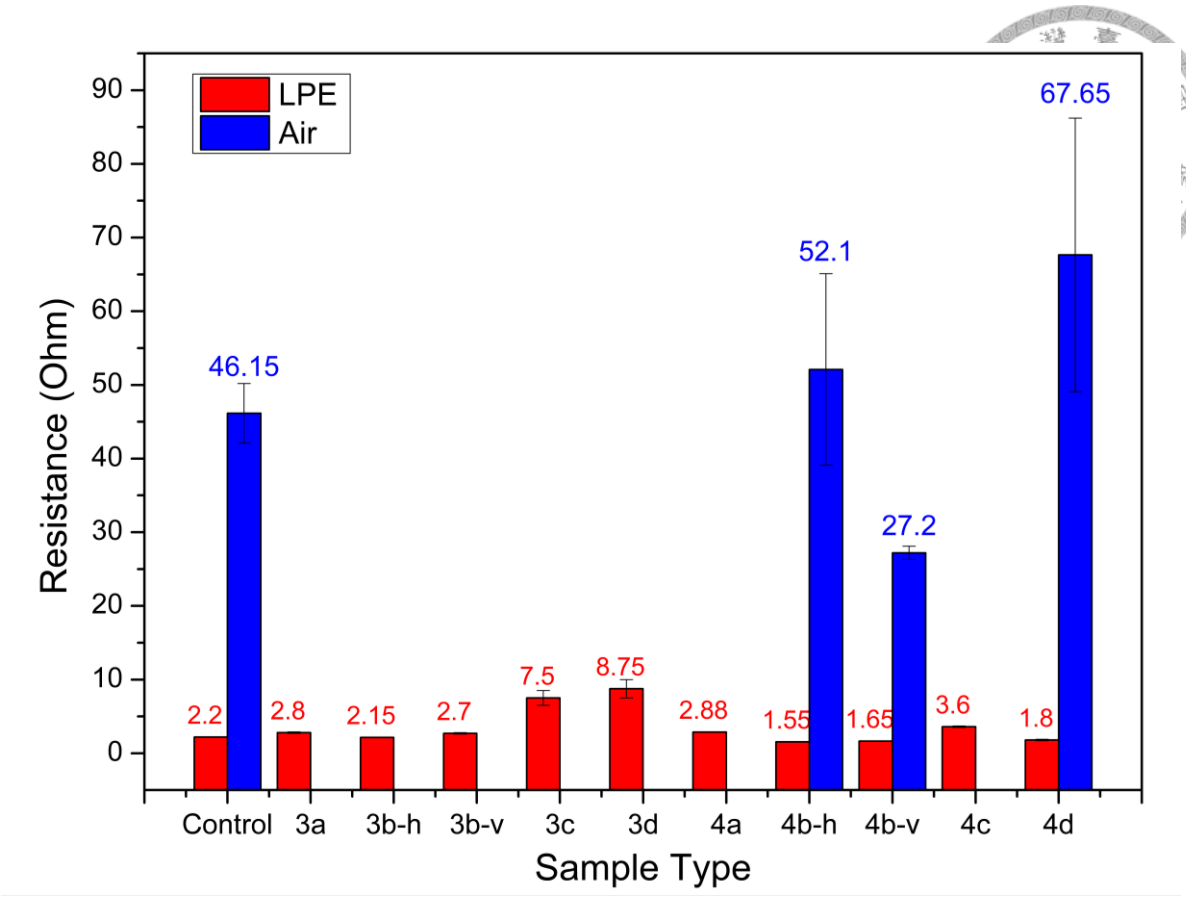

Fig. 4.9: Resistance for LIFT experiments (with 1 µm Cu donor) with laser surface texturing (LST) on hard VPP manufactured receiver substrates (thickness= 2 mm).

Laser surface texturing on polymer has a number of challenges. One of which is the low absorptivity of laser wavelength on polymer materials. To counter this, higher power may be utilized, but this may lead to polymer degradation. Furthermore, achieving greater slot depths is extremely difficult considering the mentioned limitations. Therefore, VPP is utilized to induce texturing of the receiver substrates. In places of additive manufacturing of 3D structures surface texturing can be efficiently utilized for inducing greater adhesion of the printed structures with the receiver substrates. In this work, Cu is printed first on the textured samples and checked for electrical properties for its efficient use as current collector. Results show that high resistance deposits are produced and a significant number of experiments show no conductivity (see Fig. 4.10). The deposits showing conductivity (although high) are sample which have a slot depth of 50 µm as tabulated in Table 4.4. Slot depths of > 50 µm are not conductive. Therefore, the plausible reason for this is the insufficient material filling

doi:10.6342/NTU202301493

in between the slots, since the donor has a thickness of 1 µm compared to the minimum slot dimension of 50 µm. Therefore, to make the concept of utilizing surface patterned VPP receiver substrates addition material layering or thicker donors must be utilized. The mentioned concept may be successfully investigated in the future, and is out of scope of the present work.

Table 4.4: LIFT experiments (with 1 µm donor) for optimization of electrical properties with surface patterned hard VPP manufactured receiver substrates (thickness= 2 mm).

Sample Description	**Resistance (Ω)**				
	Inter slot distance (µm)	**Slot width (µm)**	**Slot depth (µm)**	**LPE**	**Air**
V0 (Control)	--	--	--	3.7 ± 2.5	27.85 ± 2.15
V1	150	50	100	--	--
V2	150	100	150	--	--
V3	100	100	100	55.0 ± 15.0	--
V4	50	150	100	--	--
V5	50	100	150	--	--
V6	150	100	50	--	--
V7	150	100	100	50.0 ± 10.0	--
V8	50	50	50	17.0 ± 13.0	--
V9	100	50	50	400.0 ± 200	--
V10	100	150	50	13.7 ± 0.2	--
V11	100	50	150	--	--
V12	100	150	150	--	--
V13	50	50	100	700.0 ± 200.0	--
V14	50	100	50	4.0 ± 1.0	19 ± 1.0
V15	150	150	100	--	--

doi:10.6342/NTU202301493

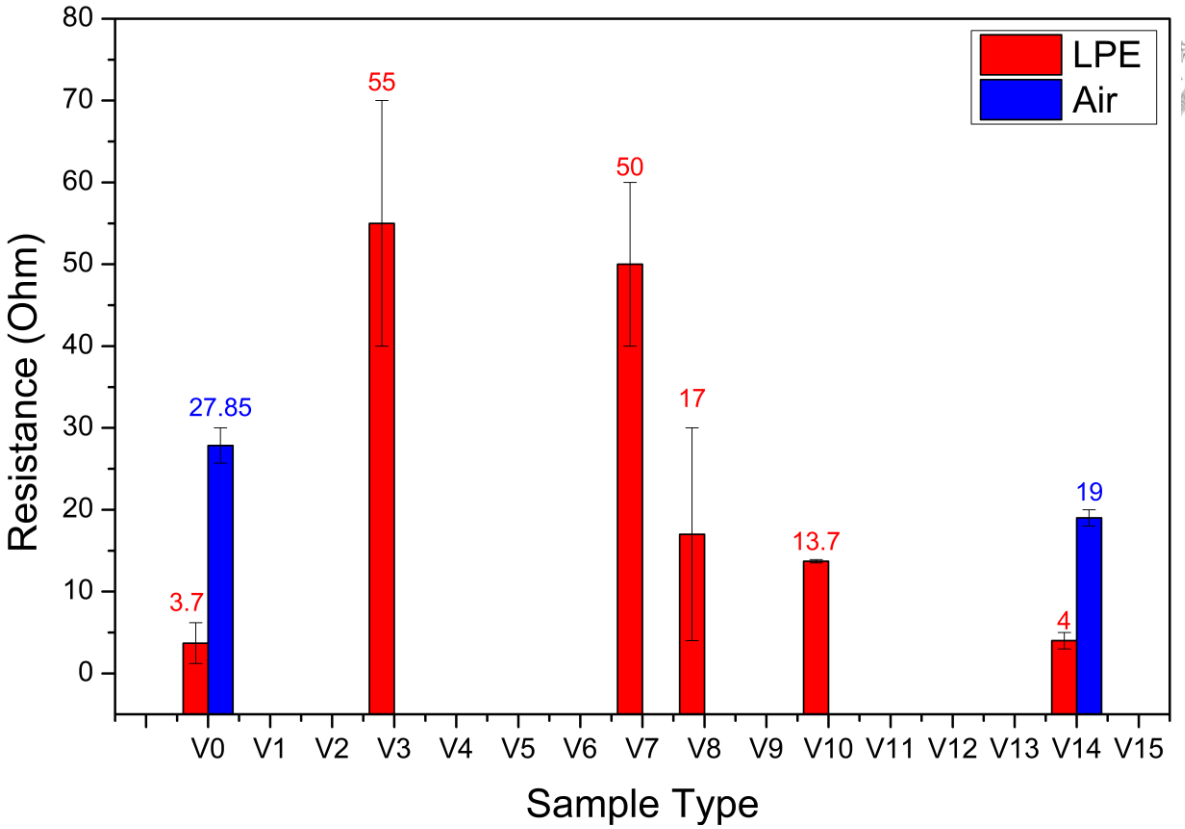

Fig. 4.10: Resistance for LIFT experiments (with 1 µm Cu donor) for optimization of electrical properties with surface patterned hard VPP manufactured receiver substrates (thickness= 2 mm).

Following the illustrated observations above, a set of experiments were made to determine the performance (in terms of conductivity) of the LIFT deposited Cu for materials with variable hardness. Table 4.5 shows the resistances observed for LIFT of Cu deposits on PET, hard and soft VPP based receiver substrate. Observed evidence shows that the conductivity for hard VPP manufactured receiver substrate is higher than that of its softer counterpart. Simultaneously, PET shows the best electrical property in terms of conductivity. However, anomaly in the PET substrate compared to the VPP based substrates is its thickness. PET has a thickness of 0.125 mm, whereas its VPP counterparts have a thickness of 2 mm. Therefore, to understand and determine if the thickness has any significant role in deposition characteristics, further experiments are carried out.

doi:10.6342/NTU202301493

Table 4.5: LIFT experiments (with 1 μm Cu donor) for understanding the effects of receiver surface hardness on the electrical properties.

Sample Description	Resistance (Ω)	
	LPE	Air
PET (t= 0.125 mm)		
3a	0.940 ± 0.010	2.32 ± 0.05
Control	1.035 ± 0.005	3.30 ± 0.40
Hard VPP (t= 2 mm)		
3a	1.030 ± 1.040	--
Control	4.150 ± 0.250	49.80 ± 21.60
Soft VPP (t= 2 mm)		
3a	2100 ± 100	--
Control	--	--

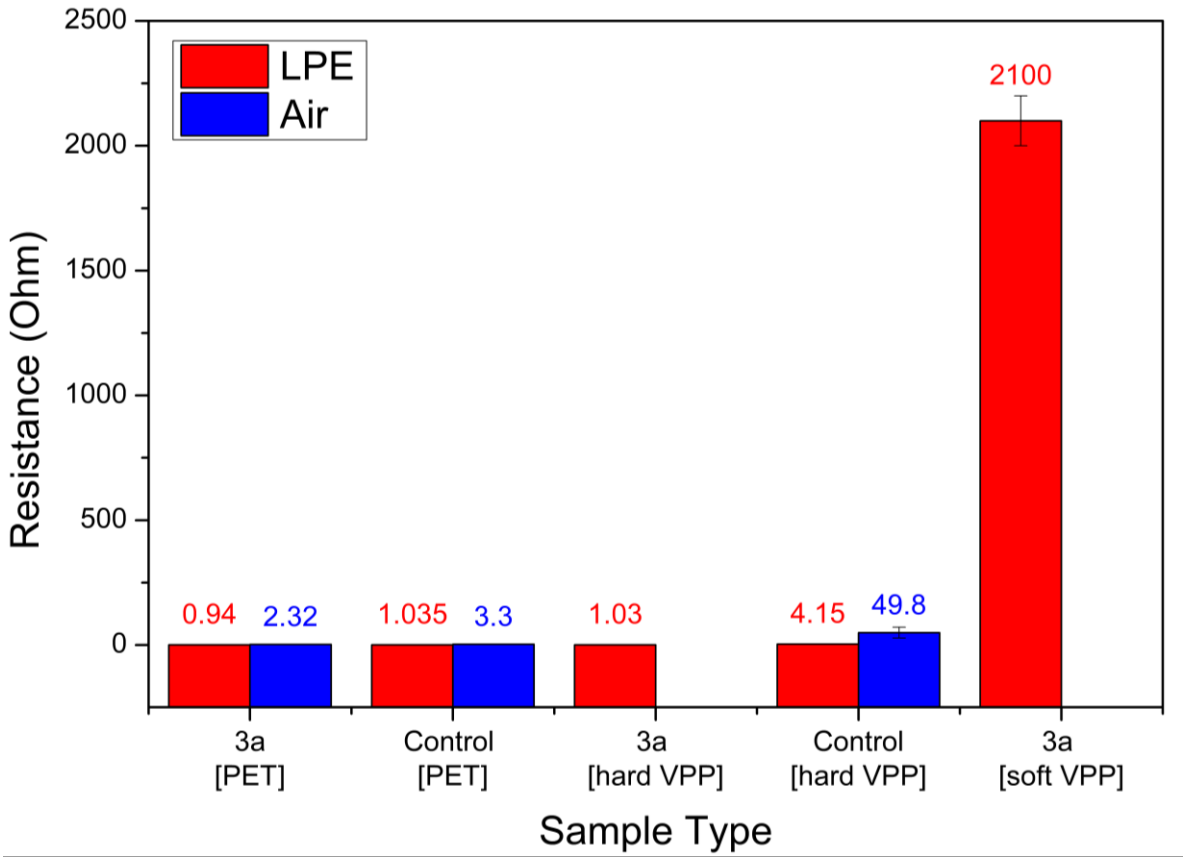

Fig. 4.11: Resistance for LIFT experiments (with 1 μm Cu donor) for understanding the effects of receiver surface hardness on the electrical properties.

doi:10.6342/NTU202301493

As mentioned above, it was guessed that the receiver thickness could play a role in the electrical properties of the deposition. Therefore, experiments were conducted using hard VPP receiver substrate material as receiver substrate material. LIFT with receiver substrate thicknesses of 1 mm, 2 mm and 3 mm were investigated under ambient and LPE (low pressure) conditions. Table 4.6 shows that the conductivity of the deposit decreases with increase in thickness.

It must be noted that thicker receiver substrates result in higher stiffness, which in turn is directly related to reduced damping capabilities (Chandra et al., 1999). Additionally, during experiments, brown fumes were observed as thicker substrates were used for the LIFT process. We expect it to be the Cu particles which were bounced away from the thick (stiff) receiver substrate.

Table 4.6: LIFT experiments (with 1 µm Cu donor) for understanding the effects of receiver surface thickness (hard VPP) on the electrical properties.

Sample Description	**Resistance (Ω)**	
	LPE	**Air**
Hard VPP (t= 1 mm)		
3a	1.77 ± 0.06	17.50 ± 4.60
Control	8.90 ± 1.20	23.5 ± 4
Hard VPP (t= 2 mm)		
3a	5.15 ± 0.35	10.55 ± 0.05
Control	10.40 ± 1.30	11.10 ± 3.10
Hard VPP (t= 3 mm)		
3a	8.40 ± 1.20	15.80 ± 0.20
Control	33.45 ± 2.25	96 ± 4

doi:10.6342/NTU202301493

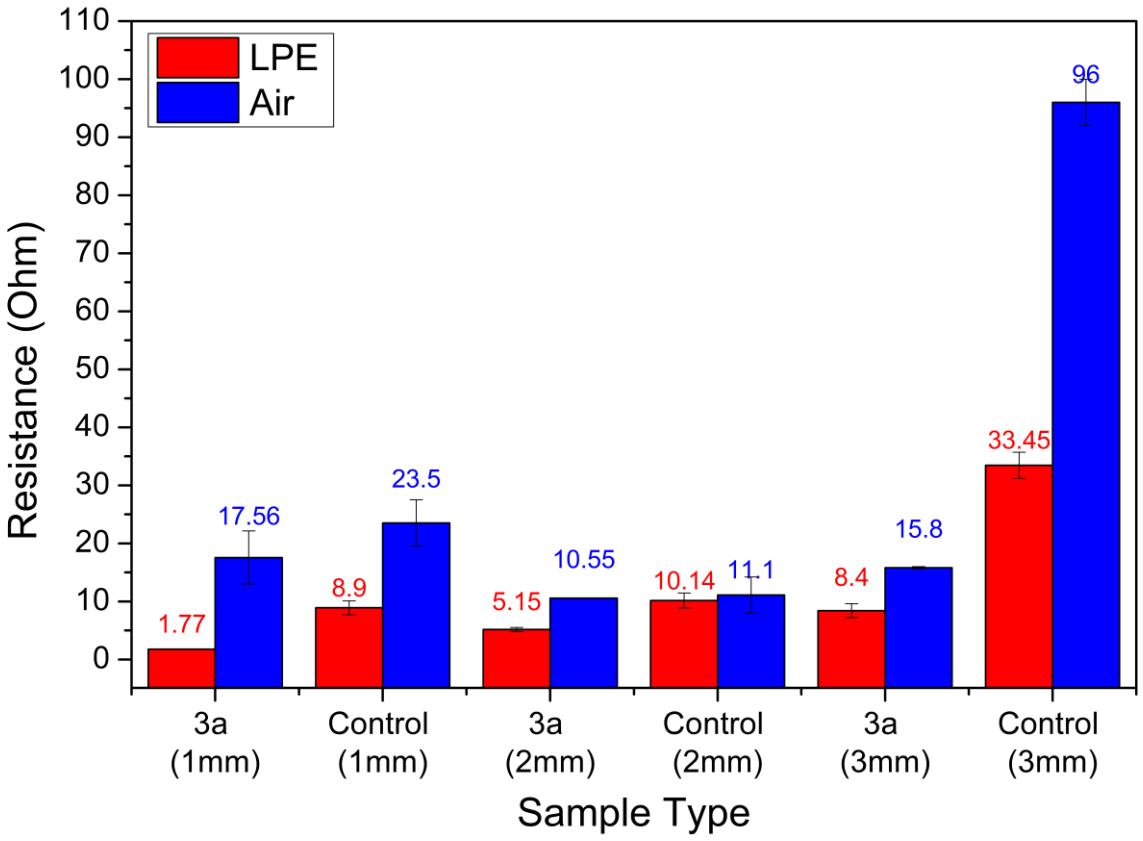

Fig. 4.12: Resistance for LIFT experiments (with 1 µm Cu donor) for understanding the effects of receiver surface thickness (hard VPP) on the electrical properties.

4.3.2. Cu-Ag LIFT

Considering, a significant amount of experiments made for Cu LIFT, for optimal deposition to be utilized as a potential working electrode (WE) and current collector (CC), efforts are now made to deposit Ag on top of Cu. Since Cu and Ag have different thermophysical properties, therefore, the LIFT parameters are different for the two materials. For the experiments, LST PET 3a receiver substrate is chosen. Previous evidence shows that LST PET 3a shows good electrical conductivity and geometrical accuracy with negligible deposition spreading. Experiments are conducted in LPE and ambient conditions with a control experiment (PET with no LST). Resistance measurements are carried out after each material deposition (Cu and Ag). Resistance values obtained after Cu deposition are reduced when Ag-LIFT is conducted. The reduction in resistance is due to the filling up of voids which were already present in the Cu deposit. Furthermore, silver has higher conductivity

doi:10.6342/NTU202301493

than copper, therefore post Ag deposition on Cu, the measured resistance reduces. Additionally, the brown colored surface of Cu turns grey after Ag-LIFT. LPE conditions show better conductivity due to the decrease of shockwaves intensity. Furthermore, LST samples show better conductivity due to possible improved adhesion between the receiver and the Cu deposit, which when impacted upon by the Ag flyer, is able to reduce disintegration of Cu. The mentioned characteristics shows successful deposition of Ag. However, the homogeneity will be double checked using EDS results. Finally, direct deposition of the Ag on PET substrate shows negligible transfer, and poor electrical property. However, trials on VPP based surface patterned receiver substrates show evidence of Ag deposition. Therefore, an argument can be made to successfully deposit Ag, surface roughness/texture/patterns must be introduced with sufficient troughs for efficient entrapment of the Ag flyer. Which in case of Ag deposited on Cu, is produced by the combined effect of LST and Cu deposits.

Table 4.7: LIFT experiments for deposition of Ag on top of Cu (current collector) for obtaining desired electrical properties, utilizing LST PET 3a receiver substrate.

Sample Description	**Resistance (Ω)**	
	LPE	**Air**
LST PET (3a) Cu-Ag		
After Cu	1.550 ± 0.050	2.750 ± 0.750
After Cu-Ag	1.375 ± 0.045	1.405 ± 0.095
LST PET (3a) Ag		
After Ag	$(41.7 \pm 27.1) \times 10^3$	--
PET (control)		
After Cu	9.450 ± 0.750	2.750 ± 0.250
After Cu-Ag	3.350 ± 0.350	1.610± 0.010

For the sake of confirmation, experiments for printing Ag on Cu were carried on different receiver substrates and laser powers of 2 W and 1.5 W (see Table 4.8). In addition, the effect of simultaneous increase in the donor-receiver distance (L) was investigated. Results indicate LST 3a PET receiver incorporated with and without simultaneous change in L can reduce the resistance by 18.96 %. It is interesting to note that LST 3a hard VPP produced receiver shows the highest percentage reduction (31.66 %) in resistance. However, the resistance magnitude

doi:10.6342/NTU202301493

is higher than the LST 3a PET samples. Figs. 4.13 and 4.14 illustrates the effects of laser power used for Ag-LIFT on the resistance of the deposits.

Table 4.8: LIFT experiments made to understand the effects of laser power and donor receiver gap length for Ag deposition on Cu layer. Receiver substrates used are optimized LST (i.e. 3a) on PET, hard VPP and VPP based surface patterned hard VPP. Fixed parameters (for Cu deposition): Power: 2 W; Frequency: 50 kHz; speed: 1300 mm/s; pitch: 0.02 mm. "*L*" refers to the donor-receiver gap (in μm), and more than one value refers to simultaneous change in *L* with each deposition.

Power (Ag) (W)	**Sample details**	**Resistance (Ω) LPE**		**% decrease in resistance**
		Post Cu	**Post Cu + Ag**	$\frac{R_{Cu} - R_{Cu+Ag}}{R_{Cu}} \times 100$
LST-PET (3a)				
2	Cu + Ag [L (μm) = 400]	1.450 ± 0.050	1.175 ± 0.055	18.96 %
	Cu + Ag [L (μm) = 400,800]	1.450 ± 0.050	1.175 ± 0.035	18.96 %
1.5	Cu + Ag [L (μm) = 400]	1.425 ± 0.025	1.305 ± 0.145	8.42 %
	Cu + Ag [L (μm) = 400,800]	1.435 ± 0.035	1.275 ± 0.145	11.14 %
LST-VPP hard (3a)				
2	Cu + Ag [L (μm) = 400]	8.050 ± 1.450	7.950 ± 1.250	1.24 %
	Cu + Ag [L (μm) = 400,800]	8.600 ± 1.50	7.450 ± 1.850	13.37 %
1.5	Cu + Ag [L (μm) = 400]	30 ± 0	20.50 ± 2.500	31.66 %
	Cu + Ag [L (μm) = 400,800]	6.950 ± 0.050	9.200 ± 0.100	-32.3 %
Surface patterning-VPP hard (V8)				
2	Cu + Ag [L (μm) = 400]	2.950 ± 0.05	2.600 ± 0.400	11.86 %
	Cu + Ag [L (μm) = 400,800]	1.550 ± 0.05	1.400 ± 0.100	9.67 %
1.5	Cu + Ag [L (μm) = 400]	9.30 ± 0.200	9.650 ± 0.550	-3.76 %
	Cu + Ag [L (μm) = 400,800]	4.050 ± 0.350	4.600 ± 0.600	-13.58 %

doi:10.6342/NTU202301493

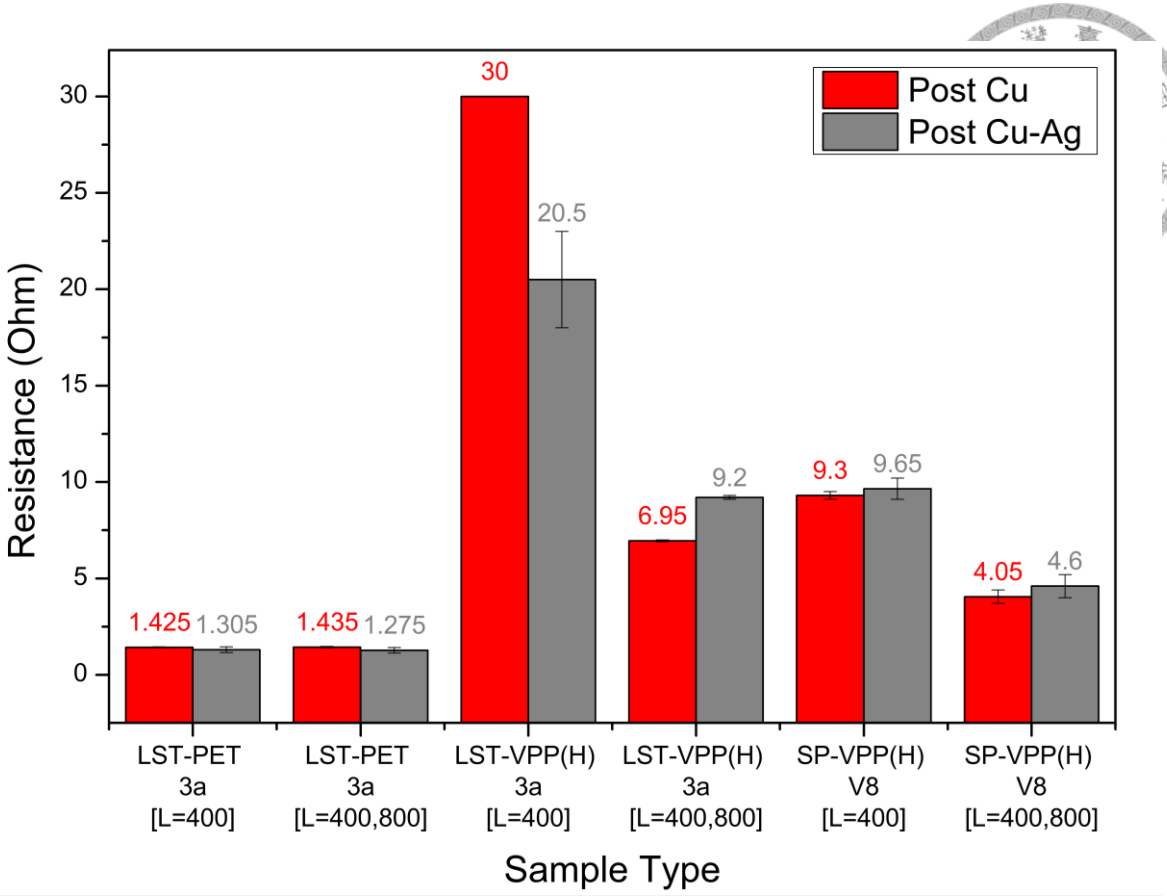

Fig. 4.13: Post Cu and Post Ag deposition resistance for LIFT experiments (with 1 µm Cu and Ag donor). The numbers in the square brackets denote the donor-receiver substrate distance (left: during Cu-LIFT, Right: during Ag-LIFT, single value: during both Cu and Ag-LIFT]. Laser power for Ag-LIFT: 1.5 W.

doi:10.6342/NTU202301493

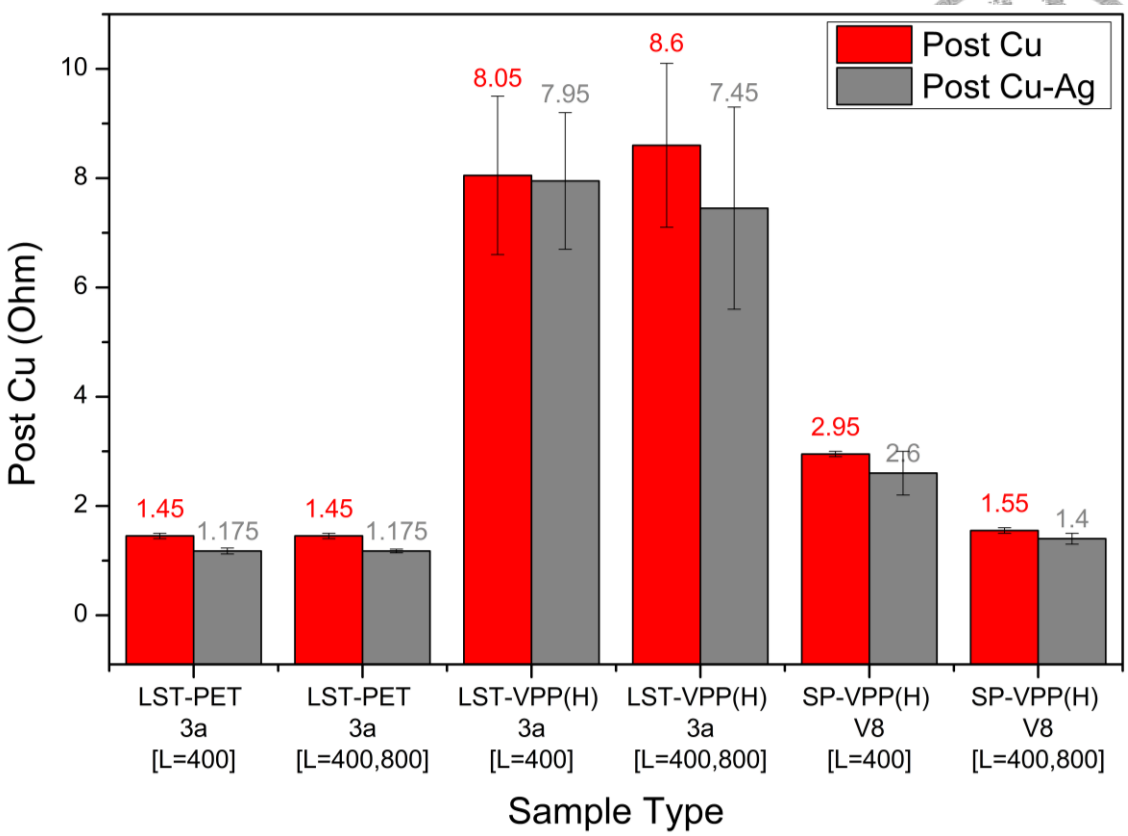

Fig. 4.14: Post Cu and Post Ag deposition resistance for LIFT experiments (with 1 µm Cu and Ag donor). The numbers in the square brackets denote the donor-receiver substrate distance (left: during Cu-LIFT, Right: during Ag-LIFT, single value: during both Cu and Ag-LIFT]. Laser power for Ag-LIFT: 2 W.

Further to solidify the claims above, experiments were carried out using 1 µm Ag films. Evidence shows that the deposition characteristics obtained in Table 4.7 (for 500 nm Ag) are followed in case of 1 µm Ag films. These characteristics are: (i) LPE produces greater conductivity samples, (ii) Ag deposition post Cu deposition leads to reduction in resistance, and (iii) double layer Ag deposition on PET receiver substrates show loss in conductivity. Considering the aforementioned highlights of the Cu-Ag depositions, further investigations were made to understand and optimize the effects of laser power (or pulse energy) and donor-receiver substrate distance for Ag (1 µm) transfer post Cu (1 µm) deposition.

During Ag deposition on Cu, brown vapors were observed when LIFT was conducted in ambient air conditions. Therefore, proving that Cu was ejected out of the PET receiver substrate. This phenomenon may be assisted by two factors: (i) presence of shockwaves, and

doi:10.6342/NTU202301493

(ii) impact of the Ag flyer material. Furthermore, degradation in conductivity for 1 μm Ag in ambient air compared to its 500 nm counterpart proves the effect of impact of the Ag flyer material. Heavier flyer (from 1 μm Ag) displaces the Cu with greater intensity, resulting in reduction in the electrical conductivity (as observed from Table 4.9)

Table 4.9: LIFT experiments made to understand the effects of donor layer thickness and environment conditions (atmospheric/low pressures) for Ag deposition on Cu layer. Receiver substrates used are optimized LST (i.e. 3a) on PET, Fixed parameters (for Cu deposition): Power: 2 W; Frequency: 50 kHz; speed: 1300 mm/s; pitch: 0.02 mm. "*L*" refers to the donor-receiver gap (in μm), and more than one value refers to simultaneous change in *L* with each deposition.

Power (Ag) (W)	**Sample details**	**Resistance (Ω)**				**% decrease in resistance**	
		LPE		**Air**		$\frac{R_{Cu} - R_{Cu+Ag}}{R_{Cu}} \times 100$	
		Post Cu	**Post Cu + Ag**	**Post Cu**	**Post Cu + Ag**	**LPE**	**Air**
LST-PET (3a) Ag (500 nm)							
2	Cu + Ag [L (μm) = 400,800]	1.600 ± 0.400	0.955 ± 0.050	1.85 ± 0.55	1.5 ± 0.3	40.31	18.91
LST-PET (3a) Ag (1 μm)							
2	Cu + Ag [L (μm) = 400,800]	1.575 ± 0.425	1.065 ± 0.055	1.75 ± 0.45	6.1 ± 5	32.38	-248.57

doi:10.6342/NTU202301493

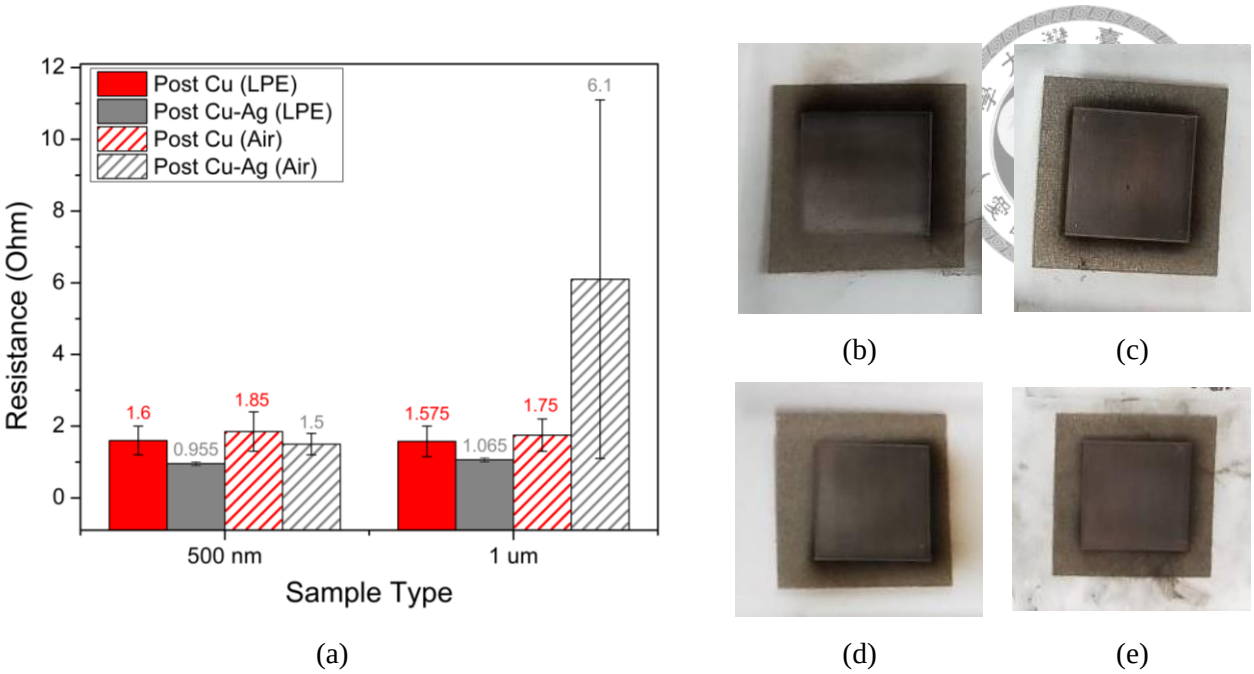

Fig. 4.15: Resistance for Cu-Ag LIFT deposits made in LPE and ambient environments with variable Ag donor thickness (500 nm and 1 µm). Cu-Ag deposition image for experiments described in Table (b) 500 nm Ag in LPE, (c) 500 nm Ag in air, (d) 1 µm Ag in LPE and (e) 1 µm Ag in air.

Previous observations show that 1 µm Ag donor have poor performance compared to its 500 nm counterpart. The probable reason for this observation is that the flyer produced from the 1 µm Ag donor is heavier than its 500 nm counterpart, thereby producing a greater impact during deposition, leading to slight degradation of the electrical conductivity. In addition, it is observed that the LIFT of Ag on Cu in ambient air produces decreases the conductivity, which is possibly due to the combined adverse effects of the shockwaves generated and the strong impact of the heavier flyer (produced from 1 µm Ag donor). Therefore, from Fig. 4.15 and Table 4.9, it can be inferred that Ag transfer is suitable with LPEs and light flyer.

In addition to the above, advanced studies on Ag were made by fabricating micropillars of Ag on top of the Ag additive layer. To achieve this, subsequent increase in the donor-receiver distance (L) and introducing defocusing during the transfer of Ag on LIFT deposited Cu (as was mentioned by Liu et al. (Liu et al., 2020b)). Furthermore, it must be noted that for the advance studies, LPE and 500 nm Ag donor was utilized. Based on the visual observations, uniform and prominent Ag deposition was observed for defocused experiments. Table 4.10

doi:10.6342/NTU202301493

shows that defocusing and increasing the donor receiver distance helped in achieving desired depositions (micropillars) with enhanced conductivity.

Table 4.10: LIFT experiments with change in donor-receiver length and defocus, for Ag deposition on Cu layer. Receiver substrates used are optimized LST (i.e. 3a) on PET, Fixed parameters (for Cu deposition): Power: 2 W; Frequency: 50 kHz; speed: 1300 mm/s; pitch: 0.02 mm. "*L*" refers to the donor-receiver gap (in μm), and more than one value refers to simultaneous change in *L* with each deposition.

Power (Ag/Pt) (W)	**Sample details**	**Resistance (Ω)**		**% decrease in resistance**
		LPE		**LPE**
		Post Cu	**Post Cu + Ag**	$\frac{R_{Cu} - R_{Cu+Ag}}{R_{Cu}} \times 100$
LST-PET (3a) Ag (500 nm)				
2	Cu + Ag [L (μm) = 400,800] Defocused (μm): 400	1.180 ± 0.120	0.985 ± 0.015	16.52
1.5	Cu + Ag [L (μm) = 400,800,1200] Defocused (μm): 400, 800	1.550 ± 0.450	1.070 ± 0.130	30.96

doi:10.6342/NTU202301493

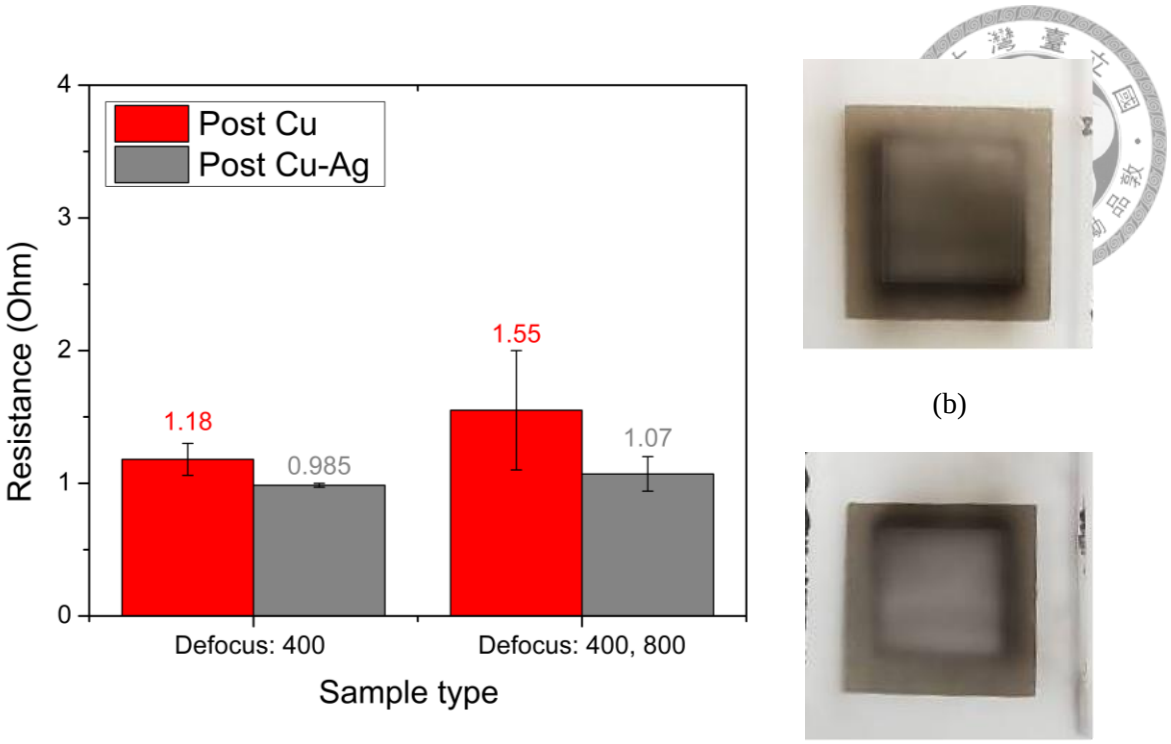

Fig. 4.16: (a) Resistance for Cu-Ag LIFT deposits made in LPE and with 500 nm Ag donor thickness with variable donor-receiver distance (L) and defocus length (in μm). Cu-Ag deposition image for experiments described in Table 4.10 (b) 2 W and (c) 1.5 W.

4.3.3. Cu-Pt LIFT

Considering all the above evidences, LST 3a PET receiver substrates are used for LIFT of Cu under LPE conditions with its predetermined optimized parameters (i.e. laser power: 2 W, f: 50 kHz, s: 100 mm/s, pitch: 0.02 mm). Following the Cu depositions as the primary layer, attempts were made to deposit Pt on the primary Cu layer. Preliminary experiments show that Pt depositions by changing the environment conditions (i.e. pressure) cannot be successful. Challenges arise due to the brittle nature of Pt and the pre-existing microcracks in the Pt donor (as mentioned above and shown in Fig. 4.17). Table 4.11 and Fig. 4.17 illustrates that although Pt can be transferred over Cu under low pressure conditions (visual observations), the transferred Pt layer do not show any conductivity. On the contrary, for ambient experiments, the Pt flyers are greatly displayed away from the target, leading very poor transfer accuracy and precision.

doi:10.6342/NTU202301493

Table 4.11: LIFT experiments made to understand the effects of laser power, donor-receiver length and environment conditions (atmospheric/low pressures) for Pt deposition on Cu layer. Receiver substrates used are optimized LST (i.e. 3a) on PET, Fixed parameters (for Cu deposition): Power: 2 W; Frequency: 50 kHz; speed: 1300 mm/s; pitch: 0.02 mm. "*L*" refers to the donor-receiver gap (in μm), and more than one value refers to simultaneous change in *L* with each deposition.

Power (Pt) (W)	**Sample details**	**Resistance (Ω)**				**% decrease in resistance**	
		LPE		**Air**		$\frac{R_{Cu} - R_{Cu+Pt}}{R_{Cu}} \times 100$	
		Post Cu	**Post Cu + Pt**	**Post Cu**	**Post Cu + Pt**	**LPE**	**Air**
2	Cu + Pt [L (μm) = 400]	2.15 ± 0.5	--	2.50 ± 1	--	--	--
	Cu + Pt [L (μm) = 400,800]	2.10 ± 1	--	26 ± 0.5	--	--	--
1.5	Cu + Pt [L (μm) = 400]	1.90 ± 0.8	--	Discarded experiments		--	--
	Cu + Pt [L (μm) = 400,800]	1.20 ± 0.2	--			--	--

doi:10.6342/NTU202301493

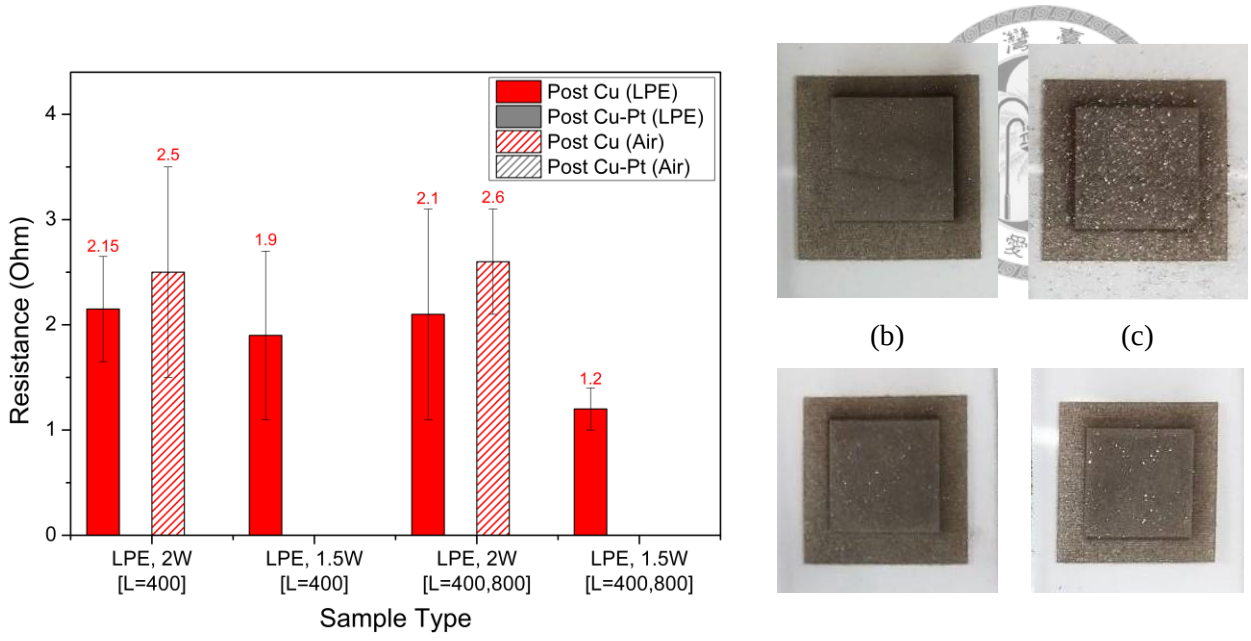

Fig. 4.17: (a) Resistance for Cu-Pt LIFT deposits made in LPE and ambient environments with 500 nm Pt donor thickness. Cu-Pt deposition image for experiments described in Table 4.11, (b) 2 W in LPE, (c) 2 W in air, (d) 1.5 W with L= 400 µm in LPE and (e) 1.5 W with L= 400 and 800 µm in LPE.

Advanced studies on Pt is made, which is similar to those of Cu-Ag. Aforementioned results on Cu-Pt discusses that although Pt could be visually observed on Cu, the non-uniform deposition and spreading of Pt leads to non-conductive deposits due to the brittle nature, presence of grain boundary ridges and microcracks in the Pt donor. Therefore, defocusing with increase in the donor-receiver distance (L) is utilized to deposit uniform additive layer along with the desired Pt micropillars. Table 4.12 shows that utilizing defocusing along with change in donor-receiver length (L) enables successful deposition of Pt and attain conductive deposits. In addition, Fig. 4.18(b) illustrates whitish surface, indicating Pt deposition. Furthermore, Pt was deposited using high defocus (2 mm), which resulted in loss in conductivity and no visual recognition for Pt deposit (i.e. no whitish deposit).

doi:10.6342/NTU202301493

Table 4.12: LIFT experiments with change in donor-receiver length and defocus, for Pt deposition on Cu layer. Receiver substrates used are optimized LST (i.e. 3a) on PET, Fixed parameters (for Cu deposition): Power: 2 W; Frequency: 50 kHz; speed: 1300 mm/s; pitch: 0.02 mm. "*L*" refers to the donor-receiver gap (in μm), and more than one value refers to simultaneous change in *L* with each deposition.

Power (Pt) (W)	**Sample details**	**LPE Resistance (Ω)**		**% decrease in resistance** $\frac{R_{Cu} - R_{Cu+Pt}}{R_{Cu}} \times 100$
		Post Cu	**Post Cu + Pt**	
LST-PET (3a) Pt (500 nm)				
1.5	Cu + Pt [L (μm) = 400,800,1200] Defocused (μm): 400, 800	1.450 ± 0.350	1.065 ± 0.035	26.55
1.5	Cu + Pt [L (μm) = 400] Defocused (μm): High (2 mm)	1.400 ± 0.300	--	--

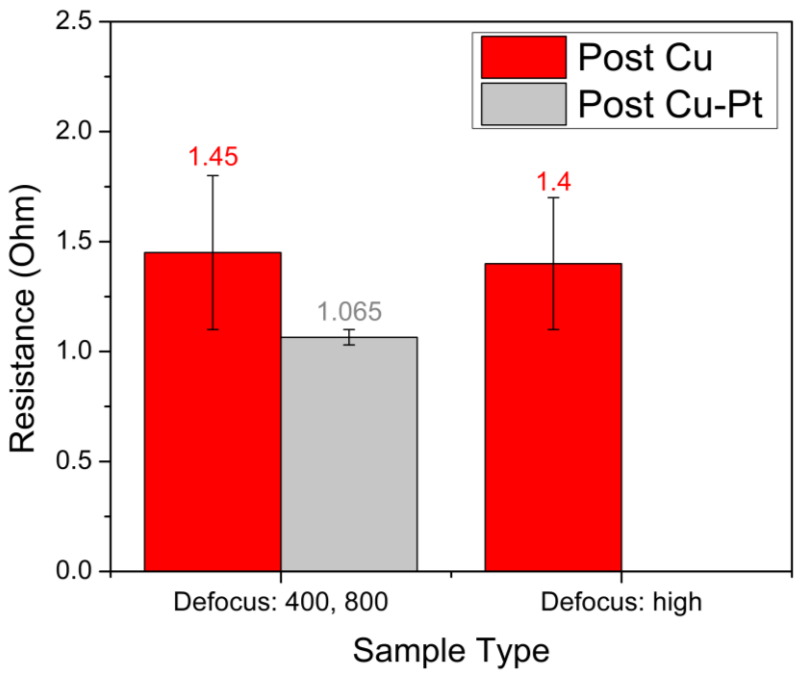

(a)

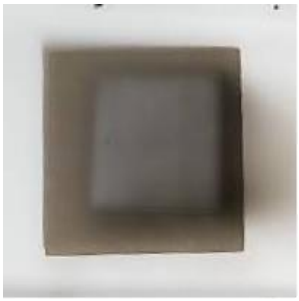

(b)

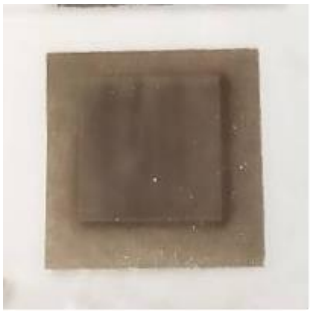

(c)

Fig. 4.18: (a) Resistance for Cu-Pt LIFT deposits made in LPE environment and with 500 nm Pt donor thickness with variable donor-receiver distance (*L*) and defocus length (in μm). Cu-Pt deposition image for experiments described in Table 4.12, (b) optimized defocus (400, 800 μm) and (c) high defocus (2 mm).

doi:10.6342/NTU202301493

4.4. Characterization results

4.4.1. FESEM

Deposition morphology has significant effects on the electrical properties of the transferred material. Coarse and irregular morphologies with porosities and voids may significantly affect the conductivity of the film. In order to understand the differences in the deposition morphology FESEM imaging has been carried out. Fig. 4.19(a) illustrates the surface morphology of Cu when LIFT is carried out in LPE conditions. The deposition morphology is not as smooth as obtained in other processes such as sputtering or vapor deposition, however, when compared to the Cu deposition made in ambient air, LPE conditions prove to be better. This can also be validated by the resistance measurements carried out in previous sections (see Table 4.2 and Fig. 4.8). Resistance is measured to be higher for LIFT deposits made in ambient air. This is because during the transfer process, the depositions made under air produces shockwaves which tend to displace neighboring already deposited materials, thereby creating discontinuities in the structure. The right parts of Fig. 4.19 illustrate validation to the aforementioned discussion. LIFT in air has high discontinuities and inaccurate edges when compared to its LPE counterparts. To further analyze the deposits quantitatively, EDS is carried out in the subsequent section.

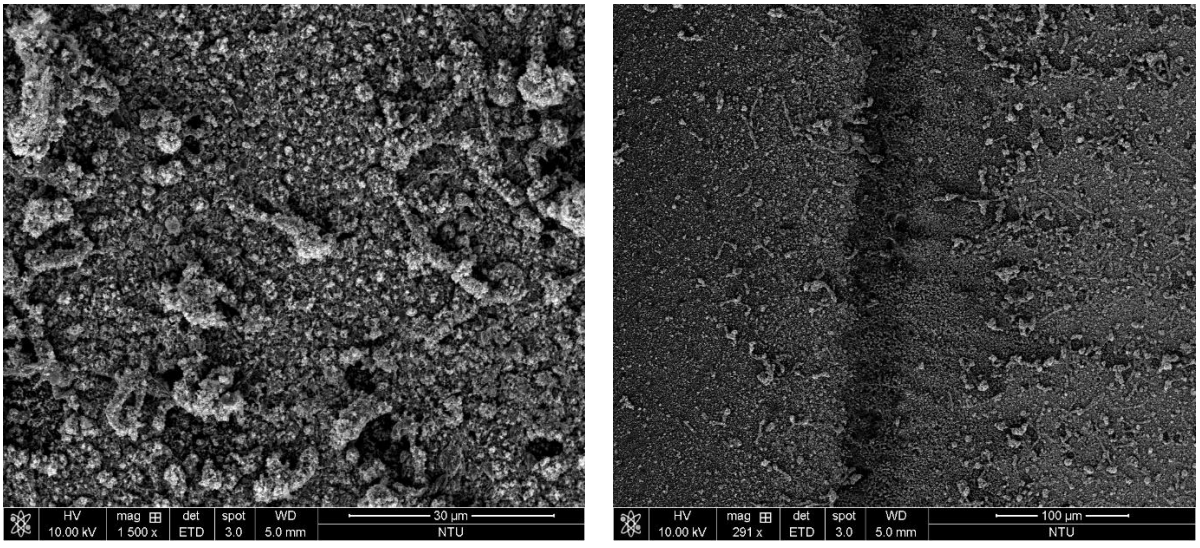

(a)

doi:10.6342/NTU202301493

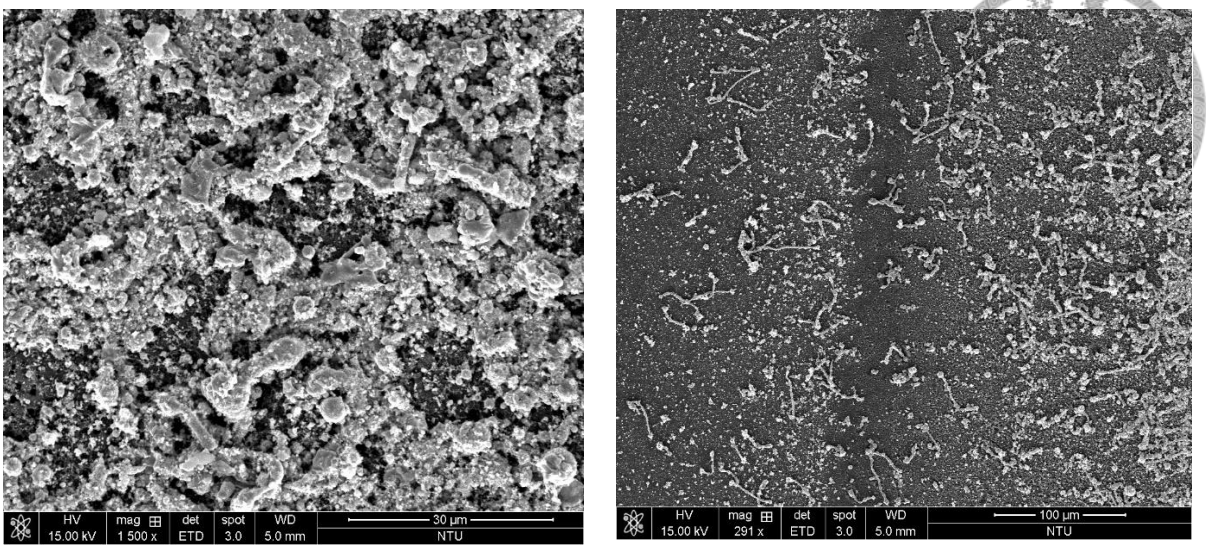

(b)

Fig. 4.19: FESEM image of surface morphology for Cu (a) in LPE, and (b) in air.

4.4.2. EDS

In order to solidify the claims of successful Cu, Ag and Pt depositions, EDS is carried out. Fig. 4.20 illustrates the elemental distribution for Cu depositions under LPE and air conditions. Results show that uniform and high Cu peak for LPE LIFT, whereas, deposits in air lower Cu content due to the presence of porosities and voids in the deposit. Therefore, it can be firmly established that LIFT under LPE conditions outstands the LIFT process conducted in air.

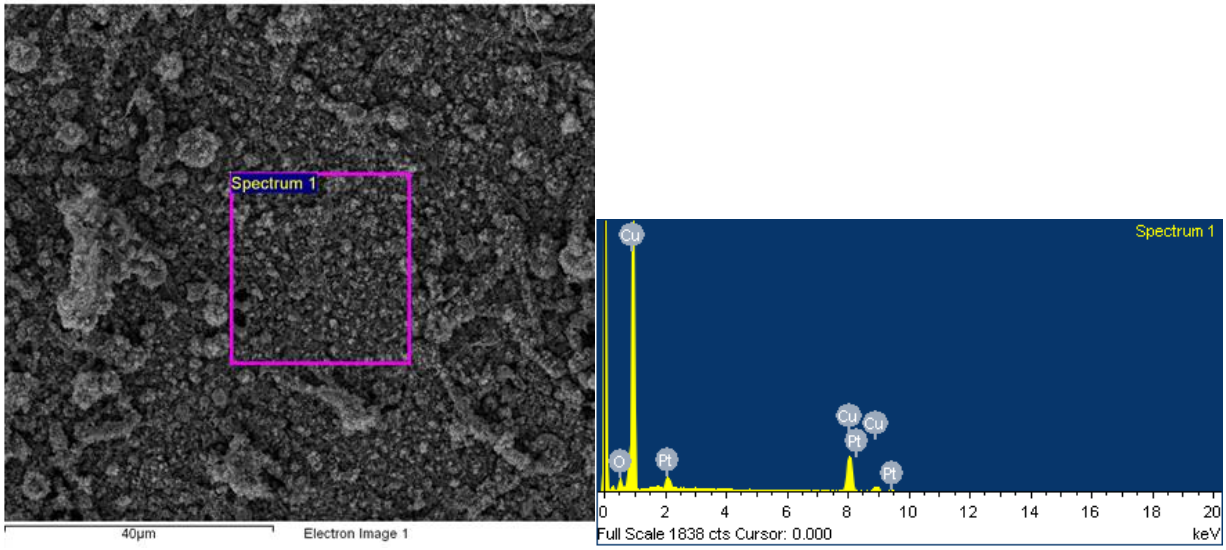

(a)

doi:10.6342/NTU202301493

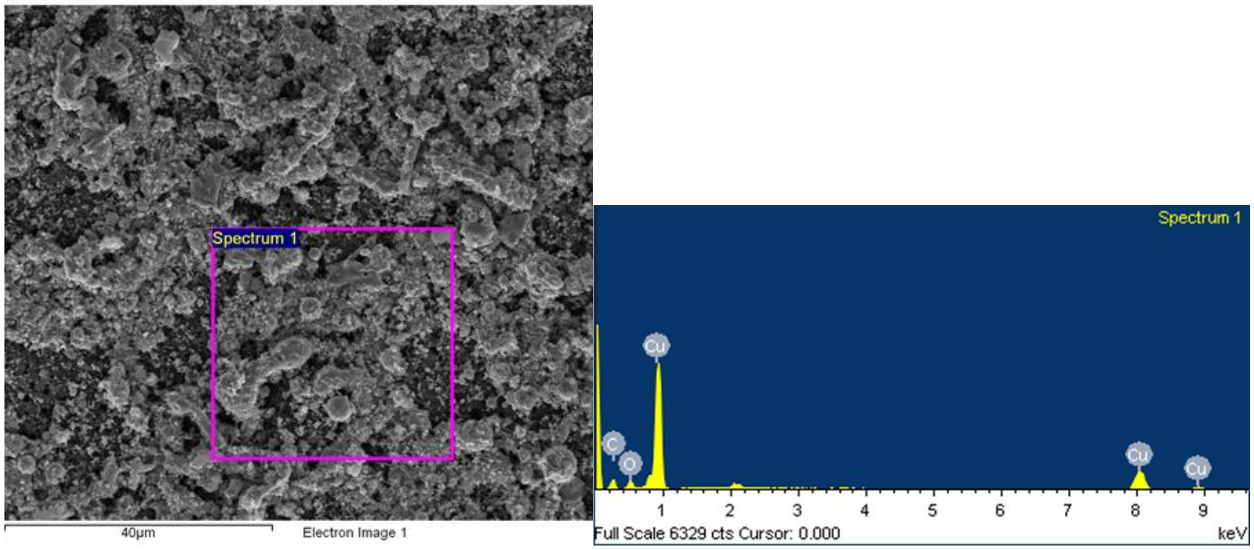

(b)

Fig. 4.20: EDS spectrum for LIFT deposited Cu in (a) LPE and (b) ambient air environments.

Subsequently, post Cu depositions, efforts were made to deposit Ag and Pt. Although success for Ag and Pt depositions over Cu was partially proved through resistance measurements and through visibility checks, further evidences were necessary. Additionally, micropillars are made on the deposited Ag and Pt layer to prove strong adhesion between layers (Ag and Pt additive layer) and Cu with the receiver substrate. If strong adhesion between the additive layer with Cu and the receiver substrate is absent, during micropillar fabrication, the already existing deposits will be displaced by the incoming material, leading to increase in resistance. Fig. 4.21 shows elemental scatter plot for Ag and Pt micropillars. Strong presence of Ag and Pt is observed in the scatter plots. Therefore, successful deposition of Ag and Pt micropillars post their respective layering is validated.

doi:10.6342/NTU202301493

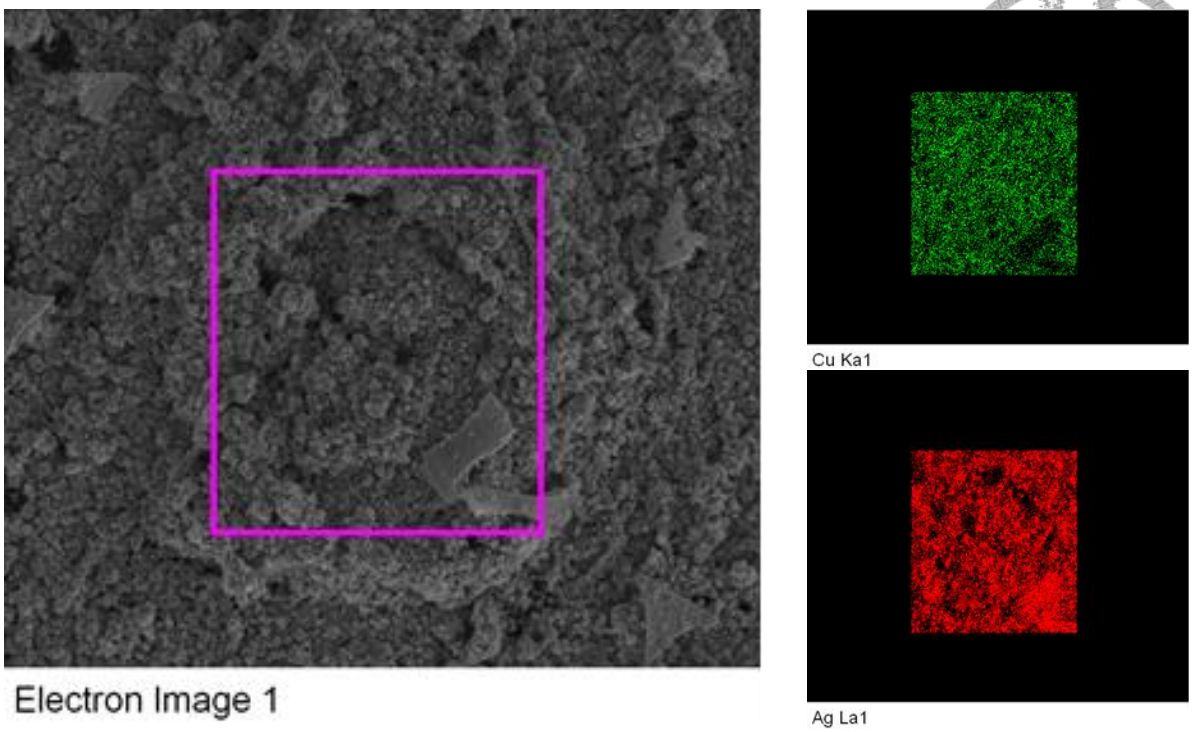

(a)

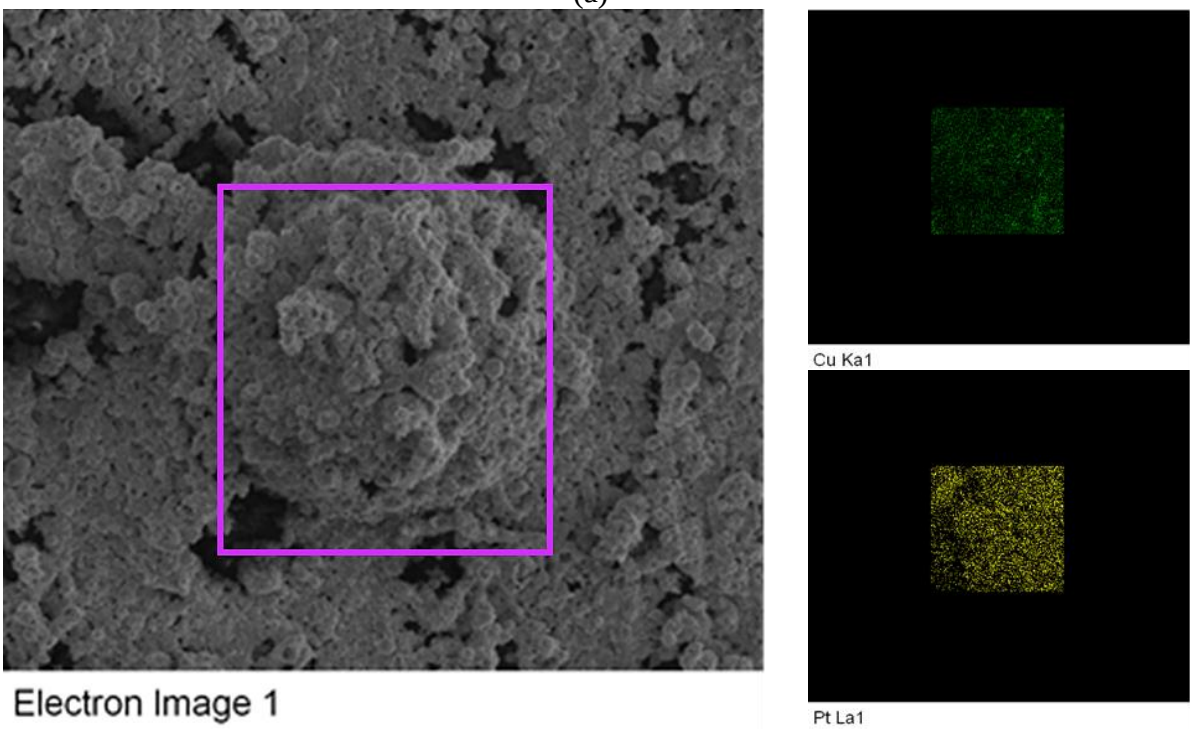

(b)

Fig. 4.21: EDS point analysis made on the deposited micropillar structure. Samples: (a) Ag micropillar on Ag layer deposited on Cu, and (b) Pt micropillar on Pt layer deposited on Cu.

doi:10.6342/NTU202301493

In addition to the above, some additional EDS results are illustrated to prove the successful deposition of Ag Pt layer on Cu. Fig. 4.22 illustrates EDS point analysis for areas outside the Ag and Pt micropillars. Significant elemental peaks of Ag and Pt are observed with minor Cu peaks. The presence of Cu peaks is evident due to the fact that the EDS data is measured at an approximate depth of 1 μm from the surface.

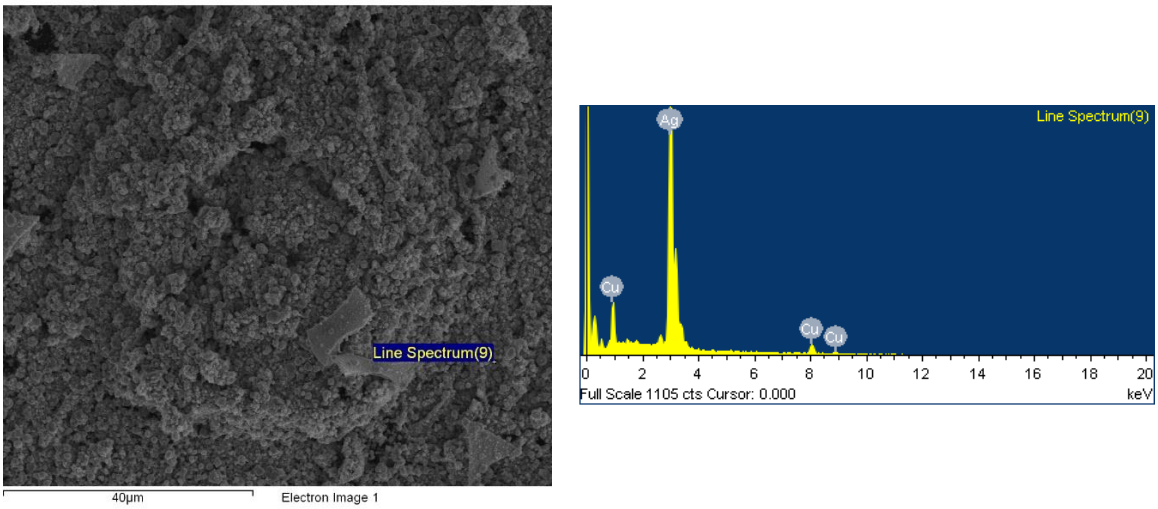

(a)

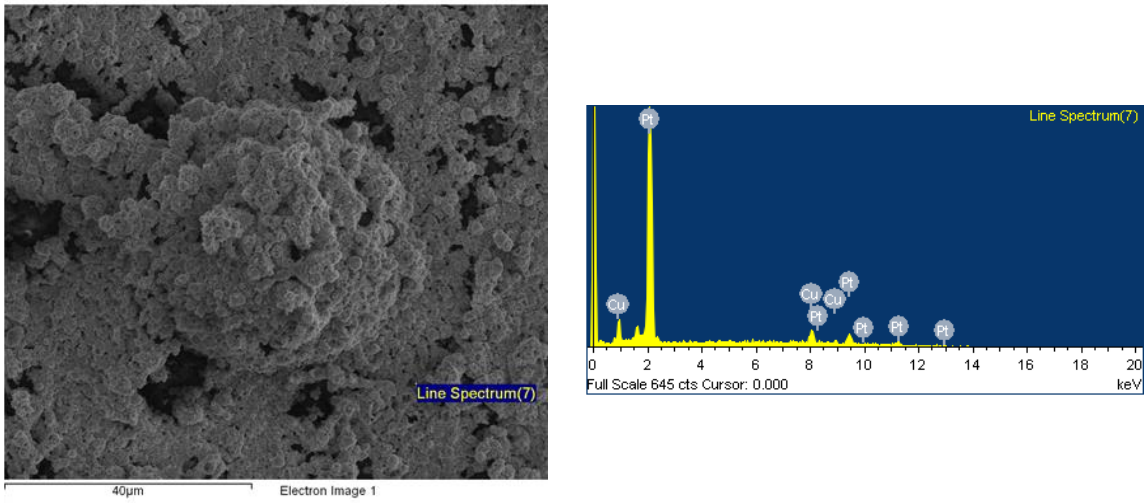

(b)

Fig. 4.22: EDS point analysis made on the deposited surface (excluding the micropillar). Samples: (a) Ag on Cu, and (b) Pt on Cu.

doi:10.6342/NTU202301493

4.4.3. XRD

In addition to the results obtained from the FESEM and the EDS analysis, investigations are made to check for possibilities of changes in the crystal structure and chemical components of the deposits via LIFT. Fig. 4.23 shows the XRD plot of Cu donor and Cu deposited via LIFT in air and low-pressure environments (LPE). The donor film exhibits high Cu (111) peaks, followed by moderate and negligible Cu (200) and CuO (111) peaks respectively. Cu deposited via LIFT shows presence of Cu_2O ((200) and (311)) and CuO (202). The presence of more than one oxidation state of Cu shows potential for utilization of such printed deposits as working electrodes for non-invasive and enzyme free sweat sensors (Zhou et al., 2021). The peaks were identified from the past research works (He et al., 2016, Yung et al., 2016, Zhou et al., 2021). Additionally, the broad peaks observed were obtained from surface reflexes and can be ignored.

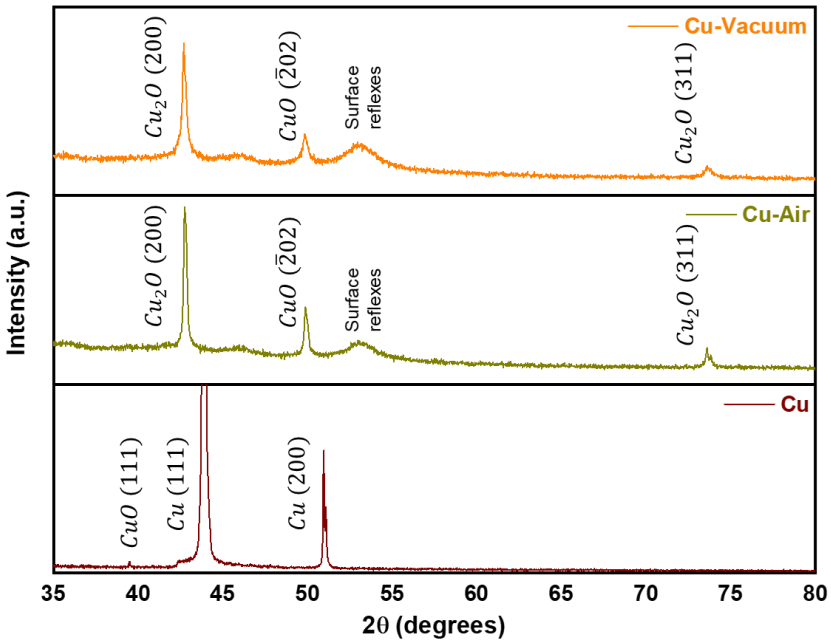

Fig. 4.23: XRD results for 1 µm Cu donor, Cu deposition by LIFT in air and LPE.

Subsequent to Ag deposition on Cu, XRD is conducted. The XRD results show presence of Ag (Ag (111), Ag (200) and Ag (311)), thereby providing evidence of successful deposition of Ag on Cu. Furthermore, possible formation of Cu-Ag metamaterials ($Cu_{0.4}Ag_{0.6}$ and $Cu_{0.3}Ag_{0.7}$) are observed due to the extreme high cooling rates achieved during the LIFT

doi:10.6342/NTU202301493

process (Gorodesky et al., 2022). However, the presence of such metamaterials is low since the transfer of Cu and Ag are made separately. Moreover, the presence of CuO and Cu_2O in the XRD validates the presence of both the elements and their successful LIFT depositions. Slight peak shifts may be observed while analyzing the XRD results, however, the phenomena is commonly observed due to the variation in the temperature of the manufacturing process (Yang and Zhou, 2013). Finally, the XRD results and its analysis as shown in Fig. 4.24 was made with reference to relevant past literatures (Gorodesky et al., 2022, Yang and Zhou, 2013, Chen et al., 2013, Mathpal et al., 2015).

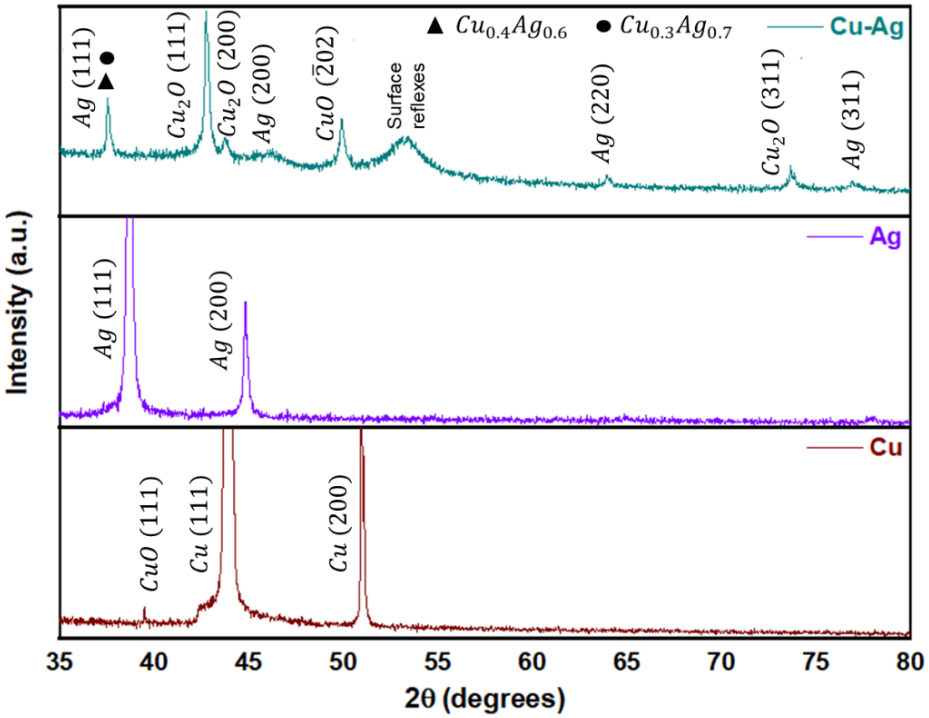

Fig. 4.25: XRD results for 1 µm Cu donor, 500 nm Ag donor and Cu-Ag deposition by LIFT in LPE.

Finally, XRD was conducted and analyzed for Pt depositions on Cu as shown in Fig. 4.26. Similar to the Ag deposition on Cu, Pt deposit on Cu shows, Pt and Cu-Pt alloy and is identified as Pt (200) and CuPt (PDF#42-1326) respectively. In addition, CuO and Cu_2O peaks could be observed, thereby validating the presence of the LIFT deposited Cu layer. Additionally, it must be noted that slight peak shifts may be observed in the Cu-Pt results when compared to the individual donors, however, such shift is common when alloys are

doi:10.6342/NTU202301493

formed and can be neglected (Liu et al., 2022). References are utilized for analysis of Pt and Cu-Pt deposits (Wysocka et al., 2019, Mo et al., 2019, Latif et al., 2014, Ding et al., 2013). As concluding remarks to XRD analysis, it can be inferred that successful deposition of Ag and Pt takes place on Cu, which can be utilized for potential applications in the fabrication of RE and CE for sensors.

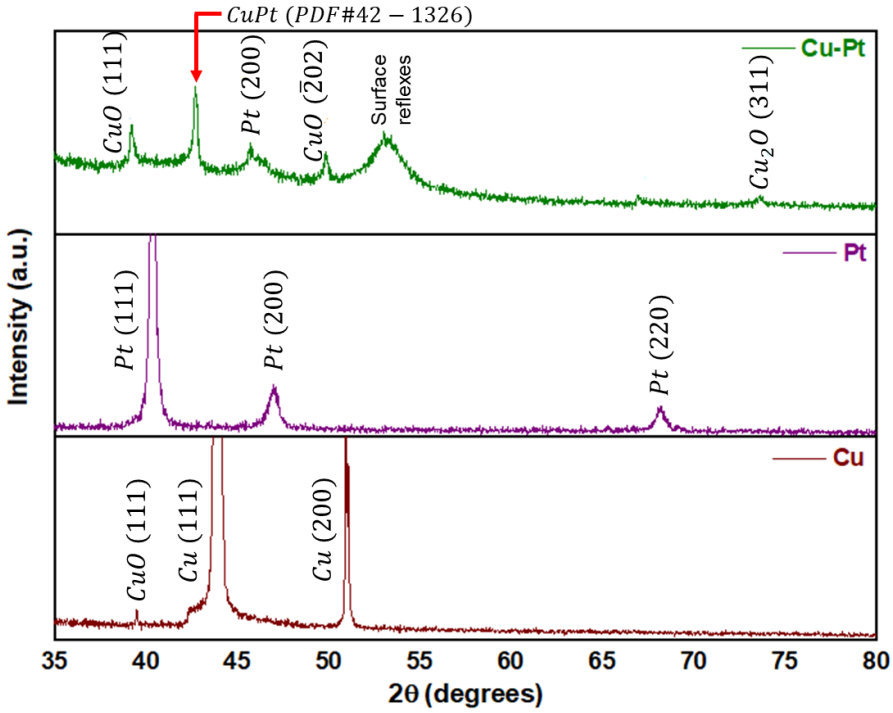

Fig. 4.26: XRD results for 1 µm Cu donor, 500 nm Pt donor and Cu-Pt deposition by LIFT in LPE.

4.4.4. Adhesion tape test

Adhesion tests were made for Cu LIFT experiments, considering the idea that Cu shall act as the receiver for subsequent material depositions for additive manufacturing applications. For example, for printing sensor electrodes, Cu can be utilized as current collector, and subsequently other noble metals like Ag and Pt can be printed as reference and counter electrodes respectively as additive layers.

In order to validate the effectiveness of LPE and receiver surface texturing on the mechanical and electrical conductivity, LIFT experiments are performed on regular and LST based PET receiver substrates. Evidence shows that significant scattering of Cu takes place during LIFT

doi:10.6342/NTU202301493

in ambient air. The scattering of Cu is reduced when LST samples are used. However, differences are observed for coarse, fine, and differently oriented LST. Although all LST based LIFT performs better than the control experiments, fine LST works the best as it helps efficient trapping of the Cu material. Furthermore, introducing LPEs enable precise transfer of Cu material without scatter, due to the reduction in shockwave intensity. Additionally, LPE results in increased transfer velocities, which helps in negligible deviation in the transfer path leading to printing of sharp and accurate structures. Finally, it can be reasonably agreed upon that the combined effect of optimized LST and LPEs can enable accurate transfer with negligible material scattering and high deposit-receiver adhesion. Preliminary tape test investigations show that LST 3a based receiver substrate in LPE conditions perform the best, considering the minimum material removal on the tape (see Fig. 4.27(a)). Consequently, the ASTM D3359 tape test is conducted for the LST 3a based receiver in LPE and air, and compared with its control counterparts. Promising results are again achieved for the LST based receiver in LPE conditions, achieving a scale rating of 5A as observed from Fig. 2.27(b). Likewise, LST 3a based deposition in ambient air is rated as 4A, and control experiments in LPE and air are rated as 3A and 2A respectively (see Fig. 4.27(b)).

doi:10.6342/NTU202301493

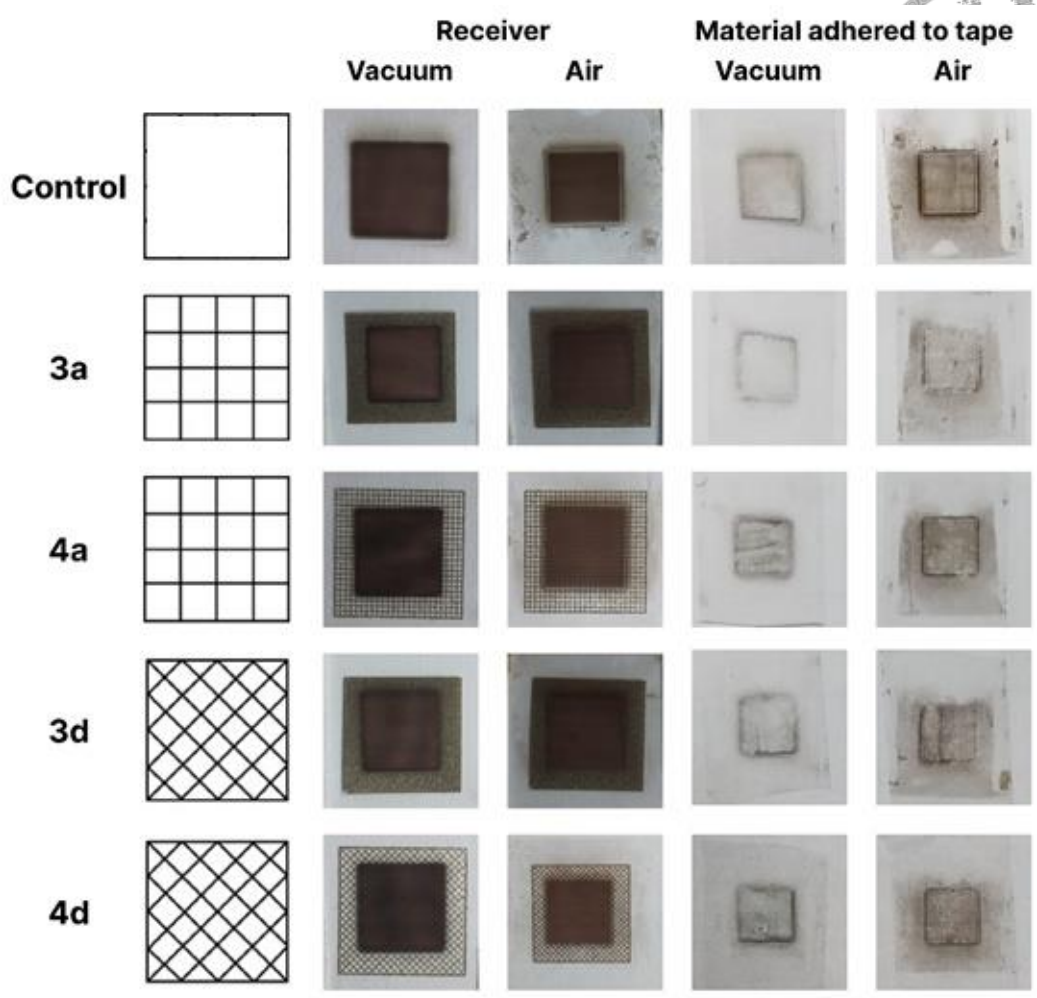

(a)

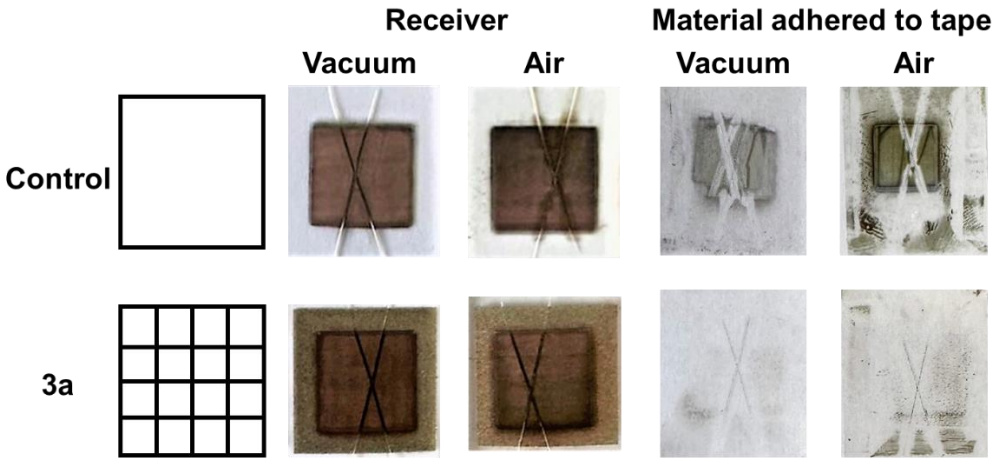

(b)

Fig. 4.27: Illustration of LIFT deposited Cu on PET for various receiver surfaces and material adhered to the 3M tape post (a) adhesion tape test (b) ASTM D3359 tape test.

doi:10.6342/NTU202301493

In addition to the tape test, conductivity of Cu before and after the adhesion testing must be carried out to solidify the claims of enhanced properties (mechanical and electrical). Table 4.13 shows the resistance magnitudes obtained along the tape test. Under low pressure conditions, results show that the LST with 0.1 mm pitch performs very well, showing a resistance increase of about 3.2%. In comparison, the other LST samples show higher increase in resistance magnitudes. Most, importantly, it is observed that the Cu deposits made in control experiments show the highest increase in resistance. On the contrary, LIFT experiments performed under ambient air conditions show very poor or no electrical conductivity post tape test. Therefore, it can be concluded that although control experiments may perform slightly better than certain LST modified samples, but the adhesion strength is comparatively poor. Again, the combined effects of LST and LPEs produce efficient LIFT manufactured Cu depositions with enhanced mechanical and electrical properties.

Table 4.13: Resistance of LIFT deposited Cu of LST receiver substrate in LPE and air environments, before and after the adhesion tape test as shown in Fig 2.27(a).

Sample type	Resistance (Ω)					
	LPE			Air		
	Before tape test (R_b)	After tape test (R_a)	% increase in resistance $\frac{R_a - R_b}{R_b} \times 100$	Before tape test (R'_b)	After tape test (R'_a)	% decrease in resistance $\frac{R'_a - R'_b}{R'_b} \times 100$
Control	1.80 ± 0.60	2.70 ± 1.30	50	53.10 ± 3.10	73 ± 3	37.4
3a	1.55 ± 0.25	1.60 ± 0.10	3.2	33.60 ± 1	--	--
4a	1.15 ± 0.05	1.20 ± 0.10	4.3	--	--	--
3d	1.25 ± 0.15	1.55 ± 0.45	24	27.90 ± 2.10	--	--
4d	1.44 ± 0.08	1.75 ± 0.05	21.5	400×10^3	--	--

4.4.5. Laser confocal microscopy

In order to solidify the aforementioned claims of accurate deposition using LST along with low pressure conditions, laser confocal microscopy is carried out. Additionally, the surface roughness of the deposits is investigated for the deposits under various experimental conditions, to put forward plausible discussions of benefit. Fig. 4.28 shows the laser confocal microscope results for LIFT of Cu under LPE conditions with and without LST (on receiver surface). Results show that a significant difference of height is observed when LST is utilized,

doi:10.6342/NTU202301493

where no such significant observations for experiments without LST. Therefore, a number of inferences can be put forward:

(i) Well defined edge observed for the deposited structure, therefore, LST enables deposition with higher accuracy, precision and resolution.

(ii) Observation of a significant difference in height denotes lower material losses during transfer, therefore, LST traps deposit materials on to the receiver substrate.

(iii) Fig. 4.28 results shows that the thickness of the Cu deposition with LST receiver substrate is around 27.789 µm. Whereas, for Cu deposition without LST to be around 3.802 µm.

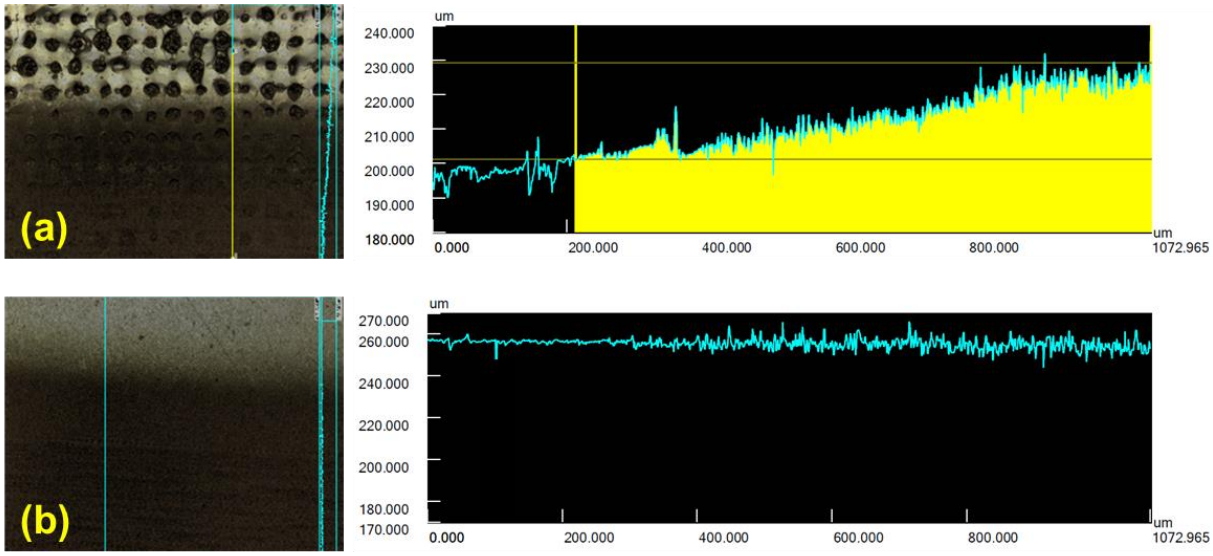

Fig. 4.28: Height difference results measured along a line (left) for Cu depositions made in LPEs. (a) with LST, and (b) without LST

In addition to deposition height analysis and its qualitative interpretations, surface roughness analysis is made for the Cu depositions, with and without LST receivers. Results show that the LIFT depositions with LST has a surface roughness (Ra) value of 7.722 µm, whereas its counterpart (without LST) has a Ra value of 3.677 µm. Fig. 4.29 illustrates the surface area where the surface roughness is determined. Therefore, LIFT with LST has greater surface uniformity. This is a positive observation because higher surface roughness provides a pseudo-LST for the future additive material layer, thereby increasing the deposition

doi:10.6342/NTU202301493

efficiency and adhesion. This observation and discussion are in line with the previous results, the reason for better performance of Ag and Pt additive layer depositions on LST based receivers. Furthermore, higher surface roughness indicates increased effective surface area. Past research evidence has shown higher surface area enhances electrocatalytic performance (enhanced electron transfer) due to increase in electroactive sites on the electrode surface. (Zaidi and Shin, 2016, Cash and Clark, 2010, Tee et al., 2017). Therefore, for electrochemical sensor applications, the proposed LST based LIFT has the potential to be utilized for fabricating electrodes.

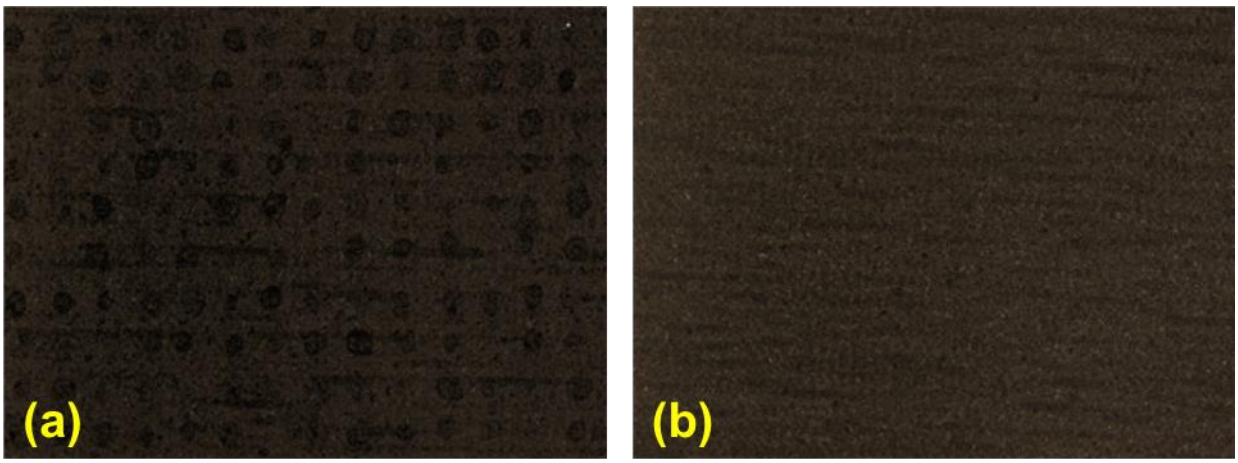

Fig. 4.29: Illustration of the center where surface roughness is determined for the Cu depositions made in LPEs. (a) with LST, and without LST.

In addition, Ag and Pt depositions made on Cu have been analyzed using the laser confocal microscope. Fig. 4.30 shows the presence of Ag and Pt both as additive layer and as micropillars. The additive layer presence is understood as the increase in the average value of the height shown in Fig. 4.29. Simultaneously, the broad peaks observed in Fig. 4.30(a) may possibly denote the presence of Ag micropillars which has been observed in the SEM images. However, for Pt, the deposition morphologies are more uniform cared to Ag. Furthermore, quantitative results can be interpreted to determine an approximate average thickness for the material layers. A height of 30 μm is approximated as the combined height of Ag layer and the micropillar, and a thickness of 15 μm for the Cu base layer.

doi:10.6342/NTU202301493

Simultaneously, Pt layer with the micropillar has a height of around 32 µm and the Cu base is determined to be around 17 µm.

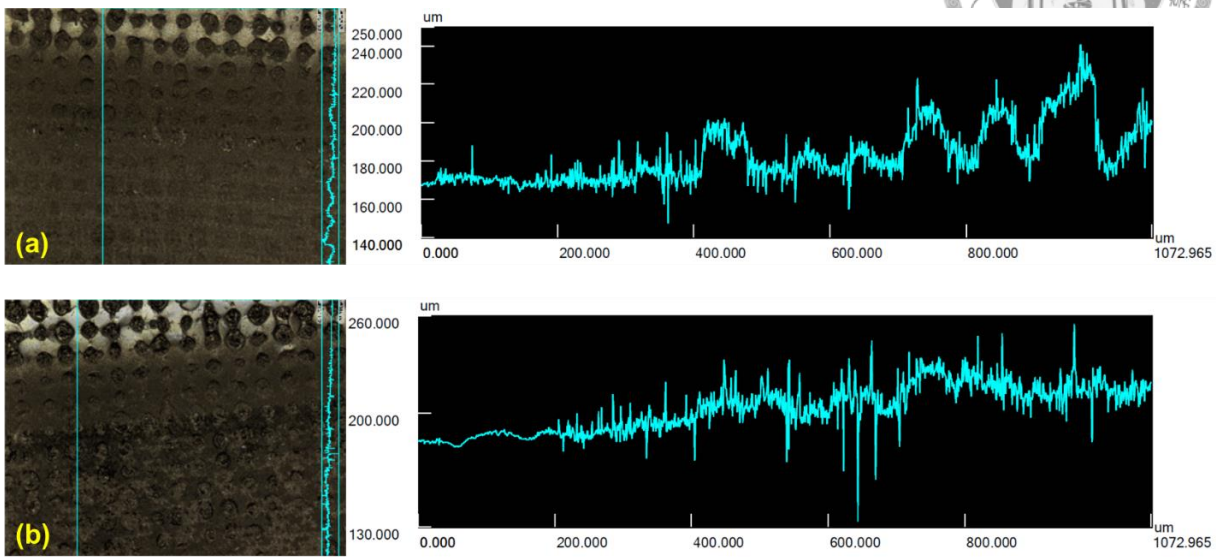

Fig. 4.30: Height difference results measured along a line (left) for (a) Ag and (b) Pt depositions made in LPEs, post Cu deposition on LST based receiver substrates.

4.5. Finite element method results

Laser heating of 1 µm Cu has been successfully carried out as per the procedure mentioned in the sections above (section 3.4) in reference to the research work of (Vora et al., 2013). Fig. 4.31 shows the temperature and isothermal contour of the Cu donor when irradiated with a laser fluence of 7390 Jm^{-2}. Subsequently, the FEM simulations for fluence values of 6660, 5920, 5180, 4440 and 3700 Jm^{-2} is made to determine the maximum temperature attained. Furthermore, Fig. 4.32 shows the temperature history of the 1 µm Cu donor under the said fluence magnitudes. Sharp cooling curves are observed from the temperature history curves, which is reasonable due to the thin film application. The maximum temperatures show a decreasing trend as the fluence is decreased which is also a reasonable observation. Subsequently, the theoretical and FEM based maximum temperatures are compared.

doi:10.6342/NTU202301493

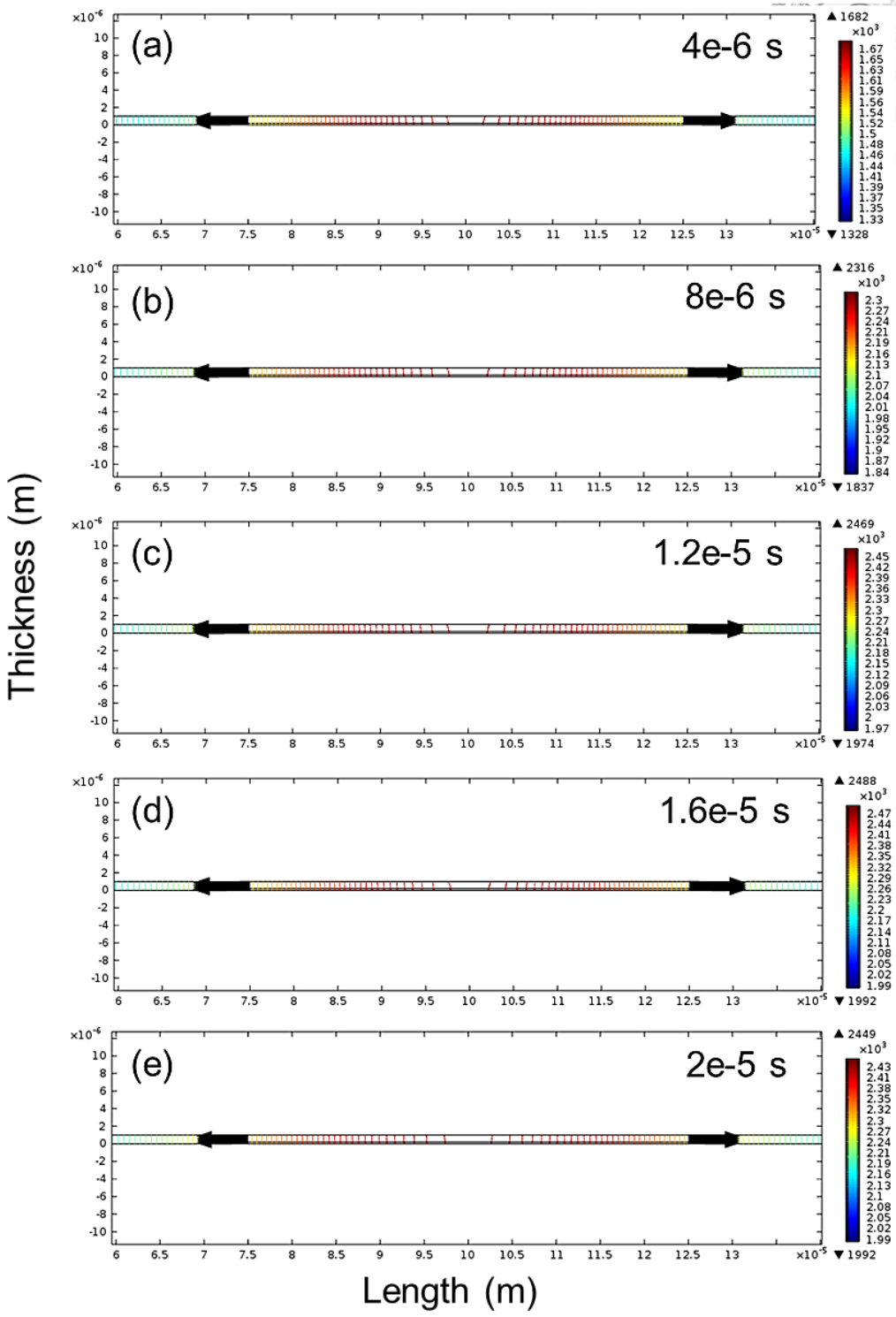

Fig. 4.31: Isotherm contours in 1 μm Cu thin film upon laser irradiation with fluence of 7390 Jm^{-2}.

doi:10.6342/NTU202301493

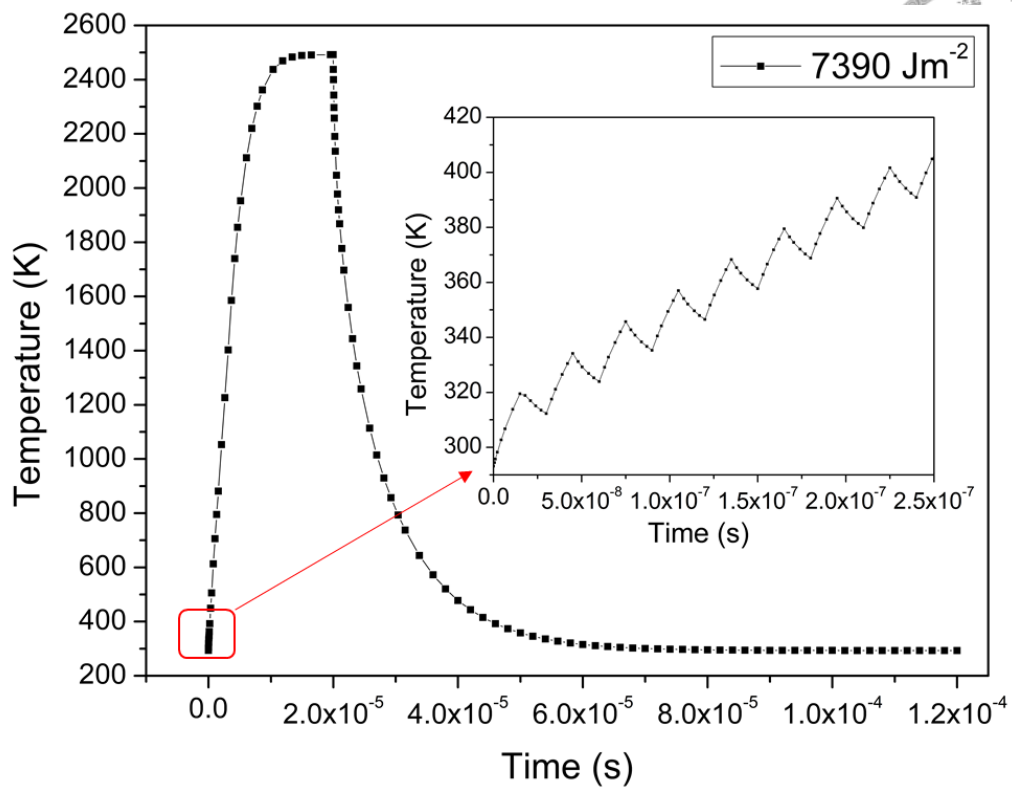

Fig. 4.32: Temperature history plot for 1 μm Cu under the fluences of 7390 Jm^{-2}.

After validating the model with relevant literature resources (Vora et al., 2013), simulations were made with the experimental parameters used for Cu-LIFT in this research. The theoretical temperature (T_{max}) was calculated using the equation proposed by Luo et al. (Luo et al., 2022),

$$T_{max} = T_0 + \frac{F}{\rho t_{film} C_l} - \frac{H_m}{C_l} \tag{4.1}$$

$$F = \frac{A_{abs} \times E_{pulse}}{A_{beam}} \tag{4.2}$$

where, T_{max} is the maximum working temperature (K), T_0 is the ambient temperature (K), F is the fluence (J/m^2), ρ is the density of solid copper approximated as 8960 kg/m^3. t_{film} is the copper film thickness i.e. 1 μm, C_l is the specific heat capacity of copper, approximated at 390 J/kg.K and H_m is the melting enthalpy of copper, calculated as 496.035 J/kg (Luo et al., 2022). A_{abs} is the absorptivity of copper (~0.45), and A is the beam area (~2.16×10^{-9}) derived from the beam diameter (~52.5 μm). The ambient temperature (T_0) is assumed to be 298 K.

doi:10.6342/NTU202301493

Table 4.14: Theoretical and simulation of the maximum temperature attained due to laser irradiation on Cu thin film.

Pulse energy (E_{pulse}) (J)×10^{-6}	**Fluence (F) (J/m^2) ×10^3**	**Theoretical temperature (T_{max}) (K)**	**FEM temperature (T_{FEM}) (K)**
40	7.39	2412.939	2491.50456
36	6.66	2201.318	2289.56635
32	5.92	1989.697	2017.2123
28	5.18	1778.076	1756.22848
24	4.44	1566.455	1563.6022
20	3.70	1354.833	1344.84641

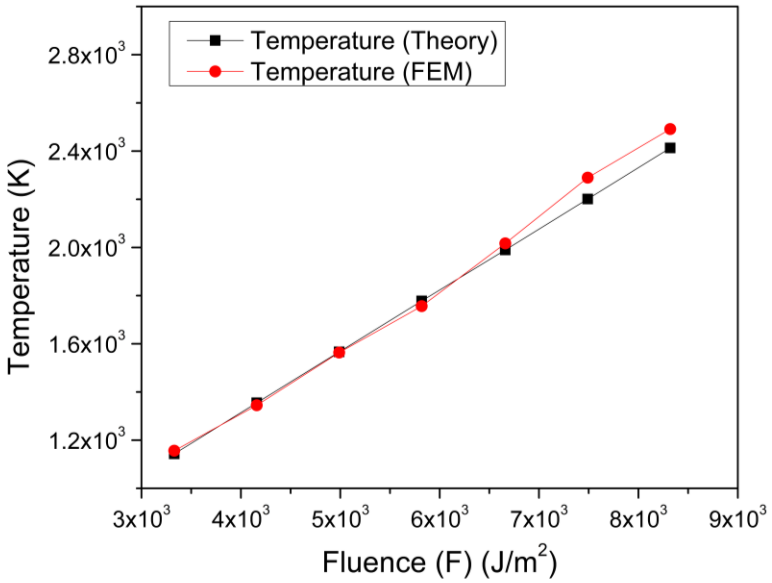

Fig. 4.33: Theoretical and FEM estimated maximum temperature for 1 μm Cu donor.

Following the heating model, the transfer phenomena of LIFT is simulated. Fig. 4.34 shows the preliminary results of the transfer process. For the preliminary investigations, transfer is simulated in accordance to the parameters mentioned in the work of Feinaeugle et al. (Feinaeugle et al., 2018). Where a material droplet is ejected from the donor and falls on the substrate under the influence of gravity. The ejected is facilitated through an applied pressure, and as time progresses, the donor material is seen to be deformed and transferred on to the

doi:10.6342/NTU202301493

receiver. In this research the phase field method is being used to simulate the transfer process accurately when parameters like the pressure magnitude and wetted wall characteristics (contact angle) to be carefully determined.

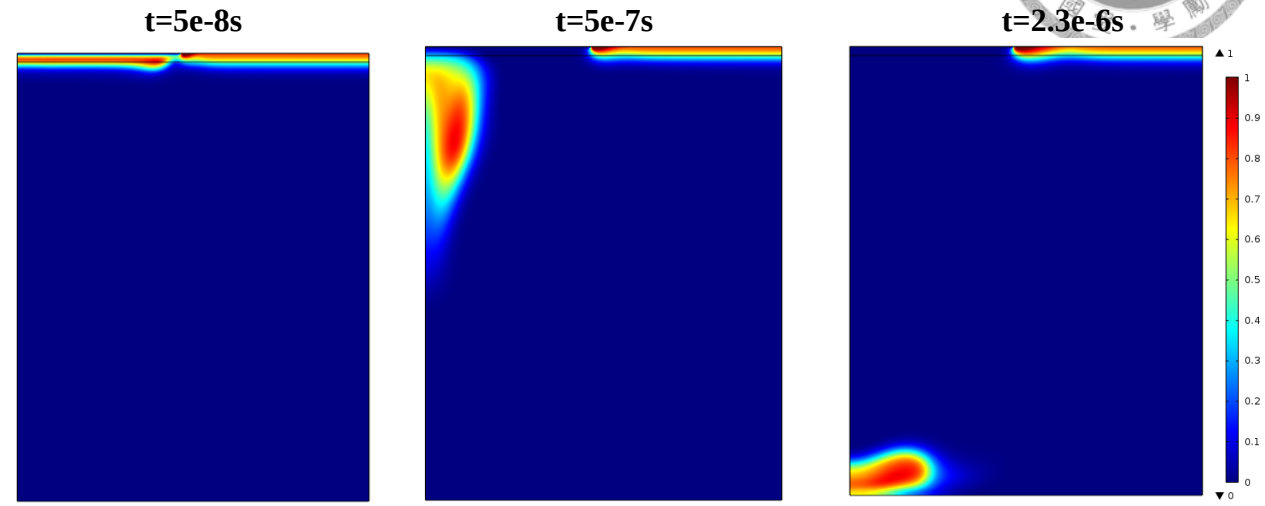

(a)

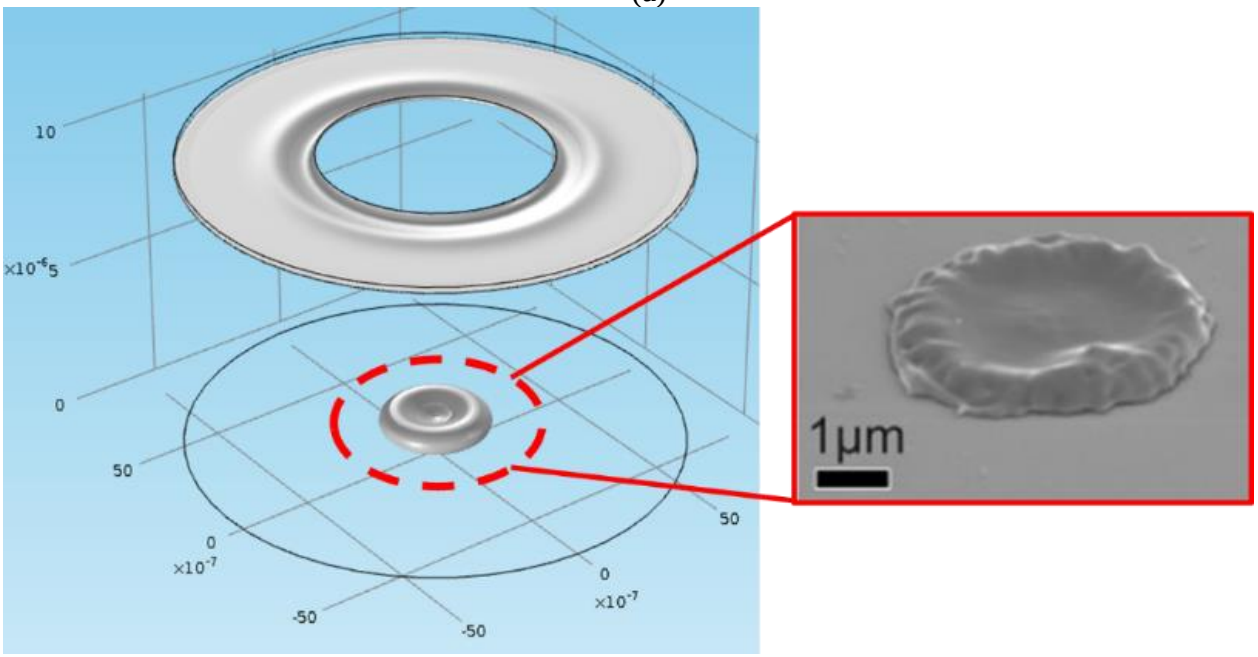

(b)

Fig. 4.34: Preliminary results of the transfer process (Blue: air, Red: Cu). (a)Time lapse illustration of volume fraction of the transfer process, (b) droplet shape compared to past literature (inset) (Feinaeugle et al., 2018).

doi:10.6342/NTU202301493

Accurate modelling of the LIFT process can open numerous avenues to higher research and process optimizations. With the simulation of thin film heating, control can be achieved in terms of temperature, by not losing excess material due to vaporization (excess heating/temperature). In addition, the heating simulations act as an input for the transfer simulations, as the pressure input in the transfer simulations are directly dependent on the temperatures obtained in the heating simulation. Higher temperatures imply higher material vaporization at the top leading to higher vapor pressure. Transfer simulations can assist in optimizations of process parameters like donor acceptor substrate distance for smooth transfer. An attempt to simulate the solidification and deposition geometry of the deposited voxel can enable us to determine the deposition/layer thickness. Finally, the aforementioned simulations are intended to be validated by experimentations or relevant literature resources. The velocities obtained in the simulations were compared with the theoretical results. According to Visser et al. (Visser et al., 2015) ejection velocity (V_{ej}) can be given as:

$$V_{ej} = \sqrt{\sigma(\rho h)^{-1}} \tag{4.3}$$

where σ is the viscosity, ρ is the density and h are the film thickness of copper. σ and ρ are functions of temperature (Assael et al., 2010, Kumykov et al., 2017, Harrison et al., 1977, Chekhovskoi et al., 2000). Additionally the authors (Visser et al. (Visser et al., 2015)) assumed that the ejection velocity (V_{ej}) is equal to the impact velocity, which means, they neglected the effects of drag and shockwaves generated in normal ambient conditions. For this analysis, density for liquid copper is given by the function:

$$\rho_{Cu} = c_1 - c_2(T - T_{ref}) \tag{4.4}$$

Where, c_1 is 7997 kgm^{-3}, c_2 is 0.819 kgm^{-3}K^{-1}, and T_{ref} is approximated as 1357.77 K (melting temperature of Cu). Subsequently, density of solid copper is fixed at 8960 kgm^{-3}. Furthermore, the surface tension (N/m) is given by the function:

$$\sigma_{Cu} = 1497 - 0.174(T) \tag{4.5}$$

where T is the working temperature (or T_{max}) derived from the work of Luo et al. (Luo et al., 2022).

doi:10.6342/NTU202301493

Table 4.15: Simulation velocity vs ejection velocity, as calculated theoretically by Visser et al. (Visser et al., 2015).

Fluence (F) (J/m^2) $\times 10^3$	Density (Kg/m^3)		Surface Tension (N/m)		Ejection velocity (m/s)	
	Theory (ρ_{Cu})	FEM (ρ'_{Cu})	Theory (σ_{Cu})	FEM (σ'_{Cu})	Theory (V_{ej})	FEM (V'_{ej})
7.39	7132.81	7068.47	1.0771	1.0634	12.21017	12.2681
6.66	7306.13	7233.85	1.1139	1.0986	12.28111	12.2682
5.92	7479.45	7456.91	1.1507	1.1460	12.34789	12.2682
5.18	7652.76	7670.66	1.1876	1.1914	12.41087	12.2683
4.44	7826.08	7828.42	1.2244	1.2249	12.47036	12.2683
3.70	7999.40	8007.58	1.2612	1.2629	12.52665	12.2684

According to the simulations, the ejection velocity is quite close to the theoretical velocity as mentioned by Visser et al. (Visser et al., 2015) in their work. However, a number of considerations must be taken when considering the energy balance analysis. This is because the velocity of ejection often influences the kinetic energy, which is dependent on the fluence of the laser. Since fluence controls the temperature rise in the film material, and the temperature is responsible for determining the dominant mechanism influencing the kinetic energy. For example, in Luo et al.'s (Luo et al., 2022) work, they discussed how surface energy which includes surface tension force is dominant for transfer in molten state and subsequently, thermal elastic energy (which includes thermal compressive stress relaxation) and interfacial binding energy is responsible for transfer in solid state. In addition, temperatures above the boiling point should lead to vaporization of the material and make vapor pressure as the dominant transfer initiator, contributing to the kinetic energy.

Considering the above discussion, an argument can be made for the ejection velocities obtained for the experiments. Since the predominant mechanism of the transfer is through melting, the flyer material has almost similar velocities, with slight variations. To support this argument, FESEM images of the donor substrate has been made, and clear evidence of resolidification is observed at the edges of the ablated region (see Fig. 4.35).

doi:10.6342/NTU202301493

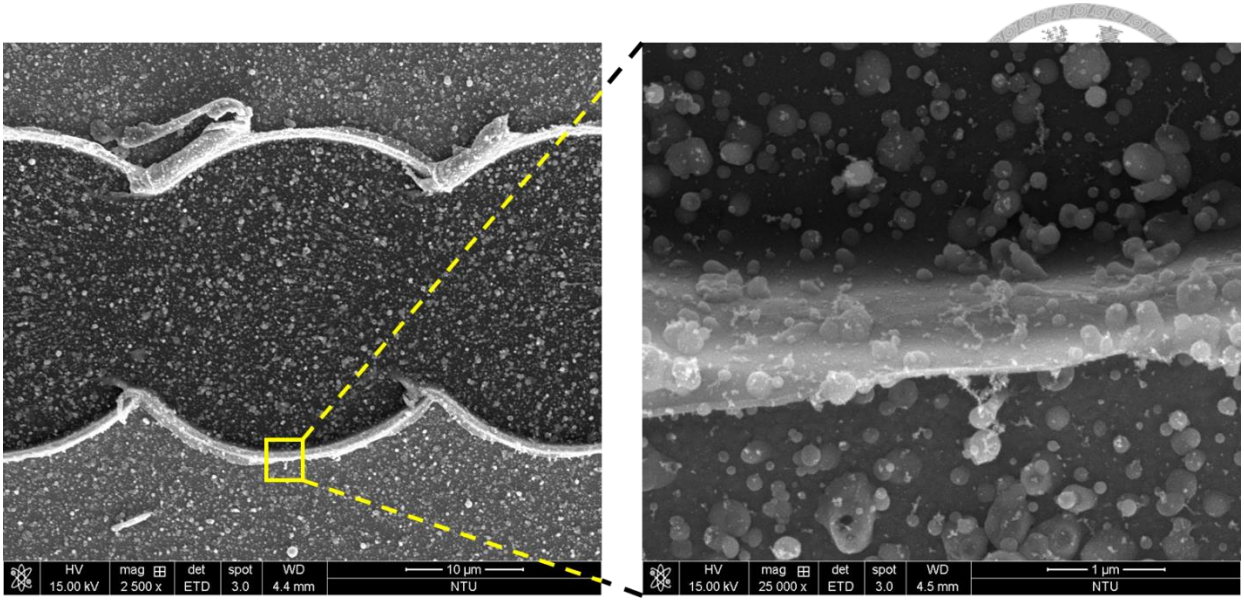

Fig. 4.35: FESEM of ablation region on 1µm Cu donor with the optimized LIFT parameters (Laser power: 2 W, frequency: 50 kHz, scan rate: 1300 mm/s, pitch 0.02 mm, pulse width: 15 ns).

4.6. Energy analysis

As described in the sections above, the LIFT process has complex transfer mechanisms, which are highly process parameter dependent. Therefore, to understand and gain insights on the energy conversions in the LIFT process, theoretical estimations are made with reference to equations illustrated in sections 3.3.3 and 3.5. The proposed energy balance equation is given as:

$$E_a = E_{in} + E_k + E_{ib} + E_f + E_{SW} + E_{loss} \quad (4.6)$$

Relevant equations were utilized to determine the respective energies mentioned in the proposed energy balance equations for various fluences. The experimental findings for the dimensions of the ablation diameter (d), ablation area (a), average power (P), pulse energy ($P.E$), fluence (F), and absorbed energy (E_a) is given in Table 4.16. Parameters such as beam diameter (D), beam area (A), frequency (f), pulse width (P_w), absorptivity (A) are kept constant.

doi:10.6342/NTU202301493

Table 4.16: Variable input parameters.

Ablation diameter (d) (m) × 10^{-5}	**Voxel area / Ablation area (a) (m^2) × 10^{-10}**	**Average power (P) (W)**	**Pulse energy ($P.E$) (J) × 10^{-5}**	**Fluence (F) (J/m^2) × 10^3**	**Absorbed energy (E_a) (J) × 10^{-6}**
1.80	2.54	2.00	4.00	7.39	1.88
1.72	2.31	1.80	3.60	6.66	1.54
1.65	2.12	1.60	3.20	5.92	1.26
1.60	2.01	1.40	2.80	5.18	1.04
1.57	1.94	1.20	2.40	4.44	0.86
1.431	1.61	1.00	2.00	3.70	0.59

A major part of the energy analysis includes the calculation of the shockwave energy. The shockwave energy has been efficiently approximated using analytical equations and calculated from the FEM model made in COMSOL. To determine the shockwave energy, the debris energy and the gas energy is calculated. For FEM based results, the parameters C_4 and C_5 are calculated numerically from their respective equations (see section 3.3.3). Subsequently, the parameter "x" is estimated from the data extracted from the COMSOL model. Table 4.17 shows the evolution of the shockwave energy (E_{sw}) with variation in fluence (F). Simultaneously, during the theoretical approximations, the position at which the shockwave energy (debris and gas) is determined and is kept similar to that obtained for FEM. Results obtained from the theoretical and FEM analysis for the shock wave energy has some dissimilarity. Since analytical results require experimental values for the position, and we do not have them, we assumed the location of the shockwave in FEM and theoretical analysis to be the same. This assumption may have led to the dissimilarity in the results since the equations utilized in the theoretical and the FEM analysis are different.

doi:10.6342/NTU202301493

Table 4.17: Shockwave energy results with variation in fluence.

Fluence (F) (J/m^2) $\times 10^3$	Debris energy		Gas energy		Shockwave Energy	
	Theory (E_{debris}) (J) $\times 10^{-11}$	FEM (E'_{debris}) (J) $\times 10^{-11}$	Theory (E_{gas}) (J) $\times 10^{-12}$	FEM (E'_{gas}) (J) $\times 10^{-12}$	Theory (E_{sw}) (J) $\times 10^{-10}$	FEM (E_{sw}) (J) $\times 10^{-10}$
7.39	619	1.17	1.12	692	61.8	7.05
6.66	640	1.09	1.13	665	63.9	6.77
5.92	661	1.03	1.14	645	66.1	6.56
5.18	682	1.01	1.15	628	68.2	6.38
4.44	703	0.995	1.16	355	70.3	3.66
3.70	724	0.841	1.17	313	72.4	3.22

Fig 4.36 illustrates the overall energy distribution with variation in fluence. The theoretical results show lower internal energy and higher energy (heat) loss approximations compared to the FEM results as shown in Fig. 4.36. However, both the theoretical and the FEM results show that the majority of the absorbed energy is converted into internal energy, and lost (as heat losses). Furthermore, additional energies such as the interfacial binding energy, shockwave energy, fracture energy are negligible compared to the internal and heat losses (see Fig. 4.36 and Table 4.18). The major and minor energies are illustrated in Figs. 4.37 and 4.38 respectively.

doi:10.6342/NTU202301493

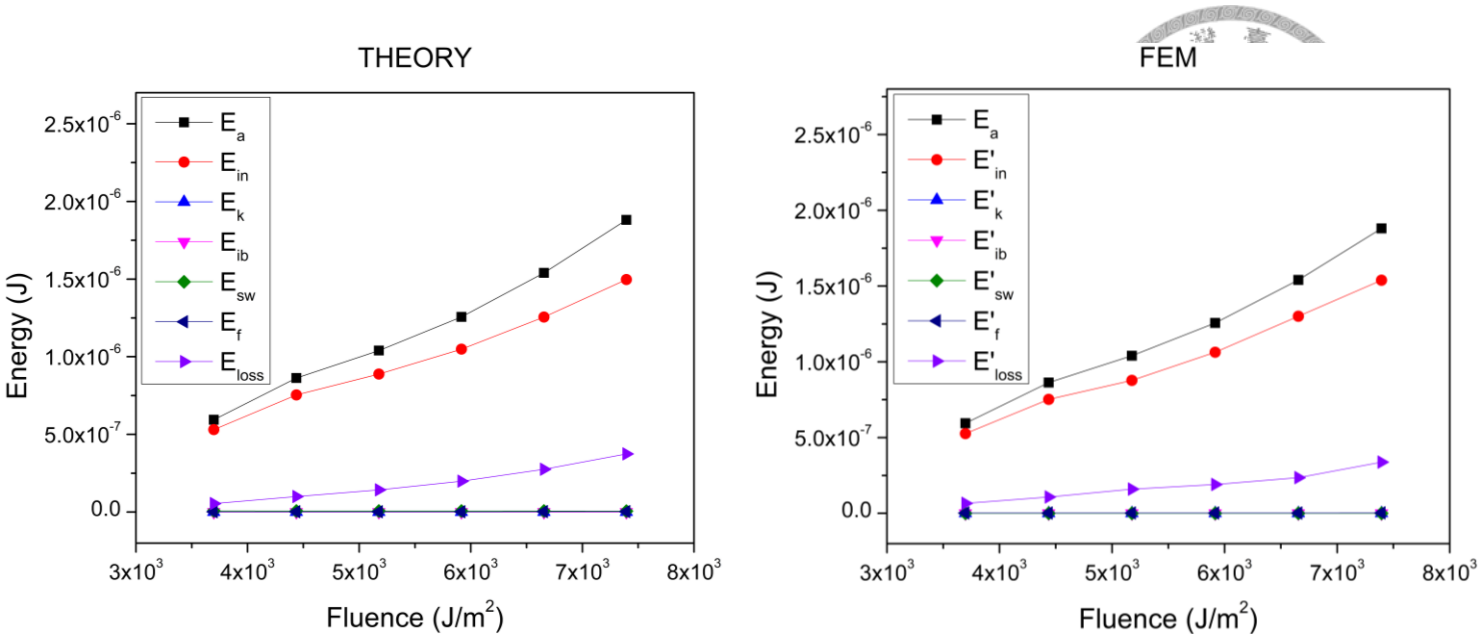

(a) (b)

Fig. 4.36: Comparing (a) theoretical and (b) FEM based energy distribution.

Table 4.18: Theoretical and FEM based estimation for internal energy, kinetic energy, interfacial binding energy, fracture energy and energy losses.

Fluence (F) (J/m^2) × 10^3	**Internal Energy**		**Kinetic Energy**		**Interfacial binding Energy (E_{ib}) (J) × 10^{-10}**	**Fracture Energy (E_f) (J) × 10^{-9}**	**Other losses**	
	Theory (E_{in}) (J) × 10^{-6}	**FEM (E'_{in}) (J) × 10^{-6}**	**Theory (E_k) (J) × 10^{-10}**	**FEM (E_k) (J) × 10^{-10}**			**Theory (E_{loss}) (J) × 10^{-7}**	**FEM (E'_{loss}) (J) × 10^{-7}**
7.39	1.49	1.62	1.43	1.37	5.09	2.54	3.74	2.50
6.66	1.25	1.35	1.35	1.27	4.63	2.31	2.75	1.80
5.92	1.05	1.12	1.28	1.20	4.25	2.12	1.98	1.28
5.18	0.88	0.94	1.25	1.16	4.02	2.01	1.42	9.52
4.44	0.75	0.78	1.25	1.15	3.89	1.94	0.99	7.62
3.70	0.53	0.53	1.06	0.96	3.21	1.61	0.54	0.53

doi:10.6342/NTU202301493

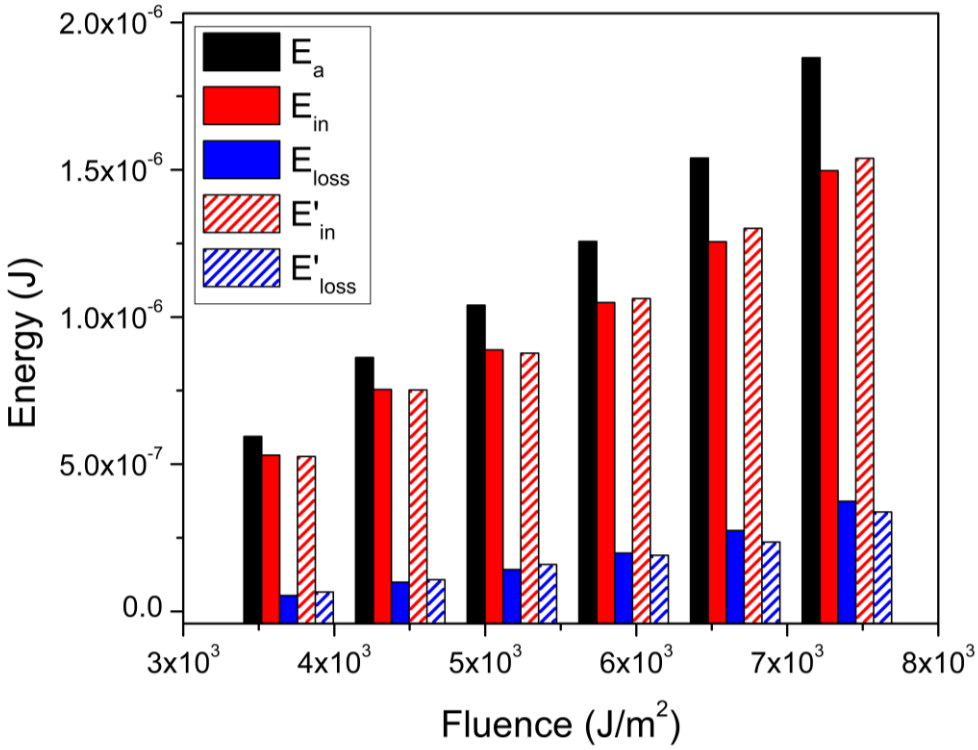

Fig. 4.37: Illustration of the absorbed energy and its conversion to major energies (internal energy and heat losses).

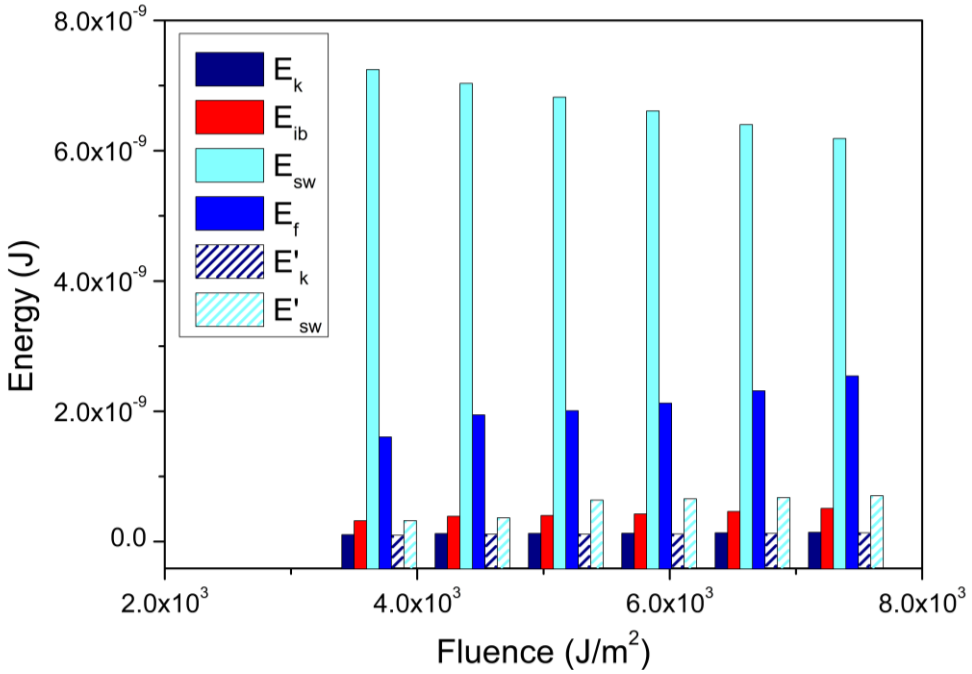

Fig. 4.38: Illustration of the minor energies (kinetic, interfacial binding, shockwave and fracture).

doi:10.6342/NTU202301493

Finally, the other losses which are assumed to be heat losses are illustrated in Fig. 4.39. Heat losses through convection, conduction and radiation are expected to contribute to the heat losses. At the moment, detailed investigations on heat losses through experimental methods are out of the scope of this research. Slight deviations in theoretical and FEM results are observed, however these can be neglected, considering probable presence of experimental errors and approximate assumptions made during study.

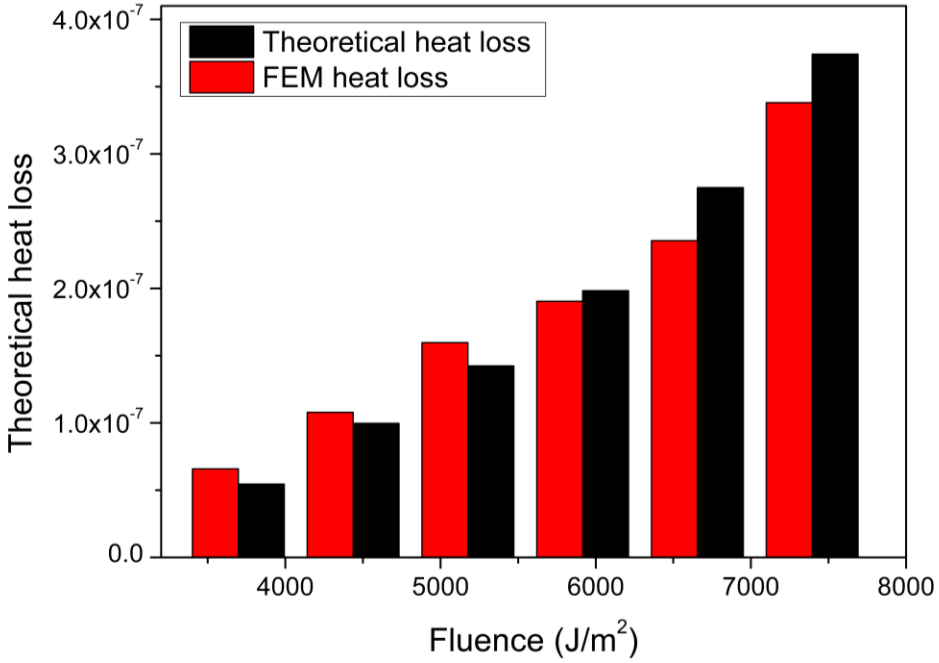

Fig. 4.39: Other losses (heat losses) obtained from the energy equations established through theoretical and FEM based calculations.

Considering the aforementioned results and discussion made, it can be inferred that there is a lot of scope for improvement in the LIFT process. This study carried out three important tasks: (i) address the LIFT challenges, (ii) determine the maximum temperature attained during laser heating, and (iii) predicted the mechanism and the contributing phenomena taking place. Experimental efforts have successfully mitigated challenges such as shockwaves, poor adhesion, etc. (see Table 4.19). Theoretical and FEM studies are carried out validating each other since experimental validation is time consuming, expensive and out of scope for this research at the moment. Finally, energy analysis has provided greater insights on the phenomena affecting the LIFT process. With the energy analysis results, researchers will know which factors and their contributing (process) parameters can be tuned

doi:10.6342/NTU202301493

to achieve a highly efficient process. Finally, Table 4.19 puts forward a brief overview summarizing the problems addressed, efforts made to mitigate them and the results of the study

Table 4.19: Overview of the work and its important highlights.

Problem determined	Efforts made	Prominent inferences
LIFT process challenges: • High resistance. • Shockwaves. • Poor adhesion. • Precision and accuracy.	• Suitable parameter determination. • Low-pressure environments. • Receiver surface modifications. • Utilize defocus techniques.	• Reduced resistance. • Improved adhesion. • Accurate and precise deposits. • Enabled fabrication of additive material layers and structures.
Determination of temperature and ejection velocity.	Theoretical and FEM analysis.	Theoretical and FEM results are fairly comparable.
Mechanism determination.	Energy analysis.	• Major energies: Internal energy and heat losses (E_{loss}). • Minor energies: Kinetic, interfacial binding, shockwave and fracture energy.

doi:10.6342/NTU202301493

Chapter 5 Conclusion and outlook

Successful efforts have been made to identify challenges associated to LIFT in additive manufacturing of metals. In addition, the possible mitigating techniques have been experimentally carried out and validated. The effective use of the proposed mitigating techniques enables additive manufacturing of multiple materials. Furthermore, theoretical and FEM based analysis of the LIFT process provides a greater insight on the transfer mechanism. Finally, energy analysis validates the proposed mechanism and helps in determining the major phenomena associated with the performed LIFT process. Consequently, a list of important inferences has been summarized as follows:

- Traditional LIFT process for printing conductive areal structures by using of continuous scan paths are limited by a number of factors such as shockwave formation, poor adhesion to substrate, and uniform morphology. The mentioned shortcomings also limit utilization of LIFT to print areal structures for additive manufacturing applications.
- Utilization of LST, LPEs, simultaneous change in donor-receiver substrate distance (L) and introduction of defocus has the potential to print multi material additive structures, while retaining the electrical properties such as conductivity.
- LIFT of Cu on PET shows enhanced adhesion and electrical conductivity for experiments with laser surface textured receiver substrates and low-pressure environments (LPE).
- Post successful Cu deposition, efforts have been made to successfully deposit Ag and Pt. The enhanced adhesion between Cu base layer and the receiver, enabled successful deposition of the Ag and Pt additive layer.
- Experimental evidence shows, thinner donors (500 nm Ag) show better electrical conductivity compared to thicker donors, due to the damage caused to the base (Cu) layer (as thick donor has higher flyer mass and thereby, momentum).
- Furthermore, to deposit additive layer micro pillars, a combination of simultaneously change in L (donor receiver distance) and defocus is utilized, along with the LST based receiver in LPE.

doi:10.6342/NTU202301493

- FESEM results show good deposition with minimum discontinuities for Cu depositions made by LIFT in LPEs. Additionally, low pressure conditions, enable higher resolution prints on the edges, since the flyer trajectory are not affected by the surrounding fluid (air).
- EDS results validate the presence of Cu, Ag and Pt depositions along with the successful deposition of the Ag and Pt micropillars.
- XRD results show that Cu oxidizes during the LIFT process. Cu_xO is observed for both LPE and air environments. The plausible reason for oxygen in LPE is sample is the exposure of the deposited material to ambient conditions post LIFT process.
- Confocal microscope results show the presence of higher material deposition for LIFT printed samples with LST based receivers in LPE conditions than the non-LST ones. Furthermore, the former shows higher surface roughness, which is helpful for the deposition of the subsequent additive material layers.
- Theoretical and FEM results for estimation of maximum temperature and are in line with each other.
- Energy analysis shows promising results. Theoretical and FEM based approximations for internal, kinetic, interfacial binding, fracture, shockwave and other loss energies are close to each other. Internal energy and the other energy losses are the majority energy consumers of the absorbed energy. Simultaneously, the kinetic, interfacial binding, fracture and shockwave energies are minor consumers of the absorbed energy.

doi:10.6342/NTU202301493

Reference

ADRIAN, F., BOHANDY, J., KIM, B., JETTE, A. N. & THOMPSON, P. 1987. A study of the mechanism of metal deposition by the laser-induced forward transfer process. *Journal of Vacuum Science & Technology B: Microelectronics Processing and Phenomena,* 5**,** 1490-1494.

ARDUINI, F., MICHELI, L., MOSCONE, D., PALLESCHI, G., PIERMARINI, S., RICCI, F. & VOLPE, G. 2016. Electrochemical biosensors based on nanomodified screen-printed electrodes: Recent applications in clinical analysis. *TrAC Trends in Analytical Chemistry,* 79**,** 114-126.

ASSAEL, M. J., KALYVA, A. E., ANTONIADIS, K. D., MICHAEL BANISH, R., EGRY, I., WU, J., KASCHNITZ, E. & WAKEHAM, W. A. 2010. Reference data for the density and viscosity of liquid copper and liquid tin. *Journal of Physical and Chemical Reference Data,* 39**,** 033105.

ASTM, S. 2009. Standard test methods for measuring adhesion by tape test. *Annu. B. ASTM Stand,* 6**,** 1-8.

BACK, S. & KANG, B. 2018. Low-cost optical fabrication of flexible copper electrode via laser-induced reductive sintering and adhesive transfer. *Optics and Lasers in Engineering,* 101**,** 78-84.

BANKS, D. P., GRIVAS, C., ZERGIOTI, I. & ROBERT, W. E. 2008. Ballistic laser-assisted solid transfer (BLAST) from a thin film precursor. *Optics Express,* 16**,** 3249-3254.

BANKS, D. P., KAUR, K. & EASON, R. W. 2009. Influence of optical standing waves on the femtosecond laser-induced forward transfer of transparent thin films. *Applied optics,* 48**,** 2058-2066.

BENNETT, J. M. & ASHLEY, E. 1965. Infrared reflectance and emittance of silver and gold evaporated in ultrahigh vacuum. *Applied Optics,* 4**,** 221-224.

BERG, Y., ZENOU, M., DOLEV, O. & KOTLER, Z. 2015. Temporal pulse shaping for smoothing of printed metal surfaces. *Optical Engineering,* 54**,** 011010-011010.

BIONDI, M. A. 1956. Optical absorption of copper and silver at 4.2 K. *Physical review,* 102**,** 964.

BIRNBAUM, A. J., KIM, H., CHARIPAR, N. A. & PIQUÉ, A. 2010. Laser printing of multi-layered polymer/metal heterostructures for electronic and MEMS devices. *Applied Physics A,* 99**,** 711-716.

BOHANDY, J., KIM, B. & ADRIAN, F. 1986. Metal deposition from a supported metal film using an excimer laser. *Journal of Applied Physics,* 60**,** 1538-1539.

BONCIU, A. F., ANDREI, F. & PALLA-PAPAVLU, A. 2023. Fabrication of Hybrid Electrodes by Laser-Induced Forward Transfer for the Detection of Cu2+ Ions. *Materials,* 16**,** 1744.

BOSE, S., SARKAR, N., VAHABZADEH, S., KE, D. & BANDYOPADHYAY, A. 2019. Additive manufacturing of ceramics. *Additive Manufacturing.* CRC Press.

BOUTOPOULOS, C., TOULOUPAKIS, E., PEZZOTTI, I., GIARDI, M. T. & ZERGIOTI, I. 2011. Direct laser immobilization of photosynthetic material on screen printed electrodes for amperometric biosensor. *Applied Physics Letters,* 98**,** 093703.

BRASZ, C. F. 2015. *Liquid jet formation in laser-induced forward transfer.* Princeton University.

doi:10.6342/NTU202301493

BRECKENFELD, E., KIM, H., AUYEUNG, R., CHARIPAR, N., SERRA, P. & PIQUÉ, A. 2015. Laser-induced forward transfer of silver nanopaste for microwave interconnects. *Applied Surface Science,* 331**,** 254-261.

BRECKENFELD, E., KIM, H., AUYEUNG, R. C. & PIQUÉ, A. 2016. Laser-induced forward transfer of Ag nanopaste. *Journal of Visualized Experiments: JoVE*.

BRITLAND, S., PEREZ-ARNAUD, E., CLARK, P., MCGINN, B., CONNOLLY, P. & MOORES, G. 1992. Micropatterning proteins and synthetic peptides on solid supports: a novel application for microelectronics fabrication technology. *Biotechnology progress,* 8**,** 155-160.

BROWN, M. S., BRASZ, C. F., VENTIKOS, Y. & ARNOLD, C. B. 2012. Impulsively actuated jets from thin liquid films for high-resolution printing applications. *Journal of Fluid Mechanics,* 709**,** 341-370.

CASH, K. J. & CLARK, H. A. 2010. Nanosensors and nanomaterials for monitoring glucose in diabetes. *Trends in molecular medicine,* 16**,** 584-593.

CHAKRABORTY, S., SAKATA, H., YOKOYAMA, E., WAKAKI, M. & CHAKRAVORTY, D. 2007. Laser-induced forward transfer technique for maskless patterning of amorphous V2O5 thin film. *Applied Surface Science,* 254**,** 638-643.

CHANDRA, R., SINGH, S. & GUPTA, K. 1999. Damping studies in fiber-reinforced composites–a review. *Composite structures,* 46**,** 41-51.

CHARIPAR, K. M., DÍAZ-RIVERA, R. E., CHARIPAR, N. A. & PIQUÉ, A. Laser-induced forward transfer (LIFT) of 3D microstructures. Laser 3D Manufacturing V, 2018. SPIE, 101-106.

CHATZIPETROU, M., TSEKENIS, G., TSOUTI, V., CHATZANDROULIS, S. & ZERGIOTI, I. 2013. Biosensors by means of the laser induced forward transfer technique. *Applied surface science,* 278**,** 250-254.

CHEKHOVSKOI, V. Y., TARASOV, V. D. & GUSEV, Y. V. 2000. Calorific properties of liquid copper. *High Temperature,* 38**,** 394-399.

CHEN, Z., MOCHIZUKI, D., MAITANI, M. M. & WADA, Y. 2013. Facile synthesis of bimetallic Cu–Ag nanoparticles under microwave irradiation and their oxidation resistance. *Nanotechnology,* 24**,** 265602.

CULLEN, D., SETHI, R. & LOWE, C. 1990. Multi-analyte miniature conductance biosensor. *Analytica Chimica Acta,* 231**,** 33-40.

D'AMICO, A. & DI NATALE, C. 2001. A contribution on some basic definitions of sensors properties. *IEEE Sensors Journal,* 1**,** 183-190.

D-17, A. 2017. Standard test methods for rating adhesion by tape test. ASTM international West Conshohocken, PA, USA.

DE GANS, B. J. & SCHUBERT, U. S. 2003. Inkjet printing of polymer micro-arrays and libraries: Instrumentation, requirements, and perspectives. *Macromolecular Rapid Communications,* 24**,** 659-666.

DELAPORTE, P. & ALLONCLE, A.-P. 2016. Laser-induced forward transfer: A high resolution additive manufacturing technology. *Optics & Laser Technology,* 78**,** 33-41.

DEMIN, M., KOROLEVA, O., ALEKSASHKINA, A. & MAZHUKIN, V. 2020. Molecular-dynamic modeling of thermophysical properties of phonon subsystem of copper in wide temperature range. *Math. Montis,* 47**,** 137-151.

doi:10.6342/NTU202301493

DI PIETRANTONIO, F., BENETTI, M., CANNATÀ, D., VARRIALE, A., D'AURIA, S., PALLA-PAPAVLU, A., SERRA, P. & VERONA, E. Surface acoustic wave biosensor based on odorant binding proteins deposited by laser induced forward transfer. 2013 IEEE International Ultrasonics Symposium (IUS), 2013a. IEEE, 2144-2147.

DI PIETRANTONIO, F., BENETTI, M., CANNATÀ, D., VERONA, E., PALLA-PAPAVLU, A., DINCA, V., DINESCU, M., MATTLE, T. & LIPPERT, T. 2012. Volatile toxic compound detection by surface acoustic wave sensor array coated with chemoselective polymers deposited by laser induced forward transfer: Application to sarin. *Sensors and Actuators B: Chemical,* 174**,** 158-167.

DI PIETRANTONIO, F., CANNATÀ, D., BENETTI, M., VERONA, E., VARRIALE, A., STAIANO, M. & D'AURIA, S. 2013b. Detection of odorant molecules via surface acoustic wave biosensor array based on odorant-binding proteins. *Biosensors and Bioelectronics,* 41**,** 328-334.

DINCA, V., FARSARI, M., KAFETZOPOULOS, D., POPESCU, A., DINESCU, M. & FOTAKIS, C. 2008. Patterning parameters for biomolecules microarrays constructed with nanosecond and femtosecond UV lasers. *Thin Solid Films,* 516**,** 6504-6511.

DING, X., ZOU, Y., YE, F., YANG, J. & JIANG, J. 2013. Pt–CuS heterodimers by sulfidation of CuPt alloy nanoparticles and their selective catalytic activity toward methanol oxidation. *Journal of Materials Chemistry A,* 1**,** 11880-11886.

DORAISWAMY, A., NARAYAN, R., LIPPERT, T., URECH, L., WOKAUN, A., NAGEL, M., HOPP, B., DINESCU, M., MODI, R. & AUYEUNG, R. 2006. Excimer laser forward transfer of mammalian cells using a novel triazene absorbing layer. *Applied Surface Science,* 252**,** 4743-4747.

DUOCASTELLA, M., FERNÁNDEZ-PRADAS, J., MORENZA, J., ZAFRA, D. & SERRA, P. 2010. Novel laser printing technique for miniaturized biosensors preparation. *Sensors and Actuators B: Chemical,* 145**,** 596-600.

EHRLICH, D. J., HIGASHI, G. S. & OPRYSKO, M. M. 1988. Laser and particle-beam chemical processing for microelectronics.

FARDEL, R., NAGEL, M., NUESCH, F., LIPPERT, T. & WOKAUN, A. 2010. Laser-induced forward transfer of organic LED building blocks studied by time-resolved shadowgraphy. *The Journal of Physical Chemistry C,* 114**,** 5617-5636.

FARDEL, R., NAGEL, M., NÜESCH, F., LIPPERT, T. & WOKAUN, A. 2007. Fabrication of organic light-emitting diode pixels by laser-assisted forward transfer. *Applied Physics Letters,* 91**,** 061103.

FARDEL, R., NAGEL, M., NÜESCH, F., LIPPERT, T. & WOKAUN, A. 2009a. Shadowgraphy investigation of laser-induced forward transfer: Front side and back side ablation of the triazene polymer sacrificial layer. *Applied Surface Science,* 255**,** 5430-5434.

FARDEL, R., NAGEL, M., NÜESCH, F., LIPPERT, T. & WOKAUN, A. 2009b. Energy balance in a laser-induced forward transfer process studied by shadowgraphy. *The Journal of Physical Chemistry C,* 113**,** 11628-11633.

FEINAEUGLE, M., ALLONCLE, A., DELAPORTE, P., SONES, C. & EASON, R. 2012. Time-resolved shadowgraph imaging of femtosecond laser-induced forward transfer of solid materials. *Applied surface science,* 258**,** 8475-8483.

doi:10.6342/NTU202301493

FEINAEUGLE, M., GREGORČIČ, P., HEATH, D., MILLS, B. & EASON, R. 2017. Time-resolved imaging of flyer dynamics for femtosecond laser-induced backward transfer of solid polymer thin films. *Applied Surface Science,* 396**,** 1231-1238.

FEINAEUGLE, M., POHL, R., BOR, T., VANEKER, T. & RÖMER, G.-W. 2018. Printing of complex free-standing microstructures via laser-induced forward transfer (LIFT) of pure metal thin films. *AddItive manufacturing,* 24**,** 391-399.

FERNÁNDEZ-PRADAS, J., DUOCASTELLA, M., COLINA, M., SERRA, P. & MORENZA, J. Production of miniaturized biosensors through laser-induced forward transfer. Bioengineered and Bioinspired Systems III, 2007. SPIE, 281-288.

FLORIAN, C., CABALLERO-LUCAS, F., FERNÁNDEZ-PRADAS, J., ARTIGAS, R., OGIER, S., KARNAKIS, D. & SERRA, P. 2015. Conductive silver ink printing through the laser-induced forward transfer technique. *Applied Surface Science,* 336**,** 304-308.

FLORIAN, C. & SERRA, P. 2023. Printing via laser-induced forward transfer and the future of digital manufacturing. *Materials,* 16**,** 698.

FREIWALD, D. & AXFORD, R. A. 1975. Approximate spherical blast theory including source mass. *Journal of Applied Physics,* 46**,** 1171-1174.

FUJISAWA, K., OHKI, M. & FUJISAWA, N. 2019. Influence of surface roughness on liquid droplet impingement erosion. *Wear,* 432**,** 202955.

FUJISAWA, K., YAMAGATA, T. & FUJISAWA, N. 2018. Liquid droplet impingement erosion on groove roughness. *Nuclear Engineering and Design,* 330**,** 368-376.

GAMELLA, M., CAMPUZANO, S., MANSO, J., DE RIVERA, G. G., LÓPEZ-COLINO, F., REVIEJO, A. & PINGARRÓN, J. 2014. A novel non-invasive electrochemical biosensing device for in situ determination of the alcohol content in blood by monitoring ethanol in sweat. *Analytica chimica acta,* 806**,** 1-7.

GERMAIN, C., CHARRON, L., LILGE, L. & TSUI, Y. Y. 2007. Electrodes for microfluidic devices produced by laser induced forward transfer. *Applied surface science,* 253**,** 8328-8333.

GHINDILIS, A. L., ATANASOV, P., WILKINS, M. & WILKINS, E. 1998. Immunosensors: electrochemical sensing and other engineering approaches. *Biosensors and Bioelectronics,* 13**,** 113-131.

GONZALEZ-MACIA, L., MORRIN, A., SMYTH, M. R. & KILLARD, A. J. 2010. Advanced printing and deposition methodologies for the fabrication of biosensors and biodevices. *Analyst,* 135**,** 845-867.

GORODESKY, N., SEDGHANI-COHEN, S., FOGEL, O., ALTMAN, M., COHEN-TAGURI, G., KOTLER, Z. & ZALEVSKY, Z. 2022. Printed Cu–Ag Phases Using Laser-Induced Forward Transfer. *Advanced Engineering Materials,* 24**,** 2100952.

GRANT-JACOB, J. A., MILLS, B., FEINAEUGLE, M., SONES, C. L., OOSTERHUIS, G., HOPPENBROUWERS, M. B. & EASON, R. W. 2013. Micron-scale copper wires printed using femtosecond laser-induced forward transfer with automated donor replenishment. *Optical Materials Express,* 3**,** 747-754.

HARRISON, D., YAN, D. & BLAIRS, S. 1977. The surface tension of liquid copper. *The Journal of Chemical Thermodynamics,* 9**,** 1111-1119.

HASENBANK, M. S., EDWARDS, T., FU, E., GARZON, R., KOSAR, T. F., LOOK, M., MASHADI-HOSSEIN, A. & YAGER, P. 2008. Demonstration of multi-analyte

doi:10.6342/NTU202301493

patterning using piezoelectric inkjet printing of multiple layers. *Analytica chimica acta,* 611**,** 80-88.
HE, J., JIANG, Y., PENG, J., LI, C., YAN, B. & WANG, X. 2016. Fast synthesis of hierarchical cuprous oxide for nonenzymatic glucose biosensors with enhanced sensitivity. *Journal of Materials Science,* 51**,** 9696-9704.
HESS, A., SCHUSTER, R., HEIDER, A., WEBER, R. & GRAF, T. 2011. Continuous wave laser welding of copper with combined beams at wavelengths of 1030 nm and of 515 nm. *Physics Procedia,* 12**,** 88-94.
HONEYCHURCH, K. C. 2012. Screen-Printed Electrochemical Biosensors and Sensors for Monitoring Metal Pollutants. *Insciences J.,* 2**,** 1-51.
HOPP, B., SMAUSZ, T., BARNA, N., VASS, C., ANTAL, Z., KREDICS, L. & CHRISEY, D. 2005. Time-resolved study of absorbing film assisted laser induced forward transfer of Trichoderma longibrachiatum conidia. *Journal of Physics D: Applied Physics,* 38**,** 833.
HOPP, B., SMAUSZ, T., SZABÓ, G., KOLOZSVÁRI, L., KAFETZOPOULOS, D., FOTAKIS, C. & NÓGRÁDI, A. 2012. Femtosecond laser printing of living cells using absorbing film-assisted laser-induced forward transfer. *Optical Engineering,* 51**,** 014302-014302.
HUANG, Y.-J., XIE, X.-Z., CUI, J.-Q. & LONG, J.-Y. 2023. Fabrication of high-performance copper circuits using laser-induced forward transfer with large receiving gaps based on beam modulation technology. *Journal of Manufacturing Processes,* 87**,** 54-64.
HUSSAIN, A., ABBAS, N. & ALI, A. 2022. Inkjet printing: a viable technology for biosensor fabrication. *Chemosensors,* 10**,** 103.
IVANOV, D. S., RETHFELD, B., O'CONNOR, G. M., GLYNN, T. J., VOLKOV, A. N. & ZHIGILEI, L. V. 2008. The mechanism of nanobump formation in femtosecond pulse laser nanostructuring of thin metal films. *Applied Physics A,* 92**,** 791-796.
JADIN, A., FILIOUGUINE, I. V., WAUTELET, M. & LAUDE, L. D. Plasma formation during excimer laser irradiation of thin selenium films in air. Laser-Assisted Processing II, 1990. SPIE, 112-117.
JALAAL, M., LI, S., KLEIN SCHAARSBERG, M., QIN, Y. & LOHSE, D. 2019. Destructive mechanisms in laser induced forward transfer. *Applied physics letters,* 114**,** 213703.
JAMES, J., SPITTLE, J., BROWN, S. & EVANS, R. 2001. A review of measurement techniques for the thermal expansion coefficient of metals and alloys at elevated temperatures. *Measurement science and technology,* 12**,** R1.
JIA, W., BANDODKAR, A. J., VALDÉS-RAMÍREZ, G., WINDMILLER, J. R., YANG, Z., RAMÍREZ, J., CHAN, G. & WANG, J. 2013. Electrochemical tattoo biosensors for real-time noninvasive lactate monitoring in human perspiration. *Analytical chemistry,* 85**,** 6553-6560.
KAMPFRATH, G. & HINTSCHE, R. 1989. Plasma-polymerized thin films for enzyme immobilization in biosensors. *Analytical letters,* 22**,** 2423-2431.
KANE, R. S., TAKAYAMA, S., OSTUNI, E., INGBER, D. E. & WHITESIDES, G. M. 1999. Patterning proteins and cells using soft lithography. *Biomaterials,* 20**,** 2363-2376.

doi:10.6342/NTU202301493

KÁNTOR, Z. & SZÖRÉNYI, T. 1995. Dynamics of long-pulse laser transfer of micrometer-sized metal patterns as followed by time-resolved measurements of reflectivity and transmittance. *Journal of applied physics,* 78**,** 2775-2781.
KANTOR, Z., TOTH, Z. & SZÖRÉNYI, T. 1995. Metal pattern deposition by laser-induced forward transfer. *Applied surface science,* 86**,** 196-201.
KÁNTOR, Z., TÓTH, Z. & SZÖRÉNYI, T. 1992. Laser induced forward transfer: The effect of support-film interface and film-to-substrate distance on transfer. *Applied Physics A,* 54**,** 170-175.
KÁNTOR, Z., TOTH, Z., SZÖRÉNYI, T. & TÓTH, A. 1994. Deposition of micrometer-sized tungsten patterns by laser transfer technique. *Applied physics letters,* 64**,** 3506-3508.
KATTAMIS, N. T., MCDANIEL, N. D., BERNHARD, S. & ARNOLD, C. B. 2011. Ambient laser direct-write printing of a patterned organo-metallic electroluminescent device. *Organic Electronics,* 12**,** 1152-1158.
KATTAMIS, N. T., PURNICK, P. E., WEISS, R. & ARNOLD, C. B. 2007. Thick film laser induced forward transfer for deposition of thermally and mechanically sensitive materials. *Applied Physics Letters,* 91**,** 171120.
KAUR, K., FARDEL, R., MAY-SMITH, T., NAGEL, M., BANKS, D., GRIVAS, C., LIPPERT, T. & EASON, R. 2009. Shadowgraphic studies of triazene assisted laser-induced forward transfer of ceramic thin films. *Journal of Applied Physics,* 105**,** 113119.
KAUR, K., FEINAEUGLE, M., BANKS, D., OU, J., DI PIETRANTONIO, F., VERONA, E., SONES, C. & EASON, R. 2011. Laser-induced forward transfer of focussed ion beam pre-machined donors. *Applied surface science,* 257**,** 6650-6653.
KAUR, K., MISSINNE, J. & VAN STEENBERGE, G. 2014. Flip-chip bonding of vertical-cavity surface-emitting lasers using laser-induced forward transfer. *Applied Physics Letters,* 104**,** 061102.
KHAIRULLINA, E. M., PANOV, M. S., ANDRIIANOV, V. S., RATAUTAS, K., TUMKIN, I. I. & RAČIUKAITIS, G. 2021. High rate fabrication of copper and copper–gold electrodes by laser-induced selective electroless plating for enzyme-free glucose sensing. *RSC advances,* 11**,** 19521-19530.
KIM, H., AUYEUNG, R., LEE, S., HUSTON, A. & PIQUÉ, A. 2009. Laser forward transfer of silver electrodes for organic thin-film transistors. *Applied Physics A,* 96**,** 441-445.
KIM, H., DUOCASTELLA, M., CHARIPAR, K., AUYEUNG, R. & PIQUÉ, A. 2013. Laser printing of conformal and multi-level 3D interconnects. *Applied Physics A,* 113**,** 5-8.
KLINI, A., LOUKAKOS, P., GRAY, D., MANOUSAKI, A. & FOTAKIS, C. 2008. Laser induced forward transfer of metals by temporally shaped femtosecond laser pulses. *Optics Express,* 16**,** 11300-11309.
KLONOFF, D. C. 1997. Noninvasive blood glucose monitoring. *Diabetes care,* 20**,** 433-437.
KONG, F.-Y., GU, S.-X., LI, W.-W., CHEN, T.-T., XU, Q. & WANG, W. 2014. A paper disk equipped with graphene/polyaniline/Au nanoparticles/glucose oxidase biocomposite modified screen-printed electrode: Toward whole blood glucose determination. *Biosensors and Bioelectronics,* 56**,** 77-82.
KONONENKO, T. V., ALLONCLE, P., KONOV, V. & SENTIS, M. 2009. Laser transfer of diamond nanopowder induced by metal film blistering. *Applied Physics A,* 94**,** 531-536.

doi:10.6342/NTU202301493

KUMYKOV, V., SERGEEV, I., SOZAEV, V. & GEDGAGOVA, M. 2017. Surface tension of copper in solid phase. *Bulletin of the Russian Academy of Sciences: Physics,* 81**,** 357-359.

KUZNETSOV, A., KIYAN, R. & CHICHKOV, B. 2010. Laser fabrication of 2D and 3D metal nanoparticle structures and arrays. *Optics express,* 18**,** 21198-21203.

LATIF, H., RAFIQUE, M. S., KHALEEQ-UR-RAHAMAN, M., SATTAR, A., ANJUM, S., USMAN, A., ZAHEER, S. & RAWAT, R. 2014. Surface modification of platinum by laser-produced X-rays. *Radiation Effects and Defects in Solids,* 169**,** 942-953.

LEVENE, M., SCOTT, R. & SIRYJ, B. 1970. Material transfer recording. *applied optics,* 9**,** 2260-2265.

LEVY, A., BERNSTEIN TOKER, G., WINTER, S., COHEN, S. S., ERMAK, O., PELED, I., KOTLER, Z. & GELBSTEIN, Y. 2021. Hybrid structural electronics printing by novel dry film stereolithography and laser induced forward transfer. *Nano Select,* 2**,** 979-991.

LI, Y. & CHING-YUE, W. 2009. Experimental study on microdeposition of the copper thin film by femtosecond laser-induced forward transfer. *Chinese Physics B,* 18**,** 4292.

LI, Y., ZHOU, X., CHEN, J., GUO, W., HE, S., GAO, S. & PENG, P. 2020. Laser-Patterned Copper Electrodes for Proximity and Tactile Sensors. *Advanced Materials Interfaces,* 7**,** 1901845.

LIM, J. H. & MIRKIN, C. A. 2002. Electrostatically driven dip-pen nanolithography of conducting polymers. *Advanced Materials,* 14**,** 1474-1477.

LIMITED, H. P. F. Available: https://www.hififilm.com/polyester-films/#:~:text=Polyester%20film%2C%20often%20referred%20to,thermal%20and%20electrical%20insulation%20properties [Accessed 1st February 2023].

LIN, Y., HUANG, G., HUANG, Y., JEREMY TZENG, T. R. & CHRISEY, D. 2010. Effect of laser fluence in laser-assisted direct writing of human colon cancer cell. *Rapid Prototyping Journal,* 16**,** 202-208.

LIN, Y., HUANG, Y., WANG, G., TZENG, T.-R. J. & CHRISEY, D. B. 2009. Effect of laser fluence on yeast cell viability in laser-assisted cell transfer. *Journal of Applied Physics,* 106**,** 043106.

LIU, D., CHEN, N., SONG, Y., SONG, X., SUN, J., TAN, C., LONG, W., ZHONG, S. & JIA, L. 2023. Mechanical and heat transfer properties of AlN/Cu joints based on nanosecond laser-induced metallization. *Journal of the European Ceramic Society,* 43**,** 1897-1903.

LIU, D., ZENG, Q., HU, C., CHEN, D., LIU, H., HAN, Y., XU, L., ZHANG, Q. & YANG, J. 2022. Light doping of tungsten into copper-platinum nanoalloys for boosting their electrocatalytic performance in methanol oxidation. *Nano Research Energy,* 1**,** e9120017.

LIU, H., LIU, Y., GUO, W., ZHOU, X., LIN, L. & PENG, P. 2020a. Laser assisted ink-printing of copper oxide nanoplates for memory device. *Materials Letters,* 261**,** 127097.

LIU, W., ZHU, K., WANG, C., ZHENG, Z., AN, R., ZHANG, W., ZHU, M., WEN, Z., WANG, X. & LIU, Y. 2020b. Laser induced forward transfer of brittle Cu3Sn thin film. *Journal of Manufacturing Processes,* 60**,** 48-53.

doi:10.6342/NTU202301493

LUO, G., WU, D., ZHOU, Y., HU, Y. & YAO, Z. 2022. Elucidating ejection regimes of metal microdroplets in voxel-based laser-induced forward transfer. *Additive Manufacturing,* 55**,** 102814.

MADDIPATLA, D., NARAKATHU, B. B. & ATASHBAR, M. 2020. Recent progress in manufacturing techniques of printed and flexible sensors: a review. *Biosensors,* 10**,** 199.

MAFUNÉ, F., KOHNO, J.-Y., TAKEDA, Y. & KONDOW, T. 2003. Formation of stable platinum nanoparticles by laser ablation in water. *The Journal of Physical Chemistry B,* 107**,** 4218-4223.

MAHMOOD, M. A. & POPESCU, A. C. 2021. 3D printing at micro-level: Laser-induced forward transfer and two-photon polymerization. *Polymers,* 13**,** 2034.

MAKRYGIANNI, M., VERRELLI, E., BOUKOS, N., CHATZANDROULIS, S., TSOUKALAS, D. & ZERGIOTI, I. 2013. Laser printing and characterization of semiconducting polymers for organic electronics. *Applied Physics A,* 110**,** 559-563.

MATHPAL, M. C., KUMAR, P., KUMAR, S., TRIPATHI, A. K., SINGH, M. K., PRAKASH, J. & AGARWAL, A. 2015. Opacity and plasmonic properties of Ag embedded glass based metamaterials. *RSC advances,* 5**,** 12555-12562.

MATSUMOTO, T., FUJII, H., UEDA, T., KAMAI, M. & NOGI, K. 2005. Measurement of surface tension of molten copper using the free-fall oscillating drop method. *Measurement Science and Technology,* 16**,** 432.

MATTLE, T., HINTENNACH, A., LIPPERT, T. & WOKAUN, A. 2013a. Laser induced forward transfer of SnO 2 for sensing applications using different precursors systems. *Applied Physics A,* 110**,** 309-316.

MATTLE, T., SHAW-STEWART, J., HINTENNACH, A., SCHNEIDER, C. W., LIPPERT, T. & WOKAUN, A. 2013b. Shadowgraphic investigations into the laser-induced forward transfer of different SnO2 precursor films. *Applied surface science,* 278**,** 77-81.

MATTLE, T., SHAW-STEWART, J., SCHNEIDER, C. W., LIPPERT, T. & WOKAUN, A. 2012. Laser induced forward transfer aluminum layers: Process investigation by time resolved imaging. *Applied surface science,* 258**,** 9352-9354.

MENEZES, V., TAKAYAMA, K., GOJANI, A. & HOSSEINI, S. 2008. Shock wave driven microparticles for pharmaceutical applications. *Shock Waves,* 18**,** 393-400.

MO, X., CHAN, K. & TSE, E. C. 2019. A scalable laser-assisted method to produce active and robust graphene-supported nanoparticle electrocatalysts. *Chemistry of Materials,* 31**,** 8230-8238.

MOGYORÓSI, P., SZÖRÉNYI, T., BALI, K., TÓTH, Z. & HEVESI, I. 1989. Pulsed laser ablative deposition of thin metal films. *Applied surface science,* 36**,** 157-163.

MORALES, M., MORENO, J., MUNOZ-MARTIN, D., MOLPECERES, C. & CENTRO LÁSER, U. COMSOL® Simulation of Blister Actuated Laser Induced Forward Transfer (BA-LIFT). Proceedings of the 2017 COMSOL Conference in Rotterdam, 2017.

MORENO-LABELLA, J., MORALES, M., MUNOZ-MARTIN, D., MÁRQUEZ, A. & MOLPECERES, C. Influence of pressure history on jet dynamics in LIFT processes: simulation and experimental analysis. 2019 Conference on Lasers and Electro-Optics Europe & European Quantum Electronics Conference (CLEO/Europe-EQEC), 2019. IEEE, 1-1.

doi:10.6342/NTU202301493

MORENO-LABELLA, J., MUNOZ-MARTIN, D., MARQUEZ, A., MORALES, M. & MOLPECERES, C. 2020. Simulation of direct and blister-assisted laser-induced forward transfer techniques. *Procedia CIRP,* 94**,** 873-878.

MORENO-LABELLA, J. J., MUNOZ-MARTIN, D., VALLEJO, G., MOLPECERES, C. & MORALES, M. 2021. Influence of the Gap between Substrates in the Laser-Induced Transference of High-Viscosity Pastes. *Materials,* 14**,** 5567.

MORENO LABELLA, J. J. 2021. *Parametrization and simulation of blister-actuated laser-induced forward transfer (BA-LIFT) and LIFT for high-viscosity pastes.* Industriales.

MOYER, J., WILSON, D., FINKELSHTEIN, I., WONG, B. & POTTS, R. 2012. Correlation between sweat glucose and blood glucose in subjects with diabetes. *Diabetes technology & therapeutics,* 14**,** 398-402.

MUGURUMA, H., KASE, Y. & UEHARA, H. 2005. Nanothin ferrocene film plasma polymerized over physisorbed glucose oxidase: high-throughput fabrication of bioelectronic devices without chemical modifications. *Analytical chemistry,* 77**,** 6557-6562.

NAGEL, M. & LIPPERT, T. 2012. Laser-induced forward transfer for the fabrication of devices. *Nanomaterials: processing and characterization with lasers***,** 255-316.

NG, M. C., LEE, S.-C., KO, G. T., LI, J. K., SO, W.-Y., HASHIM, Y., BARNETT, A. H., MACKAY, I. R., CRITCHLEY, J. A. & COCKRAM, C. S. 2001. Familial early-onset type 2 diabetes in Chinese patients: obesity and genetics have more significant roles than autoimmunity. *Diabetes Care,* 24**,** 663-671.

OHRING, M. 2002. Mechanical properties of thin films. *Materials Science of Thin Films***,** 711-781.

PALLA-PAPAVLU, A., DINCA, V., LUCULESCU, C., SHAW-STEWART, J., NAGEL, M., LIPPERT, T. & DINESCU, M. 2010a. Laser induced forward transfer of soft materials. *Journal of Optics,* 12**,** 124014.

PALLA-PAPAVLU, A., DINCA, V., PARAICO, I., MOLDOVAN, A., SHAW-STEWART, J., SCHNEIDER, C. W., KOVACS, E., LIPPERT, T. & DINESCU, M. 2010b. Microfabrication of polystyrene microbead arrays by laser induced forward transfer. *Journal of applied physics,* 108**,** 033111.

PALLA-PAPAVLU, A., PARAICO, I., SHAW-STEWART, J., DINCA, V., SAVOPOL, T., KOVACS, E., LIPPERT, T., WOKAUN, A. & DINESCU, M. 2011. Liposome micropatterning based on laser-induced forward transfer. *Applied Physics A,* 102**,** 651-659.

PALLA-PAPAVLU, A., PATRASCIOIU, A., DI PIETRANTONIO, F., FERNANDEZ-PRADAS, J.-M., CANNATA, D., BENETTI, M., D'AURIA, S., VERONA, E. & SERRA, P. 2014. Preparation of surface acoustic wave odor sensors by laser-induced forward transfer. *Sensors and Actuators B: Chemical,* 192**,** 369-377.

PAPAKONSTANTINOU, P., VAINOS, N. & FOTAKIS, C. 1999. Microfabrication by UV femtosecond laser ablation of Pt, Cr and indium oxide thin films. *Applied surface science,* 151**,** 159-170.

PAPAZOGLOU, D., KARAISKOU, A., ZERGIOTI, I. & FOTAKIS, C. 2002. Shadowgraphic imaging of the sub-ps laser-induced forward transfer process. *Applied physics letters,* 81**,** 1594-1596.

PAPAZOGLOU, S. & ZERGIOTI, I. 2017. Laser Induced Forward Transfer (LIFT) of nano-micro patterns for sensor applications. *Microelectronic Engineering,* 182**,** 25-34.

doi:10.6342/NTU202301493

PARASHKOV, R., BECKER, E., RIEDL, T., JOHANNES, H.-H. & KOWALSKY, W. 2005. Large area electronics using printing methods. *Proceedings of the IEEE,* 93**,** 1321-1329.

PAULA, K. T., SANTOS, S. N., FACURE, M. H., ARAUJO, F. L., ANDRADE, M. M., CORREA, D. S. & MENDONÇA, C. R. 2023. Fabrication of interdigitated electrodes of graphene oxide/silica by femtosecond laser-induced forward transfer for sensing applications. *Journal of Applied Physics,* 133**,** 053103.

PENG, P., LI, L., HE, P., ZHU, Y., FU, J., HUANG, Y. & GUO, W. 2019. One-step selective laser patterning of copper/graphene flexible electrodes. *Nanotechnology,* 30**,** 185301.

PIQUÉ, A., CHRISEY, D., AUYEUNG, R., FITZ-GERALD, J., WU, H., MCGILL, R., LAKEOU, S., WU, P., NGUYEN, V. & DUIGNAN, M. 1999. A novel laser transfer process for direct writing of electronic and sensor materials. *Applied Physics A,* 69**,** S279-S284.

POHANKA, M. & SKLÁDAL, P. 2008. Electrochemical biosensors--principles and applications. *Journal of applied biomedicine,* 6.

POHL, R. 2015. Laser-Induced Forward Transfer of Pure Metals. *University of Twente*.

POHL, R., VISSER, C., ROMER, G., SUN, C. & LOHSE, D. 2015a. Imaging of the ejection process of nanosecond laser-induced forward transfer of gold. *Journal of laser micro nanoengineering,* 10**,** 154-158.

POHL, R., VISSER, C. W., RÖMER, G.-W., LOHSE, D., SUN, C. & HUIS, B. 2015b. Ejection regimes in picosecond laser-induced forward transfer of metals. *Physical review applied,* 3**,** 024001.

POWNER, E. & YALCINKAYA, F. 1995. From basic sensors to intelligent sensors: definitions and examples. *Sensor Review*.

RAPP, L., AILUNO, J., ALLONCLE, A. P. & DELAPORTE, P. 2011. Pulsed-laser printing of silver nanoparticles ink: control of morphological properties. *Optics express,* 19**,** 21563-21574.

RAPP, L., CIBERT, C., ALLONCLE, A. P. & DELAPORTE, P. 2009a. Characterization of organic material micro-structures transferred by laser in nanosecond and picosecond regimes. *Applied surface science,* 255**,** 5439-5443.

RAPP, L., CONSTANTINESCU, C., DELAPORTE, P. & ALLONCLE, A. P. 2014a. Laser-induced forward transfer of polythiophene-based derivatives for fully polymeric thin film transistors. *Organic electronics,* 15**,** 1868-1875.

RAPP, L., CONSTANTINESCU, C., LARMANDE, Y., ALLONCLE, A. P. & DELAPORTE, P. 2014b. Smart beam shaping for the deposition of solid polymeric material by laser forward transfer. *Applied Physics A,* 117**,** 333-339.

RAPP, L., CONSTANTINESCU, C., LARMANDE, Y., DIALLO, A. K., VIDELOT-ACKERMANN, C., DELAPORTE, P. & ALLONCLE, A. P. 2015. Functional multilayered capacitor pixels printed by picosecond laser-induced forward transfer using a smart beam shaping technique. *Sensors and Actuators A: Physical,* 224**,** 111-118.

RAPP, L., DIALLO, A. K., ALLONCLE, A. P., VIDELOT-ACKERMANN, C., FAGES, F. & DELAPORTE, P. 2009b. Pulsed-laser printing of organic thin-film transistors. *Applied Physics Letters,* 95**,** 171109.

doi:10.6342/NTU202301493

RAPP, L., SEREIN-SPIRAU, F., LÈRE-PORTE, J.-P., ALLONCLE, A.-P., DELAPORTE, P., FAGES, F. & VIDELOT-ACKERMANN, C. 2012. Laser printing of air-stable high performing organic thin film transistors. *Organic Electronics,* 13**,** 2035-2041.

RINGEISEN, B., CALLAHAN, J., WU, P., PIQUE, A., SPARGO, B., MCGILL, R., BUCARO, M., KIM, H., BUBB, D. & CHRISEY, D. 2001. Novel laser-based deposition of active protein thin films. *Langmuir,* 17**,** 3472-3479.

RODA, A., GUARDIGLI, M., RUSSO, C., PASINI, P. & BARALDINI, M. 2000. Protein microdeposition using a conventional ink-jet printer. *Biotechniques,* 28**,** 492-496.

SANO, T., YAMADA, H., NAKAYAMA, T. & MIYAMOTO, I. 2002. Experimental investigation of laser induced forward transfer process of metal thin films. *Applied surface science,* 186**,** 221-226.

SANTA-NOKKI, H., KALLIOINEN, J., KOLOLUOMA, T., TUBOLTSEV, V. & KORPPI-TOMMOLA, J. 2006. Dynamic preparation of TiO2 films for fabrication of dye-sensitized solar cells. *Journal of Photochemistry and Photobiology A: Chemistry,* 182**,** 187-191.

SCHAAF, P. 2010. *Laser processing of materials: fundamentals, applications and developments*, Springer Science & Business Media.

SEDAGHAT, S., NEJATI, S., BERMEJO, L. H., HE, Z., ALCARAZ, A. M., ROTH, A., LI, Z., POL, V. G., WANG, H. & RAHIMI, R. 2021. Laser-induced atmospheric Cu x O formation on copper surface with enhanced electrochemical performance for non-enzymatic glucose sensing. *Journal of Materials Chemistry C,* 9**,** 14997-15010.

SEIFERT, N. & BETZ, G. 1998. Computer simulations of laser-induced ejection of droplets. *Applied surface science,* 133**,** 189-194.

SEIFERT, N., BETZ, G. & HUSINSKY, W. 1996a. Droplet formation on metallic surfaces during low-fluence laser irradiation. *Applied surface science,* 103**,** 63-70.

SEIFERT, N., BETZ, G. & HUSINSKY, W. 1996b. Hydrodynamic phenomena during laser irradiation: a finite difference approach. *Applied surface science,* 96**,** 33-38.

SEMPIONATTO, J. R., MOON, J.-M. & WANG, J. 2021. Touch-based fingertip blood-free reliable glucose monitoring: Personalized data processing for predicting blood glucose concentrations. *ACS sensors,* 6**,** 1875-1883.

SERRA, P., COLINA, M., FERNÁNDEZ-PRADAS, J. M., SEVILLA, L. & MORENZA, J. L. 2004. Preparation of functional DNA microarrays through laser-induced forward transfer. *Applied physics letters,* 85**,** 1639-1641.

SERRA, P., DUOCASTELLA, M., FERNÁNDEZ-PRADAS, J. & MORENZA, J. 2010. Laser-induced forward transfer: a laser-based technique for biomolecules printing. *Cell and Organ Printing***,** 53-80.

SERRA, P., FERNANDEZ-PRADAS, J. M., COLINA, M., DUOCASTELLA, M., DOMINGUEZ, J. & MORENZA, J. L. 2006. Laser-induced forward transfer: a direct-writing technique for biosensors preparation. *J. Laser Micro/Nanoeng,* 1**,** 236-242.

SERRA, P. & PIQUÉ, A. 2019. Laser-induced forward transfer: fundamentals and applications. *Advanced Materials Technologies,* 4**,** 1800099.

SETTI, L., FRALEONI-MORGERA, A., BALLARIN, B., FILIPPINI, A., FRASCARO, D. & PIANA, C. 2005. An amperometric glucose biosensor prototype fabricated by thermal inkjet printing. *Biosensors and Bioelectronics,* 20**,** 2019-2026.

doi:10.6342/NTU202301493

SHAW-STEWART, J., CHU, B., LIPPERT, T., MANIGLIO, Y., NAGEL, M., NŘESCH, F. & WOKAUN, A. 2011. Improved laser-induced forward transfer of organic semiconductor thin films by reducing the environmental pressure and controlling the substrate–substrate gap width. *Applied Physics A,* 105**,** 713-722.

SHAW-STEWART, J., MATTLE, T., LIPPERT, T., NAGEL, M., NÜESCH, F. & WOKAUN, A. 2013. The fabrication of small molecule organic light-emitting diode pixels by laser-induced forward transfer. *Journal of Applied Physics,* 113**,** 043104.

SICREE, R., SHAW, J. & ZIMMET, P. 2006. Prevalence and projections. *Diabetes atlas,* 3**,** 16-104.

SKOTADIS, E., VOUTYRAS, K., CHATZIPETROU, M., TSEKENIS, G., PATSIOURAS, L., MADIANOS, L., CHATZANDROULIS, S., ZERGIOTI, I. & TSOUKALAS, D. 2016. Label-free DNA biosensor based on resistance change of platinum nanoparticles assemblies. *Biosensors and Bioelectronics,* 81**,** 388-394.

SMOOTH-ON. *Durometer Shore Hardness Scale* [Online]. Available: https://www.smooth-on.com/page/durometer-shore-hardness-scale/ [Accessed].

SOLTANI, A., VAHED, B. K., MARDOUKHI, A. & MÄNTYSALO, M. 2015. Laser sintering of copper nanoparticles on top of silicon substrates. *Nanotechnology,* 27**,** 035203.

STEWART, J. S., FARDEL, R., NAGEL, M., DELAPORTE, P., RAPP, L., CIBERT, C., ALLONCLE, A., NÜESCH, F., LIPPERT, T. & WOKAUN, A. 2010a. The effect of laser pulse length upon laser-induced forward transfer using a triazene polymer as a dynamic release layer. *Journal of Optoelectronics and Advanced Materials,* 12**,** 605-609.

STEWART, J. S., LIPPERT, T., NAGEL, M., NÜESCH, F. & WOKAUN, A. Laser-Induced Forward Transfer Using Triazene Polymer Dynamic Releaser Layer. AIP Conference Proceedings, 2010b. American Institute of Physics, 789-799.

STRUTT, J. W. & RAYLEIGH, L. 1878. On the instability of jets. *Proc. London Math. Soc,* 10**,** 4-13.

TANG, Q. & SHI, S.-Q. 2008. Preparation of gas sensors via dip-pen nanolithography. *Sensors and Actuators B: Chemical,* 131**,** 379-383.

TAYLOR, G. I. 1950. The formation of a blast wave by a very intense explosion I. Theoretical discussion. *Proceedings of the Royal Society of London. Series A. Mathematical and Physical Sciences,* 201**,** 159-174.

TEE, S. Y., TENG, C. P. & YE, E. 2017. Metal nanostructures for non-enzymatic glucose sensing. *Materials Science and Engineering: C,* 70**,** 1018-1030.

THOMAS, B., ALLONCLE, A. P., DELAPORTE, P., SENTIS, M., SANAUR, S., BARRET, M. & COLLOT, P. 2007. Experimental investigations of laser-induced forward transfer process of organic thin films. *Applied Surface Science,* 254**,** 1206-1210.

TOOLBOX, T. E. *Metals and Alloys - Young's Modulus of Elasticity* [Online]. Available: https://www.engineeringtoolbox.com/young-modulus-d_773.html [Accessed 20 January 2023].

TOTH, Z., HOPP, B., KANTOR, Z., IGNACZ, F., SZOERENYI, T. & BOR, Z. Dynamics of excimer laser ablation of thin tungsten films studied by fast photography. Laser Materials Processing: Industrial and Microelectronics Applications, 1994. SPIE, 776-783.

doi:10.6342/NTU202301493

TÓTH, Z., SZÖRÉNYI, T. & TOTH, A. 1993. Ar+ laser-induced forward transfer (LIFT): a novel method for micrometer-size surface patterning. *Applied surface science,* 69**,** 317-320.

TOULOUPAKIS, E., BOUTOPOULOS, C., BUONASERA, K., ZERGIOTI, I. & GIARDI, M. T. 2012. A photosynthetic biosensor with enhanced electron transfer generation realized by laser printing technology. *Analytical and bioanalytical chemistry,* 402**,** 3237-3244.

TOULOUPAKIS, E., CHATZIPETROU, M., BOUTOPOULOS, C., GKOUZOU, A. & ZERGIOTI, I. 2014. A polyphenol biosensor realized by laser printing technology. *Sensors and Actuators B: Chemical,* 193**,** 301-305.

TSEKENIS, G., CHATZIPETROU, M., TANNER, J., CHATZANDROULIS, S., THANOS, D., TSOUKALAS, D. & ZERGIOTI, I. 2012. Surface functionalization studies and direct laser printing of oligonucleotides toward the fabrication of a micromembrane DNA capacitive biosensor. *Sensors and actuators B: Chemical,* 175**,** 123-131.

TSEKENIS, G., FILIPPIDOU, M., CHATZIPETROU, M., TSOUTI, V., ZERGIOTI, I. & CHATZANDROULIS, S. 2015. Heavy metal ion detection using a capacitive micromechanical biosensor array for environmental monitoring. *Sensors and actuators B: Chemical,* 208**,** 628-635.

TSUBOI, Y., FURUHATA, Y. & KITAMURA, N. 2007. A sensor for adenosine triphosphate fabricated by laser-induced forward transfer of luciferase onto a poly (dimethylsiloxane) microchip. *Applied surface science,* 253**,** 8422-8427.

TUOMIKOSKI, M., SUHONEN, R., VÄLIMÄKI, M., MAANINEN, T., MAANINEN, A., SAUER, M., ROGIN, P., MENNIG, M., HEUSING, S. & PUETZ, J. Manufacturing of polymer light-emitting device structures. Organic Optoelectronics and Photonics II, 2006. SPIE, 14-22.

TURNER, A. P. 2013. Biosensors: sense and sensibility. *Chemical Society Reviews,* 42**,** 3184-3196.

UDIN, H. 1949. *Surface tension of solid copper.* Massachusetts Institute of Technology.

VISSER, C., POHL, R., SUN, C. & RÖMER, G. 2015. Huis in 't Veld B, Lohse D. Toward 3D printing of pure metals by laser-induced forward transfer. *Adv. Mater,* 27**,** 4087-4092.

VISWANATHAN, M., MCCARTHY, M., SNEHALATHA, C., HITMAN, G. & RAMACHANDRAN, A. 1996. Familial aggregation of type 2 (non-insulin-dependent) diabetes mellitus in South India; absence of excess maternal transmission. *Diabetic medicine,* 13**,** 232-237.

VOLINSKY, A., TYMIAK, N., KRIESE, M., GERBERICH, W. W. & HUTCHINSON, J. 1998. Quantitative modeling and measurement of copper thin film adhesion. *MRS Online Proceedings Library (OPL),* 539**,** 277.

VORA, H. D., SANTHANAKRISHNAN, S., HARIMKAR, S. P., BOETCHER, S. K. & DAHOTRE, N. B. 2013. One-dimensional multipulse laser machining of structural alumina: evolution of surface topography. *The International Journal of Advanced Manufacturing Technology,* 68**,** 69-83.

WANG, J., AUYEUNG, R. C., KIM, H., CHARIPAR, N. A. & PIQUÉ, A. 2010. Three-dimensional printing of interconnects by laser direct-write of silver nanopastes. *Advanced Materials,* 22**,** 4462-4466.

doi:10.6342/NTU202301493

WILD, S., ROGLIC, G., GREEN, A., SICREE, R. & KING, H. 2004. Global prevalence of diabetes: estimates for the year 2000 and projections for 2030. *Diabetes care,* 27**,** 1047-1053.

WILLIS, D. A. & GROSU, V. 2005. Microdroplet deposition by laser-induced forward transfer. *Applied Physics Letters,* 86**,** 244103.

WILLIS, D. A. & GROSU, V. 2007. The effect of melting-induced volumetric expansion on initiation of laser-induced forward transfer. *Applied surface science,* 253**,** 4759-4763.

WU, P., RINGEISEN, B., CALLAHAN, J., BROOKS, M., BUBB, D., WU, H., PIQUÉ, A., SPARGO, B., MCGILL, R. & CHRISEY, D. 2001. The deposition, structure, pattern deposition, and activity of biomaterial thin-films by matrix-assisted pulsed-laser evaporation (MAPLE) and MAPLE direct write. *Thin Solid Films,* 398**,** 607-614.

WYSOCKA, I., KOWALSKA, E., RYL, J., NOWACZYK, G. & ZIELIŃSKA-JUREK, A. 2019. Morphology, photocatalytic and antimicrobial properties of TiO2 modified with mono-and bimetallic copper, platinum and silver nanoparticles. *Nanomaterials,* 9**,** 1129.

YAMANAKA, K., VESTERGAARD, M. D. C. & TAMIYA, E. 2016. Printable electrochemical biosensors: A focus on screen-printed electrodes and their application. *Sensors,* 16**,** 1761.

YAN, J., HUANG, Y. & CHRISEY, D. B. 2012. Laser-assisted printing of alginate long tubes and annular constructs. *Biofabrication,* 5**,** 015002.

YANG, G. & ZHOU, J. The annealing effect on optical properties of silver copper alloy films. Applied Mechanics and Materials, 2013. Trans Tech Publ, 329-335.

YENER, T., YENER, Ş. Ç. & MUTLU, R. 2019. Convection Coefficient Estimation of Still Air Using an Infrared Thermometer and Curve-Fitting. *Journal of Engineering Technology and Applied Sciences,* 4**,** 95-103.

YOSHIMURA, K. & HOZUMI, K. 1996. Response characteristics of a glucose electrode with a sensing membrane prepared by plasma polymerization. *Microchemical journal,* 53**,** 404-412.

YOSHIMURA, K., KITADE, T., KITAMURA, K. & HOZUMI, K. 1991. Preparation of immobilized glucose oxidase membrane by the plasma polymerization technique. *Microchemical journal,* 43**,** 133-142.

YUNG, W. K., SUN, B., MENG, Z., HUANG, J., JIN, Y., CHOY, H. S., CAI, Z., LI, G., HO, C. L. & YANG, J. 2016. Additive and photochemical manufacturing of copper. *Scientific reports,* 6**,** 1-9.

ZAIDI, S. A. & SHIN, J. H. 2016. Recent developments in nanostructure based electrochemical glucose sensors. *Talanta,* 149**,** 30-42.

ZENG, X., MAO, X., GREIF, R. & RUSSO, R. 2005. Experimental investigation of ablation efficiency and plasma expansion during femtosecond and nanosecond laser ablation of silicon. *Applied Physics A,* 80**,** 237-241.

ZENOU, M., SA'AR, A. & KOTLER, Z. 2015a. Laser transfer of metals and metal alloys for digital microfabrication of 3D objects. *Small,* 11**,** 4082-4089.

ZENOU, M., SA'AR, A. & KOTLER, Z. 2015b. Supersonic laser-induced jetting of aluminum micro-droplets. *Applied Physics Letters,* 106**,** 181905.

ZENOU, M., SA'AR, A. & KOTLER, Z. 2015c. Digital laser printing of aluminum micro-structure on thermally sensitive substrates. *Journal of Physics D: Applied Physics,* 48**,** 205303.

doi:10.6342/NTU202301493

ZENOU, M., SA'AR, A. & KOTLER, Z. 2015d. Laser jetting of femto-liter metal droplets for high resolution 3D printed structures. *Scientific reports,* 5**,** 17265.
ZERGIOTI, I., KARAISKOU, A., PAPAZOGLOU, D., FOTAKIS, C., KAPSETAKI, M. & KAFETZOPOULOS, D. 2005. Time resolved schlieren study of sub-pecosecond and nanosecond laser transfer of biomaterials. *Applied Surface Science,* 247**,** 584-589.
ZERGIOTI, I., MAILIS, S., VAINOS, N., FOTAKIS, C., CHEN, S. & GRIGOROPOULOS, C. 1998a. Microdeposition of metals by femtosecond excimer laser. *Applied Surface Science,* 127**,** 601-605.
ZERGIOTI, I., MAILIS, S., VAINOS, N., PAPAKONSTANTINOU, P., KALPOUZOS, C., GRIGOROPOULOS, C. & FOTAKIS, C. 1998b. Microdeposition of metal and oxide structures using ultrashort laser pulses. *Applied Physics A: Materials Science & Processing,* 66**,** 579-582.
ZHOU, X., GUO, W., FU, J., ZHU, Y., HUANG, Y. & PENG, P. 2019. Laser writing of Cu/CuxO integrated structure on flexible substrate for humidity sensing. *Applied Surface Science,* 494**,** 684-690.
ZHOU, X., GUO, W., YAO, Y., PENG, R. & PENG, P. 2021. Flexible Nonenzymatic Glucose Sensing with One-Step Laser-Fabricated Cu2O/Cu Porous Structure. *Advanced Engineering Materials,* 23**,** 2100192.
ZHU, J., CAO, W., JIANG, B., ZHANG, D., ZHENG, H., ZHOU, Q. & SHUNG, K. 2008. Nano-structured TiO2 film fabricated at room temperature and its acoustic properties. *Journal of physics D: Applied physics,* 41**,** 162001.

doi:10.6342/NTU202301493